Doctoral thesis

Theoretical studies on electroweak baryogenesis with extended Higgs sectors

Yushi Mura

Department of Physics, Osaka University, Toyonaka, Osaka 560-0043, Japan

Acknowledgements

First of all, I would like to acknowledge Prof. Shinya Kanemura, who is my supervisor of my research in Ph.D course. He gave me a lot of advice for research, fellowships, grants and life, and totally supported my Ph.D course. As the members of the doctoral thesis review committee, I am grateful to Associated Prof. Ryosuke Sato, Assistant Prof. Kei Yagyu, Prof. Testuya Onogi, and Associated Prof. Tatsuya Masubuchi for careful reading of this Ph.D thesis and giving worth comments to improve this Ph.D thesis. I also thank to other faculty members, Prof. Tatsuma Nishioka, Associated Prof. Satoshi Yamaguchi, Associate Prof. Norihiro Iizuka, Assistant Prof. Hidenori Fukaya, and Assistant Prof. Minoru Tanaka for providing good environment for active discussions. I also acknowledge Kazumi Asano, who is the secretary of the theory group, for doing many administrative procedures. As collaborators of my researches comprising this Ph.D thesis, I thank Dr. Kazuki Enomoto and Mr. Guohao Ying for spending much time to discuss physics. I also thank Prof. Tetsuo Shindou, Associated Prof. Motoi Endo, and Dr. Masashi Aiko for worthwhile discussions. I acknowledge all of the students and postdocs in particle physics group in Osaka University, especially, Dr. Shaoping Li, Mr. Ricardo Florentino, Mr. Sora Taniguchi, Mr. Takumu Yamanaka, Mr. Takaya Iwai, Mr. Ryuichi Tamura, Mr. Leonard Humphrey, Mr. Ryoma Masuda, and Mr. Fukataro Miya, who are the members of the phenomenology group. As nice colleagues, I thank Dr. Naoto Kan, Dr. Shoto Aoki, Mr. Hiroki Wada, and Mr. Soichiro Shimamori. During my Ph.D course, I have been supported by fellowships from Osaka University Honors Program for Graduate Schools in Science, Engineering and Informatics, and Osaka University Next Generation Researcher Development Project (JST SPRING, Grant No. JPMJSP2138). In the last two years of my Ph.D course, I have been supported by the grant from Japan Society for the Promotion of Science (the JSPS Grant-in-Aid for JSPS Fellows No. 23KJ1460). Finally, I would like to say thank you my family and Ayu Hiraoka for their understanding and for supporting my life.

Abstract

In this Ph.D thesis, we discuss electroweak baryogenesis in extended Higgs models. Despite the standard model has been established by the discovery of the Higgs boson, there are still some problems, which cannot be solved by the standard model. The baryon asymmetry of the Universe is one of them, and the particle and anti-particle asymmetry should be generated after the inflation: baryogenesis. Electroweak baryogenesis is one of the baryogenesis scenarios, the scale of which is the electroweak scale. Unfortunately, electroweak baryogenesis cannot be realized in the standard model, however, it becomes possible by considering the extended Higgs sector. Models for electroweak baryogenesis can be tested in future experiments, so that they can be well motivated to explore beyond the standard model. In the scenario of electroweak baryogenesis, electroweak first order phase transition and new sources of CP violation are needed, and new physics effects causing them appear in many physical observables. In this Ph.D thesis, we propose viable models and scenarios for electroweak baryogenesis under the current experimental data, and study phenomenology of the model. We discuss the phenomenological consequences of the first order electroweak phase transition and the CP violation in the extended Higgs models, and discuss how to test the model in future experiments. Especially, we focus on the $H^{\pm}W^{\mp}Z$ vertices, and we point out that it can be a probe of the CP violation in the model. We also discuss the Landau pole problem, which is known as a theoretical problem of electroweak baryogenesis. We find that this problem can be remedied by giving a new way to treat it. We also discuss an extended Higgs model with the $\mathrm{U}(1)_{B-L}$ gauge symmetry, in which the problems of not only the baryon asymmetry of the Universe but also the tiny mass of the neutrino and the relic abundance of the dark matter might be solved. We show that the problems of the neutrino mass and the dark matter can be solved under current experimental data.

Contents

Chapter 1

Introduction and summary of thesis

1.1 Introduction

For almost a century, the theory of elementary particle physics has been developed. The Standard Model (SM) [1–8] is a model for the electroweak and strong interactions of the elementary particles. Various phenomena of the particles are explained by the SM, and so far, almost all results in high energy collider experiments, flavor experiments, cosmological observations, and so on, are consistent with the prediction in the SM. By the discovery of the Higgs boson [9] at Large Hadron Collider (LHC) [10, 11], the existence of all the particles in the SM has been confirmed, so that the SM has been established as the most successful theory in particle physics.

However, the SM is not the perfect theory, because there are some unsolved problems Beyond the SM (BSM). The SM includes the electroweak and strong forces, but the gravity is not. There are large hierarchy between the Planck scale for the gravity ($O(10^{19})$ GeV) and the electroweak scale ($O(10^2)$ GeV), which inspires extension of the SM with the supersymmetry [12], technicolor theory [13, 14], extra dimension [15], and so on. We do not know the origin of these forces. It is still a mystery whether the electroweak and strong forces are unified or not (Grand Unified Theory: GUT [16]). In the SM, there are three generations for the quarks and the leptons. All the fermions in the SM get their masses from the Higgs boson, but the strengths of the Yukawa couplings are greatly different among the flavors. This flavor structure is also one of the problems in the SM.

In addition to the theoretical side of the problems beyond the SM, we have already known some phenomena in the experiments, which cannot be explained in the SM. For example, there are three big phenomenological problems, the mass origin of the neutrino mass, the problem of the dark sector, and the origin of the baryon asymmetry of the Universe. In the SM, the neutrinos are massless. However, by the observation of the oscillation of the atmospheric neutrino, the existence of the mass of the neutrino has been verified [17]. By the cosmological observations, it has been confirmed that the dark matter occupies almost 25% of the total energy of our Universe, and almost 70% is the dark energy, which accelerates the Universe expanding [18]. No candidates of them are contained in the SM. As visible contents of the energy density of the Universe, the baryons occupy the remaining almost 5%, while the antibaryons have not been observed in the Universe [18]. This means that our Universe is baryon asymmetric, and the origin of the Baryon Asymmetry of the Universe (BAU) cannot be solved in the SM.

Due to the remaining problems, it has been believed that our nature is described by a more fundamental theory beyond the SM. Some of those problems are related to the Higgs sector, which is not completely understood by the experiments, even after the discovery of the Higgs boson. Although we know the mass of the Higgs boson as 125 GeV, and some of the Higgs-gauge couplings and the Higgs-fermion couplings have been measured at LHC [19, 20], we do

not know the global structure of the Higgs sector. In this sense, whether the discovered Higgs at LHC is really the SM Higgs or not is still unknown.

Once we extend the Higgs sector, some of the problems can be solved, so that a lot of extended Higgs models have been proposed in many literature. Such extended Higgs models are motivated by testability in future experiments. Currently, the precision of the Higgs couplings is at most $O(10)\%$ level (e.g. the couplings between the Higgs and the W, Z bosons). In High-Luminosity LHC (HL-LHC), these couplings will be measured with about one order higher precision [21]. In International Linear Collider (ILC), which is one of the future linear e^+e^- colliders, various Higgs couplings will be measured very precisely. For example, the Higgs and the Z bosons coupling will be measured with about 0.5% precision at ILC with the center-energy-mass $\sqrt{s} = 250$ GeV [22]. The triple Higgs coupling is important to know the feature of the Electroweak Phase Transition (EWPT) in the early Universe [23], and it is expected to be measured at the 50% and 27% (10%) accuracy, in the HL-LHC and the ILC with $\sqrt{s} = 500$ GeV ($\sqrt{s} = 1$ TeV), respectively [21, 24, 25]. Through those experiments, a breakdown of the Higgs sector of the SM might be seen in the future. Therefore, studying non-minimal Higgs sectors is important to approach more fundamental theory.

In those extended Higgs sectors, the BSM problems can be solved by effects of new particles. In this Ph.D thesis, we focus on the problems of the neutrino mass, the DM, and the BAU. Especially, most parts of the Ph.D thesis are spent by discussing a scenario solving the BAU at the electroweak scale in the extended Higgs models. We also discuss the DM problem and the origin of the neutrino mass with the extended Higgs sector. In the following, brief introductions of the problem for the BAU in extended Higgs models are given.

To explain the BAU, we usually consider a mechanism generating the baryon asymmetry after the inflation of the Universe, because even if our Universe initially has an asymmetry, it will be smeared by the exponential inflation. This is "baryo"genesis. For baryogenesis, it has been known that the theory needs to have (1) baryon number violating process, (2) C and CP violation, (3) a mechanism for decoupling from the thermal equilibrium. These conditions are known as the Sakharov three conditions [26].

Electroweak Baryogenesis (EWBG) is one of the baryogenesis scenarios, in which the baryon asymmetry is generated with physics at the electroweak scale [27]. In the SM, the baryon number violating process exists at the loop level, and it is enhanced by the thermal effects (sphaleron process) [28]. The C and CP symmetry are violated by the chiral electroweak interaction and the Cabbibo–Kobayashi–Masukawa (CKM) phase [29, 30] in the quark sector, respectively. If the EWPT in the early Universe is the Strongly First Order Phase Transition (SFOPT), where the sphaleron process is in non-thermal equilibrium, the third condition is satisfied. However, in the SM, not only the CKM is insufficient to generate the observed BAU [31], but also the discovered Higgs boson with 125 GeV does not cause the SFOPT [32,33]. Therefore, we need to consider extending the Higgs sector to satisfy the conditions for the CP violation and the non-thermal equilibrium situation.

The scenario of EWBG in the extended Higgs sector has been studied for a long time. Especially, EWBG in the two Higgs Doublet Model (2HDM), in which a new $\mathrm{SU}(2)_L$ scalar doublet is added to the SM Lagrangian, has been studied in many literature [34–50]. New CP violation can easily be introduced in a relative phase of the two doublets or in new interaction between the SM fermion and the additional doublet [30]. The status of the EWPT in the model is also drastically changed from the SM, and the SFOPT is realized by quantum effects of the additional scalar bosons [51–53]. The EWBG in models with $\mathrm{SU}(2)_L$ singlet scalar is also well studied [54–57].

EWBG is physics at the electroweak scale, so that new physics effects appear in many observables for various experiments. Therefore, EWBG is the testable baryogenesis scenario in future many experiments. The SFOPT in the 2HDM can be tested by the measurement

for the deviation of the triple Higgs coupling from the SM value [23]. In addition, it has been known that the SFOPT causes stochastic gravitational waves which are generated by the bubble collision [58–62]. Therefore, the SFOPT can also be tested by the observations at future space-based interferometers, such as LISA [63], DECIGO [64] and BBO [65]. The effects of new CP violation can be measured by the Electric Dipole Moment (EDM) experiments, collider experiments, and flavor experiments.

On the contrary to the testability of EWBG, constraints of EWBG in extended Higgs models are also severe. Therefore, it is not trivial that models for EWBG satisfy current experimental data. One of the most stringent constraints is from the EDM experiments, and they give upper bounds on the CP phases in the models. In addition, the electroweak precision results in LEPII and LHC show the ρ parameter [66–70] is very close to unity [71–73]. This implies that a global symmetry in the Higgs sector, the custodial symmetry [74], is respected in the model. Current Higgs boson measurement in LHC [19, 20] also supports the SM-like Higgs boson. The absence of the Flavor Changing Neutral Current (FCNC) in collider and flavor experiments is also an important fact that the Yukawa structure is similar to the SM. From these constraints, e.g., the usual EWBG scenario in the 2HDM with the softly broken $\mathbb{Z}_2$ symmetry [36, 44, 46, 50], in which the FCNC current is forbidden, is difficult to satisfy current experimental data. Even so, there is still viable model such as the model with singlet scalar bosons [54–57], and the general 2HDM [37, 41–43, 45, 47–49], and so on. It is important to study what observables can be a probe of EWBG and how to test those models in the future.

In addition to the phenomenological difficulty, in some classes of the models such as the 2HDM, a theoretical problem has also been known. To realize the SFOPT in the 2HDM, relatively large scalar self couplings are needed. Due to the positiveness of the leading contribution of the scalar beta function, the Landau pole, where the coupling constants diverge, appears in a relatively low scale. If this scale is much lower scale than the scale of the high energy collider experiments, we already should see new physics effects. This problem is sometimes seriously taken [37, 44, 75].

As we have mentioned, in this Ph.D thesis, the mass origin of the neutrino, the DM problem, and the scenario of EWBG in the extended Higgs models are discussed. In the following paragraphs and the next section, an introduction of the author's works and the corresponding chapters are given.

After reviewing the SM and the extended Higgs models, we first present a successful model for explaining the neutrino mass and the DM under the current experiments. This model has originally been proposed by Ref. [76], however, we revisit this model with the currently available experimental data. As a result, we find still viable benchmark points in the model, which have not been recognized in the previous works [76–78]. We do not discuss baryogenesis in this model, however, as a first step to propose the viable model explaining those three problems, we show the results for the neutrino and the DM.

Second, We discuss EWBG in the 2HDM, and the viable scenarios for EWBG under experimental data are shown. We focus on the general 2HDM, which contains multiple CP phases, and show that the observed BAU can be explained with the top transport scenario [37, 47, 48, 79]. In this scenario, the severe constraints from the electron EDM can be avoided by using destructive interference of those multiple phases [80–83]. The phenomenological consequences of this scenario are also given. We also discuss another scenario of EWBG in this model for the Yukawa interaction having the FCNC couplings in the top-charm sector. We point out that the effects of the CP phase of the FCNC coupling to the BAU are much smaller compared to what was estimated in the previous studies [41, 43]. We also discuss the characteristic consequences of this top-charm transport scenario in the context of flavor physics.

Third, as an observable in the general 2HDM, we discuss loop induced $H^{\pm}W^{\mp}Z$ vertices [84, 85]. We find the relation among the custodial symmetry, the CP symmetry, and these vertices

in the general 2HDM, and give complete calculations of these vertices at the one-loop level. As an important consequence of the CP violation in the model, we point out that the difference between the decays $H^+ \to W^+ Z$ and $H^- \to W^- Z$ arises, so that they are sensitive to the CP phases in the model.

Finally, we discuss the Landau pole problem for the SFOPT. We analyze the renormalization group equation with a physical renormalization scheme, where the threshold effects of heavy particles are naturally included. As a result of taking into account these effects, we find the Landau pole problem can be weaker than previously considered.

1.2 Summary of author's works

The chapters which comprise this Ph.D thesis are based on the following author's works.

- Chapter 5

  [86] S. Kanemura, **Y. Mura**, and G. Ying. "Revisiting the model for radiative neutrino masses with dark matter in the $U(1)_{B-L}$ gauge theory", arXiv:2410.22835 [hep-ph]

- Chapter 7

  [47] K. Enomoto, S. Kanemura and **Y. Mura**, "Electroweak baryogenesis in aligned two Higgs doublet models", *JHEP* 01 (2022), p. 104.

  [48] K. Enomoto, S. Kanemura and **Y. Mura**, "New benchmark scenarios of electroweak baryogenesis in aligned two Higgs double models", *JHEP* 09 (2022), p. 121.

  [49] S. Kanemura and **Y. Mura**, "Electroweak baryogenesis via top-charm mixing", *JHEP* 09 (2023), p. 153.

- Chapter 8

  [87] S. Kanemura and **Y. Mura**, "Loop induced $H^{\pm}W^{\mp}Z$ vertices in the general two Higgs doublet model with CP violation", *JHEP* 10 (2024), p. 41.

- Chapter 9

  [88] S. Kanemura and **Y. Mura**, "Criterion of perturbativity with the mass-dependent beta function in extended Higgs models", *Phys.Rev.D* 110 (2024) 7, 075016.

1.3 Organization

This Ph.D thesis is organized as follows. In chapter 2, we review the SM, which is a theory of the electroweak and strong forces. In chapter 3, the remaining problems of the SM, especially the problems of the origin of the neutrino mass, the DM, and the BAU are introduced. In chapter 4, we introduce the 2HDM and the model for the neutrino mass and the DM with the $U(1)_{B-L}$ gauge, and some features of the models are explained. In chapter 5, based on the author's work [86], we discuss the neutrino mass and the DM problem in the extended Higgs model with $U(1)_{B-L}$ symmetry, and show the viable benchmark points for these problems under current experiments. In chapter 6, we review EWBG as a solution for the BAU. We give explanations of the mechanism of EWBG, the CP violation and the EDM, and methods to calculate the BAU in the scenario of EWBG. In chapter 7, based on the author's works [47–49], EWBG in the 2HDM is discussed. We explain the two scenarios, top-transport and top-charm transport scenarios, for the different structures of the Yukawa interaction in the model. In chapter 8, based on the author's work [87], the $H^{\pm}W^{\mp}Z$ vertices as a probe of the CP violation in the 2HDM are introduced, and the results of the decays $H^{\pm} \to W^{\pm}Z$ through these vertices are shown. We show that these vertices are sensitive to the CP violation in the model. In chapter 9, based on the author's work [88] the Landau pole problem in EWBG is introduced. We revisit this problem in some models for SFOPT, and propose an appropriate way to include threshold effects of heavy particles. In chapter 10, the summary of this Ph.D thesis is given. In appendixes A-F, some formulae and discussions, which are omitted in the main text, are shown.

Chapter 2

Standard Model

In this chapter, we review the SM (Glashow–Weinberg–Salam model [1–3] and quantum chromo dynamics [4–8]), in which phenomena of elementary particles with the strong and electroweak forces are explained.

2.1 Particle contents

The SM gauge group is composed of $\mathrm{SU}(3)_C \times \mathrm{SU}(2)_L \times \mathrm{U}(1)_Y$. The particle contents and charges under this gauge group are given by table. 2.1. We define the Nishijima–Gelmann relation as

$$Q_{\mathrm{em}} = T^3 + Y, \tag{2.1}$$

where Q_{em}, T^3 and Y are the electromagnetic charge, the $\mathrm{SU}(2)_L$ isospin charge, and the hypercharge.

We introduce the gauge bosons for $\mathrm{SU}(2)_L$ and $\mathrm{U}(1)_Y$ symmetries as W^a_μ $(a = 1, 2, 3)$ and B_μ, respectively. The gauge interaction for the leptons is written by

$$\begin{aligned}\mathcal{L}^{lepton} = & \sum_{i=1}^{3} \overline{L'_{iL}} i\gamma^\mu \left(\partial_\mu - ig\frac{\tau^a}{2}W^a_\mu - i\frac{-1}{2}g'B_\mu\right) L'_{iL} \\ & + \sum_{i=1}^{3} \overline{e'_{iR}} i\gamma^\mu \left(\partial_\mu - (-1)ig'B_\mu\right) e'_{iR},\end{aligned} \tag{2.2}$$

where τ^a is the Pauli matrix, $i = 1, 2, 3$ is the flavor (generation) index, and g and g' are the gauge couplings for $\mathrm{SU}(2)_L$ and $\mathrm{U}(1)_Y$ symmetries, respectively. The left-handed $\mathrm{SU}(2)_L$ lepton doublets L'_{iL} and the right-handed $\mathrm{SU}(2)_L$ lepton singlets e'_{iR} are defined by

$$\begin{aligned}& L'_{1L} \equiv \begin{pmatrix}\nu'_{eL} \\ e'_L\end{pmatrix}, \quad L'_{2L} \equiv \begin{pmatrix}\nu'_{\mu L} \\ \mu'_L\end{pmatrix}, \quad L'_{3L} \equiv \begin{pmatrix}\nu'_{\tau L} \\ \tau'_L\end{pmatrix}, \\ & e'_{1R} \equiv e'_R, \quad e'_{2R} \equiv \mu'_R, \quad e'_{3R} \equiv \tau'_R,\end{aligned} \tag{2.3}$$

where the subscripts L and R express the chiral projection by the operator $P_L = (1 - \gamma^5)/2$ and $P_R = (1 + \gamma^5)/2$, respectively. We here have used the primed fields to explicitly show that the fermions are defined in the gauge eigenstate. We later define the mass eigenstate for the SM fermions.

As similar to the lepton sector, the gauge interaction for the quarks is written by

$$\mathcal{L}^{quark} = \sum_{i=1}^{3} \overline{Q'_{iL}} i\gamma^\mu \left(\partial_\mu - ig\frac{\tau^a}{2}W^a_\mu - i\frac{1}{6}g'B_\mu - ig_S\frac{\lambda^b}{2}G^b_\mu\right) Q'_{iL}$$

Particle	Q_L	u_R	d_R	L_L	e_R	Φ
$\mathrm{SU(3)_c}$	**3**	**3**	**3**	**1**	**1**	**1**
$\mathrm{SU(2)_L}$	**2**	**1**	**1**	**2**	**1**	**2**
$\mathrm{U(1)_Y}$	1/6	2/3	−1/3	−1/2	−1	1/2

Table 2.1: Particle contents in the SM and their representations for the $\mathrm{SU(3)}_C \times \mathrm{SU(2)}_L \times \mathrm{U(1)}_Y$ symmetry.

$$
\begin{aligned}
&+\sum_{i=1}^{3} \overline{u'_{iR}} i\gamma^\mu \left(\partial_\mu - i\frac{2}{3}g'B_\mu - ig_S\frac{\lambda^b}{2}G^b_\mu\right) u'_{iR} \\
&+\sum_{i=1}^{3} \overline{d'_{iR}} i\gamma^\mu \left(\partial_\mu - i\frac{-1}{3}g'B_\mu - ig_S\frac{\lambda^b}{2}G^b_\mu\right) d'_{iR},
\end{aligned} \tag{2.4}
$$

where

$$
\begin{aligned}
&Q'_{1L} \equiv \begin{pmatrix} u'_L \\ d'_L \end{pmatrix}, \quad Q'_{2L} \equiv \begin{pmatrix} c'_L \\ s'_L \end{pmatrix}, \quad Q'_{3L} \equiv \begin{pmatrix} t'_L \\ b'_L \end{pmatrix}, \\
&u'_{1R} \equiv u'_R, \quad u'_{2R} \equiv c'_R, \quad u'_{3R} \equiv t'_R, \\
&d'_{1R} \equiv d'_R, \quad d'_{2R} \equiv s'_R, \quad d'_{3R} \equiv b'_R.
\end{aligned} \tag{2.5}
$$

In addition to the electroweak interaction, the quarks have the color charge, which is carried by the gluon G^b_μ $(b = 1, ..., 8)$ with the Gelmann matrix λ^b.

2.2 Higgs mechanism

The spontaneous symmetry breaking of $\mathrm{SU(2)}_L \times \mathrm{U(1)}_Y$ is described by the Higgs mechanism [9]. In the SM, a scalar doublet Φ with the hypercharge $Y = 1/2$ is introduced, and the relevant Lagrangian is given by

$$
\begin{aligned}
&\mathcal{L}^{higgs} = (D_\mu\Phi)^\dagger D^\mu\Phi - V \\
&V = \mu^2\Phi^\dagger\Phi + \frac{\lambda}{2}(\Phi^\dagger\Phi)^2,
\end{aligned} \tag{2.6}
$$

where the covariant derivative is

$$
D_\mu\Phi = \left(\partial_\mu - ig\frac{\tau^a}{2}W^a_\mu - ig'\frac{1}{2}B_\mu\right)\Phi. \tag{2.7}
$$

When we suppose $\mu^2 < 0$, the stationary point of V, where the vacuum energy density is minimized, is not $\langle\Phi\rangle = 0$. We parametrize the scalar doublet as

$$
\Phi = \begin{pmatrix} G^+ \\ \frac{1}{\sqrt{2}}(v + h + iG^0) \end{pmatrix}, \tag{2.8}
$$

where G^+ and G^0 are the charged and neutral Nambu–Goldstone (NG) bosons, respectively, and $v \in \mathbb{R}$ and h are the Vacuum Expectation Value (VEV) and the neutral Higgs boson. From the stationary condition for V, we get the relation $\mu^2 = \lambda v^2/2$, and the mass of the Higgs boson is $m_h^2 = \lambda v^2$ on this vacuum. By the doublet field getting the VEV, $\mathrm{SU(2)}_L \times \mathrm{U(1)}_Y$ symmetry is spontaneously broken to $\mathrm{U(1)}_{\mathrm{em}}$ symmetry.

The $\mathrm{SU}(2)_L \times \mathrm{U}(1)_Y$ symmetry is gauged, so that the corresponding gauge bosons become massive by the longitudinal mode of them absorbing the NG bosons [9]. From Eq. (2.6), we obtain quadratic terms of the gauge bosons, which imply

$$m_W^2 = \frac{g^2}{4}v^2, \quad m_Z^2 = \frac{g_Z^2}{4}v^2, \quad m_A^2 = 0, \tag{2.9}$$

where $g_Z \equiv \sqrt{g^2 + g'^2}$. We have defined W and Z bosons, and the photon as

$$W_\mu \equiv \frac{1}{\sqrt{2}}(W_\mu^1 - iW_\mu^2), \quad \begin{pmatrix} Z_\mu \\ A_\mu \end{pmatrix} \equiv \begin{pmatrix} \cos\theta_W & -\sin\theta_W \\ \sin\theta_W & \cos\theta_W \end{pmatrix} \begin{pmatrix} W_\mu^3 \\ B_\mu \end{pmatrix}. \tag{2.10}$$

The Weinberg angle satisfies the relations $\sin\theta_W = g'/g_Z$ and $\cos\theta_W = g/g_Z$. The photon remains massless because the $\mathrm{U}(1)_{\mathrm{em}}$ symmetry is preserved. The coupling constant for the electromagnetic interaction is given by $e = gg'/g_Z$.

2.3 Flavor structure of the standard model

The Yukawa interaction for the SM fermions are given by

$$\mathcal{L}_y = -\sum_{i,j=1}^{3} \left(Y_{ij}^{u\dagger} \overline{Q'_{iL}} \tilde{\Phi} u'_{jR} + Y_{ij}^{d} \overline{Q'_{iL}} \Phi d'_{jR} + Y_{ij}^{e} \overline{L'_{iL}} \Phi e'_{jR} + \mathrm{h.c.} \right), \tag{2.11}$$

where $\tilde{\Phi} = i\tau^2 \Phi^*$, and the matrices Y^f $(f = u, d, e)$ are generally complex matrix. After the electroweak symmetry breaking, these fermions acquire their masses. We define the mass eigenstate where each $Y^{u\dagger}, Y^{d,e}$ is diagonalized,

$$f_{iL} = (V_L^f)_{ij} f'_{jL}, \;\; f_{iR} = (V_R^f)_{ij} f'_{jR}, \tag{2.12}$$

where V_L^f and V_R^f are unitary matrices, and they satisfy

$$\begin{aligned} V_L^u Y^{u\dagger} V_R^{u\dagger} &= \frac{\sqrt{2}}{v} \times \mathrm{diag}(m_u, m_c, m_t), \\ V_L^d Y^d V_R^{d\dagger} &= \frac{\sqrt{2}}{v} \times \mathrm{diag}(m_d, m_s, m_b), \\ V_L^e Y^e V_R^{e\dagger} &= \frac{\sqrt{2}}{v} \times \mathrm{diag}(m_e, m_\mu, m_\tau). \end{aligned} \tag{2.13}$$

In this mass eigenstate, the charged and neutral current for the leptons and quarks are given by

$$\begin{aligned} \mathcal{L}_{\mathrm{int}}^c &= \sum_{i=l,q} \frac{g}{\sqrt{2}} (W_\mu^\dagger J_i^\mu + W_\mu J_i^{\mu\dagger}) \\ \mathcal{L}_{\mathrm{int}}^n &= \sum_{i=l,q} \left(e A_\mu J_{\mathrm{em},i}^\mu + g_Z Z_\mu J_{Z,i}^\mu \right), \end{aligned} \tag{2.14}$$

where

$$\begin{aligned} J_l^\mu &= \overline{e}\gamma_\mu P_L \nu_e + \overline{\mu}\gamma_\mu P_L \nu_\mu + \overline{\tau}\gamma_\mu P_L \nu_\tau, \\ J_q^\mu &= \sum_{i,j=1}^{3} \overline{u_i}\gamma_\mu P_L \left(V_{\mathrm{CKM}}\right)_{ij} d_j, \end{aligned}$$

$$
\begin{aligned}
J^{\mu}_{\mathrm{em},l} &= -\overline{e}\gamma_{\mu}e - \overline{\mu}\gamma_{\mu}\mu - \overline{\tau}\gamma_{\mu}\tau, \\
J^{\mu}_{\mathrm{em},q} &= \sum_{i=1}^{3}\left(\frac{2}{3}\overline{u_i}\gamma_{\mu}u_i - \frac{1}{3}\overline{d_i}\gamma_{\mu}d_i\right), \\
J^{\mu}_{Z,l} &= \sum_{i=1}^{3}\overline{L_i}\gamma^{\mu}P_L(\tau^3/2)L_i - \sin^2\theta_W J^{\mu}_{\mathrm{em},l}, \\
J^{\mu}_{Z,q} &= \sum_{i=1}^{3}\overline{Q_i}\gamma^{\mu}P_L(\tau^3/2)Q_i - \sin^2\theta_W J^{\mu}_{\mathrm{em},q}.
\end{aligned} \tag{2.15}
$$

In the mass eigenstate, $V_{\mathrm{CKM}} = V_L^u V_L^{d\dagger}$, which is Cabibbo–Kobayashi–Masukawa (CKM) matrix [29,30], appears in the current with the W boson. Through the CKM matrix in the charged current, a flavor can change into other flavors. On the other hand, in the neutral current, there are no flavor changing interactions. The existence of the Flavor Changing Neutral Current (FCNC) is strongly constrained by many experiments (e.g. the upper bound on $\mathrm{Br}(K \to \mu\mu)$). The SM explains this natural suppression of the FCNC processes, and this mechanism was first been proposed by Glashow, Maiani, and Iliopoulos [89].

The CKM matrix is 3×3 unitary matrix, and it can be written as

$$
V_{\mathrm{CKM}} = \begin{pmatrix} V_{ud} & V_{us} & V_{ub} \\ V_{cd} & V_{cs} & V_{cb} \\ V_{td} & V_{ts} & V_{tb} \end{pmatrix}. \tag{2.16}
$$

The degree of freedom of 3×3 unitary matrix is 3^2, and we have 2×3 rephasing degree of freedom for the up- and down-type quarks. Therefore, $2 \times 3 - 1$ phases can be eliminated from the CKM matrix. As a result, independent physical degree of freedom in the CKM matrix is five, and they can be parametrized by three orthogonal matrices and one complex phase (CKM phase). A parametrization of the CKM matrix written by

$$
V_{\mathrm{CKM}} = \begin{pmatrix} c_{12}c_{13} & s_{12}c_{13} & s_{13}e^{-i\delta} \\ -s_{12}c_{23} - c_{12}s_{23}s_{13}e^{i\delta} & c_{12}c_{23} - s_{12}s_{23}s_{13}e^{i\delta} & s_{23}c_{13} \\ s_{12}s_{23} - c_{12}c_{23}s_{13}e^{i\delta} & -c_{12}s_{23} - s_{12}c_{23}s_{13}e^{i\delta} & c_{23}c_{13} \end{pmatrix}, \tag{2.17}
$$

is often used [90], where $s_{ij} \equiv \sin\theta_{ij}, c_{ij} \equiv \cos\theta_{ij}, (0 \le \theta_{ij} \le \pi/2)$. The phase δ is the CKM phase, and many CP violating processes have been explained by this.

The property of the CP violating quantities is characterized by the Jarlskog invariant [91,92]

$$
J_{CP} \equiv \mathrm{Im}(V_{ud}V_{us}^*V_{cs}V_{cd}^*) = c_{12}c_{13}^2c_{23}s_{12}s_{13}s_{23}\sin\delta. \tag{2.18}
$$

If a pair of the up- or down-type quarks is degenerated, the mixing angle is zero, and it causes $J_{CP} = 0$. This is because, if the mass and the charges are the same, the number of the flavor decreases due to the flavor symmetry. Therefore, to get non-zero CP violation, we need at least three generations of the quark. The experimental value is [93]

$$
J_{CP}^{\mathrm{exp}} = 3.12 \times 10^{-5}. \tag{2.19}
$$

2.4 Baryon and lepton number violation

The baryon and lepton numbers for the quarks and leptons are $1/3$ and 1, respectively. The SM Lagrangian is invariant under the global transformations, $\mathrm{U}(1)_B$ for the baryon and $\mathrm{U}(1)_L$ for the lepton. However, due to the chiral anomaly for axial U(1) transformation, the baryon and

lepton numbers are not conserved in the SM. Conservation law for the corresponding currents for left-handed quarks and leptons are given by [94, 95]

$$\partial_\mu j^\mu_B = \partial_\mu j^\mu_L = \frac{N_f g^2}{32\pi^2}\mathrm{Tr}(W_{\mu\nu}\tilde{W}^{\mu\nu}), \tag{2.20}$$

where $N_f = 3$ is the number of generation, $W_{\mu\nu}$ is the field stress tensor for W_μ, and $\tilde{W}_{\mu\nu} = \frac{1}{2}\epsilon_{\mu\nu\rho\sigma}W^{\rho\sigma}$ ($\epsilon_{0123} \equiv 1$). For the baryon and lepton number violation, the non-abelian gauge field W_μ is important, so that we have omitted the $\mathrm{U}(1)_Y$ contributions. Therefore, the $B + L$ charge is violated at the quantum level, while $B - L$ charge is not.

The $B + L$ violating process is caused by a transition of the vacuum for the gauge configuration. The degenerated vacua are labeled by integers, which is called by the Chern–Simons numbers N_{CS}, and a ΔN_{CS} transition gives $\Delta(B + L) = 2N_f\Delta N_{CS}$. Therefore, a $\Delta N_{CS} = 1$ process produces nine quarks (generation $\times$ color) and three leptons.

The transition rate for $\Delta N_{CS} = 1$ is $\Gamma \sim \exp(-8\pi^2/g^2) \sim 10^{-82}$, by using the instanton solution for the W_μ field. Due to the weakness of the $\mathrm{SU}(2)_L$ gauge theory, this effect is greatly suppressed, and the baryon number violation can be neglected in the zero temperature. However, the barrier of the potential energy between the two vacua is finite, and the $B + L$ changing process frequently occurs in the finite temperature, e.g. in the early Universe. This $B+L$ violating process in the finite temperature is called by sphaleron process [28]. The energy barrier is roughly estimated by $E_{\mathrm{sph}} \sim m_W/\alpha_{\mathrm{em}} \sim O(10)$ TeV in SU(2) gauge–Higgs model [96]. Therefore, when the temperature is much higher than the scale of the electroweak symmetry breaking, the sphaleron process is active, while it begins to decouple around the electroweak scale. Actually, the sphaleron rate is suppressed by the Bolzmann factor $e^{-E_{\mathrm{sph}}/T}$, and the sphaleron process decouples after the Higgs boson getting the VEV.

2.5 Custodial symmetry

In the SM, a hidden symmetry exists in the Higgs sector. The Higgs potential can be rewritten as

$$V = \frac{\mu^2}{2}\mathrm{Tr}\left(\mathbf{\Phi}^\dagger\mathbf{\Phi}\right) + \frac{\lambda}{2}\left(\frac{1}{2}\mathrm{Tr}\left(\mathbf{\Phi}^\dagger\mathbf{\Phi}\right)\right)^2, \tag{2.21}$$

where we have defined

$$\mathbf{\Phi} \equiv (\tilde{\Phi}, \Phi) = \begin{pmatrix} \phi^{0*} & \phi^+ \\ -\phi^- & \phi^0 \end{pmatrix}. \tag{2.22}$$

The kinetic term of the Higgs doublet is

$$\mathcal{L}^{higgs}_{\mathrm{kin}} = \frac{1}{2}\mathrm{Tr}\left((D_\mu\mathbf{\Phi})^\dagger(D^\mu\mathbf{\Phi})\right), \tag{2.23}$$

where

$$D_\mu\mathbf{\Phi} \equiv \partial_\mu\mathbf{\Phi} - ig\frac{\tau^a}{2}W^a_\mu\mathbf{\Phi} + ig'B_\mu\mathbf{\Phi}\frac{\tau^3}{2}, \tag{2.24}$$

When we neglect the $\mathrm{U}(1)_Y$ interaction, these terms are invariant under the transformation

$$\mathbf{\Phi} \to \mathbf{\Phi}' = L\mathbf{\Phi}R^\dagger, \quad L \in \mathrm{SU}(2)_L, \quad R \in \mathrm{SU}(2)_R. \tag{2.25}$$

After the electroweak symmetry breaking, the matrix gets the VEV as

$$\langle \mathbf{\Phi} \rangle = \frac{1}{\sqrt{2}} \begin{pmatrix} v & 0 \\ 0 & v \end{pmatrix}. \tag{2.26}$$

Even after the electroweak symmetry breaking, the Lagrangian is invariant under $\mathrm{SU}(2)_V$ transformation, where $L = R$ is taken. Therefore, the spontaneously symmetry breaking is $\mathrm{SU}(2)_L \times \mathrm{SU}(2)_R \to \mathrm{SU}(2)_V$. This remaining global symmetry is called the custodial symmetry [74]. By the gauged $\mathrm{SU}(2)_L$ symmetry, W^a_μ bosons get their masses, but due to the custodial symmetry, their masses are degenerated.

The ρ parameter, which is defined by

$$\rho \equiv \frac{m_W^2}{m_Z^2 \cos^2 \theta_W}, \tag{2.27}$$

is one of the important observables to know the symmetry structure of the Higgs potential. If the Higgs scalar which gives the mass of the gauge bosons is different from the SM one, the ρ parameter will change. The general formula for the ρ parameter is given by

$$\rho = \frac{\sum_i \frac{v_i^2}{2} \{ I_i(I_i+1) - Y_i^2 \}}{2 \sum_i \frac{v_i^2}{2} Y_i^2}. \tag{2.28}$$

where v_i, I_i, and Y_i are the VEV, the isospin, and the hypercharge of the scalar i, respectively. When the Higgs scalar is the SM one, namely $(I_i, Y_i) = (1/2, 1/2)$, $\rho = 1$ is shown. This is the tree level relation, so that it suffers from the quantum corrections [66–70, 97, 98]. Actually, the Yukawa sector of the SM violates the custodial symmetry, and the corrections relate to the mass difference between the up and the down-type quarks.

By the dedicated experimental efforts for the ρ parameter, $\rho \simeq 1$ has been observed [71–73], so that any models for new physics have to respect this fact. Later we will discuss the custodial symmetry in the extended Higgs models.

2.6 Phenomenological status of the Higgs sector

In the left panel of figure 2.1, the production cross section for the single Higgs boson with $m_h = 125$ GeV at the hadron collider are summarized [93, 99, 100]. The main production processes are $pp \to h$ (gluon-gluon Fusion: ggF), $pp \to qqh$ (Vector Boson Fusion: VBF), $pp \to Wh, Zh$ (Higgs-strahlung: VH), and $pp \to t\bar{t}h, b\bar{b}h$ (top- and bottom-associated). The decay branching ratios for the Higgs bosons are summarized in the right panel of figure 2.1. The total decay width for the Higgs boson predicted by the SM is $\Gamma_h^{\mathrm{SM}} = 4.07$ MeV with a relative uncertainty of $^{+4\%}_{-3.9\%}$ [93].

The Higgs boson has first been discovered by ATLAS and CMS measuring the $h \to \gamma\gamma$ channel [10, 11]. The ATLAS group currently gives [101]

$$m_h = 125.11 \pm 0.09(\mathrm{stat.}) \pm 0.06(\mathrm{syst.})\ \mathrm{GeV} \quad (\mathrm{ATLAS}), \tag{2.29}$$

by using the Run-1 and full Run-2 combined results of the di-photon channel, and the CMS group reports [102]

$$m_h = 125.08 \pm 0.10(\mathrm{stat.}) \pm 0.05(\mathrm{syst.})\ \mathrm{GeV} \quad (\mathrm{CMS}), \tag{2.30}$$

by using the Run-1 and Run-2 combined results of the four-lepton final state.

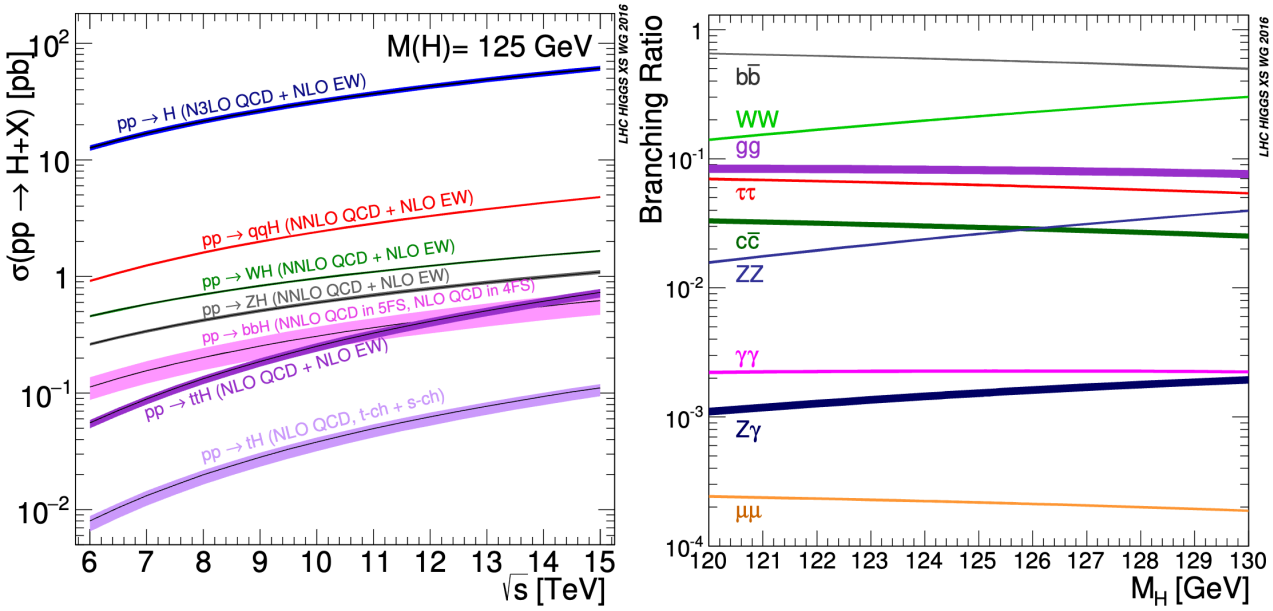

Figure 2.1: The production of the Higgs boson (left) and the decay branching ratios (right). This figure is taken by Refs. [93, 99, 100].

	ATLAS Run2	CMS Run2	HL-LHC (expected)
κ_γ	1.01 ± 0.06	1.10 ± 0.08	1.8%
κ_W	1.05 ± 0.06	1.02 ± 0.08	1.7%
κ_Z	0.99 ± 0.06	1.04 ± 0.07	1.5%
$\kappa_{Z\gamma}$	$1.38^{+0.31}_{-0.36}$	1.65 ± 0.34	9.8%
κ_g	0.95 ± 0.07	0.92 ± 0.08	2.5%
κ_t	0.94 ± 0.11	1.01 ± 0.11	3.4%
κ_b	0.89 ± 0.11	0.99 ± 0.16	3.7%
κ_τ	0.93 ± 0.07	0.92 ± 0.08	1.9%

Table 2.2: Current status for the κ parameters [93].

To discuss the experimental results for the SM Higgs boson couplings, we define κ parameters [99]

$$(\sigma \cdot \mathrm{Br})(i \to h \to f) = \frac{\sigma_i^{\mathrm{SM}} \kappa_i^2 \Gamma_f^{\mathrm{SM}} \kappa_f^2}{\Gamma_h^{\mathrm{SM}} \kappa_h^2}, \tag{2.31}$$

where σ_i^{SM} and Γ_f^{SM} are the production cross section and the decay width of the final state f, respectively. The κ parameters express deviations from the SM, and $\kappa = 1$ is the SM prediction. The signal strength is defined by

$$\mu_i^f \equiv \frac{(\sigma \cdot \mathrm{Br})}{(\sigma \cdot \mathrm{Br})_{\mathrm{SM}}} = \frac{\kappa_i^2 \kappa_f^2}{\kappa_h^2}. \tag{2.32}$$

The experimental results for the Higgs boson couplings are summarized in figure 2.2 and table 2.2.

To measure the triple Higgs self coupling, the pair production process of the Higgs bosons, $pp \to h^* \to hh$ is important. The corresponding parameter κ_λ has been measured by ATLAS [105] and CMS [20],

$$(\mathrm{ATLAS}) - 0.6 < \kappa_\lambda < 6.6,$$

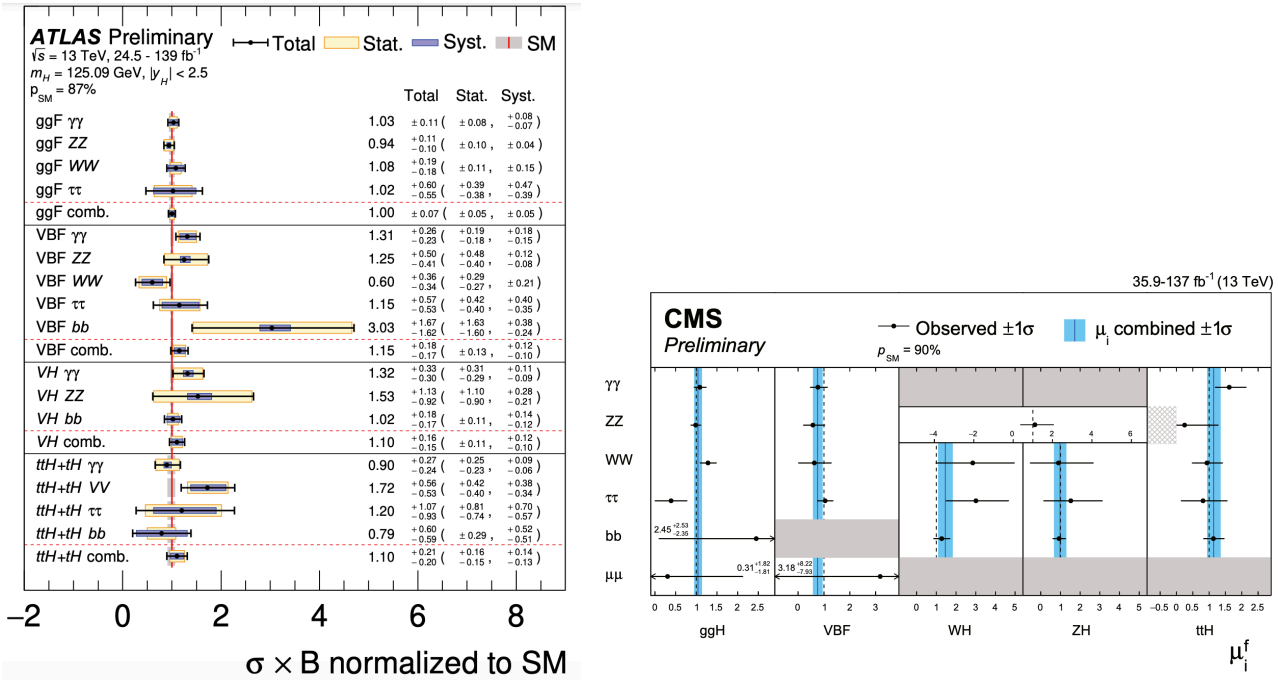

Figure 2.2: Results of the Higgs signal strengths. These figures are taken by Refs. [103, 104]

$$\text{(CMS)} \quad -1.2 < \kappa_\lambda < 6.5, \tag{2.33}$$

with the 95% C.L.

Chapter 3

Phenomenological problems beyond the standard model

As we have discussed in chapter 2, the SM has been founded, and it explains various particle phenomena. However, some beyond the SM phenomena have been known. In this chapter, we introduce three problems in the fields of particle physics and cosmology, the mass origin of the neutrino, the dark matter problem and the baryon asymmetry of the Universe.

3.1 The origin of the neutrino mass

By the observation of the oscillation of the atmospheric neutrino, the mass of the neutrino has been confirmed [17]. In the SM, due to the absence of the right-handed neutrino, the three neutrinos ν_e, ν_μ, ν_τ are massless. If these are massive, in general, the gauge eigenstate $(\nu_e, \nu_\mu, \nu_\tau)$ and the mass eigenstate (ν_1, ν_2, ν_3) are different. As a result, a Unitary matrix

$$U_{\rm PMNS} = \begin{pmatrix} c_{12}c_{13} & s_{12}c_{13} & s_{13}e^{-i\delta_{CP}} \\ -s_{12}c_{23} - c_{12}s_{23}s_{13}e^{i\delta_{CP}} & c_{12}c_{23} - s_{12}s_{23}s_{13}e^{i\delta_{CP}} & s_{23}c_{13} \\ s_{12}s_{23} - c_{12}c_{23}s_{13}e^{i\delta_{CP}} & -c_{12}s_{23} - s_{12}c_{23}s_{13}e^{i\delta_{CP}} & c_{23}c_{13} \end{pmatrix}, \tag{3.1}$$

appears in the charged current, as similar to the CKM matrix. This matrix is called Pontecorvo–Maki–Nakagawa–Sakata (PMNS) matrix [106, 107]. When we assume mass spectrum with normal ordering $m_1 < m_2 < m_3$, current experimental data gives [73]

$$\begin{aligned} &\Delta m^2_{21} = (7.53 \pm 0.18) \times 10^{-5}\ \text{eV}^2, \\ &\Delta m^2_{23} = (2.455 \pm 0.028) \times 10^{-3}\ \text{eV}^2, \\ &\sin^2\theta_{12} = 0.307 \pm 0.013, \\ &\sin^2\theta_{13} = 0.0219 \pm 0.0007, \\ &\sin^2\theta_{23} = 0.558 \pm 0.015, \\ &\delta_{CP} = (1.19 \pm 0.22)\pi, \end{aligned} \tag{3.2}$$

where $\Delta m^2_{ij} = m^2_i - m^2_j$. The δ_{CP} is the CP violation in the lepton sector.

The mass origin of the neutrino and these mixing angles cannot be explained in the SM. One easiest way to explain this is just introducing right-handed neutrinos to make Dirac mass term. However, it needs quite smaller Yukawa couplings than the one of the electron to explain the tiny mass of the neutrinos. There are many new physics models to explain the small neutrino masses, e.g., models with the seesaw mechanism [108–118] or models for radiative generation of the neutrino mass [119–125].

3.2 Dark matter problem

By the latest observation data provided by the Plank satellites supports that about one quarter of the energy density in our Universe is composed of the electrically neutral, massive, and stable matter. This matter is called Dark Matter (DM), and the observed energy density of the DM is [18]

$$\Omega_{\rm DM}h^2 = 0.120 \pm 0.001. \tag{3.3}$$

There are no candidates to be the DM in the SM. Models with Weakly Interacting Massive Particle (WIMP) [126] have been studied in many literature (for reviews, see Ref. [127]). In the WIMP scenario, the relic density of the DM is explained by the freeze out mechanism. The time evolution of the number density n for the WIMP is described by the Bolzmann equation [128]:

$$\frac{dn}{dt} + 3Hn = -\langle\sigma v\rangle(n^2 - n_{eq}^2), \tag{3.4}$$

where n_{eq} is the equilibrium solution, H is the Hubble parameter, and $\langle\sigma v\rangle$ is thermal average of the annihilation cross section for the WIMP. Whether the number density n follows the equilibrium solution or not is determined by the balance between the annihilation cross section and the expansion rate of the Universe. When $n_{eq}\langle\sigma v\rangle/H \gtrsim 1$, the annihilation processes make n into n_{eq}. On the other hand, when $n_{eq}\langle\sigma v\rangle/H \lesssim 1$, such effect becomes weak, and the annihilation processes decouple as decreasing temperature. The freeze out temperature T_f is determined by $n_{eq}\langle\sigma v\rangle(T_f) \simeq H(T_f)$, and the energy density of the WIMP can be estimated as

$$\Omega_{\rm DM}h^2 \simeq 2.75 \times 10^{-8} m_{\rm DM} Y(T_f) {\rm GeV}^{-1}, \tag{3.5}$$

where $m_{\rm DM}$ is the mass of the DM, and Y is the comoving density of the DM which is obtained by n divided by the entropy density s. From the observed relic density, we obtain $\langle\sigma v\rangle \sim 10^{-26}$ cm$^3 s^{-1}$ and $m_{\rm DM} = O(100)$ GeV. This mass range and the interaction can be proved by the DM-nucleon scattering process. Until now, the extensive parameter region for the WIMP has been searched by many direct detection experiments (XENONnT [129], PandaX-4T [130], LZ [131, 132] and so on).

In chapter 5, we discuss a model for the tiny neutrino mass and the WIMP DM with the U(1)$_{B-L}$ gauge symmetry.

3.3 Baryon asymmetry of the Universe

By the cosmological observation and the theory of the Big-Bang nucleosynthesis (BBN), it has been confirmed that our Universe has baryon–anti-baryon asymmetry. The problem of the Baryon Asymmetry of the Universe (BAU) is one of the beyond SM problems.

As we have defined in section 2.1, the quark has the baryon number $1/3$ while the anti-quark has $-1/3$. Observed baryon asymmetry is [18]

$$\eta_B \equiv \frac{n_B - n_{\overline{B}}}{s} = 8.57 \times 10^{-11}. \tag{3.6}$$

Even if we consider the origin of the asymmetry as just the initial condition, after the inflation of the Universe, such asymmetry is smeared. Therefore, the asymmetry should be generated after the inflation but before the BBN.

In order to generate the BAU, (1) baryon number violating process, (2) C and CP violation and (3) out of thermal equilibrium, need to be satisfied [26]. These conditions are known as the Sakharov conditions. We consider a 2 body decay or particle production, $X \leftrightarrow YZ$, as

an example. Let we define the baryon number $B = 0$ to X, and $B = 1/2$ to Y and Z. The anti particles $\overline{Y}$ and $\overline{Z}$ defined by C or CP conjugation have $B = -1/2$. The first condition is needed for the baryon number exchanging processes $X \leftrightarrow YZ$. When we denote the decay branching ratio of $X \to YZ$ ($\overline{X} \to \overline{YZ}$) as r ($\overline{r}$) and other non-baryonic branching ratio as $1-r$ ($1-\overline{r}$). The expectation value of the baryon number is $+r-\overline{r}$. If this decay is in thermal equilibrium, the inverse process is also active, and due to the CPT theorem, the number density is proportional to $+r-\overline{r}-(r-\overline{r}) = 0$. Therefore, we need C and CP violation ($r \neq \overline{r}$) and the out of thermal equilibrium situation.

The scenario for producing the BAU is called baryogenesis, and many baryogenesis scenarios have been proposed until now. Representative scenarios are GUT baryogenesis [133, 134], Affleck-Dine baryogenesis [135], leptogenesis [136], electroweak baryogenesis [27] and so on.

In Electroweak Baryogenesis (EWBG), the baryon asymmetry is produced within the electroweak theory as well as the SM. As we have explained, the SM has (1) baryon number violating process (sphaleron process) and (2) C and CP violation (electroweak chiral interaction and the CKM phase). As we will explain later, non-equilibrium situation in EWBG is realized by the Strongly First Order Phase Transition (SFOPT). Therefore, if SFOPT occurs in the SM, the BAU could be explained by EWBG in the SM. However, finite size scaling law in the lattice calculation is not seen with the 125 GeV Higgs boson, meaning that the electroweak phase transition is cross over phase transition [32, 33]. In addition, the CKM phases cannot generate enough baryon asymmetry to explain the observed BAU [31]. Therefore, the BAU is beyond the SM problem, so that a model of new physics is necessary to solve it.

Once the scalar sector of the SM, the Higgs sector, is extended, the problems of the SFOPT and the CP violation can be solved. In section 4.1, we introduce the two Higgs doublet model, which is one of minimal extension of the SM. In this model, as it will be shown in section 7.1, the SFOPT can be realized, and the observed BAU can be explained by the new source of the CP violation with the mechanism of EWBG.

Chapter 4

Review of extended Higgs models

4.1 Two Higgs doublet model

4.1.1 General two Higgs doublet model

We here define the most general two Higgs doublet model (2HDM). In the model, two $\mathrm{SU}(2)_L$ doublets $\Phi_k = (\phi_k^+, \phi_k^0)^T$ $(k = 1, 2)$ with the hypercharge $Y = 1/2$ are introduced. After the spontaneous electroweak symmetry breaking, without loss of generality, we can take the Higgs basis [137] as

$$\Phi_1 = \begin{pmatrix} G^+ \\ \frac{1}{\sqrt{2}}(v + h_1 + iG^0) \end{pmatrix}, \quad \Phi_2 = \begin{pmatrix} H^+ \\ \frac{1}{\sqrt{2}}(h_2 + ih_3) \end{pmatrix}, \tag{4.1}$$

where $v \simeq 246$ GeV is the VEV, G^+, G^0 are the NG bosons, $H^\pm$ are the charged scalar bosons, and h_i $(i = 1, 2, 3)$ are the electric neutral scalar bosons. In the Higgs basis, the most general Higgs potential is given by

$$\begin{aligned} V =& -Y_1^2(\Phi_1^\dagger\Phi_1) - Y_2^2(\Phi_2^\dagger\Phi_2) - \Big(Y_3^2(\Phi_1^\dagger\Phi_2) + \text{h.c.}\Big) \\ &+ \frac{1}{2}Z_1(\Phi_1^\dagger\Phi_1)^2 + \frac{1}{2}Z_2(\Phi_2^\dagger\Phi_2)^2 + Z_3(\Phi_1^\dagger\Phi_1)(\Phi_2^\dagger\Phi_2) + Z_4(\Phi_2^\dagger\Phi_1)(\Phi_1^\dagger\Phi_2) \\ &+ \left\{\Big(\frac{1}{2}Z_5\Phi_1^\dagger\Phi_2 + Z_6\Phi_1^\dagger\Phi_1 + Z_7\Phi_2^\dagger\Phi_2\Big)\Phi_1^\dagger\Phi_2 + \text{h.c.}\right\}, \end{aligned} \tag{4.2}$$

where $Y_1^2(>0)$, Y_2^2, Z_1, Z_2, Z_3 and Z_4 are real parameters, and Y_3^2, Z_5, Z_6 and Z_7 are complex parameters. By using a rotation of the phase for Φ_2, we can make Z_5 real. In the following, we call this basis of Φ_2 as *the real Z_5 basis*. From the stationary condition, we obtain

$$Y_1^2 = \frac{1}{2}Z_1v^2, \quad Y_3^2 = \frac{1}{2}Z_6v^2. \tag{4.3}$$

The squared mass of $H^\pm$ is given by

$$m_{H^\pm}^2 = -Y_2^2 + \frac{1}{2}Z_3v^2, \tag{4.4}$$

and the squared mass matrix for h_i in the real Z_5 basis is given by

$$\mathcal{M}_{ij}^2 \equiv \frac{\partial^2 V}{\partial h_i \partial h_j} = \begin{pmatrix} Z_1v^2 & Z_6^Rv^2 & -Z_6^Iv^2 \\ Z_6^Rv^2 & m_{H^\pm}^2 + \frac{1}{2}(Z_4 + Z_5)v^2 & 0 \\ -Z_6^Iv^2 & 0 & m_{H^\pm}^2 + \frac{1}{2}(Z_4 - Z_5)v^2 \end{pmatrix}, \tag{4.5}$$

where the subscripts R (I) mean the real (imaginary) part of the coupling constants. By using an orthogonal matrix $\mathcal{R}$ which represents SO(3) transformation, the mass eigenstates for the neutral scalar bosons H_i are defined as

$$H_i = \mathcal{R}_{ij} h_j. \tag{4.6}$$

The matrix $\mathcal{R}$ can be parametrized by

$$\begin{aligned}
\mathcal{R} &= \mathcal{R}_1\mathcal{R}_2\mathcal{R}_3 \\
&\equiv \begin{pmatrix} \cos\alpha_1 & -\sin\alpha_1 & 0 \\ \sin\alpha_1 & \cos\alpha_1 & 0 \\ 0 & 0 & 1 \end{pmatrix} \begin{pmatrix} \cos\alpha_2 & 0 & -\sin\alpha_2 \\ 0 & 1 & 0 \\ \sin\alpha_2 & 0 & \cos\alpha_2 \end{pmatrix} \begin{pmatrix} 1 & 0 & 0 \\ 0 & \cos\alpha_3 & -\sin\alpha_3 \\ 0 & \sin\alpha_3 & \cos\alpha_3 \end{pmatrix} \\
&= \begin{pmatrix} \cos\alpha_2\cos\alpha_1 & -\cos\alpha_3\sin\alpha_1 - \cos\alpha_1\sin\alpha_2\sin\alpha_3 & -\cos\alpha_1\cos\alpha_3\sin\alpha_2 + \sin\alpha_1\sin\alpha_3 \\ \cos\alpha_2\sin\alpha_1 & \cos\alpha_1\cos\alpha_3 - \sin\alpha_1\sin\alpha_2\sin\alpha_3 & -\cos\alpha_3\sin\alpha_1\sin\alpha_2 - \cos\alpha_1\sin\alpha_3 \\ \sin\alpha_2 & \cos\alpha_2\sin\alpha_3 & \cos\alpha_2\cos\alpha_3 \end{pmatrix},
\end{aligned} \tag{4.7}$$

where $-\pi \leq \alpha_1, \alpha_3 < \pi$, $-\pi/2 \leq \alpha_2 < \pi/2$ [138], and it satisfies

$$\mathcal{R}\mathcal{M}^2\mathcal{R}^T = \mathrm{diag}(m_{H_1}^2, m_{H_2}^2, m_{H_3}^2). \tag{4.8}$$

We can identify H_1 with the discovered Higgs boson at the LHC [10, 11], so that we set $m_{H_1} = 125$ GeV. We denote this SM-like Higgs boson as H_1, which is defined in the 2HDM, to distinguish it from the SM Higgs boson h.

In the Higgs basis, the most general Yukawa interaction is given by

$$-\mathcal{L}_Y = \sum_{k=1}^{2} \left(\overline{Q'_L} Y_k^{u\dagger} \tilde{\Phi}_k u'_R + \overline{Q'_L} Y_k^d \Phi_k d'_R + \overline{L'_L} Y_k^e \Phi_k e'_R + \mathrm{h.c.} \right). \tag{4.9}$$

We here have omitted the fermion-flavor indices. The matrices Y_1^f and Y_2^f ($f = u, d, e$) are the 3×3 Yukawa matrices. In the mass eigenstate of the fermions, in which Y_1^f are diagonalized, the Yukawa interaction is written by

$$\begin{aligned}
-\mathcal{L}_Y = &\overline{Q_L^u} Y_{\mathrm{d}}^u \tilde{\Phi}_1 u_R + \overline{Q_L^d} Y_{\mathrm{d}}^d \Phi_1 d_R + \overline{L_L} Y_{\mathrm{d}}^e \Phi_1 e_R + \mathrm{h.c.} \\
&+ \overline{Q_L^u} \rho^u \tilde{\Phi}_2 u_R + \overline{Q_L^d} \rho^d \Phi_2 d_R + \overline{L_L} \rho^e \Phi_2 e_R + \mathrm{h.c.},
\end{aligned} \tag{4.10}$$

where the $\mathrm{SU}(2)_L$ doublets are defined by $Q_L^u = (u_L, V_{\mathrm{CKM}} d_L)^T$, $Q_L^d = (V_{\mathrm{CKM}}^\dagger u_L, d_L)^T$ and $L_L = (\nu_L, e_L)^T$. The diagonalized matrices Y_{d}^f is written by $Y_{\mathrm{d}}^f = \frac{\sqrt{2}}{v}\mathrm{diag}(m_{f_1}, m_{f_2}, m_{f_3})$. On the other hand, ρ^f are not diagonalized in this mass eigenstate. We parametrize the ρ^f matrices as

$$\rho^u = \begin{pmatrix} \rho_{uu} & \rho_{uc} & \rho_{ut} \\ \rho_{cu} & \rho_{cc} & \rho_{ct} \\ \rho_{tu} & \rho_{tc} & \rho_{tt} \end{pmatrix}, \quad \rho^d = \begin{pmatrix} \rho_{dd} & \rho_{ds} & \rho_{db} \\ \rho_{sd} & \rho_{ss} & \rho_{sb} \\ \rho_{bd} & \rho_{bs} & \rho_{bb} \end{pmatrix}, \quad \rho^e = \begin{pmatrix} \rho_{ee} & \rho_{e\mu} & \rho_{e\tau} \\ \rho_{\mu e} & \rho_{\mu\mu} & \rho_{\mu\tau} \\ \rho_{\tau e} & \rho_{\tau\mu} & \rho_{\tau\tau} \end{pmatrix}, \tag{4.11}$$

and the components of each matrix are generally complex.

The kinetic term of Φ_1 and Φ_2 is given by

$$\mathcal{L}_k = |D_\mu \Phi_1|^2 + |D_\mu \Phi_2|^2. \tag{4.12}$$

The definition of the covariant derivative is given in Eq. (2.7).

	$\left(\rho^u\right)_{ll}$	$\left(\rho^d\right)_{ll}$	$\left(\rho^e\right)_{ll}$	$\left(\rho^f\right)_{lm}(l \neq m)$
Type-I	$\left(Y_{\rm d}^u\right)_{ll}\cot\beta$	$\left(Y_{\rm d}^d\right)_{ll}\cot\beta$	$\left(Y_{\rm d}^e\right)_{ll}\cot\beta$	0
Type-II	$\left(Y_{\rm d}^u\right)_{ll}\cot\beta$	$-\left(Y_{\rm d}^d\right)_{ll}\tan\beta$	$-\left(Y_{\rm d}^e\right)_{ll}\tan\beta$	0
Type-X	$\left(Y_{\rm d}^u\right)_{ll}\cot\beta$	$\left(Y_{\rm d}^d\right)_{ll}\cot\beta$	$-\left(Y_{\rm d}^e\right)_{ll}\tan\beta$	0
Type-Y	$\left(Y_{\rm d}^u\right)_{ll}\cot\beta$	$-\left(Y_{\rm d}^d\right)_{ll}\tan\beta$	$\left(Y_{\rm d}^e\right)_{ll}\cot\beta$	0

Table 4.1: The correspondence of $\left(\rho^f\right)_{lm}$ $(f = u, d, e)$ in our model to the ones in the softly-broken $\mathbb{Z}_2$ symmetric 2HDM (Type-I, II, X, and Y).

4.1.2 Softly broken $\mathbb{Z}_2$ symmetry

The off-diagonal elements of ρ^f cause the flavor changing neutral current, and it is severely constrained by the flavor experiments [139]. As one of the way to avoid this difficulty, the softly-broken $\mathbb{Z}_2$ symmetry in the 2HDM is often considered [140–149]. There are four types (Type-I, II, X, and Y [148]) of the assignment of the $\mathbb{Z}_2$ parity,

$$\begin{aligned}
&\Phi_1' : + \quad \Phi_2' : - \quad u_R : - \quad d_R : - \quad e_R : - \quad \text{(Type I)},\\
&\Phi_1' : + \quad \Phi_2' : - \quad u_R : - \quad d_R : + \quad e_R : - \quad \text{(Type II)},\\
&\Phi_1' : + \quad \Phi_2' : - \quad u_R : - \quad d_R : - \quad e_R : + \quad \text{(Type X)},\\
&\Phi_1' : + \quad \Phi_2' : - \quad u_R : - \quad d_R : + \quad e_R : - \quad \text{(Type Y)}.
\end{aligned} \tag{4.13}$$

To distinguish the double fields with the ones in the Higgs basis, we have defined the primed fields. We call this basis Φ_1' and Φ_2' as the $\mathbb{Z}_2$ basis.

The scalar potential is written by

$$\begin{aligned}
V =& -\mu_{11}^2(\Phi_1^{\dagger\prime}\Phi_1') - \mu_{22}^2(\Phi_2^{\dagger\prime}\Phi_2') - \left(\mu_{12}^2(\Phi_1^{\dagger\prime}\Phi_2') + \text{h.c.}\right)\\
&+ \frac{1}{2}\lambda_1(\Phi_1^{\dagger\prime}\Phi_1')^2 + \frac{1}{2}\lambda_2(\Phi_2^{\dagger\prime}\Phi_2')^2 + \lambda_3(\Phi_1^{\dagger\prime}\Phi_1')(\Phi_2^{\dagger\prime}\Phi_2') + \lambda_4(\Phi_2^{\dagger\prime}\Phi_1')(\Phi_1^{\dagger\prime}\Phi_2')\\
&+ \left(\frac{1}{2}\lambda_5(\Phi_1^{\dagger\prime}\Phi_2')^2 + \text{h.c.}\right),
\end{aligned} \tag{4.14}$$

where μ_{11}^2, μ_{22}^2, $\lambda_{1,\ldots,4}$ are real parameters, and μ_{12}^2 and λ_5 are complex parameters. In order to distinguish the Higgs basis and the $\mathbb{Z}_2$ basis, we use Y-Z for the Higgs basis and μ-λ for the $\mathbb{Z}_2$ basis. As same as in the general 2HDM, we can take the real λ_5 basis. Therefore, in the softly broken $\mathbb{Z}_2$ symmetric 2HDM, there are one additional CP phase.

The basis for Φ_1 and Φ_2 is not the Higgs basis, so that, in general, both doublets have the real VEVs, $\langle\Phi_i'\rangle = (0, v_i/\sqrt{2})^T$ $(i = 1, 2)$. Here we have assumed CP conserving potential, where all of the coupling constants are real. By using an orthogonal matrix, we can move to the Higgs basis as

$$\begin{pmatrix}\Phi_1\\ \Phi_2\end{pmatrix} = \begin{pmatrix}\cos\beta & \sin\beta\\ -\sin\beta & \cos\beta\end{pmatrix}\begin{pmatrix}\Phi_1'\\ \Phi_2'\end{pmatrix}, \tag{4.15}$$

where the mixing angle satisfies $\tan\beta = v_2/v_1$ $(0 \leq \beta \leq \pi/2)$. In the Higgs basis, only Φ_1 has the VEV $\sqrt{v_1^2 + v_2^2} \equiv v$. The form of the potential in the Higgs basis is same as Eq. (4.2), and the coupling constants in the Higgs basis, $Y_{1,2,3}^2$, $Z_{1,2,3,4,5,6,7}$ are functions of $\mu_{11,22,12}^2$, $\lambda_{1,2,3,4,5}$, which are defined in the $\mathbb{Z}_2$ basis [137]. The stationary conditions and the mass spectrum are same as the general 2HDM, if we use the coupling constants of the Higgs basis.

Due to the softly broken $\mathbb{Z}_2$ symmetry, the SM fermions interact to only one $\mathrm{SU}(2)_L$ scalar doublet. In the Higgs basis, we obtain the Yukawa interaction, which is same form as Eq. (4.10). The additional Yukawa matrices ρ^f couplings are functions of the $Y_{\rm d}^f$ and the mixing angle β, as summarized in table 4.1. In the softly broken $\mathbb{Z}_2$ 2HDM, the off-diagonal elements in ρ^f are zero, however, the CP violating phases cannot be introduced in the Yukawa sector.

4.1.3 Inert doublet model

The 2HDM with unbroken $\mathbb{Z}_2$ symmetry is called Inert doublet model [150]. We define unbroken $\mathbb{Z}_2$ parity as

$$\Phi : + \quad \eta : - \quad u_R : + \quad d_R : + \quad e_R : + \quad \text{(Inert)}, \tag{4.16}$$

where we denote additional $\mathrm{SU}(2)_L$ doublet as η. The potential is given by

$$\begin{aligned} V =& \mu_1^2(\Phi_1^\dagger\Phi_1) + \mu_2^2(\eta^\dagger\eta) + \frac{1}{2}\lambda_1(\Phi^\dagger\Phi)^2 + \frac{1}{2}\lambda_2(\eta^\dagger\eta)^2 \\ &+ \lambda_3(\Phi^\dagger\Phi)(\eta^\dagger\eta) + \lambda_4(\eta^\dagger\Phi)(\Phi^\dagger\eta) + \frac{1}{2}\lambda_5\Big((\Phi^\dagger\eta)^2 + \text{h.c.}\Big), \end{aligned} \tag{4.17}$$

where we take the real λ_5 basis. Therefore, no CP phase exists in the inert doublet model. We assume $\mu_1^2 < 0$ for electroweak symmetry breaking, while $\mu_2^2 > 0$ for unbroken $\mathbb{Z}_2$ symmetry.

Due to the unbroken $\mathbb{Z}_2$ symmetry, η cannot have the VEV. The components of those doublet fields can be written as

$$\Phi = \begin{pmatrix} G^+ \\ \frac{1}{\sqrt{2}}(v + h + iG^0) \end{pmatrix}, \quad \eta = \begin{pmatrix} H^+ \\ \frac{1}{\sqrt{2}}(H + iA) \end{pmatrix}. \tag{4.18}$$

The mass spectrum are

$$\begin{aligned} &m_h^2 = \lambda_1 v^2, \quad m_{H^\pm}^2 = \mu_2^2 + \frac{1}{2}\lambda_3 v^2, \\ &m_H^2 = m_{H^\pm}^2 + \frac{1}{2}(\lambda_4 + \lambda_5)v^2, \quad m_A^2 = m_{H^\pm}^2 + \frac{1}{2}(\lambda_4 - \lambda_5)v^2. \end{aligned} \tag{4.19}$$

The SM fermions have Yukawa interaction only with Φ, so that it is completely same as the SM one.

This kind of unbroken $\mathbb{Z}_2$ symmetry is often used to explain the stability of the DM. The lightest Z_2 odd particle with $Q = 0$ in the inert doublet model, namely H or A, can be the DM candidate. In addition, if we add $\mathbb{Z}_2$ odd right handed neutrinos to this model [123, 124], the masses of the light neutrinos are generated at the loop level. This model, so-called the scotogenic model, has been proposed by Tao and Ma [123, 124]. We will introduce $\mathrm{U}(1)_{B-L}$ extension of the scotogenic model in section 4.2, and discuss a scenario to explain the DM abundance and the tiny mass of the neutrino in chapter 5.

4.1.4 The conditions for the custodial and CP symmetry

In this subsection, we discuss custodial symmetry, which is a global symmetry in the 2HDM. We also discuss the CP violation in the 2HDM, and the relation with the condition for the custodial symmetry. In the following discussions in this subsection, we focus on the potential of the general 2HDM which is written in the Higgs basis, but it can also be applied to the one of the softly broken $\mathbb{Z}_2$ 2HDM or the inert doublet model.

According to Ref. [151], we derive the conditions for the custodial symmetry of the potential. We introduce bilinear forms as

$$\mathbb{M}_1 \equiv \big(\tilde{\Phi}_1, \Phi_1\big), \quad \mathbb{M}_2 \equiv \big(\tilde{\Phi}_2, \Phi_2\big) \begin{pmatrix} e^{-i\chi} & 0 \\ 0 & e^{i\chi} \end{pmatrix}, \tag{4.20}$$

where the scalar doublets Φ_1 and Φ_2 are defined in the Higgs basis. The phase χ ($0 \le \chi < 2\pi$) represents the degree of freedom of the phase rotation for Φ_2. The transformation law of global $\mathrm{SU}(2)_L \times \mathrm{SU}(2)_R$ for $\mathbb{M}_1$ and $\mathbb{M}_2$ is $\mathbb{M}_{1,2} \to L\mathbb{M}_{1,2}R^\dagger$, where $L \in \mathrm{SU}(2)_L$ and $R \in \mathrm{SU}(2)_R$. After

the spontaneous electroweak symmetry breaking, these matrices acquire the VEV as $\langle \mathbb{M}_1 \rangle = (v/\sqrt{2}) \times I_2$ and $\langle \mathbb{M}_2 \rangle = 0$, where I_2 is the 2×2 identical matrix. As a result, these matrices are invariant under the $L = R$ transformation, i.e. the custodial $\mathrm{SU}(2)_V$ transformation, even after the electroweak symmetry breaking. We can construct $\mathrm{SU}(2)_L \times \mathrm{U}(1)_Y$ gauge invariants as

$$\begin{aligned}
&\mathrm{Tr}[\mathbb{M}_1^\dagger \mathbb{M}_1] = 2|\Phi_1|^2, \quad \mathrm{Tr}[\mathbb{M}_2^\dagger \mathbb{M}_2] = 2|\Phi_2|^2, \quad \mathrm{Tr}[\mathbb{M}_1^\dagger \mathbb{M}_2] = e^{i\chi}\Phi_1^\dagger \Phi_2 + e^{-i\chi}\Phi_2^\dagger \Phi_1, \\
&\mathrm{Tr}[\mathbb{M}_1^\dagger \mathbb{M}_2 \sigma_3] = e^{i\chi}\Phi_1^\dagger \Phi_2 - e^{-i\chi}\Phi_2^\dagger \Phi_1.
\end{aligned} \tag{4.21}$$

The invariants in the first line of Eq. (4.21) are custodial $\mathrm{SU}(2)_V$ invariants, but in the second line are not. By using them, the potential which is given in Eq. (4.2) can be rewritten as

$$\begin{aligned}
V = &-\frac{1}{2}Y_1^2 \mathrm{Tr}[\mathbb{M}_1^\dagger \mathbb{M}_1] - \frac{1}{2}Y_2^2 \mathrm{Tr}[\mathbb{M}_2^\dagger \mathbb{M}_2] - \mathrm{Re}[Y_3^2 e^{-i\chi}]\mathrm{Tr}[\mathbb{M}_1^\dagger \mathbb{M}_2] \\
&+ \frac{1}{8}Z_1 \mathrm{Tr}[\mathbb{M}_1^\dagger \mathbb{M}_1]^2 + \frac{1}{8}Z_2 \mathrm{Tr}[\mathbb{M}_2^\dagger \mathbb{M}_2]^2 + \frac{1}{4}Z_3 \mathrm{Tr}[\mathbb{M}_1^\dagger \mathbb{M}_1]\mathrm{Tr}[\mathbb{M}_2^\dagger \mathbb{M}_2] \\
&+ \frac{1}{4}(Z_4 + \mathrm{Re}[Z_5 e^{-2i\chi}])\mathrm{Tr}[\mathbb{M}_1^\dagger \mathbb{M}_2]^2 \\
&+ \frac{1}{2}\Big(\mathrm{Re}[Z_6 e^{-i\chi}]\mathrm{Tr}[\mathbb{M}_1^\dagger \mathbb{M}_1] + \mathrm{Re}[Z_7 e^{-i\chi}]\mathrm{Tr}[\mathbb{M}_2^\dagger \mathbb{M}_2]\Big)\mathrm{Tr}[\mathbb{M}_1^\dagger \mathbb{M}_2] \\
&+ i\mathrm{Im}[Y_3^2 e^{-i\chi}]\mathrm{Tr}[\mathbb{M}_1^\dagger \mathbb{M}_2 \sigma_3] - \frac{1}{4}(Z_4 - \mathrm{Re}[Z_5 e^{-2i\chi}])\mathrm{Tr}[\mathbb{M}_1^\dagger \mathbb{M}_2 \sigma_3]^2 \\
&+ \frac{i}{2}\mathrm{Im}[Z_5 e^{-2i\chi}]\mathrm{Tr}[\mathbb{M}_1^\dagger \mathbb{M}_2]\mathrm{Tr}[\mathbb{M}_1^\dagger \mathbb{M}_2 \sigma_3] \\
&+ \frac{i}{2}\Big(\mathrm{Im}[Z_6 e^{-i\chi}]\mathrm{Tr}[\mathbb{M}_1^\dagger \mathbb{M}_1] + \mathrm{Im}[Z_7 e^{-i\chi}]\mathrm{Tr}[\mathbb{M}_2^\dagger \mathbb{M}_2]\Big)\mathrm{Tr}[\mathbb{M}_1^\dagger \mathbb{M}_2 \sigma_3].
\end{aligned} \tag{4.22}$$

Obviously, the last three lines in Eq. (4.22) are not custodial $\mathrm{SU}(2)_V$ invariant, so that we obtain the conditions for the custodial symmetric potential:

$$\begin{aligned}
&\mathrm{Im}[Y_3^2 e^{-i\chi}] = \mathrm{Im}[Z_5 e^{-2i\chi}] = \mathrm{Im}[Z_6 e^{-i\chi}] = \mathrm{Im}[Z_7 e^{-i\chi}] = 0, \\
&Z_4 = \mathrm{Re}[Z_5 e^{-2i\chi}].
\end{aligned} \tag{4.23}$$

In the real Z_5 basis, the conditions are

$$\text{Custodial symmetry :} \qquad Z_4 = Z_5, \quad Z_6^I = Z_7^I = 0 \quad (\chi = 0,\ \pi), \tag{4.24}$$

$$\text{Twisted custodial symmetry :} \quad Z_4 = -Z_5, \quad Z_6^R = Z_7^R = 0 \quad (\chi = \pi/2,\ 3\pi/2). \tag{4.25}$$

The conditions in the Eq. (4.24) (Eq. (4.25)) for $\chi = 0$ and π ($\chi = \pi/2$ and $3\pi/2$) have been known as the conditions for the (twisted) custodial symmetry in the potential [151–153]. We note, even if the potential satisfies Eq. (4.24) or Eq. (4.25), the $\mathrm{U}(1)_Y$ gauge interaction and the Yukawa interaction violate the custodial symmetry.

Next, we discuss the conditions for the CP symmetry in the potential. In order to preserve the CP symmetry in the potential, so-called the *real basis*, in which all parameters in the potential are real, must exist [151, 154]. The scalar doublet Φ_2 has the degree of the freedom for rephasing, so that there are three rephasing invariants in the potential, $Z_5^* Z_6^2$, $Z_5^* Z_7^2$ and $Z_6^* Z_7$. As a result, we obtain the conditions for the CP conserving potential in the real Z_5 basis [137, 151, 154, 155]:

$$Z_5 \mathrm{Im}[Z_6^2] = Z_5 \mathrm{Im}[Z_7^2] = \mathrm{Im}[Z_6^* Z_7] = 0. \tag{4.26}$$

In the general 2HDM, we also have the complex parameters in the Yukawa sector, and the additional Yukawa matrices ρ^f ($f = u, d, e$) are able to violate the CP symmetry. For example,

in the case of $\rho^d = \rho^e = 0$, the additional rephasing invariants in the model are $Z_5(\rho^u)^2$, $Z_6\rho^u$ and $Z_7\rho^u$, so that all of them have to be real matrices for the CP symmetry [151].

From Eqs. (4.24) and (4.26), we obtain important relation for the custodial symmetry violation and the CP violation in the potential: *If the CP symmetry is violated in the potential, the custodial symmetry is also violated.* In chapter 8, we will discuss $H^\pm W^\mp Z$ vertices as a consequence of the custodial symmetry violation and the CP violation.

4.1.5 Oblique parameters

The finite corrections to the self energy of the electroweak gauge bosons are parametrized by the oblique parameters, S, T, and U, which was first introduced by Peskin and Takeuchi [97, 98]. New particles interacting to electroweak bosons could affect the self energies of them, so that some models can be tested by the precision measurement of these parameters. Especially, the T parameter represents the difference between the mass corrections of the W and Z bosons, and it is related to the ρ parameter [66–70] as $\alpha_{em}T = \rho - 1$ $(= \Delta\rho)$. The T parameter can be expressed by [73]

$$\alpha_{em}T = \frac{\Pi^{\rm new}_{WW}(0)}{m_W^2} - \frac{\Pi^{\rm new}_{ZZ}(0)}{m_Z^2}, \tag{4.27}$$

where α_{em} is the fine-structure constant, and $\Pi^{\rm new}_{VV}(0)$ $(V = W, Z)$ are the corrections from new physics to the two-point self energies of the gauge bosons at the zero momentum. The observed value of the ρ parameter is very close to unity [71–73].

In the 2HDM, the additional scalar bosons radiatively contribute to the self energy of the gauge bosons, and those parameters are modified from the value in the SM. Especially, the T parameter is an important parameter to know the structure of the Higgs potential because it is sensitive to the violation of the custodial symmetry in the 2HDM [67, 69, 151, 152]. When the potential has the custodial symmetry, the corrections to the T parameter from the 2HDM are zero, and there are only corrections from the $\mathrm{U}(1)_Y$ and the Yukawa interactions. However, within the one-loop level analysis, the inverse is not true, i.e. the small T parameter does not mean that the potential has the custodial symmetry.

For example, when we take a limit $Z_6 = 0$, as one can see from Eqs. (4.5) and (4.8), the squared mass matrix for the neutral scalar bosons is diagonalized with $\mathcal{R}_{ij} = \delta_{ij}$, and the relations $m^2_{H^\pm} - m^2_{H_2} = (Z_4 + Z_5)v^2/2$ and $m^2_{H^\pm} - m^2_{H_3} = (Z_4 - Z_5)v^2/2$ are shown. Therefore, in the real Z_5 basis, the conditions for the custodial symmetric potential are given by

$$\text{Custodial symmetry :} \quad m_{H^\pm} = m_{H_3}, \quad Z_7^I = 0 \quad (\chi = 0,\ \pi), \tag{4.28}$$

$$\text{Twisted custodial symmetry :} \quad m_{H^\pm} = m_{H_2}, \quad Z_7^R = 0 \quad (\chi = \pi/2,\ 3\pi/2). \tag{4.29}$$

When we denote the new contribution of the T parameter in the 2HDM as ΔT, at the one-loop level, it is given by [151, 152]

$$\Delta T = \frac{1}{16\pi m_W^2 \sin^2\theta_W}\Big(F(m^2_{H^\pm}, m^2_{H_2}) + F(m^2_{H^\pm}, m^2_{H_3}) - F(m^2_{H_2}, m^2_{H_3})\Big), \tag{4.30}$$

where the function F is defined by

$$F(a,b) = \frac{1}{2}(a+b) - \frac{ab}{a-b}\ln\frac{a}{b}, \tag{4.31}$$

and θ_W is the Weinberg angle. Even if $Z_7 \neq 0$, by taking $m_{H_2} = m_{H^\pm}$ or $m_{H_3} = m_{H^\pm}$, ΔT can vanish at the one-loop level. This is because, at this order, the T parameter does not depend on Z_7, which is not related to the mass formulae of the scalar bosons at the tree level.

As we discussed in the former subsection, the custodial symmetry is violated by the CP violating potential. Since the T parameter does not depend on Z_7 at the one-loop level, the proposition that the potential violates the CP symmetry $\Rightarrow \Delta T \neq 0$, and its inverse are not true. The CP violating effects to ΔT from the non-zero Z_6 has been discussed in Refs. [151,152].

4.1.6 Theoretical constraints

In this subsection, we discuss the vacuum stability, the perturbative unitarity, and the triviality bound as theoretical constraints on the extended Higgs models.

First, for the stable vacuum, the potential must be Bounded From the Below (BFB). When we set the potential value at the vacuum to be zero, the potential should be positive with an infinite value of any direction of the scalar fields. These conditions are expressed by the quartic coupling constants in the tree level potential, and for the 2HDM with the softly broken $\mathbb{Z}_2$ symmetry, the necessary conditions for the BFB is known as [150, 156–161]

$$\lambda_1 \geq 0,\ \lambda_2 \geq 0,\ \lambda_3 \geq -\sqrt{\lambda_1\lambda_2},\ \lambda_3 + \lambda_4 \pm \lambda_5 \geq -\sqrt{\lambda_1\lambda_2}. \tag{4.32}$$

The conditions for the general 2HDM have been discussed in Ref. [162].

Second, when we do perturbative calculation, we need to take into account the perturbative unitarity constraint. By the partial wave expansion, amplitude of a scattering process is decomposed by

$$\mathcal{M} = 16\pi \sum_{l}^{\infty} (2l+1) a_l P_l(\cos\theta), \tag{4.33}$$

where P_l is Legendre polynomials and a_l is complex functions of the center-of-mass energy $\sqrt{s}$. If we discuss the process at the tree level, s wave amplitude, i.e. a_0, is real. The size of a_0 is bounded by a finite constant ξ, and usually it is taken to be $\xi = 0.5$ [146] or $\xi = 1$ [163]. The tree level unitarity bound in the 2HDM has been studied in Refs. [164–167].

Finally, by the Renormalization Group Equation (RGE) analysis, the Landau pole, where the coupling constants diverge, can appear in the extended Higgs models. In the SM, the self-coupling constant of the Higgs boson becomes negative between 10^9 GeV and the Plank scale, so that the electroweak vacuum is metastable [168–172]. On the other hand, due to multiple coupling constants of scalar bosons, beta functions for them tend to be positive, resulting the Landau pole at the scale much below the Planck scale. Above or near the Landau pole, the theory should be replaced by a more fundamental theory. However, if the scale of the Landau pole is very small, e.g. the scale which we have already reached in high energy collider experiment, signatures should already been measured. Once we impose the condition that the Landau pole does not appear below a scale, the parameters in the model are constrained. We call this bound the triviality bound, and it will be discussed in chapter 9.

4.1.7 Experimental constraints

In this subsection, we discuss the experimental constraints for the 2HDM. We first focus on the 2HDM with the flavor aligned Yukawa matrix, $(\rho^f)_{lm} = 0$ $(l \neq m)$. We then explain the effect of the off-diagonal coupling constants, which cause tree level FCNC processes.

Higgs boson measurement

First, the coupling constants for H_1 have been measured at LHC. In the 2HDM, the coupling constants for H_1VV are modified by the factor $\mathcal{R}_{11}$ from the SM predictions, as indicated in

Eqs. (4.6) and (4.7). The $H_1 ff$ coupling constants are also modified from the SM. Therefore, we have $\kappa_W = \kappa_Z = \mathcal{R}_{11}$ and

$$\kappa_{f_l} = \mathcal{R}_{11}\left(Y_{\rm d}^f\right)_{ll} + (\mathcal{R}_{12} \mp i\mathcal{R}_{13})\left(\rho^f\right)_{ll}, \tag{4.34}$$

and those are constrained by ATLAS [19] and CMS [20] results, as discussed in section 2.6. In table III of Ref. [173], available data for the Higgs signal strengths is summarized. When we take $\alpha_i = 0$ (alignment limit), $\mathcal{R}_{11} = 1$ and $\mathcal{R}_{12} = \mathcal{R}_{13} = 0$ are shown, and all of the $\kappa_{W,Z,f}$ parameters coincide to the SM ones at the tree level.

Direct searches for the charged scalar bosons

Second, we discuss the direct search experiments for charged Higgs bosons at LEP and LHC.

From the result at the LEP experiment [174], a lower bound of the mass is given by $m_{H^\pm} \gtrsim 80$ GeV almost independent of ρ^f.

When the mass region is 80 GeV $\lesssim m_{H^\pm} \lesssim 170$ GeV, the charged Higgs bosons are produced in the top quark decay process $t \to H^\pm b$. The upper bound of $\mathcal{B}(t \to H^\pm b) \times \mathcal{B}(H^\pm \to \tau^\pm \nu)$ in this mass region is severely constrained from ATLAS [175] and CMS data [176], and the branching ratio needs to satisfy $\mathcal{B}(t \to H^\pm b) \lesssim O(10^{-3})$ when $\mathcal{B}(H^\pm \to \tau^\pm \nu) = 1$ [83].

At LHC, $H^\pm$ is produced via the top-associated production $gb \to H^\pm t$ [100]. The coupling constants ρ^f are constrained by the following decay modes $H^\pm \to tb$ [177] or $H^\pm \to \tau^\pm \nu$ [176]. If it is kinematically allowed, $H^\pm$ also decay into an off-shell W boson and a neutral Higgs boson [83, 178].

The decays $H^\pm \to W^\pm Z$ via $pp(WZ) \to H^\pm X$ have been searched by ATLAS [179] and CMS [180]. These production and decay processes are the loop-induced processes via the $H^\pm W^\mp Z$ vertices in the 2HDM, and it will be discussed in chapter 8.

Direct searches for the additional neutral scalar bosons

Third, we discuss the direct searches for additional neutral Higgs bosons, H_2 and H_3, at LHC.

There are three important single production processes of the neutral Higgs bosons, such as $gg \to H_{2,3}$ (gluon fusion), $gg \to H_{2,3}b\bar{b}$ (bottom associated) and $gg \to H_{2,3}t\bar{t}$ (top associated). When $m_{H_{2,3}} < 2m_t$, ρ^f are constrained from the results of $H_{2,3} \to \tau\overline{\tau}$ searches by ATLAS [181]. When $m_{H_{2,3}} > 2m_t$, the decay into a top quark pair is kinematically allowed, and ρ^f are also constrained by the data of $H_{2,3} \to t\bar{t}$ searches by ATLAS [182, 183] and CMS [184]. When the mixing angles α_i are non-zero, $H_{2,3}$ can decay into W^+W^-, ZZ, H_1H_1 or ZH_1, if they are kinematically allowed [185].

The additional scalar bosons can be produced by the pair production processes [186–188]. The following multi charged lepton decays can be constrained [178] from the result by ATLAS [189].

Constraints from flavor experiments

Fourth, we discuss constraints from flavor experiments. In addition to the SM contributions, diagrams involving the additional Higgs boson exchanges contribute to many flavor observables.

When we consider ρ^f to be diagonal, such new effects in the flavor changing observables appear at the loop level. The important flavor observables which relates to diagonal elements in ρ^f are $B \to X_s\gamma$, $B_{d,s} \to \mu^+\mu^-$, $B_{d,s}$-$\overline{B_{d,s}}$ and K^0-$\overline{K^0}$ mixing [139, 173, 190–194]. The experimental value of the branching ratio for $B \to X_s\gamma$ with the photon energy cut $E_\gamma > 1.6$ GeV is given by [195, 196]

$$\mathcal{B}(B \to X_s\gamma)_{\rm exp} = (3.32 \pm 0.15) \times 10^{-4}. \tag{4.35}$$

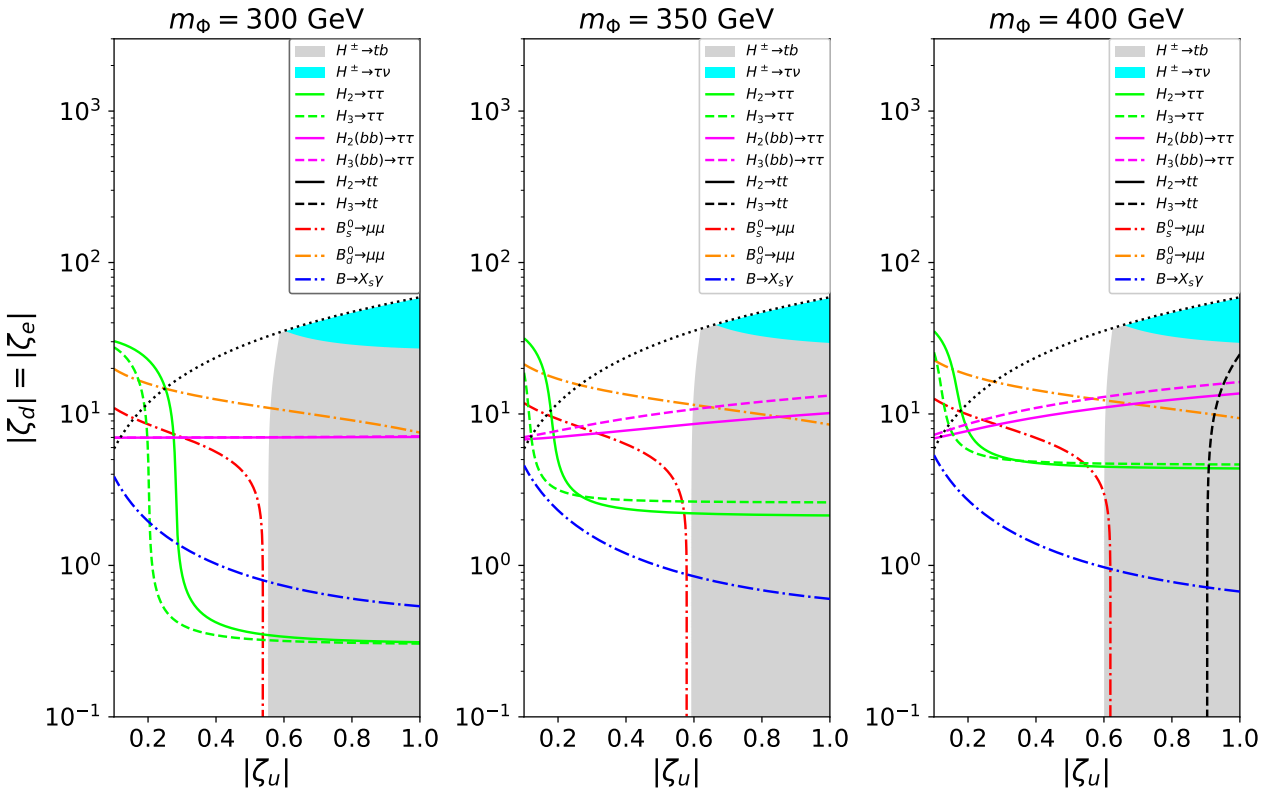

Figure 4.1: Several constraints on the additional Yukawa couplings from direct searches and flavor experiments.

Observed values of the branching ratios of $B_d \to \mu\mu$ and $B_s \to \mu\mu$ can be referred in Refs. [195, 197–199]:

$$\begin{aligned} &\mathcal{B}(B_d \to \mu\mu) < 2.1 \times 10^{-10} \ (95\% \text{ C.L.}), \\ &\mathcal{B}(B_s \to \mu\mu) = (3.1 \pm 0.6) \times 10^{-9}. \end{aligned} \tag{4.36}$$

The UTfit results [200, 201] give constraints on B_d-$\overline{B_d}$ and B_s-$\overline{B_s}$ mixing amplitudes as $C_{B_d} = [0.83, 1.29]$, $\phi_{B_d} = [-6.0^\circ, 1.5^\circ]$ and $C_{B_s} = [0.942, 1.288]$ at 95% C.L., where $C_{B_q} e^{2i\phi_{B_q}} = \left\langle B_q^0 \right| H_{\text{eff}}^{\text{full}} \left| \overline{B_q^0} \right\rangle / \left\langle B_q^0 \right| H_{\text{eff}}^{\text{SM}} \left| \overline{B_q^0} \right\rangle$ $(q = d, s)$. The upper limit of the 2HDM contribution to the indirect CP violation in K^0-$\overline{K^0}$ mixing is $|\epsilon_K^{\text{2HDM}}| < 4.0 \times 10^{-4}$ [202].

As a representative parameter space of the 2HDM, constraints from the direct searches and the flavor experiments on the additional Yukawa couplings are shown in figure 4.1. We here have assumed Pich–Tuzon parametrization [203], where all of ρ^f are diagonalized as

$$\rho^u = \zeta_u^* Y_{\text{d}}^u, \quad \rho^d = \zeta_d Y_{\text{d}}^d, \quad \rho^e = \zeta_e Y_{\text{d}}^e. \tag{4.37}$$

We also have taken conditions of alignment limit $\alpha_i = 0$, degeneration of the additional scalar bosons $m_{H^\pm} = m_{H_2} = m_{H_3} \equiv m_\Phi$, and $\zeta_e = \zeta_d$. We neglect phases of ζ_f, and take $m_\Phi = 300, 350$ and 400 GeV in the left, middle and right panels, respectively. The black dotted lines satisfy $|\zeta_d| = (m_t/m_b)|\zeta_u|$ which are the reliable bounds about the calculation of $\sigma(gb \to tH^\pm)$, where we have referred the value from Ref. [185]. The gray (cyan) regions below the black dashdot lines are excluded from $H^\pm \to tb$, $(H^\pm \to \tau\nu)$. The green solid (dashed) lines and the magenta solid (dashed) lines are the upper bounds from $H_2 \to \tau\overline{\tau}$, $(H_3 \to \tau\overline{\tau})$ and $H_2(b\bar{b}) \to \tau\overline{\tau}$, $(H_3(b\bar{b}) \to \tau\overline{\tau})$, respectively. In the right panel of figure 4.1, which is the case of $m_\Phi = 400$ GeV, the constraint from $H_3 \to t\bar{t}$ can be seen as the black dashed line. The regions above the red (orange) and blue dashdot lines are excluded from $B_s(B_d) \to \mu\mu$ and $B \to X_s\gamma$, respectively.

Constraints on ρ_{tc} coupling from direct searches

Finally, we discuss constraints on the FCNC couplings from direct searches.

The off-diagonal elements of ρ^f cause the FCNC processes at the tree level, which are severely constrained by flavor experiments. For example, according to Ref. [139], $\rho_{ds,sd}$ ($\rho_{uc,cu}$) are strongly constrained by K^0-$\overline{K^0}$ mixing and $K_L \to \mu^+\mu^-$ (D^0-$\overline{D^0}$ mixing and $\overline{D^0} \to \mu^+\mu^-$). The FCNC couplings for the leptons are constrained by Lepton Flavor Violating (LFV) processes, such as $\mu \to e\gamma$ [204], $\mu \to 3e$ [205], $\tau \to e\gamma$ [206], and so on. As a result, we only have sizable FCNC coupling in the top-charm sector. Due to the absence of the CKM suppression, ρ_{ct} receives stronger constraints, while ρ_{tc} can be $O(1)$. As it will be discussed in section 7.3, ρ_{tc} can be additional sources of the BAU in the scenario of EWBG.

The off-diagonal element ρ_{tc} contributes to the top quark decay process $t \to cH_1$ in $\alpha_i \neq 0$ case. When the mixing angle α_1 satisfies $\cos\left(\alpha_1 - \frac{\pi}{2}\right) \simeq 0.3$, $\rho_{tc} \gtrsim 0.3$ is excluded [207, 208] by ATLAS [209] and CMS [210] data.

The additional Yukawa couplings ρ_{tc} and ρ_{tt} affect production processes of the heavy neutral scalar bosons via $gg \to H_{2,3}$ and $gc \to H_{2,3}t$ and their decay processes into tc or tt. Especially ρ_{tc} produces same sign top quarks via $gc \to H_{2,3}t \to tt\bar{c}$ process, and this is constrained by the control region for $t\bar{t}W$ background (CRW) in the SM four top production searches [208,211–215]. When $m_{H_3} = 350$ GeV and H_2 decouples, Ref. [208] gives an upper bound $\rho_{tc} \sim 0.5$ by using the CMS data [216, 217]. If the mass and decay width of them are degenerated, this constraint is weakened due to the interference between $cg \to tH_2 \to tt\bar{c}$ and $cg \to tH_3 \to tt\bar{c}$ processes [211, 214]. On the other hand, $gc \to H_{2,3}t \to tt\bar{t}$ process induced by ρ_{tc} and ρ_{tt} was discussed in Ref. [213], and some parameter regions are excluded by the CMS four top searches [216, 217].

About the charged scalar bosons, the process of $pp \to H^\pm \to bc$ has a sensitivity for the large ρ_{tc} coupling [218]. For example, $\rho_{tc} \gtrsim 0.5$ with $m_{H^\pm} = 350$ GeV are constrained by the mistag rate $\not\in \to b$ analysis with the bottom flavored dijet search at LHC with $\sqrt{s} = 8$ TeV [219].

4.1.8 Triple Higgs boson coupling

In the some of extended Higgs models, such as the 2HDM, it is known that the triple Higgs boson coupling λ_{hhh} is enhanced by the quantum non-decoupling effect of the additional scalar bosons [23, 220–223]. By using the one loop effective potential in the 2HDM, as it will also be discussed in chapter 7, we obtain the deviation from the SM prediction

$$\Delta R \equiv \frac{\lambda_{hhh}}{\lambda_{hhh}^{\rm SM}} - 1 = \frac{1}{12\pi^2 v^2 m_{H_1}^2}\left\{2\frac{(m_{H^\pm}^2 + Y_2^2)^3}{m_{H^\pm}^2} + \frac{(m_{H_2}^2 + Y_2^2)^3}{m_{H_2}^2} + \frac{(m_{H_3}^2 + Y_2^2)^3}{m_{H_3}^2}\right\}. \quad (4.38)$$

This deviation corresponds to κ_λ, and it would be measured by the process of di-Higgs production at future colliders [24, 224–233]. At the HL-LHC and the ILC with $\sqrt{s} = 500$ GeV (1 TeV), this coupling is expected to be measured at the 50% [21] and 27% (10 %) [24, 25] accuracy, respectively.

The triple Higgs coupling can be a probe of the SFOPT [23], and it will be discussed in chapter 7.

Particle	Q_L	u_R	d_R	L_L	e_R	Φ	N_α	η	S
$\mathrm{SU}(3)_C$	**3**	**3**	**3**	**1**	**1**	**1**	**1**	**1**	**1**
$\mathrm{SU}(2)_L$	**2**	**1**	**1**	**2**	**1**	**2**	**1**	**2**	**1**
$\mathrm{U}(1)_Y$	1/6	2/3	−1/3	−1/2	−1	1/2	0	1/2	0
$\mathrm{U}(1)_{B-L}$	1/3	1/3	1/3	−1	−1	0	−1	0	+2
$\mathbb{Z}_2$	+	+	+	+	+	+	−	−	+

Table 4.2: Particle content and their quantum numbers.

4.2 $\mathrm{U}(1)_{B-L}$ gauge extension of Inert doublet model with the right-handed neutrino

4.2.1 Particle contents and Lagrangian

In this section, we introduce a model to explain the tiny neutrino mass and the relic abundance of the DM. We consider gauged $\mathrm{U}(1)_{B-L}$ extension of the Inert doublet model with the right handed neutrino [76]. In this model, three $\mathbb{Z}_2$ odd Right-Handed (RH) neutrinos N_α ($\alpha = 1, 2, 3$), a $\mathbb{Z}_2$ odd scalar $\mathrm{SU}(2)_L$ doublet η, a scalar singlet S and an electrically neutral $\mathrm{U}(1)_{B-L}$ gauge boson Z' are introduced. The Lagrangian is invariant under the gauge group $\mathrm{SU}(3)_C \times \mathrm{SU}(2)_L \times \mathrm{U}(1)_Y \times \mathrm{U}(1)_{B-L}$ with an unbroken $\mathbb{Z}_2$ discrete symmetry. The particle content is shown in Table 4.2.

The relevant interaction $\mathcal{L}_{\rm int}$ for our discussion is given by

$$\mathcal{L}_{\rm int} = \mathcal{L}^{\rm SM}_{\rm Yukawa} + \mathcal{L}_N - V(\Phi, \eta, S), \tag{4.39}$$

where $\mathcal{L}^{\rm SM}_{\rm Yukawa}$ is the SM Yukawa interaction, and

$$\mathcal{L}_N = \sum_{\alpha=1}^{3} \left(-\sum_{i=1}^{3} g_{i\alpha} \overline{L_i} \tilde{\eta} N_\alpha - \frac{y^R_\alpha}{2} \overline{N^c_\alpha} S N_\alpha + \text{h.c.} \right) \tag{4.40}$$

with $\tilde{\eta} = i\tau^2 \eta^*$, where $i, \alpha = 1, 2, 3$ are flavors of leptons. Without loss of generality, the Yukawa coupling y^R of RH neutrinos can be flavor diagonal. The Yukawa coupling among $\overline{L_i} \Phi N_\alpha$ is prohibited due to the unbroken $\mathbb{Z}_2$ symmetry. The active neutrinos remain massless at the tree level, and obtain tiny masses at the one-loop level.

The scalar potential $V(\Phi, \eta, S)$ in this model is given by

$$\begin{aligned} V(\Phi, \eta, S) = {} & \mu_1^2 |\Phi|^2 + \mu_2^2 |\eta|^2 + \mu_S^2 |S|^2 + \frac{\lambda_1}{2} |\Phi|^4 + \frac{\lambda_2}{2} |\eta|^4 + \lambda_3 |\Phi|^2 |\eta|^2 \\ & + \lambda_4 \left| \Phi^\dagger \eta \right|^2 + \frac{\lambda_5}{2} \left[(\Phi^\dagger \eta)^2 + \text{h.c.} \right] + \tilde{\lambda} |\Phi|^2 |S|^2 + \lambda |\eta|^2 |S|^2 + \lambda_S |S|^4, \end{aligned} \tag{4.41}$$

where λ_5 can be taken as real by rephasing of η. We assume $\mu_1^2 < 0, \mu_S^2 < 0, \mu_2^2 > 0$, so that Φ and S receive non-zero VEVs by spontaneously symmetry breaking of the $\mathrm{SU}(2)_L \times \mathrm{U}(1)_Y$ and $\mathrm{U}(1)_{B-L}$ gauge symmetries, respectively. This potential is an extension of the Inert doublet model given in Eq. (4.17), so that the VEV of η remains zero.

The $\mathrm{U}(1)_{B-L}$ gauge symmetry is assumed to be spontaneously broken above the electroweak scale. The scalar singlet S is parameterized as

$$S = \frac{1}{\sqrt{2}} (v_S + \phi_S + i z_S), \tag{4.42}$$

where v_S is the VEV of the $\mathrm{U}(1)_{B-L}$ symmetry breaking, ϕ_S is a neutral scalar boson, and z_S is the NG boson. The Z' boson obtains its mass as $m_{Z'} = 2 g_{B-L} v_S$ by its longitudinal

mode absorbing z_S, where g_{B-L} is the gauge coupling for the $\mathrm{U}(1)_{B-L}$ symmetry. In the $\mathrm{SU}(2)_L \times \mathrm{U}(1)_Y \times \mathrm{U}(1)_{B-L}$ gauge sector, we suppose that the kinetic mixing between Z and Z' is negligible. RH neutrinos N_α also receive their masses as

$$m_{N_\alpha} = \frac{y_\alpha^R v_S}{\sqrt{2}}. \tag{4.43}$$

After the electroweak symmetry breaking, the $\mathrm{SU}(2)_L$ scalar doublet Φ is parameterized as

$$\Phi = \begin{pmatrix} G^+ \\ \frac{1}{\sqrt{2}}(v + \phi + iG^0) \end{pmatrix}, \tag{4.44}$$

where v is the VEV of the electroweak symmetry breaking, G^+ and G^0 are NG bosons absorbed by longitudinal modes of the electroweak gauge bosons, i.e., W and Z bosons, respectively. The stationary conditions give the following relations

$$\mu_1^2 + \frac{\lambda_1}{2}v^2 + \frac{\tilde{\lambda} v_S^2}{2} = 0, \quad \mu_S^2 + \lambda_S v_S^2 + \frac{\tilde{\lambda} v^2}{2} = 0. \tag{4.45}$$

The mixing between ϕ and ϕ_S leads to the following mass terms

$$\frac{1}{2}\begin{pmatrix}\phi & \phi_S\end{pmatrix}\mathcal{M}^2\begin{pmatrix}\phi \\ \phi_S\end{pmatrix} = \frac{1}{2}\begin{pmatrix}\phi & \phi_S\end{pmatrix}\begin{pmatrix}\lambda_1 v^2 & \widetilde{\lambda} v v_S \\ \widetilde{\lambda} v v_S & 2\lambda_S v_S^2\end{pmatrix}\begin{pmatrix}\phi \\ \phi_S\end{pmatrix}. \tag{4.46}$$

The squared mass matrix $\mathcal{M}^2$ can be diagonalized by an orthogonal matrix with the mixing angle α

$$\begin{pmatrix}h_1 \\ h_2\end{pmatrix} = \begin{pmatrix}\cos\alpha & -\sin\alpha \\ \sin\alpha & \cos\alpha\end{pmatrix}\begin{pmatrix}\phi \\ \phi_S\end{pmatrix}, \tag{4.47}$$

where h_1 and h_2 are mass eigenstate of neutral scalar bosons

$$m_{h_1}^2 = \lambda_1 v^2 \cos^2\alpha + 2\lambda_S v_S^2 \sin^2\alpha - \widetilde{\lambda} v v_S \sin 2\alpha, \tag{4.48}$$

$$m_{h_2}^2 = \lambda_1 v^2 \sin^2\alpha + 2\lambda_S v_S^2 \cos^2\alpha + \widetilde{\lambda} v v_S \sin 2\alpha, \tag{4.49}$$

with the constraint

$$\widetilde{\lambda} v v_S \cos 2\alpha + \left(\frac{\lambda_1}{2}v^2 - \lambda_S v_S^2\right)\sin 2\alpha = 0. \tag{4.50}$$

In this model, we fix the mass eigenstate h_1 to be the SM-like Higgs boson with $m_{h_1} = 125$ GeV, and h_2 is the additional scalar boson.

The $\mathbb{Z}_2$-odd scalar $\mathrm{SU}(2)_L$ doublet field η can be parameterized as

$$\eta = \begin{pmatrix} H^+ \\ \frac{1}{\sqrt{2}}(H + iA) \end{pmatrix}. \tag{4.51}$$

The mass spectrum of $\mathbb{Z}_2$-odd scalar particles is

$$m_{H^\pm}^2 = \mu_2^2 + \frac{\lambda}{2}v_S^2 + \frac{\lambda_3}{2}v^2, \tag{4.52}$$

$$m_H^2 = \mu_2^2 + \frac{\lambda}{2}v_S^2 + \frac{\lambda_3 + \lambda_4 + \lambda_5}{2}v^2, \tag{4.53}$$

$$m_A^2 = \mu_2^2 + \frac{\lambda}{2}v_S^2 + \frac{\lambda_3 + \lambda_4 - \lambda_5}{2}v^2. \tag{4.54}$$

There are 11 parameters $\mu_{1,2}^2, \mu_S^2, \lambda_{1,2,3,4,5}, \lambda, \lambda_S, \tilde{\lambda}$ in the scalar potential in Eq.(4.41). They can be replaced by 9 new physics parameters $\mu_2^2, m_{h_2}, m_H, m_A, m_{H^\pm}, \alpha, v_S, \lambda_2$ and λ, in addition to the two SM parameters v and m_{h_1}.

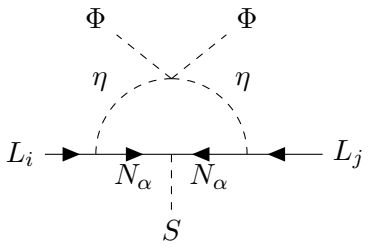

Figure 4.2: The one-loop diagram which generates small neutrino masses.

4.2.2 Radiative generation of the neutrino mass

In this model, tiny neutrino masses are generated via the one-loop induced dimension-six operator $S\overline{(L\Phi)^c}L\Phi/\Lambda^2$, where Λ is an energy scale parameter, as shown in FIG. 4.2.

Following the framework of Ref. [123, 124], after the electroweak symmetry breaking, the mass matrix of light neutrinos at one-loop level is

$$m_\nu^{ij} = \sum_\alpha g_{i\alpha} g_{j\alpha} \Lambda_\alpha \equiv (g\Lambda g^T)^{ij}, \tag{4.55}$$

where the diagonal matrix Λ is defined by

$$\Lambda_\alpha = \frac{m_{N_\alpha}}{32\pi^2}\left[\frac{m_H^2}{m_{N_\alpha}^2 - m_H^2}\ln\left(\frac{m_{N_\alpha}^2}{m_H^2}\right) - \frac{m_A^2}{m_{N_\alpha}^2 - m_A^2}\ln\left(\frac{m_{N_\alpha}^2}{m_A^2}\right)\right]. \tag{4.56}$$

In order to evaluate the Yukawa coupling of neutrinos, we adopt the Casas-Ibarra (CI) parametrization [234]. The matrix of the Yukawa coupling can be parameterized as

$$g_{i\alpha} = \left(U_{\rm PMNS}\sqrt{\mathcal{M}_\nu}R\sqrt{\Lambda^{-1}}\right)_{i\alpha}, \tag{4.57}$$

where $U_{\rm PMNS}$ is the PMNS matrix [106,107], and the diagonalized mass matrix of active neutrinos is defined as $\mathcal{M}_\nu \equiv {\rm diag}(m_{\nu_1}, m_{\nu_2}, m_{\nu_3})$. The matrix R is an arbitrary complex orthogonal matrix. In the benchmark analysis which is given in chapter 5, where the problems of the neutrino mass and the DM are solved, we will take $R = I$.

4.2.3 Constraints on the model

In this subsection, we discuss several constraints on the ${\rm U}(1)_{B-L}$ extension of the Inert doublet model with the RH neutrino.

First, BFB conditions for this model is given by [150, 156–161, 235–237]

$$\begin{aligned}&\lambda_1 \geq 0,\ \lambda_2 \geq 0,\ \lambda_3 \geq -\sqrt{\lambda_1\lambda_2},\ \lambda_3 + \lambda_4 \pm \lambda_5 \geq -\sqrt{\lambda_1\lambda_2},\\ &\lambda_S \geq 0,\ \lambda \geq -\sqrt{2}\sqrt{\lambda_2\lambda_S},\ \tilde{\lambda} \geq -\sqrt{2}\sqrt{\lambda_1\lambda_S}.\end{aligned} \tag{4.58}$$

Second, as a perturbative criterion, we require that all the quartic vertices of scalar fields should satisfy $\lambda_{1,2,3,4,5}, \lambda_S, \widetilde{\lambda}, \lambda < 4\pi$, and for Yukawa couplings, it is $(y_1^R)^2, (y_2^R)^2, (y_3^R)^2 < 4\pi$.

Third, in the following analysis, we consider normal mass ordering of the light neutrinos, and adopt the latest data from the PDG [73], which is given in Eq. (3.2).

Fourth, we consider constraints from charged LFV. In this model, charged LFV decay processes are generated by one-loop diagrams mediated by $H^\pm$ and N_α. We consider constraints from $l_i \to l_j\gamma$ and $l_i \to l_j l_k \bar{l_k}$, as shown in Table 4.3.

LFV processes	Current bounds on branching ratios
$\mu^+ \to e^+\gamma$	3.1×10^{-13} [204]
$\mu^+ \to e^-e^+e^-$	1.0×10^{-12} [205]
$\tau^+ \to e^+\gamma$	3.3×10^{-8} [206]
$\tau^+ \to \mu^+\gamma$	4.2×10^{-8} [238]
$\tau^- \to e^-e^+e^-$	2.7×10^{-8} [239]
$\tau^- \to e^+\mu^-\mu^-$	1.7×10^{-8} [239]
$\tau^- \to e^-\mu^+\mu^-$	2.7×10^{-8} [239]
$\tau^- \to \mu^+e^-e^-$	1.5×10^{-8} [239]
$\tau^- \to \mu^-e^+e^-$	1.8×10^{-8} [239]
$\tau^- \to \mu^-\mu^+\mu^-$	2.1×10^{-8} [239]
$\mu^-\mathrm{Ti} \to e^-\mathrm{Ti}$	4.3×10^{-12} [240]
$\mu^-\mathrm{Au} \to e^-\mathrm{Au}$	7.0×10^{-13} [241]

Table 4.3: Current experimental bounds for LFV processes.

Fifth, this model basically provides two candidates of the DM, which are the lightest RH neutrino or the lightest neutral $\mathbb{Z}_2$ odd scalar particle, H or A. The relic density of the DM candidates should satisfy observation results from the Planck satellite $\Omega h^2 = 0.120 \pm 0.001$ [18]. Direct detection experiments can also give constraints to this model. We apply limits from the LZ experiment [131, 132] on the WIMP-nucleon spin independent elastic scattering cross section. Detailed analysis is given in chapter 5.

Sixth, collider experiments give rich constraints on this model. This model includes the Inert doublet model, so that some constraints are same as the 2HDM.

By the chargino searches at the LEPII experiment [174], the region of $m_{H^\pm} > 80$ GeV are constrained. The LEPII experiment also excludes the intersection of the following mass region for inert scalar particles [242]:

$$m_H < 80 \text{ GeV},\ m_A < 100 \text{ GeV},\ m_A - m_H > 8 \text{ GeV}. \tag{4.59}$$

With precise measurements of decay widths of W and Z bosons [73], kinematically allowed regions for decay processes $W/Z \to \eta\eta$ are excluded.

For the constraints of the Z' gauge boson, the LEP II experiment gives the lower limit of the ratio, as given by $m_{Z'}/g_{B-L} > 7$ TeV [243–245]. The null result in searching for the Z' boson at ATLAS [246, 247] and CMS [248, 249] gives strong constraints on the Z' boson, $m_{Z'} > 5.15$ TeV.

In addition, the mixing angle α predicts the deviation of the Higgs couplings from the SM. For example, κ parameter for the h_1ZZ coupling in this model is obtained by

$$\kappa_Z = \cos\alpha, \tag{4.60}$$

and current experimental results for the Higgs boson coupling [19, 20] constrain the mixing angle α. From the CMS constraints for κ_Z which have been already shown in table. 2.2, we have

$$0.90 < \cos\alpha \leq 1.0, \tag{4.61}$$

as a criterion of 95% CL. As similar to h_1, the additional neutral scalar boson h_2 can also be constrained by the Higgs signal strength at LHC [250, 251]. For $m_{h_2} \gtrsim 125$ GeV ($m_{h_2} \lesssim 125$ GeV), $\sin\alpha \simeq 0.3$ ($\sin\alpha \simeq 0.1$) can be a conservative upper bound.

Finally, we consider constraints from the electroweak precision test. Especially, the oblique parameter T gives the strongest constraint on this model among S, T, U parameters. In this

model, inert doublet fields $H^{\pm}, H, A$ and scalar singlet h_2 contribute to deviations of T [67,252, 253]:

$$\Delta T = \frac{3\sin^2\alpha}{16\pi s_W^2}\left[f_T\left(\frac{m_{h_2}^2}{m_W^2}\right) - f_T\left(\frac{m_{h_1}^2}{m_W^2}\right) - \frac{1}{c_W^2}\left(f_T\left(\frac{m_{h_2}^2}{m_Z^2}\right) - f_T\left(\frac{m_{h_1}^2}{m_Z^2}\right)\right)\right] + \frac{1}{16\pi m_W^2 s_W^2}\left[F(m_{H^\pm}^2, m_H^2) + F(m_{H^\pm}^2, m_A^2) - F(m_H^2, m_A^2)\right], \tag{4.62}$$

where $F(a,b)$ is defined in Eq. (4.31), and

$$f_T(x) = \frac{x\log x}{x-1}. \tag{4.63}$$

Chapter 5

Radiative neutrino mass and dark matter in $\mathrm{U}(1)_{B-L}$ gauge theory

In this chapter, we discuss a concrete scenario where the tiny mass of the neutrinos and the relic abundance of the DM are solved. We do not discuss baryogenesis in this chapter, however, this model has a possibility to explain the BAU, as we will mention in section 5.3.

The seesaw mechanism [108–118] is a famous explanation of the tiny neutrino mass, and it has been studied for a long time. There are three types of the seesaw mechanism, in which different types of particles generate the neutrino mass. For example, in the type-I seesaw mechanism [108–111], the left-handed neutrino mass is suppressed by the inverse of the heavy mass of RH neutrinos. On the other hand, models for generating neutrino mass at the loop level (radiative seesaw model) have been considered [119–125]. In some of these models, DM candidates run in loop diagrams of the light neutrinos, and the DM problem can be solved simultaneously [122–125]. A representative example is the model proposed by Tao and Ma [123, 124], which can explain observed neutrino masses with TeV scale dark matter. In the Tao-Ma model, the $\mathbb{Z}_2$ odd RH neutrinos and the $\mathbb{Z}_2$ scalar doublet η radiatively generate the neutrino mass. Due to the unbroken $\mathbb{Z}_2$ symmetry, the stability of the DM candidates is guaranteed. In Ref. [254], a model of type-I seesaw mechanism has been proposed, where the RH neutrinos get their Majorana masses from the spontaneous breaking of the $\mathrm{U}(1)_{B-L}$ gauge symmetry. This idea is extended in the radiative seesaw model, and $\mathrm{U}(1)_{B-L}$ gauge extension of the Inert doublet model with the $\mathbb{Z}_2$ odd RH neutrino has been proposed [76]. In Ref. [76], the observed DM relic abundance can be realized through the pair annihilation via the s-channel scalar exchange by the mixing between the SM-like Higgs boson and the extra $\mathrm{U}(1)_{B-L}$ scalar singlet. Some phenomenology of this model have been studied by Ref. [77, 78].

In section 4.2, we have explained this model, $\mathrm{U}(1)_{B-L}$ gauge extension of the Inert doublet model with the RH neutrino. In the original work [76], it has been shown that the mass generation of the light neutrino and the DM relic abundance can be explained. However, after the Higgs boson discovery, there are many available experimental results, such as the Higgs boson measurement, Z' search at LHC, Direct Detection of the DM, and so on. Therefore, we revisit this model to make new benchmark scenarios for solving the problems of the neutrino mass and the DM.

In the following sections, we first discuss the LFV processes in the model. As discussed in section 4.2, the neutrino mass can be generated by the RH neutrino at the loop level. The neutrino mass is generated by lepton flavor violating couplings among the SM leptons, the $\mathbb{Z}_2$ odd RH neutrinos and the $\mathbb{Z}_2$ odd scalar doublet η. As a consequence of this LFV couplings, LFV processes, e.g., $\mu \to e\gamma$, occur. We then discuss two scenarios for the DM candidates, the Z_2 odd RH neutrinos and η. The first scenario is a fermionic DM scenario where N_1 is the lightest particle in the $\mathbb{Z}_2$ odd sector, and shows allowed parameter spaces which can explain the

relic abundance of the DM and the neutrino mass under the experimental data. The second one is a scalar DM scenario in the model, whose discussions are similar to several previous studies [242, 255–258]. In the end of this chapter, we give discussions and comments on the results.

5.1 Lepton flavor violation

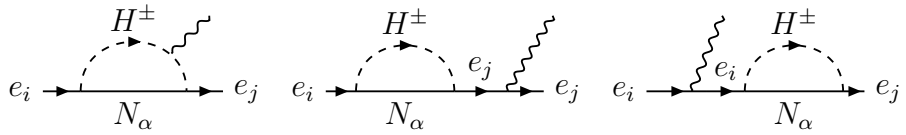

Figure 5.1: $e_i \to e_j\gamma$ decay

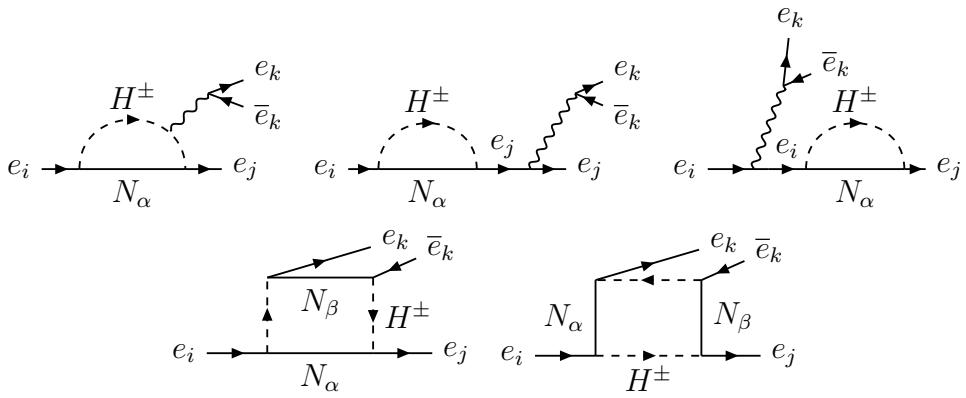

Figure 5.2: $e_i \to e_j e_k \overline{e}_k$ decay

In this section, we consider current constraints and future prospects of the LFV processes. As shown in figures 5.1-5.2, LFV processes $e_i \to e_j\gamma$ and $e_i \to 3e_j$ can be enhanced through N_α–$H^\pm$ loop diagrams in this model.

5.1.1 $e_i \to e_j\gamma$ decay

The branching ratio for $e_i \to e_j\gamma$ is calculated as [259]

$$\mathrm{Br}(e_i \to e_j\gamma) = \frac{48\pi^3\alpha_{\mathrm{em}}|A_D|^2}{G_F^2}\mathrm{Br}(e_i \to e_j\overline{\nu}_j\nu_i), \tag{5.1}$$

with the amplitude from dipole operator

$$A_D = \sum_\alpha \frac{ig^*_{i\alpha}g_{j\alpha}}{32\pi^2 m^2_{H^\pm}}F(\xi_\alpha), \tag{5.2}$$

where ξ_α is defined as $\xi_\alpha \equiv m^2_{N_\alpha}/m^2_{H^\pm}$, α_{em} is the fine structure constant, G_F is the Fermi constant, and the function $F(x)$ is defined as

$$F(x) = \frac{1 - 6x + 3x^2 + 2x^3 - 6x^2\ln x}{6(x-1)^4}. \tag{5.3}$$

5.1.2 $e_i \to 3e_j$ decay

The $e_i \to 3e_j$ processes include photon penguin diagrams and box diagrams. The branching ratio of $e_i \to 3e_j$ processes is given by [259]

$$\mathrm{Br}(e_i \to e_j e_j \bar{e_j}) = \frac{3(4\pi)^2\alpha_{\rm em}}{8G_f^2}\left\{|A_{ND}|^2 + |A_D|^2\Big(\frac{16}{3}\log\frac{m_{e_i}}{m_{e_j}} - \frac{22}{3}\Big) + \frac{1}{6}|B|^2 + \frac{1}{3}(2|F_{RR}|^2 + |F_{RL}|^2)\right\}$$
$$+\Big(-2A_{ND}A_D^* + \frac{1}{3}A_{ND}B^* - \frac{2}{3}A_D B^* + \mathrm{h.c.}\Big) \times \mathrm{Br}(e_i \to e_j \nu_j \overline{\nu_j}). \tag{5.4}$$

The amplitudes A_{ND}, B, F_{RR} and F_{RL} are the photonic non-dipole contribution, the box contribution and the contributions from the Z penguin diagrams, respectively. These amplitudes are given by [259]

$$\begin{aligned}
A_{ND} &= \sum_{\alpha=1}^{3} \frac{g_{i\alpha}^* g_{j\alpha}}{6(4\pi)^2 m_{H^\pm}^2} G_2(\xi_\alpha),\\
B &= \frac{1}{(4\pi)^2 m_{H^\pm}^2 e^2} \sum_{\alpha,\beta=1}^{3} \Big\{\frac{1}{2} D_1(\xi_\alpha,\xi_\beta) g_{j\beta} g_{j\beta}^* g_{j\alpha} g_{i\alpha}^* + \sqrt{\xi_\alpha \xi_\beta} D_2(\xi_\alpha,\xi_\beta) g_{j\beta} g_{j\beta} g_{j\alpha}^* g_{i\alpha}^*\Big\},\\
F_{RR} &= \frac{g_R^l}{g^2 s_W^2 m_Z^2} \sum_{\alpha=1}^{3} \frac{g_{i\alpha}^* g_{j\alpha} m_{e_i} m_{e_j}}{2(4\pi)^2 m_{H^\pm}^2} \frac{g}{c_W} F_2(\xi_\alpha),\\
F_{RL} &= \frac{g_L^l}{g^2 s_W^2 m_Z^2} \sum_{\alpha=1}^{3} \frac{g_{i\alpha}^* g_{j\alpha} m_{e_i} m_{e_j}}{2(4\pi)^2 m_{H^\pm}^2} \frac{g}{c_W} F_2(\xi_\alpha),
\end{aligned} \tag{5.5}$$

where $g_L^l = g(1/2 - s_W^2)/c_W$ and $g_R^l = -g s_W^2/c_W$, and the loop functions are given by

$$\begin{aligned}
G_2(x) &= \frac{2 - 9x + 18x^2 - 11x^3 + 6x^3\log x}{6(1-x)^4},\\
D_1(x,y) &= -\frac{1}{(1-x)(1-y)} - \frac{x^2\log x}{(1-x)^2(x-y)} - \frac{y^2\log y}{(1-y)^2(y-x)},\\
D_2(x,y) &= -\frac{1}{(1-x)(1-y)} - \frac{x\log x}{(1-x)^2(x-y)} - \frac{y\log y}{(1-y)^2(y-x)}.
\end{aligned} \tag{5.6}$$

When the processes are dominated by the photon penguin diagrams, the branching ratio has a simple relation [259–261]:

$$\mathrm{Br}(e_i \to e_j e_j \bar{e_j}) \simeq \frac{\alpha_{\rm em}}{3\pi}\left[2\log\left(\frac{m_{e_i}}{m_{e_j}}\right) - \frac{11}{4}\right]\mathrm{Br}(e_i \to e_j\gamma), \tag{5.7}$$

$$\mathrm{Br}(e_i \to e_j e_k \bar{e_k}) \simeq \frac{\alpha_{\rm em}}{3\pi}\left[2\log\left(\frac{m_{e_i}}{m_{e_j}}\right) - 3\right]\mathrm{Br}(e_i \to e_j\gamma) \quad (j \neq k). \tag{5.8}$$

The box diagrams can be dominant when $\xi \gg 1$ or $\xi \ll 1$ if masses of RH neutrinos are degenerate.

The $\mu \to e$ conversion in muonic atoms is also a signature of LFV. However, $\mu \to e\gamma$ is more stringent than this process [259]. Detailed analysis of LFV can be seen in Ref. [259–262].

Considering the constraints from neutrino oscillations and LFV measurements, we choose the following parameters for later use:

$$\begin{aligned}
&m_{N_2} = m_{N_1} + 2500\ \mathrm{GeV},\ m_{N_3} = m_{N_1} + 3000\ \mathrm{GeV},\ m_H = 1000\ \mathrm{GeV},\\
&m_{H^\pm} = m_A,\ \delta \equiv m_{H^\pm} - m_H = 10^{-5}\ \mathrm{GeV}.
\end{aligned} \tag{5.9}$$

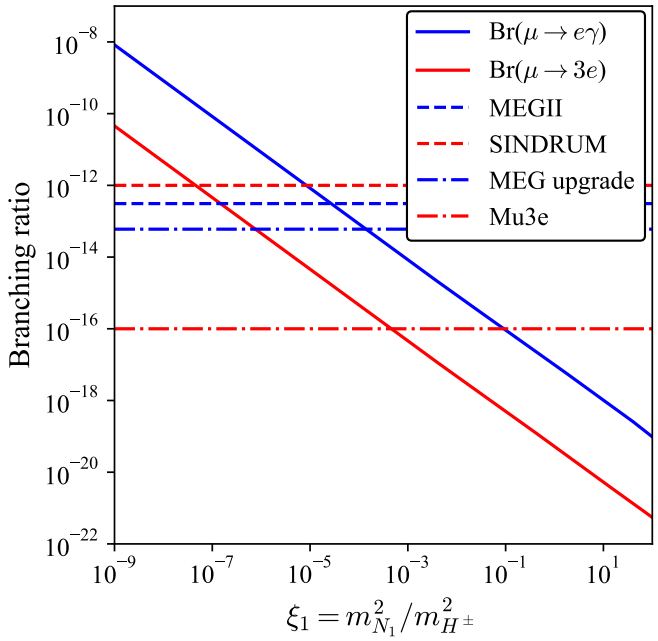

Figure 5.3: Br($\mu \to e\gamma$) (blue) and Br($\mu \to 3e$) (red) as a function of $\xi = m^2_{N_1}/m^2_{H^\pm}$. Horizontal dashed lines show the current upper bounds from MEGII experiment (blue) [204] and SINDRUM experiment (red) [205]. The dot-dashed lines show the future bounds from MEG upgrade (blue) [263] and Mu3e (red) [264].

LFV constraints on the mass of N_1 are shown in figure 5.3. The blue (red) solid line shows Br($\mu \to e\gamma$) (Br($\mu \to 3e$)). The horizontal dashed blue and red lines are current upper bounds from MEGII [263] and SINDRUM [264], respectively. Future expected bounds from MEG upgrade [263] and Mu3e [264] are shown as dot-dashed lines. As m_{N_1} is increasing, branching ratios of LFV processes are decreasing, which provides the lower bound of m_{N_1} around $m_{N_1} \simeq 5.1$ GeV.

5.2 Dark matter

In this section, we consider the freeze-out mechanism for DM candidates. The relic abundance of the DM particle can be calculated by solving the Boltzmann equation [265]:

$$\frac{\mathrm{d}Y}{\mathrm{d}x} = -\sqrt{\frac{g_*\pi}{45}}\frac{m_{\mathrm{DM}}m_{Pl}}{x^2}\langle\sigma v\rangle\,(Y^2 - Y_{EQ}^2), \tag{5.10}$$

where $x \equiv m_{\mathrm{DM}}/T$ is an independent variable, $Y \equiv n_{\mathrm{DM}}/s$ is the comoving density of the DM. The thermal averaged cross section $\langle\sigma v\rangle$ contains cross sections of all annihilation processes before the DM freezes out. Integrating the Boltzmann equation from $x = 0$ to $x_F = m_{\mathrm{DM}}/T_F$, the relic abundance is given by

$$\Omega_{\mathrm{DM}}h^2 \simeq 2.75 \times 10^{-8} m_{\mathrm{DM}} Y(T_F)\mathrm{GeV}^{-1}, \tag{5.11}$$

where T_F is the freeze-out temperature of the DM. In the following analysis, we use `micrOMEGAs6.0` [266] to calculate the relic abundance of the DM.

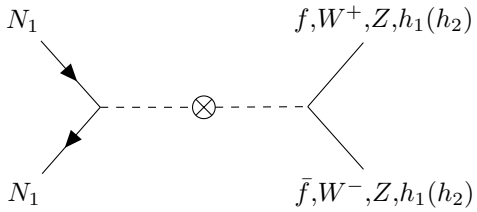

Figure 5.4: Annihilation processes $N_1N_1 \to h_1(h_2) \to f\bar{f}, ZZ, W^+W^-, h_1(h_2)h_1(h_2)$ through the mixing between ϕ and ϕ_S.

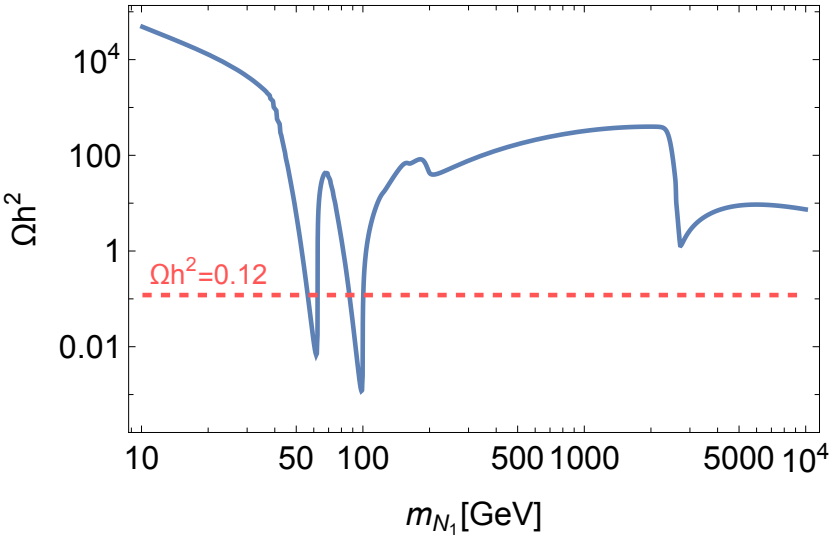

Figure 5.5: Relic abundance of N_1 as a function of m_{N_1}. The red dashed line is the current bound of the DM relic abundance from the Planck experiment [18].

5.2.1 N_1 dark matter

In this scenario, we consider N_1 as the lightest $\mathbb{Z}_2$ odd particle.

First, we consider the relic abundance of the N_1 DM. In the Tao-Ma model [123, 124], there are no sufficient annihilation rates for the N_1 DM due to strong constraints from LFV experiments [267]. However, it is possible for N_1 to satisfy the DM abundance with the mixing between the Higgs field Φ and the extra scalar singlet S, because N_1 can annihilate via $N_1N_1 \to h_1(h_2) \to f\bar{f}, ZZ, W^+W^-, h_1(h_2)h_1(h_2)$ processes [254], as shown in figure 5.4.

In figure 5.5, the relic abundance of N_1 is shown as a function of m_{N_1}. We use the following parameters to calculate the relic abundance:

$$\begin{aligned} &\cos\alpha = 0.97,\ v_S = 30\ \text{TeV},\ m_{h_2} = 200\ \text{GeV},\ m_{Z'} = 5.2\ \text{TeV}, \\ &m_{N_2} = m_{N_1} + 2500\ \text{GeV},\ m_{N_3} = m_{N_1} + 3000\ \text{GeV},\ \lambda = 10^{-6},\ \lambda_3 = 0.1, \\ &m_H = m_{N_1} + 10^3\ \text{GeV},\ m_{H^\pm} = m_A = m_H + 10^{-5}\ \text{GeV}. \end{aligned} \tag{5.12}$$

The relic abundance of N_1 is reduced significantly around $m_{N_1} \simeq m_{h_1}/2$ and $m_{N_1} \simeq m_{h_2}/2$, respectively. Annihilation of the RH neutrinos to the SM particles is enhanced resonantly via s-channel exchange of h_1 and h_2. We also notice that it is possible for the RH neutrinos to annihilate via Z' boson exchange. However, this process is not dominant since the cross section of Z' boson exchange $\langle\sigma v\rangle$ is proportional to $1/v_S^4$, which is much smaller than Higgs boson exchange processes in the low mass region $m_{N_1} \ll m_{Z'}/2$. In the mass region near the Z' pole $m_{N_1} \simeq m_{Z'}/2$, even if annihilation can be enhanced due to Z' resonance, it cannot realize the required relic abundance.

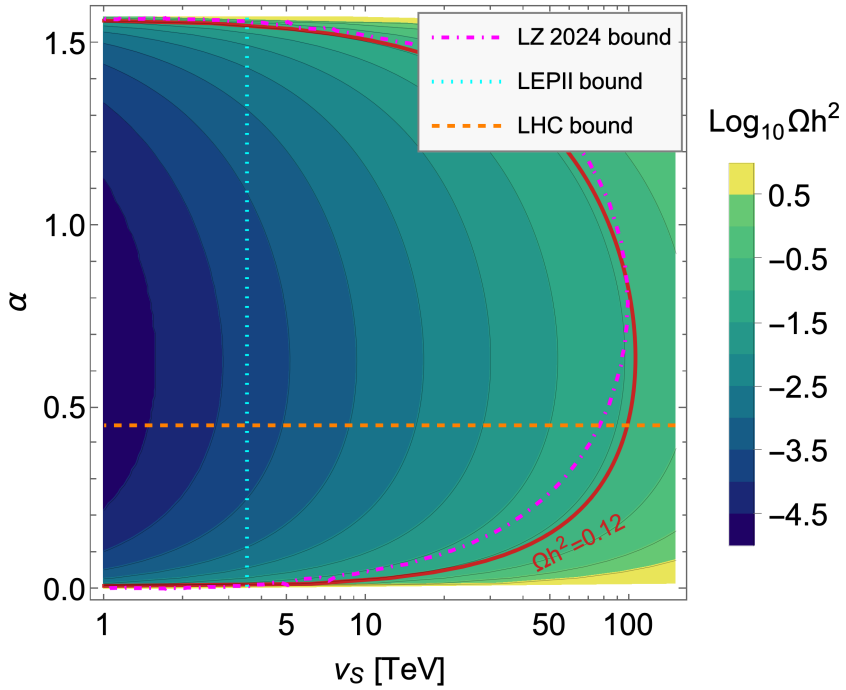

Figure 5.6: Parameter space of $m_{N_1} = 100 + 10^{-4}$ GeV with constraints from LEPII [243, 244], ATLAS [19], CMS [20] and LZ 2024 [132] experiments. The red line is the bound from the Planck experiment [18].

Second, we consider the direct detection of the N_1 dark matter. The lightest RH neutrino N_1 can have elastic scattering with nucleons by Higgs exchange processes. The Spin Independent (SI) cross section for the proton target is

$$\sigma^p_{\rm SI} = \frac{4\mu^2}{\pi} f_p^2, \tag{5.13}$$

where $\mu \equiv \dfrac{m_{N_1} m_p}{m_{N_1} + m_p}$ is the DM-nucleus reduced mass in the center of mass frame. The hadronic matrix element f_p [268] is given by

$$f_p = \sum_{q=u,d,s} c_q \frac{m_p}{m_q} f^p_{Tq} + \frac{2}{27} f^p_{TG} \sum_{q=c,b,t} c_q \frac{m_p}{m_q}, \tag{5.14}$$

where f^p_{Tq} and f^p_{TG} express mass contributions to the nucleon from quarks and gluons, and m_q is the mass of a quark. The effective vertex c_q is defined as

$$c_q = y^\alpha_R \frac{\sqrt{2} m_q}{v} \left[\left(\frac{\sin\alpha}{\sqrt{2}} \right) \frac{1}{m^2_{h_1}} \left(\frac{\cos\alpha}{\sqrt{2}} \right) - \left(\frac{\sin\alpha}{\sqrt{2}} \right) \frac{1}{m^2_{h_2}} \left(\frac{\cos\alpha}{\sqrt{2}} \right) \right]. \tag{5.15}$$

The SI cross section $\sigma^p_{\rm SI}$ has a simple relation with the BSM parameters in this model:

$$\sigma^p_{\rm SI} \propto \left(\frac{m_{N_1} \sin(2\alpha)}{v_S} \right)^2 \times \left(\frac{1}{m^2_{h_1}} - \frac{1}{m^2_{h_2}} \right)^2. \tag{5.16}$$

In figure 5.6, the relic abundance of N_1 DM is shown as colored contour in the v_S-α plane. We choose the following parameter set:

$$m_{h_2} = 200 \text{ GeV}, \; m_{N_1} = \frac{m_{h_2}}{2} + 10^{-4} \text{ GeV}, \; m_{N_2} = 2500 \text{ GeV}, \; m_{N_3} = 3000 \text{ GeV},$$

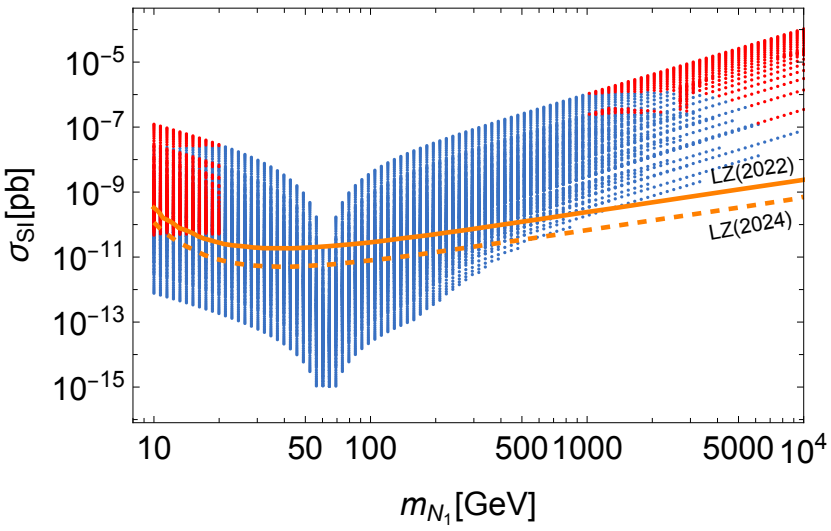

Figure 5.7: The possible SI cross section of N_1 as a function of m_{N_1} in our parameter space. The red points are excluded by theoretical constraints. The orange line is the upper bound from the LZ 2022 results [131]. The dashed orange line is the upper bound from the LZ 2024 results [132].

$$\lambda = 10^{-6},\ \lambda_3 = 0.1,\ m_H = 1000\ \text{GeV},\ m_{H^\pm} = m_A,\ \delta \equiv m_{H^\pm} - m_H = 10^{-5}\ \text{GeV}. \tag{5.17}$$

The allowed parameter space is the region encircled by the LZ 2024 [132] (magenta dot-dashed), LHC [19, 20] (orange dashed) and Planck experiment [18] (red solid), which is on the right side of the LEPII constraint [243, 244] (cyan dotted). The contour lines of the relic abundance are not symmetric with respect to α because the cross sections of s-channels for the annihilation processes $N_1 N_1 \to h_1(h_2) h_1(h_2)$ are not symmetric with respect to α. As we can see from this figure, the relic abundance decreases with large mixing angle α and small v_S. This is because the dominant annihilation cross sections are approximately proportional to a factor which also appears in Eq. (5.16), and we have

$$\langle \sigma v \rangle_{\text{dom}} \propto \left(\frac{m_{N_1} \sin(2\alpha)}{v_S} \right)^2. \tag{5.18}$$

Therefore, the benchmark point given in Ref. [76], where the large mixing angle $\alpha = \pi/4$ and the small U(1)$_{B-L}$ VEV, $v_S = 3.7$ TeV were taken, has already been excluded by the Higgs boson measurement and the LZ 2024. Nevertheless, we still have room in the small mixing angle α and the large v_S. We also investigate the parameter space of the SM-like Higgs resonance near the region $m_{N_1} \simeq m_{h_1}/2$. We find that there are still parameter spaces for the N_1 DM with the SM-like Higgs resonance if m_{h_2} is near m_{h_1}.

Third, we explore the allowed mass region of N_1 with h_2 resonance scenario. We choose the following parameter space

$$\cos\alpha \in [0.9, 1],\ v_S \in [3.5, 80]\ \text{TeV},\ m_{h_2} \in [10, 10^4]\ \text{GeV} \tag{5.19}$$

with

$$\begin{aligned} &m_{N_2} = m_{N_1} + 2500\ \text{GeV},\ m_{N_3} = m_{N_1} + 3000\ \text{GeV},\ m_{h_2} = 2m_{N_1} + 0.2\ \text{GeV}, \\ &\lambda = 10^{-6},\ \lambda_3 = 0.1,\ m_H = m_{N_1} + 10^3\ \text{GeV},\ m_{H^\pm} = m_A = m_H + 10^{-5}\ \text{GeV}. \end{aligned} \tag{5.20}$$

We scan $\cos\alpha$, v_S and m_{h_2} with $20 \times 20 \times 100$ points, respectively. The allowed parameter space of N_1 is shown in figure 5.7, in which all points satisfy the constraint $\Omega_{\text{DM}} h^2 < 0.12$.

The blue points satisfy all the theoretical and experimental constraints, while the red points are excluded by the theoretical constraints. In the mass region near $m_{N_1} \simeq m_{h_1}/2$, the SI cross section greatly reduces due to the destructive interference of the two Higgs states. In the mass region $m_{N_1} \gtrsim 80$ GeV, the SI cross section increases as m_{N_1} is increasing. In the mass region $m_{N_1} > 500$ GeV, the SI cross section exceeds the LZ bound, therefore the current direct detection experiments give the upper bound on the mass of N_1.

5.2.2 Scalar dark matter

In this scenario, we consider H to be the lightest $\mathbb{Z}_2$ odd particle. The H DM scenario has been studied extensively in the Inert doublet model [242, 255, 256, 269, 270], and discussions here are similar to the Inert doublet model with an additional scalar singlet [257, 258].

In the Inert doublet model, when the mass of H is below the W boson mass, a pair of H mainly annihilates into the SM fermions. The relic abundance greatly decreases at $m_H \simeq m_h/2$ and $m_H \simeq m_Z/2$, because $HH \to b\bar{b}$ and $HH \to q\bar{q}$ mediated by the SM Higgs and Z boson, respectively, are enhanced. In $m_H \gtrsim m_W$, the annihilation channels $HH \to W^+W^-$ and $HH \to ZZ$ start to be opened, and predicted relic abundance is not sufficient to explain the observed value. In the high mass region, $m_H \gtrsim 500$ GeV, the (co)annihilation channels into the SM gauge bosons, which are controlled by $\lambda_L = \lambda_3 + \lambda_4 + \lambda_5$, can be dominant. As a result, depending on the combination of λ_3, λ_4 and λ_5, preferred relic density can be obtained again.

In our model, there are two differences with the inert doublet model. First, the relic density can be satisfied by the additional Higgs resonance near the mass region $m_H \simeq m_{h_2}/2$. H can annihilate via $HH \to h_1(h_2) \to f\bar{f}, W^+W^-, ZZ, h_1(h_2)h_1(h_2)$ processes. Second, the SI cross section in direct detections can be changed due to the h_2 exchange processes. The SI cross section of H is given by

$$\sigma^H_{\rm SI} = \frac{\mu_H^2}{4\pi m_H^2} f_p^2, \ \mu_H \equiv \frac{m_H m_p}{m_H + m_p}, \tag{5.21}$$

where f_p has the same definition as Eq. (5.14), and c_q is defined as [1]

$$c_q = \frac{m_q}{2v}\left[\frac{\lambda v_S \sin\alpha\cos\alpha - \lambda_L v\cos^2\alpha}{m_{h_1}^2} - \frac{\lambda_L v\sin^2\alpha + \lambda v_S \sin\alpha\cos\alpha}{m_{h_2}^2}\right]. \tag{5.22}$$

We here choose the following parameter space

$$m_H \in [50, 90] \text{ GeV}, \ \cos\alpha \in [0.9, 1], \ \mu_2^2 \in [2000, 4000] \text{ GeV}^2, \ m_{H^\pm} = m_A = m_H + 50 \text{ GeV}, \tag{5.23}$$

and fix the following parameters for the H DM scenario:

$$\begin{aligned} &v_S = 5000 \text{ GeV}, \ m_{h_2} = 120 \text{ GeV}, \ \lambda = 10^{-4}, \\ &m_{N_1} = 3000 \text{ GeV}, \ m_{N_2} = 3500 \text{ GeV}, \ m_{N_3} = 4000 \text{ GeV}. \end{aligned} \tag{5.24}$$

The allowed parameter space of H is shown in figure 5.8. The red and blue points satisfy $\Omega_{\rm DM}h^2 = 0.12$ and $\Omega_{\rm DM}h^2 < 0.12$, respectively. The allowed parameter space is near 60 GeV due to the destructive interference of the two Higgs states, indicating that there is still allowed parameter space for the H DM scenario in this model.

5.3 Discussions

In this section, we give some comments on the results shown in section 5.1 and 5.2. In section 5.1, we have shown that experiment results give the lower bound of m_{N_1}. At present, the

[1] The SI cross section can be modified depending on the size of λ_2 via loop corrections [271].

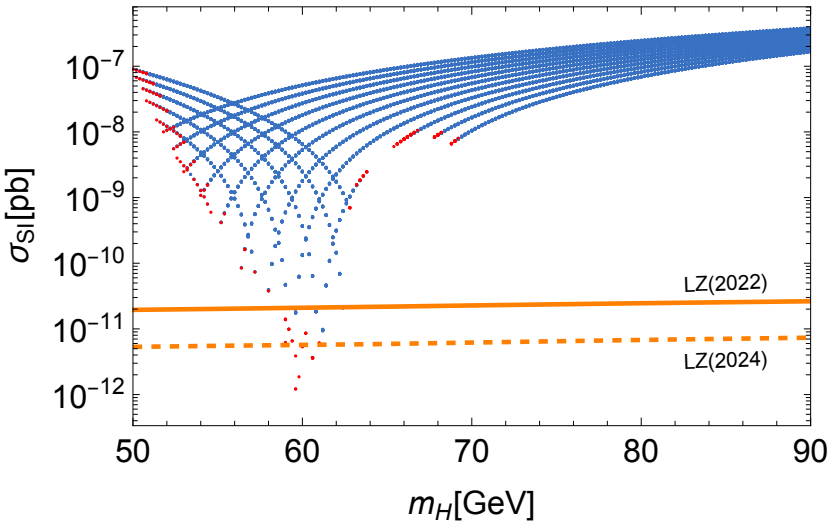

Figure 5.8: The possible SI cross section of H as a function of m_H in our parameter space. The red points satisfy $\Omega_{\rm DM}h^2 \simeq 0.12$, and the blue points satisfy $\Omega_{\rm DM}h^2 < 0.12$. The solid and dashed orange line is the upper bound from the LZ 2022 results [131] and LZ 2024 results [132], respectively.

most stringent constraint comes from the $\mu \to e\gamma$ process, which gives the lower bound on $m_{N_1} > 5.2$ GeV in our N_1 DM scenario. In the future, the MEG experiment [263] may improve its sensitivity down to $\mathrm{Br}(\mu \to e\gamma) \simeq 6 \times 10^{-14}$, and the Mu3e experiment [264] may upgrade the sensitivity to $\mathrm{Br}(\mu \to 3e) \simeq 1 \times 10^{-16}$. Future LFV experiments would give the lower bound $m_{N_1} > 21$ GeV in our N_1 DM scenario, which is 4 times better than the current bound.

In section 5.2, we have shown benchmark points and parameter space of the DM candidates in this model. We here very briefly mention the prospect for collider searches in each scenario. In the N_1 DM scenario, N_1 could be tested through $H^\pm \to l^\pm N_1$ signals at LHC and HL-LHC if it is kinematically allowed, mainly via $pp \to H^+H^- \to N_1N_1l^+l^-$ [178, 255, 269, 272–274]. In the H DM scenario, inert scalar particles can be produced through monojet processes (e.g., $q\bar{q} \to Zg \to HAj$ and $q\bar{q} \to h_1 g \to HHg$) in hadron colliders. Detailed analysis of the inert scalars in LHC can be found in Ref. [178, 255, 273]. Inert scalars can also be produced in lepton colliders through $e^+e^- \to Z \to AH(H^+H^-)$ processes [269, 274].

The existence of the Z' boson is another difference from the Tao-Ma model. Though searches in LHC give strong constraints on the mass of Z' boson, it can be lighter with smaller gauge couplings. Since hadron colliders (e.g., LHC and HL-LHC) have large backgrounds, it can only reach the gauge coupling g_{B-L} of $O(10^{-2})$ [275]. However, lepton colliders (e.g., ILC) can reach smaller gauge coupling of $O(10^{-3})$ [275]. Decays of the Z' boson into SM particles are proportional to $(B-L)^2$. Due to its large mass, the branching ratios of $Z' \to q\bar{q}, l^+l^-, \nu_L\bar{\nu}_L, N_1N_1, h_1h_1, h_1h_2$ and h_2h_2 for the parameter set Eq. (5.12) are given approximately by 0.20, 0.29, 0.15, 0.15, 6.9×10^{-4}, 4.4×10^{-2}, 0.17, respectively [76, 244].

Direct detection experiments become more and more stringent for DM candidates. The LZ 2024 results give the upper bound of N_1 DM around 500 GeV. The inert scalar DM is still viable due to the destructive interference of the two Higgs states in the low mass region. Future DM detection experiments may give stronger bounds on the DM mass in this model.

In this model, there are CP phases in R matrix for the RH neutrinos. Therefore, a baryogenesis scenario in this model, e.g. leptogenesis [136] or electroweak baryogenesis [27], could be considered [276].

5.4 Short summary of chapter 5

The radiative seesaw model with gauged $U(1)_{B-L} \times \mathbb{Z}_2$ extension is a well-motivated scenario which gives consistent predictions of active neutrino masses and the abundance of the DM. Majorana masses of the RH neutrinos, the lightest of which can be identified as the DM, are given by the spontaneous breaking of the $U(1)_{B-L}$ gauge symmetry. We have revisited this model with the latest constraints from the DM searches, neutrino oscillations, flavor experiments and collider experiments. We have explored the feasible parameter space of this model, and have found that there is still allowed region for this model under the latest experimental constraints. We have presented new viable benchmark scenarios for this model, i.e., the RH neutrino DM scenario and the scalar DM scenario. We also have mentioned the testability of these benchmark scenarios in future experiments.

Chapter 6

Review of electroweak baryogenesis

6.1 Mechanism of electroweak baryogenesis

6.1.1 Wash out of $B + L$

As we have mentioned in section 2.4, by the sphaleron process, the sum of baryon and lepton numbers $B + L$ is not conserved in the early Universe. After the EWPT, the sphaleron process is exponentially suppressed, while it is in thermal equilibrium before the symmetry breaking. Therefore, created $B + L$ much before the electroweak era is washed out.

If the sphaleron $\left(|0\rangle \leftrightarrow \prod_i u_L d_L d_L \nu_{iL}\right)$ is in thermal equilibrium before the electroweak symmetry breaking, the baryon and lepton number can be written as

$$B = \frac{8N_f + 4m}{22N_f + 13m}(B - L), \quad L = -\frac{14N_f + 9m}{22N_f + 13m}(B - L), \tag{6.1}$$

where N_f and m are the generation of quarks and the number of the Higgs doublet ($N_f = 3$ and $m = 1$ in the SM), respectively. Therefore, in order to get non-zero baryon asymmetry, non-zero $B - L$ must be created before freezing out of the sphaleron process, i.e. electroweak symmetry breaking. Alternatively, we can consider non-equilibrium situation of the sphaleron process, which can be satisfied during first order EWPT. The former scenario corresponds to the cases of the GUT baryogenesis [133, 134], leptogenesis [136] and so on, while EWBG uses the latter mechanism.

6.1.2 First order phase transition

In thermal situations, such as in the early Universe, the effective potential which describes properties of the vacuum is corrected by finite temperature effects [277]. As a simple example, we consider $\lambda\phi^4$ theory with a negative mass term $\mu^2 < 0$

$$\mathcal{L} = \frac{1}{2}\partial_\mu\phi\partial^\mu\phi - \frac{1}{2}\mu^2\phi^2 - \frac{1}{4!}\lambda\phi^4. \tag{6.2}$$

With the high temperature expansion and the resummation of the leading diagrams [277], we obtain

$$V(\varphi; T) = \frac{1}{2}\left(\mu^2 + \frac{1}{24}\lambda T^2\right)\varphi^2 - \frac{1}{12\pi}\left(\mu^2 + \frac{1}{24}\lambda T^2 + \frac{1}{2}\lambda\varphi^2\right)^{\frac{3}{2}} T + \frac{1}{4!}\lambda\varphi^4 + O(\tilde{m}^4), \tag{6.3}$$

where $\varphi = \langle\phi\rangle$ and $\tilde{m}^2 = \mu^2 + \lambda T^2/24$. In the high temperature, the quadratic term can be positive, and the symmetry of the vacuum recovers. When we define $T = T_1$ satisfying

$$\mu^2 + \frac{1}{24}\lambda T^2 = 0, \tag{6.4}$$

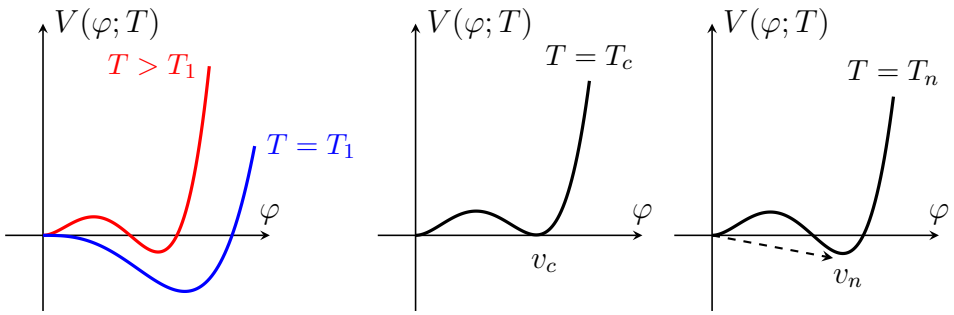

Figure 6.1: Shape of the effective potential in finite temperature.

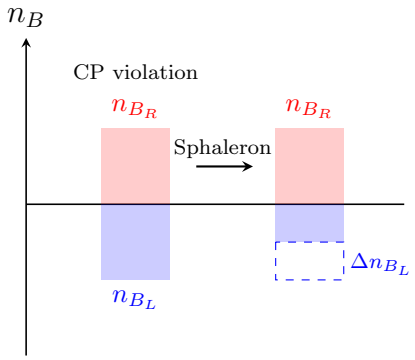

Figure 6.2: Baryon number density in front of the bubble wall.

the effective potential at this temperature is $V \sim -\lambda^{3/2}\varphi^3 + \lambda\varphi^4$, which has the vacuum at $\varphi \neq 0$ (blue line in the left of figure 6.1). At the temperature little higher than T_1, depending on λ, two local vacua can exist simultaneously (red line). In this case, the phase transition is caused by the quantum tunneling effect, and expanding bubble walls are created [278–280]. The temperature, where the two vacua are degenerated, is defined by the critical temperature T_c. The temperature, where the nucleation probability is large enough to decay (the decay rate is comparable to the Hubble rate), is called the nucleation temperature T_n. The VEVs at these temperature are denoted as

$$\begin{aligned} \varphi(T = T_c) &= v_c, \\ \varphi(T = T_n) &= v_n, \end{aligned} \tag{6.5}$$

respectively. For EWBG, EWPT must be first order to realize non-equilibrium situation for the sphaleron process.

6.1.3 Non-equilibrium situation around expanding bubble

In the mechanism of EWBG, the baryon asymmetry is created around the expanding bubble walls during the SFOPT. We here assume the scattering processes of the SM fermions are much faster than the sphaleron process in the symmetric phase, i.e. the mean paths of them satisfy $l_{\text{scat}} \ll l_{\text{sph}}^{\text{sym}}$.

Due to the CP violating interactions between the bubble and the SM fermions, the asymmetry between left-handed (right-handed) quarks and anti-quarks $n_{B_L} = n_{q_L} - n_{\overline{q_L}}$ ($n_{B_R} = n_{q_R} - n_{\overline{q_R}}$) can be non-zero, but from the baryon number conservation in this process, they satisfy $n_B = n_{B_L} + n_{B_R} = 0$ (figure 6.2). The number density of the left-handed baryon is changed by the sphaleron process $n_{B_L} \to n_{B_L} + \Delta n_{B_L}$, and just in front of the bubble wall, we get the non-zero baryon asymmetry $n_R + n_L + \Delta n_L = \Delta n_L$.

EDM	Current limit (90% C.L.)	EDM	Future prospect
d_e (ACME-II)	1.1×10^{-29} e cm [282]	d_e (ACME-III)	3×10^{-31} e cm [287]
d_e (JILA)	4.1×10^{-30} e cm [283]	d_e (EDM^3)	$O(10^{-33})$ e cm [288, 289]
d_n (nEDM)	1.8×10^{-26} e cm [284]	d_n (nEDM)	2×10^{-28} e cm [290]
d_p (UWash)	2.1×10^{-25} e cm [285, 286]	d_p (srEDM)	$O(10^{-29})$ e cm [291]

Table 6.1: Current status of the EDMs.

If the velocity of the expansion v_w is comparable to the sphaleron rate, i.e. $v_w \Delta t \sim l_{\rm sph}^{\rm sym}$, the sphaleron process might be no longer in thermal equilibrium. This is because, inside the bubble wall, the sphaleron rate is exponentially suppressed by the VEV of the Higgs doublet, as we have mentioned in section 2.4. In order to decouple the sphaleron process from the thermal equilibrium,

$$\Gamma_{\rm sph}^{\rm brk}(T) < H(T), \tag{6.6}$$

should be satisfied, where $\Gamma_{\rm sph}^{\rm brk}$ and H are the sphaleron rate in the broken phase and the Hubble rate, respectively. The sphaleron rate inside the bubble is expressed by the sphaleron energy as $\Gamma_{\rm sph}^{\rm brk} \propto e^{-E_{\rm sph}/T}$, which is a function of the VEV and the temperature, and we obtain the sphaleron decoupling condition [281]

$$\frac{v_c}{T_c} \simeq \frac{v_n}{T_n} \gtrsim 1. \tag{6.7}$$

The phase transition which satisfies this condition is called Strongly First Order electroweak Phase Transition (SFOPT). If the above processes are all successful, the created baryon asymmetry is frozen out until now.

6.2 CP violation and electric dipole moment

The EDM is one of the powerful tools to test the CP violation in the model. With the non-relativistic limit, the interaction Hamiltonian of the spin of a fermion ψ and the electric field is given by

$$H_{\rm EDM} = -d_{\rm EDM} \frac{\boldsymbol{S}}{|\boldsymbol{S}|} \cdot \boldsymbol{E}, \tag{6.8}$$

where $\boldsymbol{S}$ and $\boldsymbol{E}$ are the spin and the electric field vectors, respectively. The time reversal transformations are $\mathcal{T}(\boldsymbol{E}) = \boldsymbol{E}$ and $\mathcal{T}(\boldsymbol{S}) = -\boldsymbol{S}$, so that this interaction Hamiltonian violates time reversal symmetry.

The relativistic interaction is given by the dimension five effective operator

$$\mathcal{L}_{\rm EDM} = -\frac{d_\psi}{2} \overline{\psi} \sigma^{\mu\nu} i\gamma_5 \psi F_{\mu\nu}, \tag{6.9}$$

where $\sigma^{\mu\nu} = \frac{i}{2}[\gamma^\mu, \gamma^\nu]$. This operator is also $\mathcal{T}$ odd, so that, from the CPT theorem, this is the $\mathcal{CP}$ odd operator.

The effects of CP violation in the model can appear in the EDM operator, so that by the measurement of the EDM in the experiments, we can test the CP violation. Until now, there are null results of the finite value of the EDM, and we only have upper limits on the EDM. There are various systems for measuring the EDM, e.g., neutron [284], atoms [285] and molecules [282, 283]. From those EDM bounds, we can obtain upper bounds for more

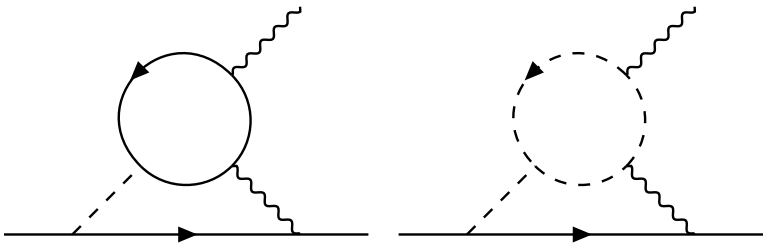

Figure 6.3: The Barr–Zee type diagrams including the fermion loop (left) and the scalar loop (right).

fundamental particles, such as the electron, proton, and so on. In the table 6.1, several upper bounds on the EDMs and the future prospects are summarized.

In the SM, we have one CP violating phase, i.e. CKM phase [1]. However, the predicted EDM in the SM is much smaller than the current bound: e.g. the electron EDM predicted by the SM is $O(10^{-38})e$ cm [294]. Due to the smallness of the SM prediction, the EDM can be a good probe of the CP violation from new physics.

6.2.1 Electric dipole moments in the two Higgs doublet model

In the extended Higgs models for the EWBG, the EDM is induced by the new source of the CP violation. In this subsection, we discuss the EDMs in the general 2HDM, which is introduced in section 4.1.

We here take the Pich–Tuzon parametrization, which is shown in Eq. (4.37), for the Yukawa interactions between the SM fermions and the additional scalar bosons. When we consider the alignment limit $\alpha_i = 0$ for the neutral scalar bosons, there are three CP phases in the Yukawa sector, $\theta_u = \arg[\zeta_u]$, $\theta_d = \arg[\zeta_d]$ and $\theta_e = \arg[\zeta_e]$ and one CP phase $\arg[Z_7]$ in the potential.

In this setup, two loop Barr–Zee type diagrams [295] in figure 6.3 are leading contributions to the eEDM in the model. The left diagram in figure 6.3 has a fermion loop, and the right one has a scalar loop. Since there are multiple CP-violating phases in the model, each diagram depends on different CP-violating phases. We can further categorize the Barr–Zee type diagrams depending on the scalar boson which couples to the external fermion line being either neutral or charged.

In the fermion loop contributions, we only consider the top quark loop diagrams because of the hierarchy in the Yukawa coupling constants. Therefore, when $|\zeta_u|, |\zeta_d|$ and $|\zeta_e|$ are in the same order, the contributions from the fermion loop diagrams are approximately proportional to $|\zeta_u||\zeta_e| \sin(\theta_u - \theta_e)$. On the other hand, the contributions from the heavy scalar loop diagrams are approximately proportional to $|\lambda_7||\zeta_e| \sin(\theta_7 - \theta_e)$.

We next discuss the neutron EDM. By using the QCD sum rule, d_n is given by [296–300]

$$d_n = 0.73 d_d - 0.18 d_u + e(0.20\tilde{d}_d + 0.10\tilde{d}_u) \pm 23 \times 10^{-3} \text{ GeV } ew, \tag{6.11}$$

where $\tilde{d}_{u,d}$ are the chromo EDMs, and w is the Weinberg operator [301, 302]. The sign of w has not been determined yet, because of the theoretical uncertainties [303, 304]. In the parameter

[1] In the strong sector, we have CP odd term

$$\mathcal{L}_{\text{CPV}} = \theta \frac{g_S^2}{32\pi^2} \tilde{G}^a_{\mu\nu} G^{a\mu\nu}, \tag{6.10}$$

which is known as the theta term. This operator induces the neutron EDM, and from the current bound [284], $|\theta|$ must be smaller than $O(10^{-10})$. The problem of the smallness of θ is known as the strong CP problem. In this Ph.D thesis, we do not further enter this problem and assume some mechanisms working to suppress this term, e.g. the Peccei-Quinn mechanism [292, 293].

regions which we discuss later, the contributions from the four fermi interaction [305] are negligibly small [304]. According to the formulae shown in Refs. [83, 299, 303, 304, 306, 307], when $m_{H_2} = m_{H_3}$, the nEDM is approximately proportional to $|\zeta_u||\zeta_d|\sin(\theta_u - \theta_d)$.

6.3 Transport equations for electroweak baryogenesis

In this section, according to Refs. [79, 308, 309], we derive transport equations around the bubble wall. We discuss so-called semi-classical force method [79,308–312], based on the WKB approximation. Although the wall velocity v_w is an important parameter for the calculation of the baryon density, we treat it as a free parameter, following to the former discussions [36, 37, 79, 308, 309] [2].

We start from the relativistic Boltzmann equation for a particle i

$$(\partial_t + \boldsymbol{v}_g \cdot \partial_{\boldsymbol{x}} + \boldsymbol{F} \cdot \partial_{\boldsymbol{p}}) f_i = C[f_i, f_j, \dots], \tag{6.12}$$

where f is the distribution function, $\boldsymbol{v}_g$ and F are the group velocity and the force acting on the particle i. The left-hand side of the equation is called Liouvill term $\boldsymbol{L}[f_i]$, which denotes the time evolution of f. On the other hand, the right-hand side is called the collision term, which expresses particle number changing via scattering or decay processes.

In order to derive $\boldsymbol{v}_g$ and $\boldsymbol{F}$, we see the dispersion relation of the particle in the background bubble wall. One-dimensional Dirac equation for z axis is given by

$$(i\not{\partial} - \mathcal{M}P_R - \mathcal{M}^* P_L)\psi = 0, \quad \mathcal{M}(z) = m(z)e^{i\theta(z)}, \tag{6.13}$$

where ψ is the wave function of the particle, $P_{R,L}$ are the chiral projection operator, and $m(z)$ and $\theta(z)$ are the space dependent mass and phase, respectively. Here we consider a single-flavor case, but we will discuss a multi-flavor case in section 7.3. In this Dirac equation, only the effects of the bubble wall appearing in the mass term as a background are taken into account, and all other interactions are neglected. We can boost to the wall frame with $(p_x, p_y) = (0, 0)$. In this frame, the wave function for the particle with the positive energy ω can be written by

$$\Psi_s \equiv e^{-i\omega t} \begin{pmatrix} R_s \\ L_s \end{pmatrix} \otimes \chi_s, \quad (\tau_3 \chi_s \equiv s\chi_s), \tag{6.14}$$

where R_s, L_s are two component spinors, and χ_s is the eigenstate of the spin in z axis. By substituting this into the Dirac equation, we have

$$(\omega - is\partial_z)L_s = \mathcal{M}R_s, \quad (\omega + is\partial_z)R_s = \mathcal{M}^* L_s. \tag{6.15}$$

For L_s[3], we obtain

$$\left(\mathcal{M}(\omega + is\partial_z)\frac{1}{\mathcal{M}}(\omega - is\partial_z) - |\mathcal{M}|^2\right) L_s = 0. \tag{6.16}$$

To solve this equation perturbatively, we use the WKB ansatz [308]

$$L_s = we^{i\int^z p_{cz}(z')dz'}, \tag{6.17}$$

[2] In order to calculate the wall velocity v_w, one has to solve equations of motion of the bubble in the fluid [313,314]. The wall velocity v_w has been calculated in several models [44,56,315–317]. In the THDMs like our model, the order of magnitude of v_w agrees with the SM one, and it is evaluated as $\mathcal{O}(10^{-1})$ [44,316].

[3] Discussions for R_s are completely same as for L_s.

where p_c is the canonical momentum. In this ansatz, the derivative expansion corresponds to the $\hbar$ expansion. Up to $O(\hbar)$, we obtain

$$p_{cz} = p_0 \pm \frac{s\omega + p_0}{2p_0}\theta' + \alpha' + O(\hbar^2), \tag{6.18}$$

where $p_0 \equiv \sqrt{\omega^2 - m^2}$, and α is came from the redundancy of the phase in Eq. (6.17). The upper sign is the result for particle, and the lower one is for anti-particle. By replacing $\omega^2 \to \omega^2 + p_x^2 + p_y^2$, we again move back to the non-zero (p_x, p_y) frame. We obtain the dispersion relation

$$\omega^2 = (p_{cz} - \alpha_{\rm CP})^2 + p_x^2 + p_y^2 + m^2 \mp s\theta'\sqrt{(p_{cz} - \alpha_{\rm CP})^2 + m^2}, \tag{6.19}$$

where we have defined $\alpha_{\rm CP} \equiv \alpha' \pm \theta'/2$. Equivalently, we obtain the energy formula

$$\omega = \omega_0 \mp s\frac{\theta'}{2}\frac{\omega_{0z}}{\omega_0}, \tag{6.20}$$

where

$$\omega_0 \equiv \sqrt{(p_{cz} - \alpha_{\rm CP})^2 + p_x^2 + p_y^2 + m^2}, \quad \omega_{0z} \equiv \sqrt{(p_{cz} - \alpha_{\rm CP})^2 + m^2}, \tag{6.21}$$

The WKB wave packet follows the equation of motion

$$v_g = \dot{z} = \left(\frac{\partial\omega}{\partial p_{cz}}\right)_z, \quad \dot{p}_{cz} = -\left(\frac{\partial\omega}{\partial z}\right)_{p_{cz}}. \tag{6.22}$$

The group velocity is the physical quantity, while the canonical momentum itself is not, because it depends on the arbitrary phase $\alpha_{\rm CP}$. Therefore, we define physical momentum as

$$p_z \equiv \omega v_g = (p_{cz} - \alpha_{\rm CP})\left(1 \mp s\frac{\theta'}{2\omega_{0z}}\right). \tag{6.23}$$

By using this momentum, the energy and group velocity can be rewritten as

$$\begin{aligned} \omega &= E \mp s\frac{m^2\theta'}{2EE_z} = E \pm s\Delta E, \\ v_g &= \frac{p_z}{E}\left(1 \pm s\frac{m^2\theta'}{2E^2E_z}\right) = \frac{p_z}{E}\left(1 \mp s\frac{\Delta E}{E}\right), \end{aligned} \tag{6.24}$$

where

$$E \equiv \sqrt{p_x^2 + p_y^2 + p_z^2 + m^2}, \quad E_z \equiv \sqrt{p_z^2 + m^2}, \quad \Delta E \equiv -\frac{m^2\theta'}{2EE_z}. \tag{6.25}$$

Finally, the physical force acting on the WKB packet is obtained by $F = \dot{p}_z$, resulting

$$F = -\frac{(m^2)'}{2E} \pm s\frac{(m^2\theta')'}{2EE_z} \mp s\frac{m^2\theta'(m^2)'}{4E^3E_z} = -\frac{(m^2)'}{2E} \pm s\left(\frac{(m^2\theta')'}{2EE_z} + \frac{\Delta E(m^2)'}{2E^2}\right). \tag{6.26}$$

Here we have used the energy conservation law $d\omega/dt = 0$.

From the above discussion, we get the group velocity and the semi-classical force, $\boldsymbol{v}_g = (0, 0, v_g)$, $\boldsymbol{F} = (0, 0, F)$. The Liouvill term is

$$\boldsymbol{L}[f] = (v_g\partial_z + F\partial_{p_z})f, \tag{6.27}$$

where we have omitted the subscript i. The distribution function of the particle in the equilibrium with the energy ω in the wall frame is given by

$$f_{eq} = \frac{1}{e^{\beta[\gamma(E \pm s\Delta E + v_w p_z)]} \pm 1}, \tag{6.28}$$

where $\gamma \equiv \sqrt{1 - v_w^2}$. We assume solutions of the Boltzmann equation are expressed by the deviation from f_{eq}, and the ansatz is given by

$$f = \frac{1}{e^{\beta[\gamma(E \pm s\Delta E + v_w p_z) - \mu(z)]} \pm 1} + \delta f(z, p), \tag{6.29}$$

where $\mu(z)$ is the space-dependent chemical potential, and $\delta f(z, p_z)$ denotes deviation from the kinetic equilibrium, which satisfies

$$\int d^3p \ \delta f = 0, \tag{6.30}$$

from the conservation law of the particle number. Up to the second derivative order, the distribution function can be expanded as

$$f = f_{0w} \pm \gamma s f'_{0w} \Delta E - f'_{0w} \mu \mp \gamma s f''_{0w} \Delta E \mu + \frac{1}{2} f''_{0w} (\gamma \Delta E)^2 + \delta f, \tag{6.31}$$

where $f_{0w} = 1/(e^{\beta\gamma(E + v_w p_z)} \pm 1)$ and $f'_{0w} = df_{0w}/d(\gamma E)$. The chemical potential and the kinetic perturbation δf are decomposed by the CP-even and CP-odd parts,

$$\begin{aligned} \mu &= \mu_e \pm \mu_o, \\ \delta f &= \delta f_e \pm \delta f_o, \end{aligned} \tag{6.32}$$

where the upper (lower) sign is for (anti-) particles. We note that the CP-even part is caused by contributions at the first order derivative expansion, while the CP-odd part is the second order. In the calculation of the baryon asymmetry, we need the CP-odd solutions, so that we will evaluate CP violating sources at the second order derivative expansion as the leading order contributions.

By substituting Eqs. (6.31)-(6.32) into the Liouvill term, we get

$$\begin{aligned} \frac{\boldsymbol{L}[f - \overline{f}]}{2} = &- \frac{p_z}{E} f'_{0w} \mu'_o + \gamma v_w \frac{(m^2)'}{2E} f''_{0w} \mu_o + \frac{p_z}{E} \partial_z \delta f_o - \frac{(m^2)'}{2E} \partial_{p_z} \delta f_o \\ &+ s\gamma v_w \frac{(m^2\theta')'}{2EE_z} f'_{0w} + s\gamma v_w \frac{m^2\theta'(m^2)'}{4E^2 E_z} \left(\gamma f''_{0w} - \frac{f'_{0w}}{E} \right). \end{aligned} \tag{6.33}$$

We have neglected higher order contributions which came from the CP-even part. The terms in the second line are leading order sources for asymmetry. When the particles are relativistic, the spin can be decomposed by the helicity as $s = h \ \mathrm{sign}(p_z)$. In the following discussions, only the CP-odd part of μ and δf appear, so that we will omit the subscript o.

To solve this equation with respect to μ and δf, we take momentum average. The lth moment of the kinetic perturbation respect to p_z/E is defined by

$$u_l \equiv \left\langle \left(\frac{p_z}{E} \right)^l \delta f \right\rangle = \frac{1}{N_1} \int d^3p \ \left(\frac{p_z}{E} \right)^l \delta f, \tag{6.34}$$

where N_1 is expressed by massless Fermi–Dirac distribution, $N_1 = \int d^3p \ f'_{\mathrm{FD},m=0}$. The 0th and 1st order moment equations for the particle i are given by

$$\begin{cases} -D_1 \mu'_i + u'_{1,i} + \gamma v_w (m_i^2)' Q_{1i} \mu_i - K_{0i} \overline{\Gamma}_i = h S_{1i}. \\ -D_{2i} \mu'_i - v_w u'_{1,i} + \gamma v_w (m_i^2)' Q_{2i} \mu_i + (m_i^2)' \overline{R}_i u_{1,i} + \Gamma_{i,\mathrm{tot}} u_{1,i} + v_w K_{0i} \overline{\Gamma}_i = h S_{2i}. \end{cases} \tag{6.35}$$

The source term S_{li} is defined as

$$S_{li} = -\gamma v_w (m_i^2 \theta_i')' Q_{li}^8 + \gamma v_w m_i^2 \theta_i' (m_i^2)' Q_{li}^9, \quad (l = 1, 2). \tag{6.36}$$

The symbol $\Gamma_{i,\mathrm{tot}}$ denotes the total reaction rate of the particle i, and $\overline{\Gamma}_i$ is the sum of the reaction rate for inelastic scattering processes including i. The definitions of the functions D, Q, $\overline{R}$ are given in appendix B. In the derivation of Eq. (6.35), we have assumed a factorization assumption, such that

$$\langle X \delta f \rangle = \frac{\int d^3p \; X \delta f}{N_1} \to \frac{\int d^3p \; X f_{0w} \frac{E}{p_z}}{N_0} \times \frac{\int d^3p \; \frac{p_z}{E} \delta f}{N_1} \equiv \left[X \frac{E}{p_z} \right] u_1, \tag{6.37}$$

where $N_0 = \int d^3p f_{0w}$. From this factorization rule, we get truncation relation as

$$u_2 = \left\langle \frac{p_z^2}{E^2} \delta f \right\rangle = \left[\frac{p_z}{E} \right] u_1 = -v_w u_1. \tag{6.38}$$

For the CP-odd part of the collision terms, we also have used the relation [308]

$$\langle C_o \rangle = K_0 \overline{\Gamma}_i, \quad \left\langle \frac{p_z}{E} C_o \right\rangle = -\Gamma_{i,\mathrm{tot}} u_{1,i} - v_w \langle C_o \rangle , \tag{6.39}$$

where $K_0 = -N_0/(N_1 T)$.

By solving the above transport equations for active particles, the distributions of the chemical potentials are obtained. By using these distributions, the produced baryon number density normalized by the entropy density can be evaluated as [37, 308]

$$\eta_B = \frac{405 \Gamma_{\mathrm{sph}}}{4\pi^2 v_w g_* T_n} \int_0^\infty dz \; \mu_{B_L} f_{\mathrm{sph}}(z) \exp\left(-\frac{45 \Gamma_{\mathrm{sph}} z}{4 v_w} \right), \tag{6.40}$$

where μ_{B_L} is defined as

$$\mu_{B_L} \equiv \frac{1}{2} (\mu_{u_L} + \mu_{d_L} + \mu_{c_L} + \mu_{s_L} + \mu_{b_L} + \mu_{t_L}), \tag{6.41}$$

The symbol g_* is the effective degree of freedom for the entropy. The weak sphaleron rate in the symmetric phase is denoted by Γ_{sph}. By the lattice calculations, Γ_{sph} is evaluated as $\Gamma_{\mathrm{sph}} = 1.0 \times 10^{-6} T$ [318]. The function $f_{\mathrm{sph}}(z)$ describes the suppression of the weak sphaleron rate outside the bubble caused by the nonzero VEV. According to Ref. [37], we evaluate f_{sph} as

$$f_{\mathrm{sph}}(z) = \min\left\{ 1, \; \frac{2.4T}{\Gamma_{\mathrm{sph}}} e^{-40 v_n(z)/T} \right\}. \tag{6.42}$$

Chapter 7

Electroweak baryogenesis in the two Higgs doublet model

7.1 Electroweak phase transition in the two Higgs doublet model

In this section, we discuss the EWPT in the 2HDM, which is defined in section 4.1. In this section, just for simplicity of analyses, we consider the alignment limit $\alpha_i = 0$ to avoid mixing among the neutral scalar bosons.

7.1.1 Effective potential

In this subsection, we derive the effective potential of the 2HDM. We start discussions from the Higgs basis and consider only the electrically neutral VEVs. The VEVs of the two doublet fields can be written as

$$\langle \Phi_1 \rangle = \frac{1}{\sqrt{2}} \begin{pmatrix} 0 \\ \varphi_1 \end{pmatrix}, \quad \langle \Phi_2 \rangle = \frac{1}{\sqrt{2}} \begin{pmatrix} 0 \\ \varphi_2 + i\varphi_3 \end{pmatrix}, \tag{7.1}$$

where $\varphi_i \in \mathbb{R}$. We here have eliminated the imaginary part of the neutral component of $\langle \Phi_1 \rangle$ by rephasing Φ_2. The space dependence of this rephasing angle appears in the CP violating source term, as we will discuss later.

At the one-loop level, the effective potential at zero temperature is given by

$$V^{\text{eff}}_{T=0}(\varphi_1, \varphi_2, \varphi_3) = V_0 + V_1 + V_{\text{CT}}, \tag{7.2}$$

where V_0, V_1 and V_{CT} are tree-level potential, the Coleman–Weinberg (CW) potential [319] and the counter term, respectively.

The tree level potential is

$$\begin{aligned} V_0(\varphi_1, \varphi_2, \varphi_3) = &- \frac{1}{2} Y_1^2 \varphi_1^2 - \frac{1}{2} Y_2^2 (\varphi_2^2 + \varphi_3^2) - (Y_{3,R}^2 \varphi_2 - Y_{3,I}^2 \varphi_3)\varphi_1 \\ &+ \frac{1}{8} Z_1 \varphi_1^4 + \frac{1}{8} Z_2 (\varphi_2^2 + \varphi_3^2)^2 + \frac{1}{4} (Z_3 + Z_4)(\varphi_2^2 + \varphi_3^2)\varphi_1^2 \\ &+ \frac{1}{4} Z_5^R (\varphi_2^2 - \varphi_3^2)\varphi_1^2 - \frac{1}{2} Z_5^I \varphi_1^2 \varphi_2 \varphi_3 + \frac{1}{2} Z_6^R \varphi_1^3 \varphi_2 - \frac{1}{2} Z_6^I \varphi_1^3 \varphi_3 \\ &+ \frac{1}{2} Z_7^R \varphi_1 \varphi_2 (\varphi_2^2 + \varphi_3^2) - \frac{1}{2} Z_7^I \varphi_1 \varphi_3 (\varphi_2^2 + \varphi_3^2). \end{aligned} \tag{7.3}$$

If we take the real Z_5 basis, $Z_5^I = 0$.

We calculate the CW potential, in which the top quarks (t), the gauge bosons (W,Z, γ), the scalar bosons ($H^{\pm}, H_{1,2,3}$) and the NG bosons ($G^{\pm}, G_0$) give contributions, and obtain

$$\begin{aligned} V_1 =& -\frac{4\times 3}{64\pi^2}\tilde{m}_t^4\left(\ln\frac{\tilde{m}_t^2}{Q^2}-\frac{3}{2}\right)+\frac{3}{64\pi^2}\mathrm{Tr}\left[\tilde{m}_{\mathrm{gauge}}^4\left(\ln\frac{\tilde{m}_{\mathrm{gauge}}^2}{Q^2}-\frac{3}{2}\right)\right] \\ &+\frac{2}{64\pi^2}\mathrm{Tr}\left[\tilde{m}_{\pm}^4\left(\ln\frac{\tilde{m}_{\pm}^2}{Q^2}-\frac{3}{2}\right)\right]+\frac{1}{64\pi^2}\mathrm{Tr}\left[\tilde{m}_{\mathrm{neu}}^4\left(\ln\frac{\tilde{m}_{\mathrm{neu}}^2}{Q^2}-\frac{3}{2}\right)\right], \end{aligned} \tag{7.4}$$

where $\tilde{m}$ is the field dependent mass, which is given in appendix A. We here adopt the Landau gauge to calculate the CW potential, and set renormalization scale as $Q = m_Z$.

The counter term V_{CT} is written by

$$\begin{aligned} V_{\mathrm{CT}} =& -\frac{1}{2}\delta Y_1^2\varphi_1^2-(\delta Y_{3,R}^2\varphi_2-\delta Y_{3,I}^2\varphi_3)\varphi_1 \\ &+\frac{1}{8}\delta Z_1\varphi_1^4+\frac{1}{4}\delta Z_3(\varphi_2^2+\varphi_3^2)\varphi_1^2 \\ &+\frac{1}{4}\delta Z_5^R(\varphi_2^2-\varphi_3^2)\varphi_1^2-\frac{1}{2}\delta Z_5^I\varphi_1^2\varphi_2\varphi_3+\frac{1}{2}\delta Z_6^R\varphi_1^3\varphi_2-\frac{1}{2}\delta Z_6^I\varphi_1^3\varphi_3. \end{aligned} \tag{7.5}$$

We determine these counter terms not to change the vacuum and the curvatures at the vacuum from the tree-level potential. At the tree level, due to the stationary condition, $\boldsymbol{\varphi} = (\varphi_1,\varphi_2,\varphi_3) = (v,0,0) \equiv \boldsymbol{\varphi}_{vac}$ gives the minimized value of the potential. We impose nine renormalization conditions,

$$\begin{aligned} &\left.\frac{\partial V_{T=0}^{\mathrm{eff}}}{\partial\varphi_i}\right|_{\boldsymbol{\varphi}=\boldsymbol{\varphi}_{vac}} = 0, \quad (i=1,2,3), \\ &\left.\frac{\partial^2 V_{T=0}^{\mathrm{eff}}}{\partial\varphi_i\partial\varphi_j}\right|_{\boldsymbol{\varphi}=\boldsymbol{\varphi}_{vac}} = \mathcal{M}_{ij}^2, \quad (i,j=1,2,3), \end{aligned} \tag{7.6}$$

and remaining parameters are renormalized by $\overline{\mathrm{MS}}$ scheme. In the second condition, the massless NG bosons cause IR divergence, so that we take a cutoff $m_{NG} = 1$ GeV [320] in numerical calculation. This problem is sometimes called Goldstone catastrophe [321]. We have checked the final results are hardly dependent on this cutoff scale. The explicit renormalization conditions are given in appendix A.

We next consider thermal corrections to the effective potential. The effective potential at finite temperature is given by

$$V^{\mathrm{eff}}(\varphi_1,\varphi_2,\varphi_3;T) = V_{T=0}^{\mathrm{eff}} + V_T. \tag{7.7}$$

The thermal correction V_T is given by [277]

$$V_T = \sum_{s_k}(-1)^{s_k}\frac{n_k}{2\pi^2\beta^4}\int_0^\infty dx\; x^2\log\left(1+(-1)^{s_k+1}\exp\left(-\sqrt{x^2+\beta^2\tilde{m}_k^2}\right)\right), \tag{7.8}$$

where $\beta = 1/T$, $s_k = 0$ for bosons and $s_k = 1$ for fermions. We employ Parwani resummation scheme [322] to include leading order corrections from thermal mass.

7.1.2 Electroweak phase transition

By using the effective potential at finite temperature, we can calculate EWPT. The nucleation temperature of the bubble T_n satisfies $\Gamma/H^4 = 1$, where H is the Hubble parameter, and Γ is the probability of tunneling at the temperature T per unit time and volume, given by [278–280]

$$\Gamma = A(T)\exp\left(-\frac{S_3}{T}\right). \tag{7.9}$$

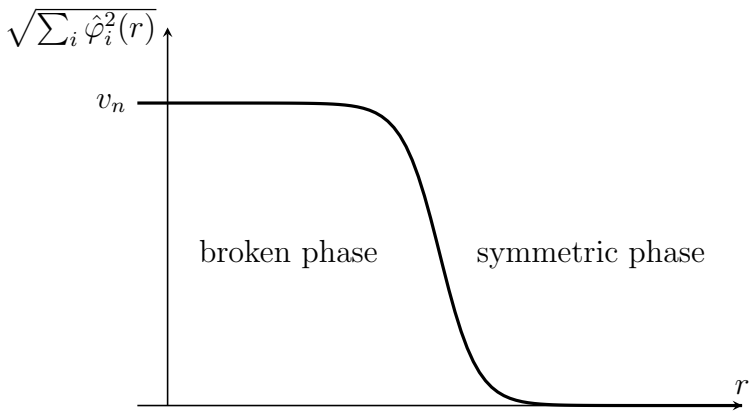

Figure 7.1

The pre-factor $A(T)$ is roughly evaluated as $A(T) \sim T^4$ by the dimensional analysis, and S_3 is the three-dimensional Euclidian action. With the assumption of spherical symmetry with the spatial radius r, we have

$$S_3 = 4\pi \int_0^\infty dr\, r^2 \left[\sum_{i=1}^{3} \frac{1}{2} \left(\frac{d\hat{\varphi}_i}{dr} \right)^2 + V^{\text{eff}}(\hat{\varphi}_1, \hat{\varphi}_2, \hat{\varphi}_3; T) \right]. \tag{7.10}$$

The quantities $\hat{\varphi}_i$ are the solution of the equation of motions

$$\frac{d^2\varphi_i}{dr^2} + \frac{2}{r}\frac{d\varphi_i}{dr} = \frac{\partial V^{\text{eff}}}{\partial \varphi_i}, \quad (i = 1, 2, 3), \tag{7.11}$$

with the boundary conditions

$$\varphi_i(r = \infty) = 0, \quad \left.\frac{d\varphi_i}{dr}\right|_{r=0} = 0. \tag{7.12}$$

The typical shape of the solution is drawn in figure 7.1. In $r \to \infty$, the VEVs are zero (symmetric phase), while the fields get the VEV in $r \to 0$ (broken phase). The actual bubble is the spherical, however, the typical scale of particle reactions around the bubble wall for EWBG is much smaller compared to the radius of the bubble. Therefore, in the following discussions, we neglect the curvature of the walls and take one-dimensional coordinate along to the radius of the bubble. We define $z = 0$ as the center of the bubble, and $z = \infty$ ($z = -\infty$) is the infinite point outside (inside) the bubble.

We here show numerical evaluations of the electroweak phase transition in the 2HDM. For simplicity, we consider only the single-step phase transition. For numerical evaluation, we use `CosmoTransitions` [323], which is a set of Python modules for calculating the effective potential and the Euclidean action.

In figure 7.2, we show the behavior of the EWPT for various masses of the additional Higgs bosons and the decoupling parameter $M \equiv \sqrt{-Y_2^2}$. Here, we take the additional Higgs bosons have the same mass $m_{H^\pm} = m_{H_2} = m_{H_3} \equiv m_\Phi$. We show the figures for $Z_2 = 0.1$ (left) and $Z_2 = 2.0$ (right). Other parameters of the effective potential are set to be $|\zeta_u| = 0.15, \theta_u = -2.7, |Z_7| = 0.8, \arg[Z_7] = -0.9$.

In the lower gray region, the EWPT is two step or second-order. In the upper gray region, the nucleation rate per Hubble volume Γ_n/H^4 is less than 1. In such a region, the EWPT is not completed until the present.

In the white regions, the EWPT is first-order, and occurs in a single step. For successful electroweak baryogenesis, the EWPT has to be strongly first-order, where the sphaleron transition decouples inside the bubble quickly enough. In figure 7.2, contours for v_n/T_n are shown

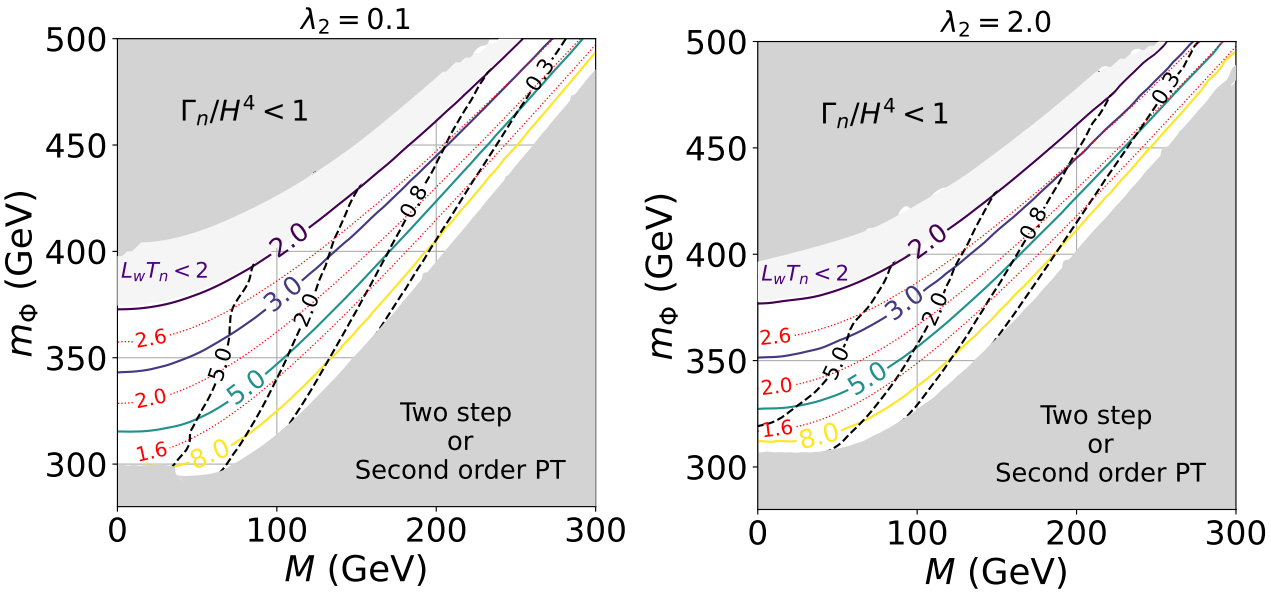

Figure 7.2: The behavior of the EWPT for various masses of the additional Higgs bosons and the decoupling parameter M. The masses of the additional Higgs bosons are assumed to be degenerated and given by m_Φ. The red dotted lines are contours for v_n/T_n, and the black dashed lines are $10 \times \partial_z\theta|_{\max}$. Other colored lines are contours for $L_w T_n$. In the left (right) figure, Z_2 is set to be 0.1 (2.0).

by the red lines. For a fixed value of M, the heavier m_Φ gives the larger v_n/T_n because of the non-decoupling effect of the additional Higgs bosons [23, 47]. The minimum value of v_n/T_n in the white regions is approximately 1.2, so that we can see that the sphaleron decoupling condition is satisfied in all the white regions.

Another important parameter for the strength of the EWPT is the wall width of the bubble L_w. For the stronger phase transition, L_w is smaller. We evaluate L_w by fitting the profile of the VEV $v(z) = \sqrt{\hat{\varphi}_1^2 + \hat{\varphi}_2^2 + \hat{\varphi}_3^2}$ with the function

$$v(z) = \frac{v_n}{2}\left(1 - \tanh\frac{z}{L_w}\right). \tag{7.13}$$

In figure 7.2, contours for $L_w T_n = 2.0$, 3.0, 5.0, and 8.0 are shown in purple, dark blue, dark green, and yellow lines, respectively. For a fixed value of M, $L_w T_n$ is smaller for the heavier additional Higgs bosons.

For producing baryon asymmetry, the phase of the local mass of the top quark is important, as we will discuss later [308]. It is defined as

$$\mathcal{L}_{\text{mass}} = -m_t(z) e^{i\theta(z)} \overline{t_L} t_R + \text{h.c.}, \tag{7.14}$$

where $m_t(z)$ and $\theta(z)$ are the absolute value and the phase of the local mass of the top quark, respectively. The explicit forms of them will be given in section 7.2, but the spatial variation of $\theta(z)$ provides the source of CP violation. In figure 7.2, contours for the maximal value of $\partial_z\theta$ are shown: $10 \times \partial_z\theta|_{\max} = 0.3$, 0.8, 2.0, and 5.0 in GeV^{-1}. We can see that the maximum value $\partial_z\theta|_{\max}$ decreases as the decoupling parameter M increases. In addition, it is smaller for the larger Z_2. This behavior can be understood as follows. The parameter M^2 and Z_2 is the coefficient of $|\Phi_2|^2$ and $|\Phi_2|^4$ in the scalar potential. The potential is thus higher along to the directions of φ_2 and φ_3 with larger M^2 and Z_2. As a result, $\hat{\varphi}_2$ and $\hat{\varphi}_3$ as the solutions of Eq. (7.11) cannot be large enough with large M^2 and Z_2, causing smaller $\partial_z\theta|_{\max}$.

7.2 Top transport scenario

In this section, we discuss the top transport EWBG scenario [36], where the leading CP violating source is caused by the top quarks, and show the numerical results which are obtained by solving the transport equations in the 2HDM. As we have discussed in section 6.3, the CP violating source terms are proportional to the mass of the particle. The top quarks have the largest coupling to the bubble wall, so that the CP violations of them are typically most important for the BAU.

In general, what particles become the most important for the EWBG depends on the model, and its parameters. In the 2HDM, it is determined by the additional Yukawa matrices ρ^f. In the following, we discuss the scenario in which the top quarks generate the CP asymmetry, so that we take the Pich–Tuzon parametrization given in Eq. (4.37), and neglect the effects from $\zeta_{d,e}$ in the CP violating source terms.

7.2.1 Transport equation network

In this top transport scenario, we neglect the masses except for the top quarks. The relevant particles in the transport equations are the (right-) left-handed top quarks denoted by t (t^c), the right-handed top quarks denoted by t the left-handed bottom quarks b and the scalar doublets h. For inelastic scattering processes, we take into account the strong sphaleron process, the W boson scattering, the top Yukawa interaction, the top helicity flips in the broken phase and the Higgs number violation. The reaction rates for each inelastic process are denoted by $\Gamma_{ss}, \Gamma_W, \Gamma_y, \Gamma_m$ and Γ_h, respectively. We refer to their values in Ref. [309].

For the light quarks, $u_{L,R}, d_{L,R}, c_{L,R}, s_{L,R}$ and b_R, only relevant scattering process is the strong sphaleron, so that we obtain

$$\mu_{u_L,d_L,c_L,s_L} = -\mu_{u_R,d_R,c_R,s_R} = -\mu_{b_R}. \tag{7.15}$$

By using the fact that the baryon number is conserved in this process, we obtain

$$\mu_{B_L} = \frac{1}{2}(1+4D_{0t})\mu_t + \frac{1}{2}(1+4D_{0b})\mu_b - 2D_{0t}\mu_{t^c}. \tag{7.16}$$

The transport equations for top quarks, the left-handed bottom quarks and the scalar doublets are given as follows [309];

- Left-handed top quarks (t)

$$\begin{cases} -D_{1t}\mu_t' + u_t' + \gamma v_w (m_t^2)' Q_{2t}\mu_t - K_{0t}\overline{\Gamma}_t = -S_{1t}, \\ -D_{2t}\mu_t' - v_w u_t' + \gamma v_w (m_t^2)' Q_{t2}\mu_t + (m_t^2)'\overline{R}_t u_t + \Gamma_{t,\mathrm{tot}} u_t + v_w K_{0t}\overline{\Gamma}_t = -S_{2t}. \end{cases} \tag{7.17}$$

- Left-handed bottom quarks (b)

$$\begin{cases} -D_{1b}\mu_b' + u_b' - K_{0b}\overline{\Gamma}_b = 0, \\ -D_{2b}\mu_b' - v_w u_b' + \Gamma_{b,\mathrm{tot}} u_b + v_w K_{0b}\overline{\Gamma}_b = 0. \end{cases} \tag{7.18}$$

- Charge conjugation of right-handed singlet top quarks (t^c)

$$\begin{cases} -D_{1t}\mu_{t^c}' + u_{t^c}' + \gamma v_w (m_t^2)' Q_{2t}\mu_{t^c} - K_{0t}\overline{\Gamma}_{t^c} = -S_{1t}, \\ -D_{2t}\mu_{t^c}' - v_w u_{t^c}' + \gamma v_w (m_t^2)' Q_{t2}\mu_{t^c} + (m_t^2)'\overline{R}_t u_{t^c} + \Gamma_{t,\mathrm{tot}} u_{t^c} + v_w K_{0t}\overline{\Gamma}_{t^c} = -S_{2t}. \end{cases} \tag{7.19}$$

- The scalar doublets (h)

$$\begin{cases} -D_{1h}\mu_h' + u_h' - K_{0h}\overline{\Gamma}_h = 0, \\ -D_{2h}\mu_h' - v_w u_h' + \Gamma_{h,\mathrm{tot}} u_h + v_w K_{0h}\overline{\Gamma}_h = 0. \end{cases} \tag{7.20}$$

The inelastic reaction rates for each particle is written by [309]

$$\begin{aligned} \overline{\Gamma}_t &= \Gamma_{ss}\Big((1+9D_{0t})\mu_t + 10\mu_b + (1-9D_{0t})\mu_{t^c}\Big) \\ &\quad + \Gamma_W(\mu_t - \mu_b) + \Gamma_y(\mu_t + \mu_{t^c} + \mu_h) + 2\Gamma_m(\mu_t + \mu_{t^c}), \qquad (7.21) \\ \overline{\Gamma}_b &= \Gamma_{ss}\Big((1+9D_{0t})\mu_t + 10\mu_b + (1+9D_{0t})\mu_{t^c}\Big) \\ &\quad + \Gamma_W(\mu_b - \mu_t) + \Gamma_y(\mu_b + \mu_{t^c} + \mu_h), \qquad (7.22) \\ \overline{\Gamma}_{t^c} &= \Gamma_{ss}\Big((1+9D_{0t})\mu_t + 10\mu_b + (1-9D_{0t})\mu_{t^c}\Big) \\ &\quad + 2\Gamma_m(\mu_{t^c} + \mu_t) + \Gamma_y(2\mu_{t^c} + \mu_t + \mu_b + 2\mu_h), \qquad (7.23) \\ \overline{\Gamma}_h &= \frac{3}{4}\Gamma_y(2\mu_h + \mu_t + \mu_b + 2\mu_{t^c}) + \Gamma_h\mu_h. \qquad (7.24) \end{aligned}$$

From the Yukawa interaction in the 2HDM, m_t and θ_t' are derived as

$$\begin{aligned} m_t^2 &= \frac{y_t^2}{2}\Big(\varphi_1^2 + |\zeta_u|^2(\varphi_2^2+\varphi_3^2) + 2|\zeta_u|\varphi_1\big(\varphi_2\cos\theta_u - \varphi_3\sin\theta_u\big)\Big), \\ \theta_t' &= \frac{y_t^2|\zeta_u|}{2m_t^2}\Big\{(\varphi_3\varphi_1' - \varphi_1\varphi_3')\cos\theta_u - (\varphi_1\varphi_2' - \varphi_2\varphi_1')\sin\theta_u + |\zeta_u|(\varphi_3\varphi_2' - \varphi_2\varphi_3')\Big\} \\ &\quad + \frac{1}{\varphi_1^2+\varphi_2^2+\varphi_3^2}(\varphi_3\varphi_2' - \varphi_2\varphi_3'). \end{aligned} \tag{7.25}$$

As we have mentioned in section 7.1, we have taken the local z dependent basis of $\langle\Phi_2\rangle$ to absorb the imaginary part of the neutral component of $\langle\Phi_1\rangle$. In this basis, classical Z boson current appears around the bubble wall, which is caused by the varying phase of the neutral part of $\langle\Phi_2\rangle$, i.e. φ_2 and φ_3 [37]. This current makes the mass term of the top quarks around the bubble via the axial vector interaction, resulting in the finial term in the equation of θ_t'.

7.2.2 Numerical analysis

In this subsection, we show the numerical evaluations for the BAU in the 2HDM.

In figure 7.3, the correlation between $|d_e|/|d_e^{\mathrm{exp}}|$, which is the eEDM normalized by $|d_e^{\mathrm{exp}}| = 1.0\times10^{-29}$ e cm, and the absolute value of the normalized baryon density $|\eta_B|\times10^{11}$ is shown. Input parameters are $Z_2 = 0.1$, $M = 30$ GeV, $m_\Phi = 350$ GeV, $v_w = 0.1$, and we scan the other parameters for the regions of $\theta_u = \theta_d = [0, 2\pi)$, $|\zeta_u| = [0, 0.6]$, $|\zeta_d| = |\zeta_e| = [0, 10]$, $|Z_7| = [0.5, 1.0]$ and $\arg[Z_7] = [0, 2\pi)$. Black, magenta, and green points are the cases of $0.1 \le |\delta_e| \le 0.5$, $0.01 \le |\delta_e| \le 0.1$, $0 \le |\delta_e| \le 0.01$, respectively. Here, we have defined $\delta_e \equiv \theta_u - \theta_e$. The black dashed line is the ACMEII bound [282], and above this line is excluded by this bound. Currently, JILA group has been provided approximately one-half smaller bound [283], as mentioned in section 6.2.1. The vertically parallel pink region explains the observed BAU from the BBN with 95% C.L. Each point is allowed by the theoretical and current experimental constraints except for the eEDM data. As we have mentioned in section 6.2.1, the Barr–Zee type fermion and scalar loop diagrams which contribute to the eEDM are approximately proportional to $|\zeta_u||\zeta_e|\sin\delta_e$ and $|\zeta_e||\lambda_7|\sin(\theta_7 - \theta_e)$, respectively. Due to the interference of the diagrams contributing to the eEDM, predicted eEDM value

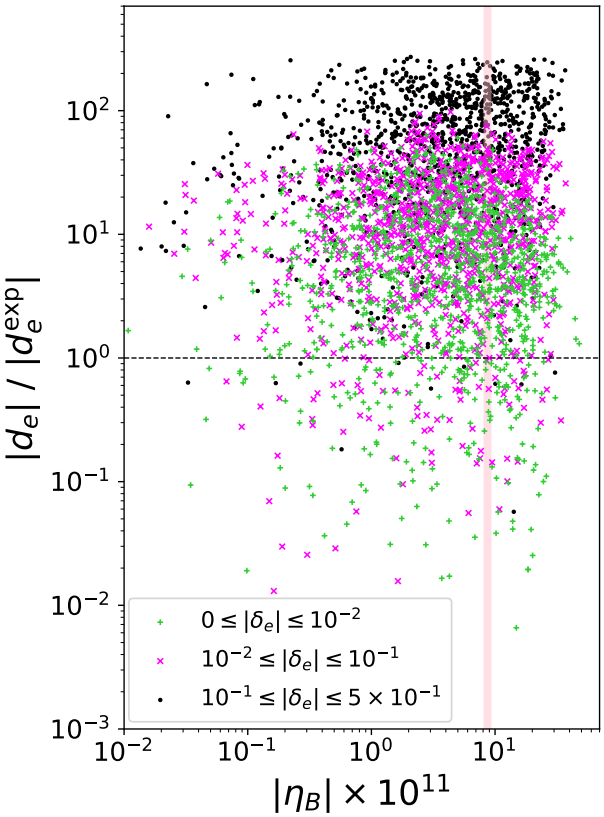

Figure 7.3: The correlation between $|d_e|/|d_e^{\rm exp}|$ and $|\eta_B| \times 10^{11}$. Input parameters are given by $\lambda_2 = 0.1$, $m_\Phi = 350$ GeV, $M = 30$ GeV and $v_w = 0.1$. We scan the other parameters for the regions of $\theta_u = \theta_d = [0, 2\pi)$, $|\zeta_u| = [0, 0.6]$, $|\zeta_d| = |\zeta_e| = [0, 10]$, $|\lambda_7| = [0.5, 1.0]$ and $\theta_7 = [0, 2\pi)$. Black, magenta and green points are the cases of $0.1 \le |\delta_e| \le 0.5$, $0.01 \le |\delta_e| \le 0.1$ and $0 \le |\delta_e| \le 0.01$, respectively. Here, we have defined $\delta_e \equiv \theta_u - \theta_e$. The vertically parallel pink region explains the observed BAU from the BBN within 95% C.L.

takes a broad range from $|d_e| = O(10^{-31})e$ cm to $O(10^{-27})e$ cm. The eEDM decreases in the order of black, magenta and green, because of the size of fermion contribution decreasing in this order, and a lot of magenta and green points can generate sufficient BAU under the eEDM constraints.

Top (bottom) panel of figure 7.4 shows generated BAU in the case of $v_w = 0.1$ (0.45) in the following benchmark point, $M = 30$ GeV, $Z_2 = 0.1, |Z_7| = 0.8, \arg[Z_7] = -0.9, |\zeta_u| = |\zeta_d| = |\zeta_e| = 0.18, \theta_u = \theta_d = -2.7, \delta_e = -0.04$. At the point in the gray region in figure 7.4, the EWPT is two step or second order. The black dashed lines in figure 7.4 are the contour of $v_n/T_n = 1.7$ and 2.3. Therefore, the SFOPT for the sphaleron decoupling condition occurs above the gray region. The black solid line is the contour of $L_w T_n = 4.0$. The white region satisfies $L_w T_n < 2$, where the WKB approximation becomes invalid [36]. As shown in figure 7.2, since the invariant mass parameter M is fixed, increasing the mass of heavy scalars makes the electroweak phase transition stronger, and makes $L_w T_n$ smaller. In the case of $v_w = 0.1$, the generated BAU increases as the masses of the additional Higgs bosons increase up to $L_w T_n = 4.0$, and then turns to decrease. On the other hand, in the case of $v_w = 0.45$, the BAU gets larger as the phase transition is stronger. In both panels of figure 7.4, the pink regions which are sandwiched by green and orange regions can explain the observed BAU.

In the blue lines in figure 7.4, various values of the eEDM $d_e/|d_e^{\rm exp}|$ are shown. The line of $d_e/|d_e^{\rm exp}| = 0.0$ in figure 7.4 is due to the destructive interference between the fermion and boson type diagram, which is shown in figure 6.3.

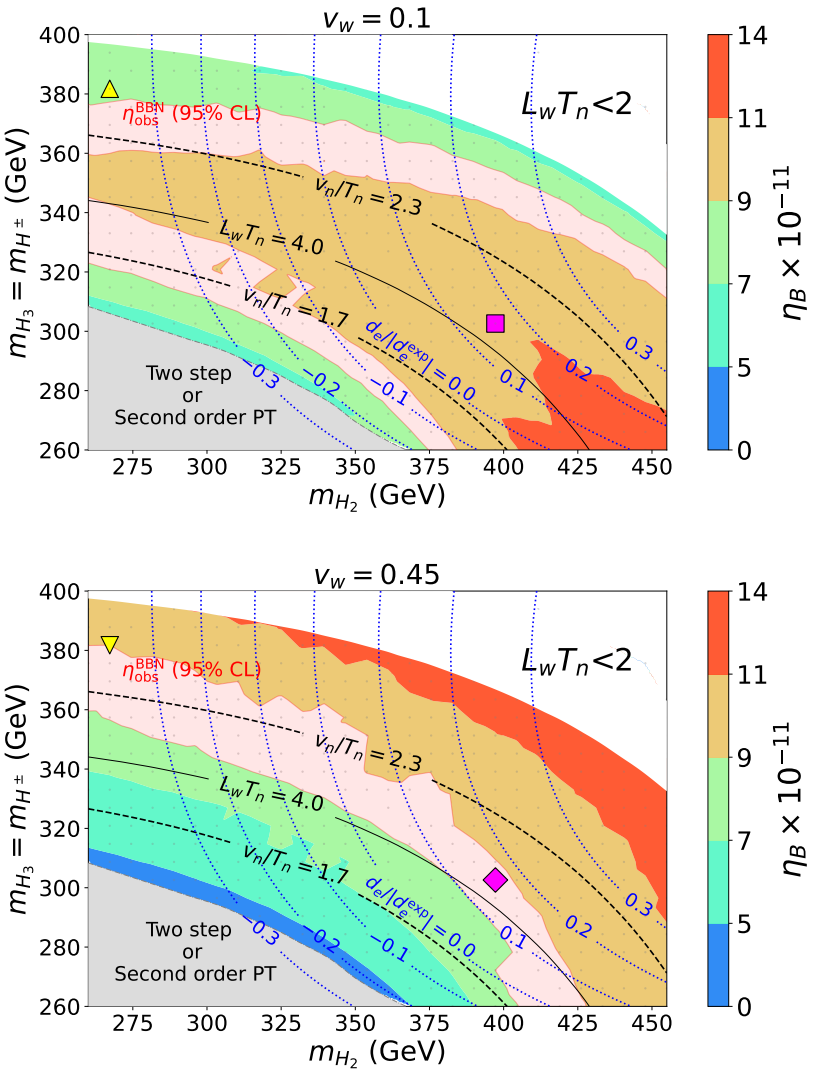

Figure 7.4: Contour of the BAU on the plane of m_{H_2} and $m_{H_3} = m_{H^\pm}$ in the case of $v_w = 0.1$ (top) and $v_w = 0.45$ (bottom). Input parameters are $M = 30$ GeV, $Z_2 = 0.1, |Z_7| = 0.8, \arg[Z_7] = -0.9, |\zeta_u| = |\zeta_d| = |\zeta_e| = 0.18, \theta_u = \theta_d = -2.7, \delta_e = -0.04$. The pink regions correspond to the observed BAU.

7.2.3 Phenomenological discussions

In this subsection, we discuss phenomenological predictions for future experiments. We here set benchmark points which are colored with yellow and magenta in each panel of figure 7.4. We define the upward triangle (downward triangle) point with yellow as BP1a (BP1b), and the square (diamond) point with magenta as BP2a (BP2b). Magnitudes of the electroweak phase transitions v_n/T_n in the BP1a and the BP1b are relatively stronger than the ones in the BP2a and the BP2b. Table 7.1 shows the input parameters of the four benchmark points v_w, m_{H_2}, $m_{H_3}(= m_{H^\pm})$ and M, as well as v_n/T_n, $L_w T_n$ and η_B in these points are also shown. BP1b and BP2b, which are the cases of $v_w = 0.45$, explain the observed BAU.

First, we discuss some testability for the SFOPT. It is known that the loop effects of heavy Higgs bosons for the SFOPT increase ΔR which is the deviation of triple Higgs boson coupling from the SM value [23]. We already have shown the formula of ΔR at the one-loop level in Eq. (4.38). In Table 7.1, the values of ΔR are shown. In the BP1 and BP2, the deviations of the triple Higgs boson coupling ΔR become 61% and 44%, respectively. Therefore, these points would be tested at the HL-LHC or the future updated ILC.

	v_w	m_{H_2}	$m_{H_3,H^\pm}$	M	v_n/T_n	L_wT_n	η_B	ΔR	$\sigma\mathrm{Br}(H_1 \to \gamma\gamma)$
BP1a	0.1	267 GeV	381 GeV	30 GeV	2.4	2.6	7.8×10^{-11}	0.61	104 ± 5 fb
BP1b	0.45						9.1×10^{-11}		
BP2a	0.1	397 GeV	302 GeV	30 GeV	2.0	4.1	10.8×10^{-11}	0.44	
BP2b	0.45						9.0×10^{-11}		

Table 7.1: The input parameters of the four benchmark points v_w, m_{H_2}, $m_{H_3}(= m_{H^\pm})$ and M are shown. In addition, v_n/T_n, L_wT_n and η_B in each benchmark point are shown. As phenomenological predictions, we show the values of ΔR and $\sigma\mathrm{Br}(H_1 \to \gamma\gamma)$ in these benchmark points. ΔR is the deviation in the triple Higgs boson coupling. σ is the production cross section of the SM Higgs boson, and $\mathrm{Br}(H_1 \to \gamma\gamma)$ is the branching ratio of the decay into a photon pair.

In addition to the triple Higgs boson coupling, the decay of the Higgs boson into a photon pair is affected by the non-decoupling effect of the charged Higgs boson [324–331]. From the latest data at ATLAS Collaboration [332], the observed value of $\sigma\mathrm{Br}(H_1 \to \gamma\gamma)$ is given by

$$\sigma\mathrm{Br}(H_1 \to \gamma\gamma)_{\mathrm{obs}} = 127 \pm 10 \text{ fb}, \tag{7.26}$$

where σ is the production cross section of the SM Higgs boson and $\mathrm{Br}(H_1 \to \gamma\gamma)$ is the branching ratio of the decay into di-photon. The theoretical value of $\sigma\mathrm{Br}(H_1 \to \gamma\gamma)$ in BP1 and BP2 is shown in the last column of Table 7.1. In BP1 and BP2, we obtain $\sigma\mathrm{Br}(H_1 \to \gamma\gamma) = 104 \pm 5$ fb, and the uncertainty stems from theoretical errors of the production cross section of the SM Higgs boson. Unlike the behavior of the non-decoupling effect in ΔR in Eq. (4.38), the Higgs di-photon decay depends on a coupling proportional to $(m_{H^\pm}^2 - M^2)/m_{H^\pm}^2$. This effect does not decouple and becomes a constant for $m_{H^\pm} \to \infty$. Therefore, the values of $\sigma\mathrm{Br}(H_1 \to \gamma\gamma)$ in the BP1 and BP2 are the same within the range of significant figures. The predictions on $\sigma\mathrm{Br}(H_1 \to \gamma\gamma)$ in BP1 and BP2 overlap with the observed value within 2σ significance. These benchmark points would be tested by the precision measurement of the Higgs di-photon search at the future colliders such as the HL-LHC.

Furthermore, the GWs can also be produced from the collision of the bubbles which are created at the first order phase transition [58–62]. The sources of the GWs are composed of the contributions from the scalar field $\Omega_\phi(f)$, the sound waves of the plasma $\Omega_{\mathrm{sw}}(f)$, and the magnetohydrodynamics turbulence $\Omega_{\mathrm{turb}}(f)$, where f is the frequency of the GWs. Each contribution is decided by the wall velocity v_w, the latent heats α, and the time duration $\tilde{\beta}$ at the phase transition. These can be defined by

$$\alpha = \frac{\rho_{\mathrm{vac}}(T_n)}{\rho_{\mathrm{rad}}(T_n)}, \quad \tilde{\beta} = T_n \left(\frac{dS_3}{dT} \right)_{T=T_n}, \tag{7.27}$$

where,

$$\rho_{\mathrm{vac}}(T_n) = \left(-\Delta V + T \frac{\partial \Delta V}{\partial T} \right)_{T=T_n}, \quad \rho_{\mathrm{rad}}(T_n) = \frac{g_* T_n^4}{30} \pi^2, \tag{7.28}$$

where ΔV is the difference between the values of the effective potential of the true vacuum and the false vacuum. The total energy density of the GWs is given by

$$h^2 \Omega_{\mathrm{GW}}(f) = h^2 \Omega_\phi + h^2 \Omega_{\mathrm{sw}} + h^2 \Omega_{\mathrm{turb}}. \tag{7.29}$$

In THDMs, the terminal wall velocity does not reach the speed of light [59]. For simplicity, we assume that the velocity for the numerical analysis of the GWs matches the one used in the

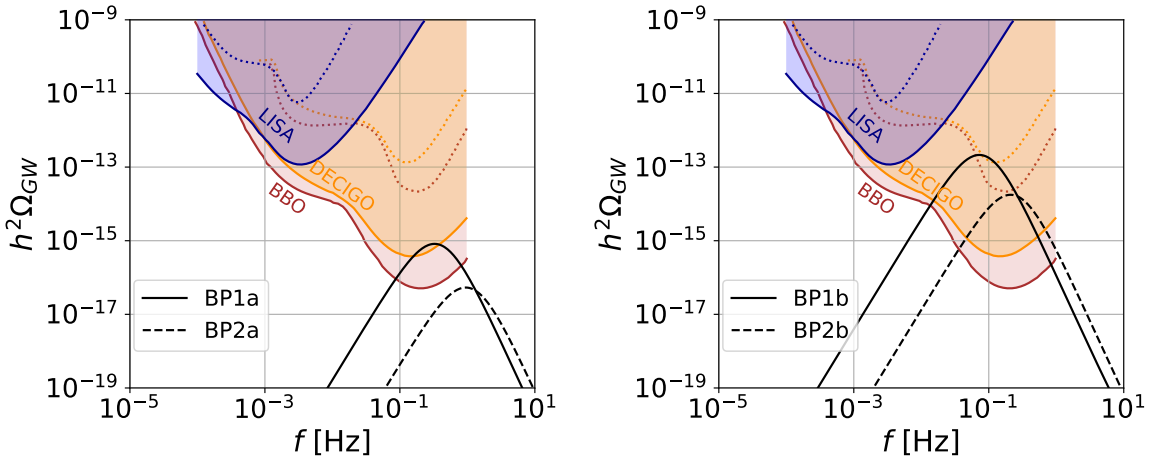

Figure 7.5: The GW spectra calculated at the benchmark points in Table 7.1. The purple, orange and red lines are the sensitivity curves of LISA, DECIGO, and BBO. The black solid and dashed lines are the GW spectra which are produced by the first order phase transition in these points.

calculations of the BAU. In this scenario, the leading contribution is the sound waves [60], and the contribution from the scalar field is negligible.[1]

The GW spectra calculated at the benchmark points in Table 7.1 are shown in figure 7.5. The purple, orange and red dashed curves are the sensitivity curves of LISA [63], DECIGO [64], and BBO [65], while the solid curves in each color are the peak-integrated sensitivity curves. We have taken these curves from Ref. [56]. The solid and dashed black lines in the left panel of figure 7.5 are the GW spectra at the BP1a and BP2a, respectively, while the ones at the BP1b and BP2b are shown in the right panel. At BP1, where the EWPT is relatively strong, both of the peaks reach the peak integrated sensitivity curves of DECIGO and BBO. On the other hand, at BP2, where the EWPT is relatively weak, only the one in the BP2b, in which $v_w = 0.45$ is assumed, reaches DECIGO and BBO.

The parameter in our model ζ_d, which controls the strength of down-type quark couplings to the additional Higgs bosons, can be constrained by future measurements of $B \to X_s\gamma$ and $\Delta\mathcal{A}_{CP}$ [45]. The observable $\Delta\mathcal{A}_{CP}$ is related to CP violation in the process of $B \to X_s\gamma$. It is defined by [333]

$$\Delta\mathcal{A}_{CP} = A_{CP}(B^+ \to X_s^+\gamma) - A_{CP}(B^0 \to X_s^0\gamma), \tag{7.30}$$

where,

$$\begin{aligned} A_{CP}(B^+ \to X_s^+\gamma) &= \frac{\Gamma(B^- \to X_s^-\gamma) - \Gamma(B^+ \to X_s^+\gamma)}{\Gamma(B^- \to X_s^-\gamma) + \Gamma(B^+ \to X_s^+\gamma)}, \\ A_{CP}(B^0 \to X_s^0\gamma) &= \frac{\Gamma(\overline{B}^0 \to \overline{X}_s^0\gamma) - \Gamma(B^0 \to X_s^0\gamma)}{\Gamma(\overline{B}^0 \to \overline{X}_s^0\gamma) + \Gamma(B^0 \to X_s^0\gamma)}. \end{aligned} \tag{7.31}$$

By using the Wilson coefficients C_7 and C_8, $\Delta\mathcal{A}_{CP}$ is given by [333]

$$\Delta\mathcal{A}_{CP} \simeq 0.12 \left(\frac{\tilde{\Lambda}_{78}}{100\ \text{MeV}}\right) \text{Im}\left(\frac{C_8}{C_7}\right), \tag{7.32}$$

[1]The contribution from the turbulence is decided by a part of the latent heats $\epsilon\kappa_v\alpha$, where κ_v is defined by how the latent heats are transformed into the bulk motion of the plasma fluid. In the following analysis, we set $\epsilon = 0.05$ [59, 61].

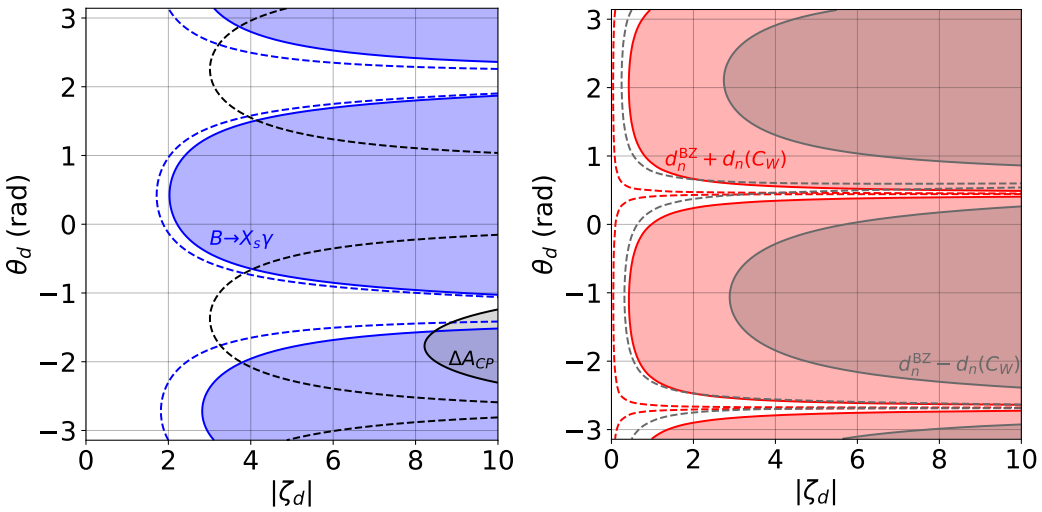

Figure 7.6: The constraints on $|\zeta_d|$-θ_d plane at the BP1 from the flavor (left) and nEDM (right) experiments. The blue (black) shaded regions in the left panel are the excluded regions from $B \to X_s\gamma$ ($\Delta\mathcal{A}_{CP}$). The red (gray) regions in the right panel are excluded by the current nEDM experimental data when the Weinberg operator positively (negatively) contributes to the nEDM. The dashed lines in each panel are future expected bounds.

where $\tilde{\Lambda}_{78}$ implies uncertainties from the hadronic scale, and it is estimated as 17 MeV $< \tilde{\Lambda}_{78} <$ 190 MeV [333]. In the following analysis, we set $\tilde{\Lambda}_{78} = 89$ MeV as the average value [45]. In the SM, $\Delta\mathcal{A}_{CP} = 0$, because both the Wilson coefficients C_7 and C_8 are real, so that it has a sensitivity to CP violation from new physics. From the current experimental data at Belle [334], we obtain $\Delta\mathcal{A}_{CP} = (+3.69 \pm 2.65 \pm 0.76)\%$, where the first uncertainty is the statistical error and the second is the systematical one. At Belle-II [335] with 50 ab^{-1} as the future flavor experiment, it is expected that the absolute uncertainty is reduced to be 0.3 %. It is also expected at Belle-II with 50 ab^{-1} that the relative uncertainty in the measurement of $B \to X_s\gamma$ can be reduced to be 3.2 % [335].

As implied in section 6.2.1, the nEDM can be used to constrain ζ_d. The upper bound of the nEDM is expected to be about one order higher accuracy in future nEDM experiments [336]. However, there are still some uncertainties, especially including the sign of the contribution from the Weinberg operator.

Figure 7.6 shows that the current and future expected bounds for ζ_d. The input parameters are the same as the BP1. First, we explain the left panel of figure 7.6. Blue (black) regions are the excluded regions at 2σ level from the current measurement of $B \to X_s\gamma$ ($\Delta\mathcal{A}_{CP}$), and the dashed lines are the future excluded bounds at Belle-II. In the left figure, $B \to X_s\gamma$ and $\Delta\mathcal{A}_{CP}$ cover the different regions of θ_d, and we find $|\zeta_d| \gtrsim 3$ can be excluded at Belle-II.

The nEDM constraints on ζ_d are shown in the right panel of figure 7.6. Red (gray) regions are excluded by the current experimental data [284] when the contribution from the Weinberg operator $d_n(C_W)$ positively (negatively) contributes. The dashed lines are the one order higher accurate bound expected in future nEDM experiments [336]. In the constructive case, where the total value of the nEDM is given by the sum of the two loop contribution $d_n^{\rm BZ}$ and the Weinberg operator contribution $d_n(C_W)$, the vast region of ζ_d has been already excluded except for $\theta_d \simeq \theta_u$ or $\theta_u + \pi$. In such a case, almost all regions would be excluded by future nEDM experiments. On the other hand, in the destructive case, where the Weinberg operator negatively contributes to the nEDM, $|\zeta_d| \gtrsim 3$ has already been excluded at $\theta_d = \theta_u \pm \pi/2$, and $|\zeta_d| \gtrsim 0.3$ is expected to be excluded in the future. As a result, ζ_d is constrained by the combination of $B \to X_s\gamma$ and $\Delta\mathcal{A}_{CP}$ at the Belle-II and the current nEDM constraint. By future nEDM experiments, even in the destructive case, the large region of ζ_d can be constrained.

7.3 Top-charm transport scenario

In this section, we discuss the top-charm transport scenario, where the FCNC coupling between the top and charm quarks is switched on. In the previous top-transport scenario, we have adopted the Pich–Tuzon for the additional Yukawa matrices ρ^f. On the contrary, in this scenario, we only consider the top-charm sector and parametrize them as

$$\rho^u = \begin{pmatrix} 0 & 0 & 0 \\ 0 & \rho_{cc} & \rho_{ct} \\ 0 & \rho_{tc} & \rho_{tt} \end{pmatrix}, \quad \rho^d = \rho^e = \mathbf{0}. \tag{7.33}$$

As we have already mentioned in section 4.1, the ρ_{tc} coupling can be sizable about $O(1)$ under the constraints from the flavor experiments.

In the following discussions, we first derive the CP violating source term for the top-charm transport scenario. We then show the impacts on the BAU of those coupling constants. We also give phenomenological discussions for flavor physics.

7.3.1 CP violating source with flavor mixing

We consider two flavor (top and charm) system $q = (c, t)^T$, where the field dependent mass matrix is given by

$$\mathcal{L}_{\rm mass} = -\overline{q_L} M q_R + \text{h.c.}, \tag{7.34}$$

$$M(z) = \frac{1}{\sqrt{2}} \begin{pmatrix} y_c\varphi_1 + \rho_{cc}(\varphi_2 - i\varphi_3) & \rho_{ct}(\varphi_2 - i\varphi_3) \\ \rho_{tc}(\varphi_2 - i\varphi_3) & y_t\varphi_1 + \rho_{tt}(\varphi_2 - i\varphi_3) \end{pmatrix}. \tag{7.35}$$

The off-diagonal elements of the matrix arise due to the non-zero VEVs $\varphi_{2,3}$ along to the wall. By the same discussions as the section 6.3, we have

$$\Big\{\omega^2 + \partial_z^2 - MM^\dagger + is(M\partial_z M^{-1})(\omega - is\partial_z)\Big\} L_s = 0. \tag{7.36}$$

In general, $M^\dagger M$ is not diagonalized, so that by using a Unitary matrix U, we take a local basis $M^\dagger M$ to be diagonalized and obtain[2]

$$\Big\{\omega^2 + \partial_z^2 - m_D^2 + 2U_1\partial_z + U_2 + isA_1(\omega - is\partial_z) + A_2\Big\} L_s^D = 0, \tag{7.37}$$

where

$$\begin{aligned} &U_1 \equiv U\partial_z U^\dagger, && A_1 \equiv U(M\partial_z M^{-1})U^\dagger, \\ &U_2 \equiv U\partial_z^2 U^\dagger, && A_2 \equiv A_1 U_1, \\ &L_s^D \equiv UL_s, && m_D^2 \equiv UMM^\dagger U^\dagger \equiv \mathrm{diag}(m_+^2, m_-^2). \end{aligned} \tag{7.38}$$

If we define 2×2 operator as

$$\Big\{\omega^2 + \partial_z^2 - m_D^2 + 2U_1\partial_z + U_2 + isA_1(\omega - is\partial_z) + A_2\Big\}_{ij} \equiv \begin{pmatrix} D_{++} & -D_{+-} \\ -D_{-+} & D_{--} \end{pmatrix}, \tag{7.39}$$

the equations can be expressed by

$$D_{--}L_-^D - D_{-+}L_+^D = 0,$$

[2]We here have defined $m_+^2 \geq m_-^2$.

$$D_{++}L_+^D - D_{+-}L_-^D = 0, \tag{7.40}$$

or

$$\begin{aligned}(D_{--}D_{++} - D_{+-}D_{-+})L_+^D + [D_{+-}, D_{--}]L_-^D = 0,\\ (D_{++}D_{--} - D_{-+}D_{+-})L_-^D + [D_{-+}, D_{++}]L_+^D = 0.\end{aligned} \tag{7.41}$$

We here have omitted the spin index s. The operators D_{+-} and D_{-+} at least include $O(\partial_z)$ parts, so that up to $O(\partial_z)$, we have

$$D_{\pm\pm}L_\pm^D = 0. \tag{7.42}$$

Therefore, up to this order, we just need to solve the Dirac equation for each flavor ($\pm$) in locally diagonalized basis.

By using the WKB ansatz in the wall frame with $(p_x, p_y) = (0, 0)$,

$$L_\pm^D = w_\pm e^{i\int p_\pm dz}, \tag{7.43}$$

we obtain

$$\Big(\omega^2 - m_\pm^2 - p_\pm^2 + ip_\pm' + 2ip_\pm\partial_z + 2ip_\pm(U_1)_{\pm\pm} + is(\omega + sp_\pm)(A_1)_{\pm\pm}\Big)w_\pm = 0, \tag{7.44}$$

We obtain the dispersion relation,

$$\omega^2 - m_\pm^2 - p_\pm^2 = \mathrm{Im}\Big(2p_\pm(U_1)_{\pm\pm} + s(\omega + sp_\pm)(A_1)_{\pm\pm}\Big), \tag{7.45}$$

and find the correspondence $\theta_\pm' = -\mathrm{Im}[(A_1)_{\pm\pm}]$ to the single flavor case. The $(U_1)_{\pm\pm}$ contributions can be absorbed into the definition of $\alpha_{\rm CP}$.

If we assume a hierarchy of the mass matrix in Eq. (7.35) as $|M_{11}|/|M_{22}| \simeq |M_{12}|/|M_{22}| \equiv \delta$, we obtain $(A_1)_{++} = (M_{22}^* M_{22}' + M_{21}^* M_{21}')\big(1 + O(\delta^2)\big)/m_+^2$, where the prime denotes a derivative of z. When $\sqrt{\varphi_2^2 + \varphi_3^2} \ll \varphi_1$, $|\rho_{cc}| \ll y_t$ and $|\rho_{ct}| \ll y_t$, this $O(\delta^2)$ correction is negligibly small: $\delta_{\max} \simeq 0.06$ with the bubble profile in the left panel of figure 7.7 and $|\rho_{cc}|, |\rho_{ct}| < 0.1$. Neglecting this correction of at most 0.4%, we obtain the source term of the heavy component as

$$\begin{aligned}\mathrm{Im}[(A_1)_{++}] = &-\frac{1}{2m_+^2}\Bigg\{(|\rho_{tc}|^2 + |\rho_{tt}|^2)(\varphi_3\varphi_2' - \varphi_2\varphi_3')\\ &\qquad + y_t|\rho_{tt}|\Big((\varphi_3\varphi_1' - \varphi_1\varphi_3')\cos\theta_{tt} + (\varphi_1\varphi_2' - \varphi_2\varphi_1')\sin\theta_{tt}\Big)\Bigg\}\\ &- \frac{1}{\varphi_1^2 + \varphi_2^2 + \varphi_3^2}(\varphi_3\varphi_2' - \varphi_2\varphi_3'),\end{aligned} \tag{7.46}$$

where,

$$m_+^2 = \frac{1}{2}\Big(y_t^2\varphi_1^2 + (|\rho_{tc}|^2 + |\rho_{tt}|^2)(\varphi_2^2 + \varphi_3^2) + 2y_t|\rho_{tt}|\varphi_1\big(\varphi_2\cos\theta_{tt} + \varphi_3\sin\theta_{tt}\big)\Big). \tag{7.47}$$

The second term of Eq. (7.46), which has no dependence of ρ_{tc} and ρ_{tt}, is stemmed from the axial vector interaction of charm and top quarks with Z boson [37]. For the transport equations, we just replace the source terms of the top quarks given in Eqs. (7.17)-(7.19) as

$$S_{lt} \to -\gamma v_w x' Q_{lt}^8 + \gamma v_w x (m_+^2)' Q_{lt}^9, \quad (l = 1, 2) \tag{7.48}$$

where $x \equiv -m_+^2 \mathrm{Im}(A_1)_{++}$. The source terms of the light fermion in the local flavor basis are proportional to $m_- \simeq 0$, so that we neglect it.

We give a comment on the CP violating source terms shown in Eqs. (7.46)-(7.48). In the limit of vanishing the top-charm mixing coupling $\rho_{tc} \to 0$, Eq. (7.48) coincides with the source terms in the top transport scenario [37, 47, 48]. The source term with top-charm mixing only depends on the absolute value of ρ_{tc} through the CP violating VEV φ_3. Therefore, the phase of ρ_{tc} does not affect the BAU up to $O(\delta^2)$, and the $|\rho_{tc}|$ dependence of the BAU vanishes with the CP conserving VEV limit $\varphi_3 \to 0$. These results have been obtained by using the WKB method in the calculation of the source term of the Boltzmann equation.

Although our analysis of evaluating the BAU is now based on the WKB method, to see the consistency we also have examined the source terms in the VEV insertion approximation (VIA) [337], which are based on the closed time path formalism. [3] As shown in appendix C, the CP violating source terms do not have any ρ_{tc} dependence for $\varphi_3 \to 0$ at the leading order in the VIA. Even if we consider the case of $\varphi_3 \neq 0$, $|\rho_{tc}|$ contributes to the CP violating source terms while the phase does not.

However, these results for the source terms are different from the previous works in Refs. [41, 43], where the source terms are calculated at leading order in the VIA. For example in Ref. [43], they have assumed that VEVs induced by the CP conserving Higgs potential are real, and the phase of ρ_{tc} generates the BAU. However, we have found that if one focuses on only one flavor in the weak basis as considered in Refs. [41, 43], the VIA source terms depend on the rotation matrices V_L or V_R in the flavor space which can be taken to be arbitrary. Namely, the phase effect of ρ_{tc} on the CP violating source terms used in those literature is unphysical.

In other words, if we consider contributions from the other flavor in the weak basis in a consistent way, we could easily see that the effect of the phase of ρ_{tc} is unphysical. For example, in Ref. [43], it seems that the authors have not included the source terms of left-handed charm quarks (second generation) defined in the weak basis.[4] If one sum up the source terms of both the top and charm quarks in the weak basis, the source terms have to coincide with the ones calculated in the mass basis in which independence of the phase of ρ_{tc} is manifest, as we discuss in appendix C. In the appendix, we have also explicitly confirmed that the source terms calculated by the WKB methods are basis independent in the leading order approximation.

7.3.2 Numerical analyses

First, we discuss SFOPT for EWBG. We assume that the bubble wall velocity is constant and set $v_w = 0.1$ in the following discussions. We neglect the curvature of the wall and define radius coordinate as z. We take input parameters which are relevant to the phase transition as $m_\Phi \equiv m_{H_2} = m_{H_3} = m_{H^\pm} = 350$ GeV, $M = 20$ GeV, $Z_2 = 0.01$, $|Z_7| = 1.0$, $\arg(Z_7) = -2.4$, $|\rho_{tt}| = 0.1$ and $\theta_{tt} = -0.2$, and we numerically obtain the bounce solutions at this benchmark point. The left panel of figure 7.7 shows the solutions. The center of the bubble $z = 0$ is defined by the spatial point maximizing $dv(z)/dz$, where $v(z) \equiv \sqrt{\sum_i \varphi_i^2(z)}$. The black solid and blue dashed lines are CP conserving VEV φ_1 and φ_2, respectively, and the red dotted line is CP violating VEV φ_3. At this benchmark point, the ratio of the VEV inside the wall $v_n \equiv v(-\infty)$ and the nucleation temperature T_n is $v_n/T_n = 2.4$ with $T_n = 84.6$ GeV, so that the sphaleron process inside the wall sufficiently decouples. The wall width L_w, which can be obtained by fitting $v(z)$ with the function $\frac{v_n}{2}\left(1 - \tanh\frac{z}{L_w}\right)$, satisfies $L_w T_n = 3.3$, so that the

[3] It has been pointed out that the VIA source terms within leading order in derivative expansion exactly vanish by performing correct resummation of 1PI self energy [338, 339].

[4] In Ref. [41], only left-handed τ leptons are considered for evaluating the source terms for the lepton flavor mixing scenario of EWBG. Therefore, the similar problem as the top-charm mixing is seen. If μ_L in the weak basis is included in the transport equations, the effect of CP violating phases in the τ-μ element of Yukawa matrix should disappear.

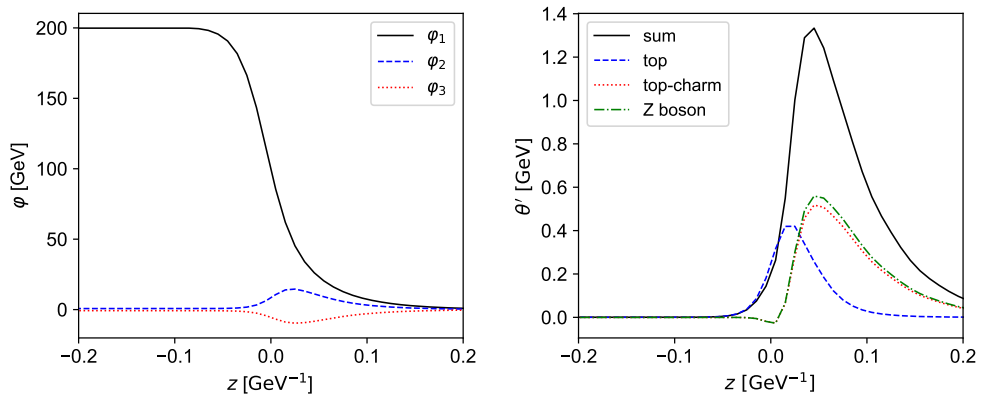

Figure 7.7: Left: Black solid and blue dashed lines are CP conserving VEVs φ_1 and φ_2 respectively, and red dotted line is CP violating VEV φ_3, as bounce solutions. Right: black solid line shows derivative of the phase θ' in the benchmark point with $|\rho_{tc}| = 1.0$ and $|\rho_{tt}| = 0.1$. Blue dashed (red dotted) and green dashdot lines are the top (top-charm) transport source and the source from chiral interaction with Z boson and top and charm quarks, respectively.

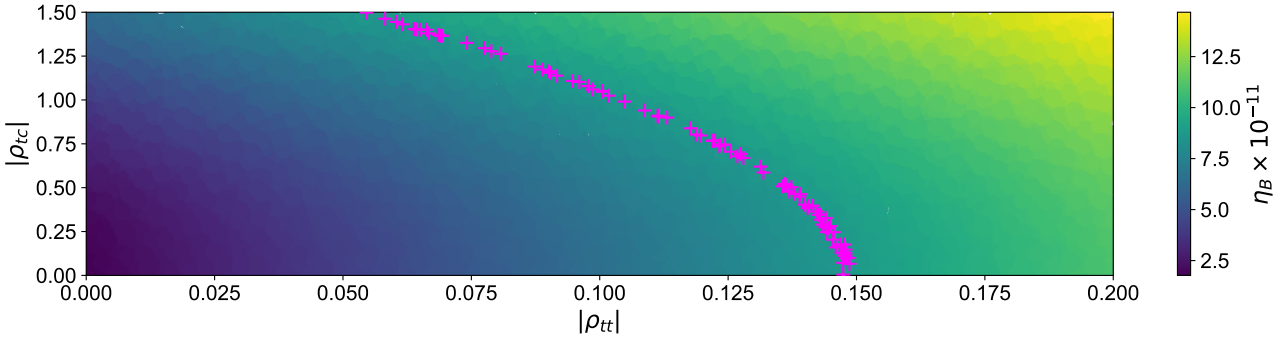

Figure 7.8: $|\rho_{tc}|$ and $|\rho_{tt}|$ dependence of baryon number density η_B with $\theta_{tt} = -0.2$. Colored points represent magnitude of η_B, and magenta points satisfy $\eta_B = (8.65{-}8.74) \times 10^{-11}$.

derivative expansion in the WKB approximation is still valid [36]. In the following analyses, we use these bubble profiles for the calculations of BAU related to the top-charm mixing couplings.

In the right panel of figure 7.7, θ' is shown as a function of z by the black solid line, when we take $|\rho_{tc}| = 1.0$, $|\rho_{tt}| = 0.1$ and use the bubble profiles shown in the left panel of figure 7.7. The blue dashed (red dotted) line is a contribution from top (top-charm) transport scenario which can be obtained by taking ρ_{tc} (ρ_{tt}) $\to 0$ in the first term in Eq. (7.46). The green dashdot line is a contribution from the second term in Eq. (7.46), which is CP violating source caused by the interaction with Z boson current and top and charm quarks [37].

Finally, we discuss baryogenesis in this scenario. The BAU parameter $\eta_B = (n_B - n_{\overline{B}})/s$, where n_B ($n_{\overline{B}}$) and s are the (anti-) baryon density and the entropy density, respectively, is invariant in the adiabatic expanding Universe. By using the source terms in Eq. (7.48) based on the relativistic semi-classical force mechanism [309], we have calculated the BAU. We have fixed the phase as $\theta_{tt} = -0.2$, and calculated η_B at many points in the $|\rho_{tc}|$-$|\rho_{tt}|$ plane. The result is shown in figure 7.8. The color in the figure corresponds to the magnitude of the BAU, and the magenta points satisfy the observed value $\eta_B = (8.65{-}8.74) \times 10^{-11}$. In figure 7.8, the impact of $|\rho_{tc}|$ to the BAU is shown. It is seen that regions of large $|\rho_{tt}|$ and $|\rho_{tc}|$ generate large BAU. Even in a small $|\rho_{tt}|$, the non-zero effect of the top-charm mixing coupling $|\rho_{tc}|$ gives a sufficient BAU by picking up the contributions from the CP violating VEV $\varphi_2'\varphi_3 - \varphi_2\varphi_3'$.

7.3.3 Phenomenological discussions

In this subsection, we discuss specific phenomenological predictions in our scenario of EWBG with the top-charm mixing.

In general, the top-charm mixing couplings give significant contributions of K meson processes via the loop induced penguin or box diagrams. In our model, we consider rare decay processes $K_L \to \pi^0\nu\overline{\nu}$ and $K^+ \to \pi^+\nu\overline{\nu}$ which are sensitive to additional Yukawa couplings. These processes are produced by four fermi operators which are induced by penguin diagrams involving the charged scalar bosons [340, 341].

The observed branching fraction of $K^+ \to \pi^+\nu\overline{\nu}$ is given from the data collected from 2016 to 2019 in NA62 experiment at the CERN SPS as [342]

$$\mathcal{B}(K^+ \to \pi^+\nu\overline{\nu})_{\rm EXP} = (10.6^{+4.0}_{-3.4} \pm 0.9) \times 10^{-11}, \tag{7.49}$$

where the first and second uncertainties are statistical and systematical errors, respectively. $O(10)\%$ accuracy is expected by the end of NA62 experiments with the data collected from 2021 [343].

For the process $K_L \to \pi^0\nu\overline{\nu}$, KOTO experiment at J-PARK gives an upper bound on this branching fraction as [344]

$$\mathcal{B}(K_L \to \pi^0\nu\overline{\nu})_{\rm EXP} < 3.0 \times 10^{-9}, \tag{7.50}$$

at 90% C.L. This upper limit is greater than the Grossman–Nir bound [345]. It is expected that KOTO step-2, which is an extended version of KOTO expected to be launched from 2029 in the earliest scenario, achieves the accuracy predicted by SM and observes the events with 4.2σ significance [346].

We define quantities relevant to these processes [341].

$$\Delta\mathcal{R}^+_\nu \equiv \mathcal{R}^+_\nu - 1, \quad \Delta\mathcal{R}^0_\nu \equiv \mathcal{R}^0_\nu - 1, \tag{7.51}$$

where,

$$\mathcal{R}^+_\nu = \frac{\mathcal{B}(K^+ \to \pi^+\nu\overline{\nu})}{\mathcal{B}(K^+ \to \pi^+\nu\overline{\nu})_{\rm SM}}, \quad \mathcal{R}^0_\nu = \frac{\mathcal{B}(K_L \to \pi^0\nu\overline{\nu})}{\mathcal{B}(K_L \to \pi^0\nu\overline{\nu})_{\rm SM}}. \tag{7.52}$$

SM predictions of these processes in our input parameters are $\mathcal{B}(K^+ \to \pi^+\nu\overline{\nu})_{\rm SM} = 9.3 \times 10^{-11}$ and $\mathcal{B}(K_L \to \pi^0\nu\overline{\nu})_{\rm SM} = 3.1 \times 10^{-11}$, and these are consistent with the ones shown in Ref. [347] within 1σ.

The additional Yukawa couplings in our model also affect the direct CP violation ϵ'/ϵ in $K_L \to 2\pi$ process [340]. The observed value is given by $(\epsilon'/\epsilon)_{\rm EXP} = (16.6 \pm 2.3) \times 10^{-4}$ [348–350]. Lattice results give the SM prediction as $(\epsilon'/\epsilon)_{\rm SM} = (21.7 \pm 8.4) \times 10^{-4}$ [341, 351, 352], while a result of chiral perturbation gives $(\epsilon'/\epsilon)_{\rm SM} = (14 \pm 5) \times 10^{-4}$ [353].

Relevant parameters about the BAU are $|\rho_{tt}|$, $|\rho_{tc}|$, and θ_{tt}. In addition to the input parameters of figure 7.8, we take a benchmark point about the other Yukawa parameters for the K meson observables as$|\rho_{cc}| = 0.09, |\rho_{ct}| = 0.05, \theta_{cc} = 0, \theta_{ct} = -2.8, \theta_{tc} = -0.2, |\rho_{bb}| = 1.0 \times 10^{-3}$ and $\theta_{bb} = 1.5$.

In figure 7.9, the green and gray regions are excluded by the data of $B_s \to \mu\mu$ and $|\epsilon_K|$, respectively. The other flavor constraints are out of this figure, and we have confirmed $|\rho_{tc}| \gtrsim 1.5$ is excluded by the data of B^0-$\overline{B^0}$ mixing. As shown in figure 7.9, $B_s \to \mu\mu$ constrains $\rho_{tt} \gtrsim 0.16$. Since $B_s \to \mu\mu$ process mainly depends on $\rho_{ct}\rho_{tt}$ in our setup, this process only sets the upper bound on $|\rho_{tt}|$. On the other hand, $|\epsilon_K|$ constrains the lower region of $|\rho_{tc}|$ in this benchmark point, and $|\rho_{tc}| \lesssim 0.25$ is excluded with $|\rho_{tt}| \simeq 0.1$. This behavior of $|\epsilon_K|$ constraint in $|\rho_{tc}|$-$|\rho_{tt}|$ plane changes with other values of ρ_{cc} and ρ_{ct}. In figure 7.9, predictions of $\Delta\mathcal{R}^+_\nu \times 10^2$ (blue

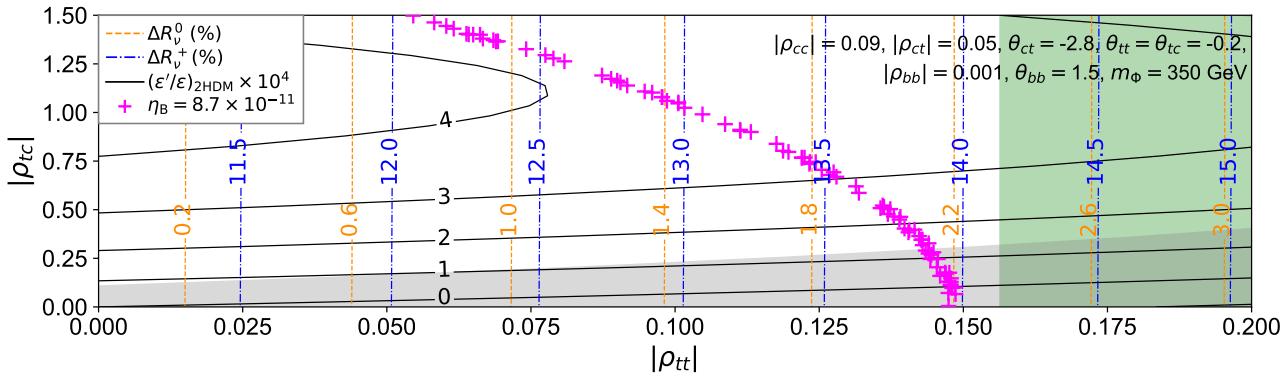

Figure 7.9: Constraints from flavor experiments and predictions on K meson rare decays. Green and gray regions are excluded regions by the data of $B_s \to \mu\mu$ and ϵ_K, respectively. Blue dotted dash and orange dashed lines correspond to $\Delta\mathcal{R}^+_\nu \times 10^2$ and $\Delta\mathcal{R}^0_\nu \times 10^2$, respectively, which are defined in the text. Black solid lines are the contour of $(\epsilon'/\epsilon)_{\rm 2HDM} \times 10^4$. Magenta points are the same as shown in figure 7.8 and satisfy $\eta_B = (8.65\text{–}8.74) \times 10^{-11}$.

dotted dash) and $\Delta\mathcal{R}^0_\nu \times 10^2$ (orange dash) at the benchmark point are shown. The new physics contribution of the direct CP violation $(\epsilon'/\epsilon)_{\rm 2HDM} \times 10^4$ (black solid) is also shown in figure 7.9. We have used formulae shown in Ref. [340] to calculate these processes. The magenta points are the same as shown in figure 7.8, corresponding to the observed baryon asymmetry. The processes $K_L \to \pi^0\nu\overline{\nu}$ and $K^+ \to \pi^+\nu\overline{\nu}$ mainly depend on $\rho_{ct}\rho_{tt}$ [340], so that only $|\rho_{tt}|$ changes the values in figure 7.9. At the point $|\rho_{tt}| \simeq 0.15$, predicted deviations from SM branching fractions of $K_L \to \pi^0\nu\overline{\nu}$ and $K^+ \to \pi^+\nu\overline{\nu}$ are $\Delta\mathcal{R}^0_\nu \simeq 2.2\%$ and $\Delta\mathcal{R}^+_\nu \simeq 14\%$, respectively. Therefore, the branching fractions are greater than the SM predictions at this point. On the other hand, for $|\rho_{tt}| \simeq 0.05$, they are about 0.8% and 12%, respectively. The direct CP violation $(\epsilon'/\epsilon)_{\rm 2HDM}$ depends not only on $\rho_{ct}\rho_{tt}$ but also on $\rho_{tc}\rho_{cc}$, so that it changes along $|\rho_{tc}|$ axis. In the region where the observed BAU can be explained under the experimental constraints, allowed maximal value of $|\rho_{tt}|$ predicts $(\epsilon'/\epsilon)_{\rm 2HDM} \simeq 1 \times 10^{-4}$, while it is about 4×10^{-4} for $|\rho_{tt}| \simeq 0.05$. We note that if we set ρ_{ct} and ρ_{cc} to be 0 in figure 7.9, only $|\rho_{tc}| \gtrsim 0.8$ is excluded by $B \to X_s\gamma$ constraint, almost without depending on $|\rho_{tt}|$. In this case, $\Delta\mathcal{R}^0_\nu$ and $\Delta\mathcal{R}^+_\nu$ are small and less than 1%.

7.4 Discussions and summary

In this section, we give some discussions about the results shown in the previous sections.

7.4.1 Discussions for top transport scenario

As shown in figure 7.4, successful EWBG can be realized by the masses of the heavy Higgs bosons becoming around 300-400 GeV. In this mass region, $|\zeta_u|$ is constrained from above by $H_{2,3} \to \tau\tau$ and $H^\pm \to tb$ searches as shown in figure 4.1. Thus our model can be tested by the direct search of the heavy Higgs bosons at the HL-LHC. If the additional scalar masses are smaller than about 300 GeV, the multi lepton search at the HL-LHC might be used to test our model [178]. In the analyses, we have assumed the alignment condition $\alpha_i = 0$ to avoid the mixing among the neutral scalar states. If this alignment condition is slightly broken, decay branching ratios of the additional Higgs bosons, the vacuum stability, and the perturbative unitarity condition are changed. As a result, the testability of the model at the HL-LHC and the future upgraded ILC can be much enhanced [185, 354, 355].

The effect of the heavy Higgs bosons appears in the flavor physics, so that the future flavor experiments such as Belle-II [335] or LHCb [356] can be used to test the model. As shown in figure 4.1 and figure 7.6, observables of $B \to X_s\gamma$, $B_s \to \mu\mu$ and $\Delta\mathcal{A}_{\rm CP}$ have some sensitivities about the quantum loop effect of the heavy Higgs bosons or the CP violation in the model.

CP violation in the Higgs potential can be detected by the ILC and the measurements of the EDM. As we have mentioned in section 7.2, both the upper bounds of the nEDM and the ACMEII bound for the eEDM in future experiments have about an order higher accuracy than the current bounds [282, 336]. Therefore, for example, by the future ACME experiment [282], we can exclude many points in figure 7.3. In the case of $|\zeta_e| \gg |\zeta_u|$ and $\theta_e = \mathcal{O}(1)$, the CP-violating phase of ζ_e in the model would be decided at the ILC by the measurement of the azimuthal angular distribution where a tau pair from decay of the additional neutral bosons decays into hadrons [357, 358].

In section 7.2, we have discussed the triple Higgs coupling, the GWs, and $H_1 \to \gamma\gamma$ as a probe of SFOPTs. The triple Higgs coupling in our model is measured by the process of di-Higgs production at future colliders [24, 224–233]. At the HL- LHC and the ILC with $\sqrt{s} = 500$ GeV (1 TeV), this coupling is expected to be measured at the 50% [21] and 27% (10 %) [24, 25] accuracy, respectively. BP1 and BP2 in figure 7.4 and Table 7.1, $\Delta R = 41\%$ and 66%, respectively, so that the SFOPT in these benchmark points can be tested at these future colliders.

In Table 7.1, we have shown the branching ratio of $H_1 \to \gamma\gamma$ in the benchmark points. In future collider experiments, the measurement of the Higgs di-photon decay would become more precise. For example in the HL-LHC, the relative uncertainty of the branching ratio of $H_1 \to \gamma\gamma$ is expected to be 2.6% [21]. Therefore, our model can also be tested via the precise measurement of the Higgs di-photon decay.

We have shown the GW spectra at some benchmark points in figure 7.5, while these do not reach the sensitivity curve of LISA. Nevertheless, we expect that these GW spectra can be detected at LISA by using the Fisher matrix analysis discussed in Ref. [359]. The possibilities of detection of the GWs at DECIGO and BBO are also expected to be enhanced by using this analysis. We can obtain a GW spectrum which has a larger height of the peak by making the phase transition stronger, however in such a case, the WKB approximation for the BAU is no longer valid because of decreasing $L_w T_n$.

7.4.2 Discussions for top-charm transport scenario

In section 7.3, we have calculated the source term in the WKB approximation for the top-charm mixing EWBG. From Eq. (7.46) it has been shown that phases of off-diagonal elements of additional Yukawa matrices do not contribute to the source terms up to $O(\delta^2)$. The contributions to the source terms from the top-charm Yukawa couplings are proportional to the square of the absolute values of ρ_{tc} through the CP violating VEV φ_3. On the other hand, in the previous work for flavor mixing EWBG studied in Refs. [41, 43], the phases of the off-diagonal complex couplings, e.g. $\rho_{\tau\mu}$ or ρ_{tc}, play an important role in the source terms evaluated in the VIA method even considering real VEVs. However, we note that this discrepancy does not come from the difference between WKB and VIA methods [309, 360]. As we show in appendix C, the CP violating source terms calculated at leading order in the VIA in the mass basis do not depend on ρ_{tc} in the CP conserving limit ($\varphi_3 \to 0$). Furthermore, in appendix C, we also show that the VIA source terms are basis independent. Namely, the source terms calculated in the weak basis coincide with those in the mass basis. From these considerations, we would conclude that in Refs. [41, 43] the transport equations defined in the mass basis are considered, but in which the source terms evaluated in the weak basis are used. Therefore, there would be a mismatch in the transport equations, and the phase effects of the off-diagonal Yukawa

couplings discussed in Refs. [41, 43] may be unphysical.

In figure 7.8, at the points $(|\rho_{tt}|, |\rho_{tc}|) = (0, 0)$ and $(0.2, 1.5)$, we have obtained $\eta_B \simeq 1.8 \times 10^{-11}$ and 1.5×10^{-10}, respectively. At the former point, only the CP violating VEV φ_3 which is induced by a complex coupling λ_7 in the general 2HDM with the Higgs alignment [47,48] produces the BAU. On the other hand, at the latter one, ρ_{tc} and ρ_{tt} also contribute to the BAU. The magnitude depends on θ_{tt}, and the maximal BAU $\eta_B \simeq 2.8 \times 10^{-10}$ at the point is given by $\theta_{tt} \simeq 1.0$ with the other fixed input parameters. In this case, magenta points will be shifted to left from figure 7.8, and for example, $(|\rho_{tt}|, |\rho_{tc}|) \simeq (0.06, 0)$ and $(0.025, 1.5)$ satisfy the observed BAU. We note that some θ_{tt} at the point give negative η_B.

The rare decay processes of K meson, $K^+ \to \pi^+ \nu\overline{\nu}$ and $K_L \to \pi^0 \nu\overline{\nu}$, are sensitive to $\rho_{tt}\rho_{ct}$, and we have considered a non-zero ρ_{ct} coupling in figure 7.9. In this benchmark point, the branching fraction of $K^+ \to \pi^+ \nu\overline{\nu}$ is up to about 14% larger than the SM value. This is consistent with the current experimental value in Eq. (7.49) within 1σ level. At the future NA62 experiment, about 10% precision is expected [343], so that this benchmark point would be tested. In our benchmark points, $K_L \to \pi^0 \nu\overline{\nu}$ process, which KOTO step-2 [346] experiment aims to measure, is about up to 2.2% larger than the SM value. If these excesses in the K^+ and K_L rare decays are detected in the future experiments, we can confirm non-zero $\rho_{tt}\rho_{ct}$, and then it is expected that the scenario of top transport EWBG with ρ_{tt} is realized in our model. In addition, if we observe these observables with about 1% experimental uncertainties, we can know from the magenta points in figure 7.9 how $|\rho_{tc}|$ coupling affects the BAU. However, we note that these branching fractions vary in ρ_{ct}. In order to know the effect of $|\rho_{tc}|$ to the BAU with arbitrary ρ_{ct}, ϵ_K and ϵ'/ϵ which contain ρ_{tc} dependence become important observables. These results motivate us to improve the accuracies of theoretical predictions and experimental observations about K meson physics.

The upper bound on $|\rho_{tt}|$ is given by the data of $B_s \to \mu\mu$ in figure 7.9. The expected total uncertainty of this process at the LHCb [356] is 4.4% with the integrated luminosity of 300 fb^{-1} [361]. Also, from our benchmark point if we take $\rho_{ct} = 0$ without changing other parameters, the upper bound on $|\rho_{tc}|$ is given by the data of $B \to X_s\gamma$. The relative uncertainty of this measurement is expected to be reduced about 3.2% at the Belle-II [335] with 50 ab^{-1}. Therefore, B meson physics is equivalently important as K meson physics for testing our scenario.

The off-diagonal ρ_{tc} coupling predicts some interesting signals at future high energy collider experiments. In our benchmark point where the heavy neutral scalar bosons are degenerated, even at the HL-LHC it is difficult to measure the processes of $gc \to tH_{2,3} \to tt\overline{c}$ due to the interference effect. It is known that if the neutral scalar bosons have a mass difference as $m_{H_2} - m_{H_3} = 30$ GeV, the interference effect enhances such processes [208, 211]. In the case that only H_3 has the mass of 350 GeV while H_2 is much heavier, $\rho_{tc} \gtrsim 0.2$ will be excluded at 2σ level by the same-sign top search at the HL-LHC [208, 362]. On the other hand, triple top production processes $gc \to tH_{2,3} \to tt\bar{t}$ are not disturbed by that interference, so that we may be able to detect the signals even in the case of $m_{H_2} = m_{H_3}$ [213]. About the charged scalar production induced by ρ_{tc}, the process of $pp \to H^\pm \to bc$ has a sensitivity for the large ρ_{tc} coupling [218]. In addition, signatures of $cg \to H^+ b \to bt\bar{b}$ may also be tested at the HL-LHC [208, 363, 364].

In the top-charm transport scenario, we have assumed $v_w = 0.1$. It is known that large wall velocity enhances possibilities to observe GWs produced by first order phase transition [58, 60, 61, 359, 365] at LISA, DECIGO and BBO. On the other side, the BAU decreases as the velocity approaches the speed of light [309]. For example, if we set the velocity to 0.45, the BAU decreases, and all the magenta points shown in figs. 7.8 and 7.9 move to the right. In this case, some points constrained by the data of $B_s \to \mu\mu$ and $|\epsilon_K|$, but the other points, e.g. $(|\rho_{tt}|, |\rho_{tc}|) = (0.15, 0.8)$, satisfy $\eta_B = 8.65{-}8.74 \times 10^{-11}$ under the experimental constraints.

The shape of GW spectra predicted at these points is similar to the ones in the top transport scenario, and we have obtained the energy density of GW at the peak point as $h^2\Omega_{\rm GW}(f_{\rm peak}) = 6 \times 10^{-14}$ with $f_{\rm peak} = 0.14$ Hz. This point is above the peak integrated sensitivity curves of DECIGO and BBO shown in Ref. [56], so that the points are testable by the future GWs observations.

In this scenario, we have neglected $(1,1)$ components of the 3×3 matrices ρ^u and ρ^d, which are relevant parameters to the nEDM. The CP violating phases of the top-charm mixing couplings can contribute to the nEDM through the Weinberg operator induced by the charm chromo EDM [366]. Although these phases are not directly connected with the BAU, some parameter regions may be constrained by the current nEDM bound [284]. In this analysis, we have set $\rho^e = 0$. If we consider ρ^e to be a non-zero 3×3 matrix, especially its $(1,1)$ component of ρ_{ee}, the eEDM becomes sensitive to the CP violation in our model. Clearly, if accuracies are substantially improved at future EDM experiments [282, 367], wider parameter regions can be explored.

7.4.3 Short summary of chapter 7

In this chapter, we have discussed EWBG in the 2HDM. We have first reviewed the mechanism of EWBG and derived the transport equations based on the semi-classical force mechanism. We also have explained the EDMs as a consequence of the CP violation in the model. We have discussed the two transport scenarios depending on the additional Yukawa matrices in the 2HDM. We first have discussed the top-transport scenario, and shown the viable parameter spaces under the current experimental data. We have discussed how we can test these benchmark scenarios at future collider experiments, various flavor experiments and gravitational wave observations. In particular, the model can be tested by the di-photon decay of the Higgs boson and the triple Higgs boson coupling due to the non-decoupling effect which causes SFOPT. We then have investigated the top-charm transport scenario with the quark flavor mixing. We have derived the CP violating source term for this scenario, and found that CP violating phases of the off-diagonal element in the source term in the Boltzmann equation are eliminated by the rephasing. This result is somewhat different from previous works on electroweak baryogenesis by flavor off-diagonal Yukawa couplings. Instead, we have found that the absolute value of the top-charm off-diagonal element enhances CP violating phases in the Higgs potential, by which a sufficient amount of the baryon number can be generated to explain the observed baryon asymmetry of the Universe. Finally we have discussed characteristic predictions in Kaon rare decays for this scenario, $K^+ \to \pi^+ \nu\overline{\nu}$ and $K_L \to \pi^0 \nu\overline{\nu}$.

Chapter 8

Loop induced $H^{\pm}W^{\mp}Z$ vertices as a probe of CP violation

In this chapter, we discuss loop induced $H^{\pm}W^{\mp}Z$ vertices in the general 2HDM with the CP violation. As we have discussed in chapter 7, the 2HDM is motivated by EWBG, and new sources of the CP violation can generate the observed BAU. As a consequence of the CP violation, there are some observables which would be measured by future experiments, such as the EDMs. We introduce the $H^{\pm}W^{\mp}Z$ vertices for measuring the CP violation at high energy experiments.

The custodial symmetry is important to classify extended Higgs models, because violation of it affects the mass relation between the W and Z boson, i.e. the ρ parameter. In the 2HDM, loop corrections from custodial symmetry violation shift the ρ parameter from unity. This deviation is parametrized by the T parameter, defined by $\alpha_{\rm em}T = \rho - 1$. If the scalar potential respects the custodial symmetry, the correction from the 2HDM is zero.

In addition to this ρ parameter, the $H^{\pm}W^{\mp}Z$ vertices have also been known as a consequence of the violation of the custodial symmetry. These vertices are absent at the tree level [84]. However, it can be induced by loop effects [85]. These $H^{\pm}W^{\mp}Z$ vertices have been analyzed in the context of the CP conserving 2HDM [85, 354, 368–372], the Minimal Supersymmetric Standard Model (MSSM) [368, 373, 374], and the CP violating MSSM [371, 375]. In general, such a one loop induced vertex is suppressed by the factor $1/16\pi^2$, so that one might expect that effects from these vertices are small. In the 2HDM, however, it has been pointed out that these vertices can be enhanced by non-decoupling quantum effects of particles in the loop [369]. Besides the 2HDM, the feature of the $H^{\pm}W^{\mp}Z$ vertices have been studied in the models with $\mathrm{SU}(2)_L$ triplets [84, 115, 116, 376, 377], the three Higgs doublet model [378], and the model with one colored scalar boson [379]. Through these vertices, at high energy colliders, the charged scalar bosons can be produced, and they can decay into the W and Z bosons. Phenomenological impacts of these vertices at the collider experiments have been discussed in Refs. [380–393]. From the current ATLAS [179] and CMS [180] data related to the $H^{\pm}W^{\mp}Z$ vertices, some of the models, e.g., the Georgi–Machacek model [376, 377], have been already constrained.

As we have already discussed in section 4.1, the CP violating scalar potential also violates the custodial symmetry. Therefore, we expect the $H^{\pm}W^{\mp}Z$ vertices from the CP violating effects in the model. In the following sections, we first give a tree-level discussion for the $H^{\pm}W^{\mp}Z$ vertices. We also mention the relation to the ρ parameter. We then discuss the loop induced $H^{\pm}W^{\mp}Z$ vertices in the 2HDM. We calculate the $H^{\pm}W^{\mp}Z$ vertices at the one-loop level, and we confirm that there are two contributions from the CP conserving and CP violating coupling constants. We show the relation between these vertices and the violation of the custodial and CP symmetry. We discuss the decays $H^{\pm} \to W^{\pm}Z$ via these vertices. We find that these decays are significantly enhanced by the loop effects of the additional scalar bosons. Finally, we find

that an asymmetry between the decay rates of $H^+ \to W^+Z$ and $H^- \to W^-Z$ can be a useful observable to see the CP violating phases in the model. We also give a short discussion on the testability of these vertices at current and future high energy collider experiments.

8.1 The tree level $H^\pm W^\mp Z$ vertices and the ρ parameter

According to Refs. [84, 146], we explain the tree-level $H^\pm W^\mp Z$ vertex and the ρ parameter in a scalar gauge theory.

We consider models of multi scalars with arbitrary representations of $\mathrm{SU}(2)_L \times \mathrm{U}(1)_Y$, which is given by

$$\mathcal{L} = \sum_k (D_\mu \phi_k)^\dagger D^\mu \phi_k + \frac{1}{2}\sum_i (D_\mu \eta_i)^T D^\mu \eta_i, \tag{8.1}$$

where ϕ_k are $\mathrm{SU}(2)_L$ complex representation with the hypercharge Y, and η_i are $\mathrm{SU}(2)_L$ real representation with $Y = 0$. The covariant derivative is given by

$$D_\mu = \partial_\mu - igW_\mu^a T^a - ig' Y B_\mu. \tag{8.2}$$

First, as we have discussed in section 2.5, the ρ parameter is given by

$$\rho \equiv \frac{m_W^2}{m_Z^2 \cos^2\theta_W} = \frac{\sum_k \Big(T_k(T_k+1) - Y_k^2\Big)|v_k|^2 + \frac{1}{2}\sum_i T_i(T_i+1)|u_i|^2}{\sum_k 2Y_k^2 |v_k|^2}, \tag{8.3}$$

where T is given by the eigenvalue of $\boldsymbol{T}^2 = T^a T^a$ and v_k and u_i are the VEV of the neutral component of ϕ_k and η_i, respectively. From this equation, when η_i has a VEV, ρ must be deviated from 1. The condition for $\rho = 1$ with the arbitrary VEV is

$$\sum_k \Big(T_k(T_k+1) - 3Y_k^2\Big)|v_k|^2 + \frac{1}{2}\sum_i T_i(T_i+1)|u_i|^2 = 0. \tag{8.4}$$

Suppose a model with multi doublet fields with $Y = 1/2$ (N Higgs doublet model), and we get $\rho = 1$. A model with one $Y = 1$ triplet and one $Y = 0$ triplet (the Georgi–Machacek model [376, 377]), up to $v_k = u_i$, results $\rho = 1$.

Second, the vertex among a negatively charged scalar, the W boson and the Z boson is obtained by the kinetic term shown above, and we have

$$\begin{aligned}\mathcal{L}_{\phi^- W^+ Z} = \frac{g^2}{\sqrt{2}c_W} W_\mu^+ Z^\mu \Bigg\{ c_W^2 \Big(\sum_k \big(\phi_k^\dagger T_k^+ v_k - (T_k^- v_k)^\dagger \phi_k\big) + \sum_i \eta_i^T T_i^+ u_i \Big) \\ - \sum_k 2Y_k \Big(\phi_k^\dagger T_k^+ v_k + (T_k^- v_k)^\dagger \phi_k \Big) \Bigg\},\end{aligned} \tag{8.5}$$

where $T^\pm = T^1 \pm iT^2$, which are raising and lowering operators for $\mathfrak{su}(2)$ algebra. Here we have treated the VEVs as the vector which satisfies $Qv_k = Qu_i = 0$. We note that $QT_k^+ v_k = +T_k^+ v_k$ and $QT_k^- v_k = -T_k^- v_k$ are shown, so that non-zero terms of ϕ_k and η_i contain electromagnetically negative singly charged scalars. Without loss of generality, we can choose $Y_k \geq 0$, so that $T_k^+ v_k \neq 0$. In this formula, the charged NG boson is included.

The NG boson can be identified by seeing the $W\partial G$ mixing term, which will be absorbed into the gauge fixing term. The charged NG boson is given by the combination of those fields as

$$G^- = \frac{g}{\sqrt{2}m_W} \Bigg\{ \sum_k \Big(\phi_k^\dagger T_k^+ v_k - (T_k^- v_k)^\dagger \phi_k \Big) + \sum_i \eta_i^T T_i^+ u_i \Bigg\}. \tag{8.6}$$

We here have explicitly shown the real representations, but we can extend the definition of ϕ_k in the way of $\phi_{\tilde{k}}$ for $\{\tilde{k}\} = \{k\} \oplus \{i\}$. Concretely, we can write

$$\eta^T T^+ u = \frac{1}{2}\Big(\eta^T T^+ u + u^T (T^+)^T \eta\Big) = \frac{1}{2}\Big(\eta^T T^+ u - u^T T^+ \eta\Big), \tag{8.7}$$

because of $(T^a)^* = -T^a$ for the real representation. The G^- state is normalized to be unit, so that we can show $G^\pm \cdot G^\pm = 1$.

We can rewrite the above formula for the vertex as

$$\mathcal{L}_{\phi^- W^+ Z} = \frac{g^2}{\sqrt{2} c_W} W^+_\mu Z^\mu \Big\{ c_W^2 \frac{\sqrt{2} m_W}{g} G^- - \sum_k 2 Y_k \Big(\phi_k^\dagger T_k^+ v_k + (T_k^- v_k)^\dagger \phi_k \Big) \Big\}. \tag{8.8}$$

We may derive the conditions for the non-zero tree level $H^\pm W^\mp Z$ vertex. There are two possible conditions for vanishing this vertex: Models contain

- no $Y \neq 0$ representations ϕ_k getting non-zero VEVs.
- only $Y \neq 0$ representations ϕ_k getting non-zero VEVs, such that Y_k are all same and they satisfy $T_k^- v_k = 0$.

When we prepare representations with different hypercharge, the vertex exists even if $T_k^- v_k = 0$. For example, in model with $\phi_1 \sim (T^3, Y) = (1/2, 1/2)$ and $\phi_2 \sim (1, 1)$ representations, we can check $T^- v_1 = T^- v_2 = 0$, but we have the $H^\pm W^\mp Z$ vertex.

By defining the physical charged scalar bosons which are orthogonal to the NG boson, we obtain

$$\mathcal{L}_{H^- W^+ Z} = -g m_Z \xi H^- W^+_\mu Z^\mu, \tag{8.9}$$

where

$$|\xi|^2 = \frac{g^2}{m_W^2} \Big\{ \sum_k 4 Y_k^2 \big(T_k(T_k+1) - Y_k^2 \big) |v_k|^2 \Big\} - \frac{1}{\rho^2}. \tag{8.10}$$

We note the W boson mass is given by

$$m_W^2 = g^2 \Big(\sum_k \Big(T_k(T_k+1) - Y_k^2 \Big) |v_k|^2 + \frac{1}{2} \sum_i T_i(T_i+1) |u_i|^2 \Big), \tag{8.11}$$

Up to now, the discussion is general for any number of representations, and we can find the relation between the ρ parameter and the $H^\pm W^\mp Z$ vertex by seeing these equations.

Third, we see several examples. In models with the SM Higgs $(1/2, 1/2)$ plus

$$\begin{aligned}
&\phi_1 \sim (1/2, 1/2) \to \rho = 1, \xi = 0, \\
&\eta_1 \sim (1, 0) \to \rho \neq 1, \xi = 0, \\
&\phi_1 \text{ satisfying } T(T+1) - 3Y^2 = 0 \to \rho = 1, \xi \neq 0, \\
&\phi_1 \sim (1, Y) \to \rho \neq 1, \xi \neq 0.
\end{aligned} \tag{8.12}$$

These examples are the two scalar models. When we consider a three or more scalars model, e.g. the GM model, $\rho = 1$ can be satisfied, and $\xi \neq 0$.

Finally, in the 2HDM which we are now focusing on, $\xi = 0$ and $\rho = 1$ are clearly shown. This feature will be changed by quantum corrections [85]. As we have introduced in sections 2.5 and 4.1, the custodial symmetry for the two scalar doublets can be defined. When the custodial symmetry (see Eq. (4.29)) is preserved in the potential, the leading loop correction to the ρ

parameter from the 2HDM vanishes: $\Delta T = 0$ is explicitly shown by Eq. (4.29) at the one-loop level. As we see in the following sections, when the potential respects the custodial symmetry, the $H^\pm W^\mp Z$ vertices induced by the potential terms are also zero [1]. When the custodial symmetry is violated by the potential, ΔT could be non-zero, and the $H^\pm W^\mp Z$ vertices could be induced. From the relation between the CP violation and the custodial symmetry violation, we can expect that the $H^\pm W^\mp Z$ vertices are induced by the CP violating effects. Actually, it has been known that the CP violating effects in the potential induce non-zero ΔT, e.g. with $\mathcal{R}_{11} \simeq \mathcal{R}_{12} \simeq \mathcal{R}_{13} \simeq 3/\sqrt{3}$, which corresponds to $\mathrm{Im}[Z_6^2] \neq 0$ [152]. In the following discussions, we will see there are CP violating contributions to the $H^\pm W^\mp Z$ vertices.

8.2 Loop induced $H^\pm W^\mp Z$ vertices

We define the $H^\pm W^\mp Z$ vertices as

$m_W g V^\pm_{\mu\nu} =$ 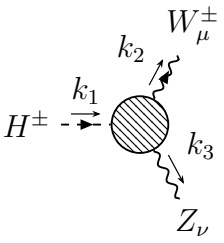

, (8.13)

where k_1 (k_2 and k_3) is the incoming (outgoing) momentum. Subsequently, $V^\pm_{\mu\nu}$ can be decomposed by

$$V^\pm_{\mu\nu} = F_\pm g_{\mu\nu} + \frac{G_\pm}{m_W^2} k_\mu^3 k_\nu^2 + \frac{H_\pm}{m_W^2} \epsilon_{\mu\nu\rho\sigma} k_3^\rho k_2^\sigma, \tag{8.14}$$

where $\epsilon_{\mu\nu\rho\sigma}$ ($\epsilon_{0123} = 1$) is the completely antisymmetric tensor and the external W and Z bosons satisfy the on-shell conditions for $\partial_\mu W^\mu = 0$ and $\partial_\mu Z^\mu = 0$, respectively. We distinguish $V^+_{\mu\nu}$ and $V^-_{\mu\nu}$ for the discussion of the CP violation. These vertices come from the following effective operators,

$$\mathrm{Tr}[\sigma_3 (D_\mu \mathbb{M}_1)^\dagger (D^\mu \mathbb{M}_2)], \quad \mathrm{Tr}[\sigma_3 \mathbb{M}_1^\dagger \mathbb{M}_2 F_Z^{\mu\nu} F^W_{\mu\nu}], \quad i\epsilon_{\mu\nu\rho\sigma} \mathrm{Tr}[\sigma_3 \mathbb{M}_1^\dagger \mathbb{M}_2 F_Z^{\mu\nu} F^W_{\rho\sigma}], \tag{8.15}$$

and the hermitian conjugate of them, where $F_W^{\mu\nu}$ and $F_Z^{\mu\nu}$ are the field tensors of the W and Z bosons, respectively. All of these operators violate the custodial $\mathrm{SU}(2)_V$ symmetry. In the 2HDM, these effective operators do not exist at the tree level, however, when the Lagrangian violates the custodial symmetry, these are induced by the loop effects. Especially, the first operator in Eq. (8.15), which corresponds to the $F_\pm$ term in Eq. (8.14), is the dimension-four operator, so that non-decoupling quantum effects of the additional scalar bosons are enhanced [369]. On the other hand, the second and third operators, which are dimension-six, are suppressed by the quadratic scale of the heavy particles. Therefore, the $F_\pm$ term contribution is important to discuss the quantum effects of the additional heavy scalar bosons. We note that the third operator also breaks the parity symmetry which is conserved in the bosonic sector, so that only the fermion-loop contributions cause non-zero $H_\pm$.

Although it has also been known that the $H^\pm W^\mp \gamma$ vertices are generated at the loop level in the 2HDM [368, 370, 394–398], due to the Ward–Takahashi identity $p_\gamma^\mu V_{\mu\nu} = 0$, the $F_\pm$ term must vanish. In this sense, a large enhancement by the heavy scalar bosons cannot be expected,

[1] We note, the Yukawa and $\mathrm{U}(1)_Y$ interactions violate the custodial symmetry, so that corresponding corrections appear in both of them.

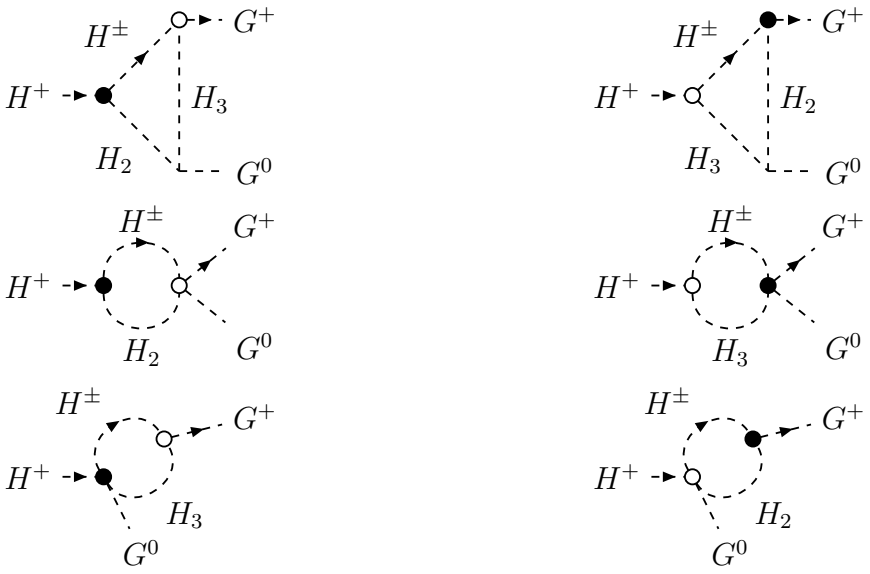

Figure 8.1: The scalar contributions of the decay $H^+ \to G^+G^0$ under the condition $Z_6 = 0$. The white (black) dots express the interaction which violates the (twisted) custodial symmetry.

compared with the $H^\pm W^\mp Z$ vertices. In this chapter, we focus on the $H^\pm W^\mp Z$ vertices to see the quantum effects of the additional scalar bosons.

When $m_{H^\pm} > m_W + m_Z$, the decays $H^\pm \to W^\pm Z$ through these vertices are kinematically allowed. The decay rates of $H^\pm \to W^\pm Z$ are given by

$$\Gamma(H^\pm \to W^\pm Z) = \frac{m_{H^\pm}\lambda^{\frac{1}{2}}(1,w,z)}{16\pi}\Big(|\mathcal{M}_{LL}|^2 + |\mathcal{M}_{TT}|^2\Big), \tag{8.16}$$

where $w = m_W^2/m_{H^\pm}^2$, $z = m_Z^2/m_{H^\pm}^2$ and $\lambda(a,b,c) = (a-b-c)^2 - 4bc$. The amplitudes $\mathcal{M}_{LL}$ and $\mathcal{M}_{TT}$ are the contributions from the longitudinal and transverse modes of the external gauge bosons, respectively. These amplitudes are given by

$$\begin{aligned} |\mathcal{M}_{LL}|^2 &= \frac{g^2}{4z}\left|(1-w-z)F_\pm + \frac{\lambda(1,w,z)}{2w}G_\pm\right|^2, \\ |\mathcal{M}_{TT}|^2 &= g^2\left(2w|F_\pm|^2 + \frac{\lambda(1,w,z)}{2w}|H_\pm|^2\right). \end{aligned} \tag{8.17}$$

8.3 Understanding aspects of the $H^\pm W^\mp Z$ vertices with the equivalence theorem

In this section, we discuss the relation among the decays $H^\pm \to W^\pm Z$, the custodial symmetry, and the CP symmetry in our model. In section 8.4 and appendix E, we will give all diagrams and the full formulae for $F_\pm$, $G_\pm$ and $H_\pm$ in the general 2HDM. However, in order to see the essence, we here take the heavy mass limit, where $m_{W,Z}/m_{H^\pm} \to 0$. In this limit, the longitudinal contribution $\mathcal{M}_{LL}$ is dominant in the decays $H^\pm \to W^\pm Z$. In addition, thanks to the equivalence theorem [163, 399], the calculation of $\mathcal{M}_{LL}$ can be much simpler than the original calculation by replacing the external gauge bosons to the corresponding NG bosons.

To see the features of these vertices, we here take the $Z_6 = 0$ condition just for simplicity. The diagrams which contribute to $\Gamma(H^+ \to G^+G^0)$ from the scalar potential are shown in figure 8.1. Here we have employed the Landau gauge and calculated in the real Z_5 basis. The

white (black) dots in the figure 8.1 are proportional to Z_7^I (Z_7^R) or $m_{H^\pm}^2 - m_{H_3}^2$ ($m_{H^\pm}^2 - m_{H_2}^2$), so that they break the (twisted) custodial symmetry, as it can be understood from Eq. (4.29). At the one-loop level, the amplitudes are given by

$$\begin{aligned}\mathcal{M}(H^\pm \to G^\pm G^0) = &\frac{\pm i Z_7^R}{16\pi^2 v}(m_{H^\pm}^2 - m_{H_3}^2)\Big\{(m_{H_2}^2 - m_{H_3}^2)C_0[-k_2, -k_3; m_{H^\pm}^2, m_{H_3}^2, m_{H_2}^2] \\ &+ B_0[-k_2; m_{H^\pm}^2, m_{H_3}^2] - B_0[-k_1; m_{H^\pm}^2, m_{H_2}^2]\Big\} \\ &+ \frac{Z_7^I}{16\pi^2 v}(m_{H^\pm}^2 - m_{H_2}^2)\Big\{(m_{H_2}^2 - m_{H_3}^2)C_0[-k_2, -k_3; m_{H^\pm}^2, m_{H_2}^2, m_{H_3}^2] \\ &- B_0[-k_2; m_{H^\pm}^2, m_{H_2}^2] + B_0[-k_1; m_{H^\pm}^2, m_{H_3}^2]\Big\}, \end{aligned} \tag{8.18}$$

where the B_0 and C_0 functions are the scalar Passarino–Veltmann functions [400, 401], whose definitions are summarized in appendix D. We can see the equivalence of the custodial and the twisted custodial symmetry from Eq. (8.18). When the conditions for the (twisted) custodial symmetry, $Z_7^I = 0$ and $m_{H^\pm}^2 = m_{H_3}^2$ ($Z_7^R = 0$ and $m_{H^\pm}^2 = m_{H_2}^2$), are satisfied, the amplitude is $\mathcal{M}(H^\pm \to G^\pm G^0) = 0$. Due to the CP violating potential, there are two terms which are proportional to the real or imaginary part of Z_7. In the CP conserving 2HDM, there are no corresponding coupling constants to Z_7^I in the Higgs basis. Therefore, the second term in Eq. (8.18) is the new part from the CP violating potential. We note that, however, the existence of only the second term does not mean the CP violation in the potential. This is because, under the $Z_6 = 0$ condition, the remaining rephasing invariant is $Z_5^* Z_7^2$ (see section 4.1), so that $\mathrm{Im}[Z_7^2] \propto Z_7^R Z_7^I$ dependence in the real Z_5 basis is needed for the CP violation. Actually, the loop functions in Eq. (8.18) are always real, so that both squared amplitudes for H^+ and H^- take forms as $(Z_7^R)^2 c + (Z_7^I)^2 c'$, where c and c' are real constants. As a result, the decays $H^\pm \to W^\pm Z$ cannot be observable to measure $\mathrm{Im}[Z_7^2]$.

Even in the general formulae which are shown in appendix E, this feature is not changed. However, under the existence of the fermion-loop contributions with the additional Yukawa matrices ρ^f, an asymmetry between the decay rates of $H^+ \to W^+ Z$ and $H^- \to W^- Z$ can appear. This is because the loop functions in those contributions can have imaginary parts, and $\mathrm{Im}[Z_7 \rho^f]$ related differences appear in these decay rates. In the following sections, we also give discussions and results for the CP asymmetry in these decays.

We note, unlike ΔT, the $H^\pm W^\mp Z$ vertices are sensitive to the custodial symmetry violation by non-zero Z_7 at the one-loop level. This is because, the one-loop formula for ΔT does not have any dependence of Z_7, so that even if the custodial symmetry is violated by $Z_7 \neq 0$, ΔT can be zero by taking $m_{H_2} = m_{H^\pm}$ or $m_{H_3} = m_{H^\pm}$.

8.4 The analyses for the decays $H^\pm \to W^\pm Z$ in the general two Higgs doublet model

In this section, we discuss the decays $H^\pm \to W^\pm Z$ in the general 2HDM. We calculate the decay in the t'Hooft–Feynman gauge at the one-loop level. The full analytic expressions for the $H^\pm W^\mp Z$ vertices are given in appendix E. All numerical results which are shown in the following subsections are given by using these formulae.

In figures 8.2-8.5, all contributions to the decay $H^+ \to W^+ Z$ are shown. The diagrams of the decay $H^- \to W^- Z$ can be obtained by changing the directions of the arrows for the charged particles. The boson contributions are shown in figure 8.2 and figure 8.3, where i, j ($= 1, 2, 3$) are the indices of the neutral scalar bosons in the mass eigenstate. The diagrams given in figure 8.2 and figure 8.3 can be expressed by the C and B type Passarino–Veltmann

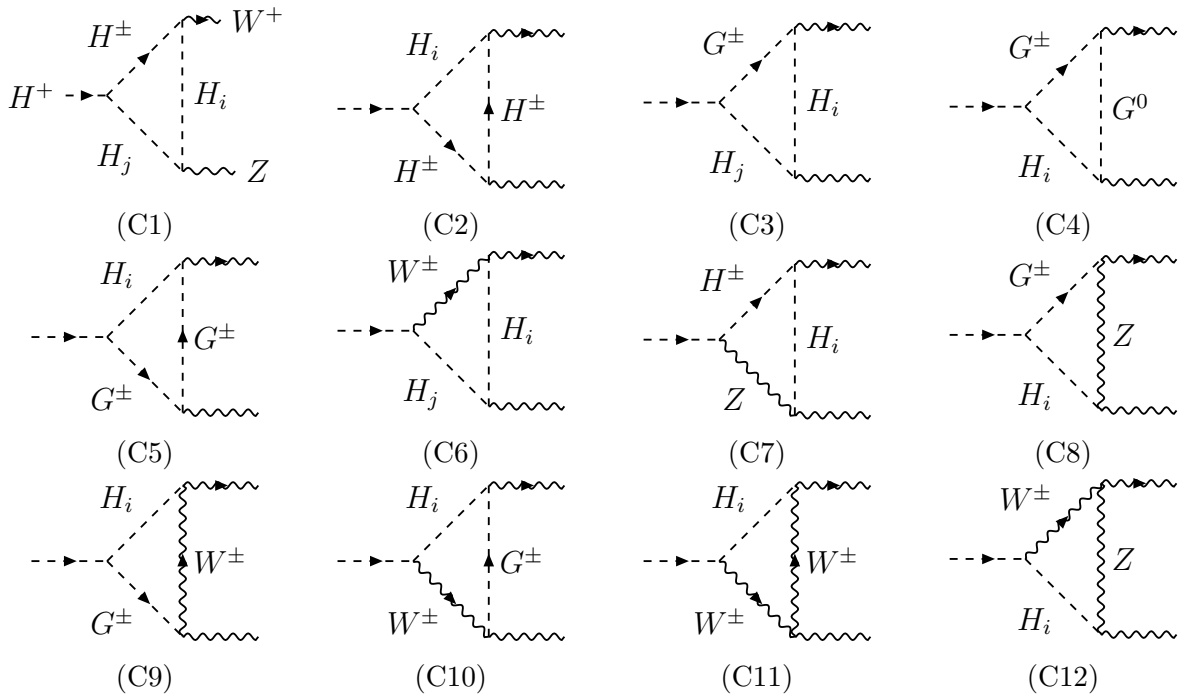

Figure 8.2: The C type contributions. The indices i and j run $1, 2, 3$, which denote the mass eigenstates of the neutral scalar bosons.

functions, respectively. The fermion contributions are shown in figure 8.4, where l, m $(= 1, 2, 3)$ are the fermion-flavor indices. Only the fermion contributions give the $H_{\pm}$ term in Eq. (8.14) because the SM fermions have the chiral interaction. There are other contributions from the diagrams of the tadpole and the H^+G^- mixing, which are shown in figure 8.5. These diagrams are expressed by the A_0 scalar one-point function. Analytic expressions for all diagrams are given in appendix E.

Here we give a comment on a method for renormalization. In our model, the effective operators which cause the $H^{\pm}W^{\mp}Z$ vertices are absent at the tree level, so that such a one-loop-induced vertex must be finite in the renormalizable theory. By summing all of those contributions, the divergences in each diagram, which are also shown in appendix E, cancel out. Therefore, a renormalization method to absorb these divergences in these vertices is not needed. However, once a renormalization scheme is adopted and the counter terms in this scheme are fixed, they might give finite corrections to these vertices at the one-loop level. We expect that those corrections are small, and we do not specify the renormalization scheme in this thesis.

8.4.1 Setup of model parameters

First, in this subsection, we explain a method to determine the input parameters for numerical analysis. The free independent parameters in our model are $Y_2^2, Z_{1,2,3,4,5}, Z_6^R, Z_6^I, Z_7^R, Z_7^I$, and ρ^f $(f = u, d, e)$. We take the mixing angles α_i and the mass m_{H_i} $(i = 1, 2, 3)$ as the input parameters. Therefore, the related coupling constants Z_1, Z_4, Z_5, Z_6^R and Z_6^I are determined by

$$\mathcal{M}^2 = \mathcal{R}^T \mathrm{diag}(m_{H_1}^2, m_{H_2}^2, m_{H_3}^2)\mathcal{R}. \tag{8.19}$$

where $\mathcal{M}^2$ is given in Eq. (4.5). In order to take the real Z_5 basis, a set of input parameters $(\alpha_1, \alpha_2, \alpha_3, m_{H_1}, m_{H_2}, m_{H_3})$ must satisfy $(\mathcal{M}^2)_{23} = (\mathcal{M}^2)_{32} = 0$. First we determine $(\alpha_1, \alpha_2, m_{H_1}, m_{H_2}, m_{H_3})$ and then numerically get $\alpha_3 = \alpha_3^*$, which satisfies $(\mathcal{M}^2)_{23} = (\mathcal{M}^2)_{32} = 0$. In the following numerical studies, we choose α_3^* such that the coupling Z_6

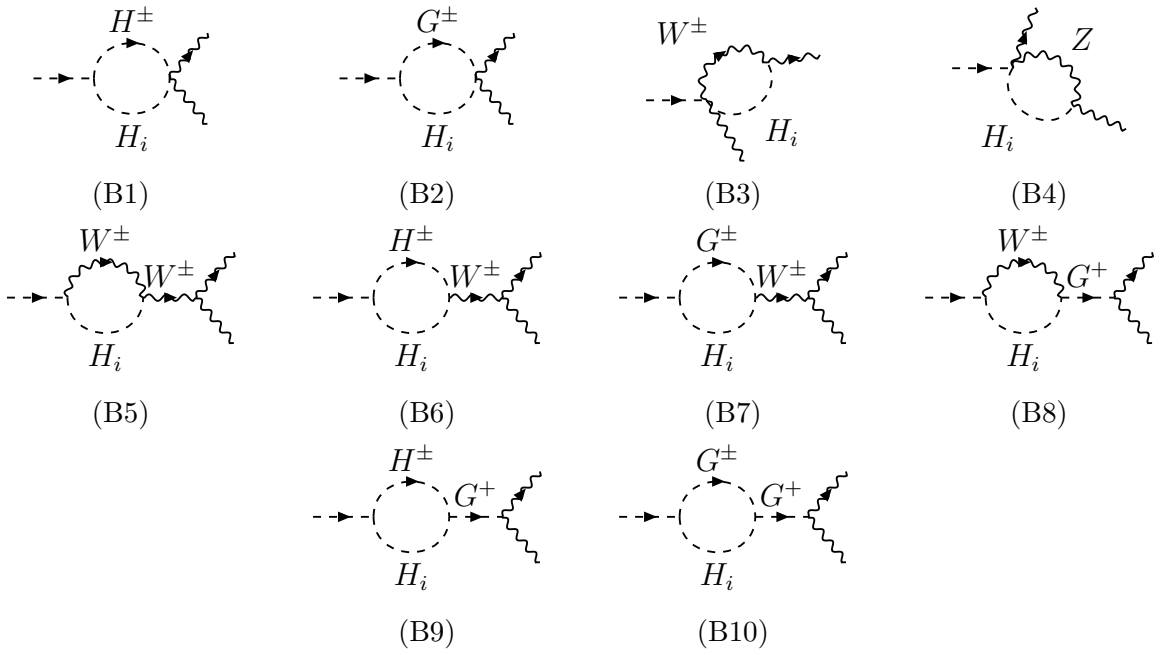

Figure 8.3: The B type contributions.

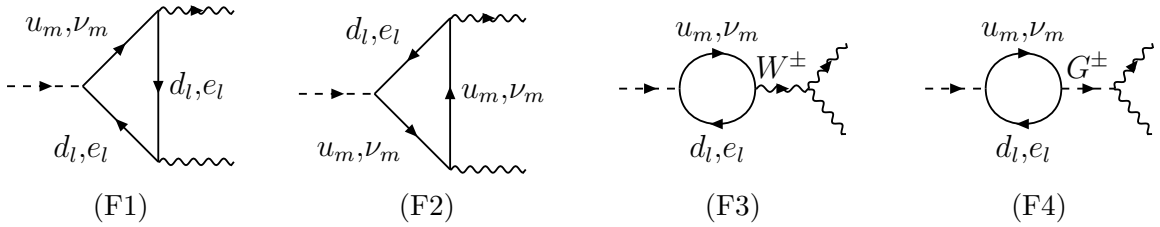

Figure 8.4: The fermion contributions. The indices l, m denote the fermion flavors.

satisfies $0 \leq \arg[Z_6] < \pi/2$. We also treat $m_{H^\pm}$ and Y_2^2 as the input parameters and fix $-Y_2^2 = (20\ \text{GeV})^2$. The coupling constant Z_2, which is irrelevant to the decays $H^\pm \to W^\pm Z$ at the one-loop level, is set by $Z_2 = 2$.

Second, we have the general complex Yukawa matrices ρ^f in our model. Although the formulae of the $H^\pm W^\mp Z$ vertices with general ρ^f are shown in appendix E, the contributions from each flavor give similar results. Under the data from the flavor experiments, ρ_{tt} and ρ_{tc}, which are $(3,3)$ and $(3,2)$ elements in ρ^u, respectively, are normally allowed to be larger than the other additional Yukawa coupling constants [139]. In addition, effects from ρ_{tc} are small because the contributions to the $H^\pm W^\mp Z$ vertices from ρ^u are approximately proportional to $\sum_{l,m=2,3}(V^\dagger)_{lm}(\rho^{u\dagger}V)_{ml}f(m_{u_m}) = \rho^*_{cc}f(m_c) + \rho^*_{tt}f(m_t)$, where the function f is expressed by the loop functions. Therefore, in the following analyses, we only focus on the ρ_{tt} dependence as the fermion contributions.

Finally, we consider the experimental and theoretical constraints on the 2HDM, which has already been discussed in section 4.1. As a conservative bound on the mixing angles α_i and the coupling constant ρ_{tt}, we set $|\alpha_i| \leq 0.01$ and $|\rho_{tt}| \leq 0.2$ in the following analyses.

8.4.2 Numerical analyses for the decay $H^+ \to W^+Z$

In this subsection, we give numerical results for the decay $H^+ \to W^+Z$ in our model. As other decay modes for $H^\pm$, we consider $H^\pm \to ff'$ and $H^\pm \to W^\pm H_i$, if it is kinematically allowed.

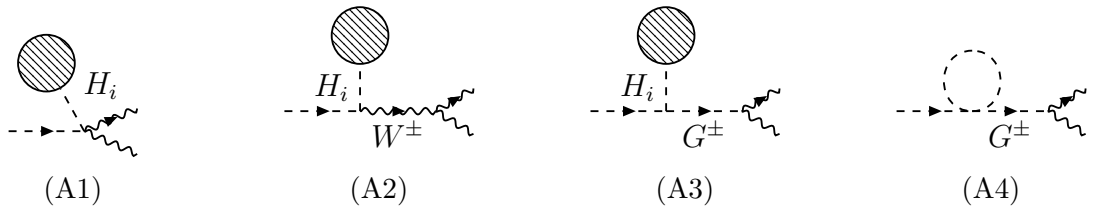

(A1) (A2) (A3) (A4)

Figure 8.5: The A type contributions.

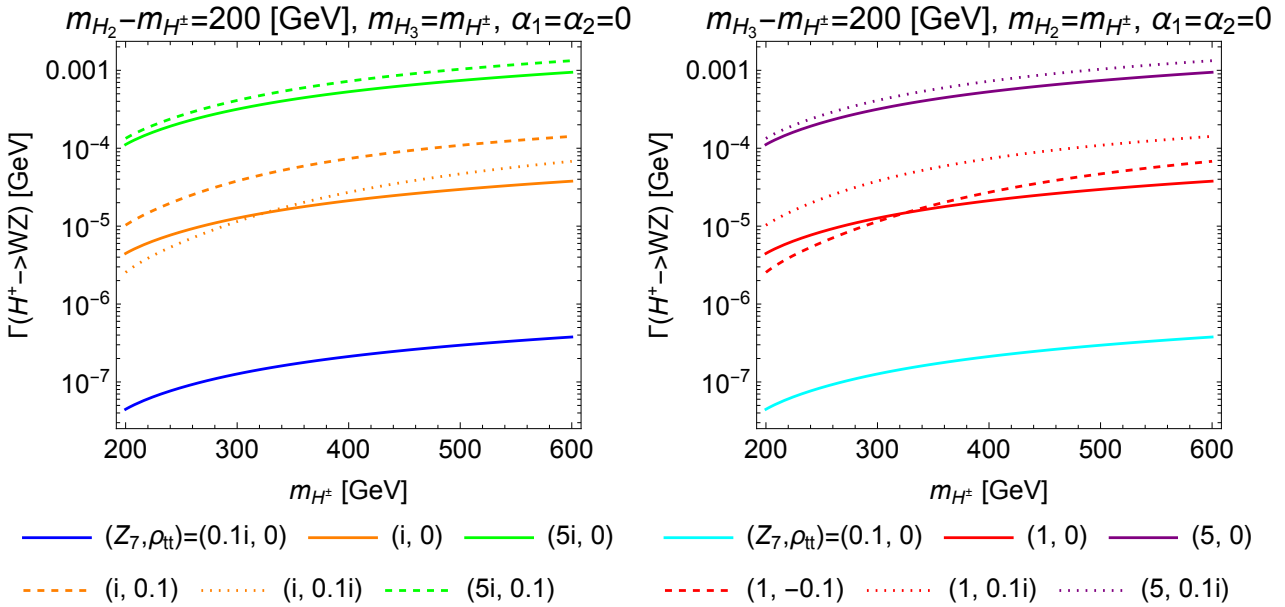

Figure 8.6: The decay rate $\Gamma(H^+ \to W^+Z)$ as a function of $m_{H^{\pm}}$. In the left (right) panel, the mass difference $m_{H_2} - m_{H^{\pm}}$ ($m_{H_3} - m_{H^{\pm}}$) and the coupling constant Z_7^I (Z_7^R) are switched on. The solid lines show the results for $\rho_{tt} = 0$, and both dashed and dotted lines show the impacts from non-zero ρ_{tt}.

Each decay rates are given by

$$\begin{aligned}
\Gamma(H^{\pm} \to u_i d_j) &= \frac{N_c \lambda^{1/2}(m_{H^{\pm}}^2, m_{u_i}^2, m_{d_j}^2)}{8\pi m_{H^{\pm}}^3} \Big\{ \frac{1}{2}(|\Gamma_{ij}^u|^2 + |\Gamma_{ij}^d|^2)(m_{H^{\pm}}^2 - m_{u_i}^2 - m_{d_j}^2) \\
&\qquad - 2 m_{u_i} m_{d_j} \mathrm{Re}[(\Gamma_{ij}^u)^* \Gamma_{ij}^d] \Big\}, \\
\Gamma(H^{\pm} \to e_i \nu_j) &= \frac{|\Gamma_{ij}^e|^2}{16\pi m_{H^{\pm}}^3}(m_{H^{\pm}}^2 - m_{e_i}^2)^2, \\
\Gamma(H^{\pm} \to W^{\pm} H_i) &= \frac{\lambda^{3/2}(m_{H^{\pm}}^2, m_{W^{\pm}}^2, m_{H_i}^2)}{16\pi v^2 m_{H^{\pm}}^3}(\mathcal{R}_{i2}^2 + \mathcal{R}_{i3}^2),
\end{aligned} \tag{8.20}$$

where $\Gamma_{ij}^u = \rho^{u\dagger} V_{\mathrm{CKM}}$, $\Gamma_{ij}^d = -V_{\mathrm{CKM}} \rho^d$ and $\Gamma_{ij}^e = -\rho^e$.

In figure 8.6, $\Gamma(H^+ \to W^+Z)$ is shown as a function of $m_{H^{\pm}}$. In the left panel, we take $m_{H_2} - m_{H^{\pm}} = 200$ GeV, $m_{H_3} = m_{H^{\pm}}$ and $\alpha_1 = \alpha_2 = 0$. The results of $Z_7^I = 0.1$, 1, and 5 are shown as the blue, orange, and green solid lines, respectively. We note that taking $Z_7^I = 5$ is dangerous due to the perturbative unitarity or the BFB conditions, however, it is shown just for illustration. These solid lines are purely caused by the scalar and gauge contributions, and the decay rate increases as taking large Z_7^I. This is because, in the left panel, the custodial symmetry violation in the potential is realized by non-zero Z_7^I. When the fermion contribution from ρ_{tt} is switched on, as shown by the dashed ($\rho_{tt} = 0.1$) and the dotted ($\rho_{tt} = 0.1i$) lines,

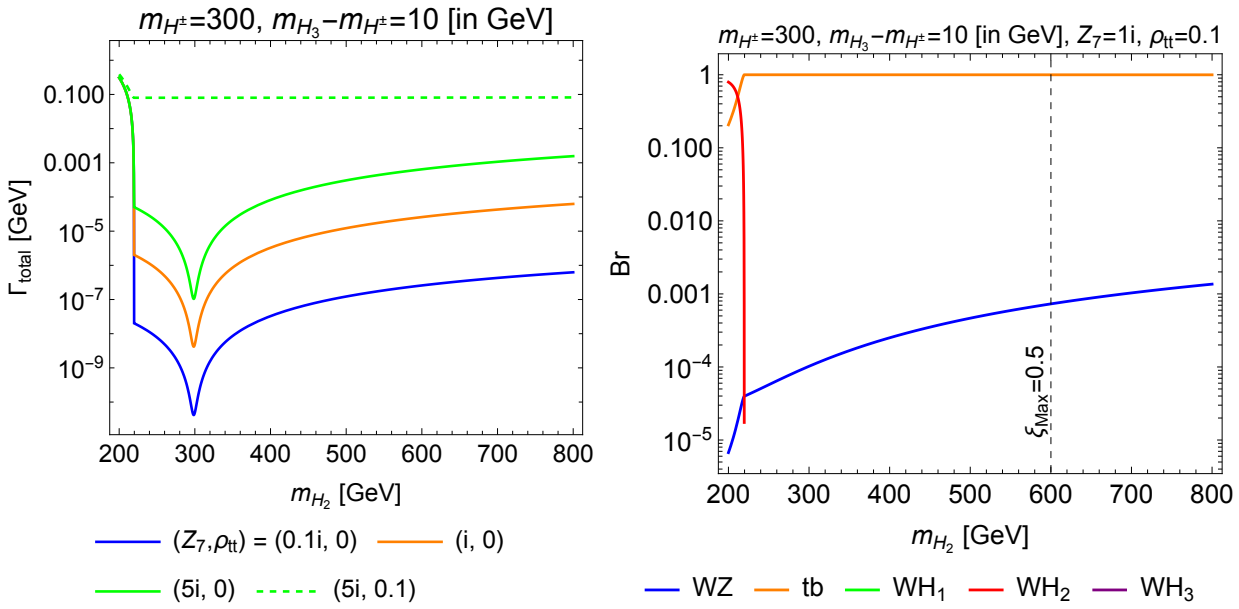

Figure 8.7: Left: m_{H_2} dependence of the total decay rate of H^+. The blue, orange, and green lines show the results of $Z_7^I = 0.1$, 1, and 5, respectively. The result with non-zero ρ_{tt} is shown as the dashed line. Right: m_{H_2} dependence of the branching ratio of H^+. The decay modes are $H^+ \to W^+Z$ (blue), tb (orange), W^+H_1 (green), W^+H_2 (red), and W^+H_3 (purple). In this parameter set, only the decay modes $H^+ \to W^+Z$, tb and W^+H_2 can be significant. The black dashed line shows the criterion where the maximal s-wave scattering amplitude among the scalar and the gauge bosons is 0.5.

the decay width is changed. In the right panel of figure 8.6, $m_{H_3} - m_{H^\pm} = 200$ GeV and $m_{H_2} = m_{H^\pm}$ are taken. Namely, the masses of H_2 and H_3 are exchanged from the left panel. The cyan, red, and purple lines are the results of $Z_7^R = 0.1$, 1, and 5, respectively, and the impacts of setting $\rho_{tt} = -0.1$ and $0.1i$ are shown by the dashed and dotted lines, respectively. In this right panel, the violation of the twisted custodial symmetry in the potential is realized by $Z_7^R \neq 0$. We can see the equivalent results in the left and right panels, which are related to the violation of the custodial or the twisted custodial symmetry.

In the left panel of figure 8.7, m_{H_2} dependence of the total decay width of H^+ is shown. We have taken $m_{H^\pm} = 300$ GeV, $m_{H_3} - m_{H^\pm} = 10$ GeV and $\alpha_1 = \alpha_2 = 0$. In the left panel, the blue, orange, and green solid lines show the total decay width $\Gamma_{\rm total}$ with $Z_7^I = 0.1$, 1, and 5. Again, taking $Z_7^I = 5$ is dangerous due to the perturbative unitarity or the BFB conditions, however, the result is shown just for illustration. When $m_{H_2} < m_{H^\pm} - m_W$, the $H^+ \to W^+H_2$ decay is kinematically allowed. On the other hand, in the region $m_{H_2} > m_{H^\pm} - m_W$, only the decay mode $H^+ \to W^+Z$ is possible if $\rho_{tt} = 0$, and it almost disappears at the point $m_{H^\pm} = m_{H_2}$, where the potential recovers the twisted custodial symmetry. As shown in the green dashed line, when ρ_{tt} is switched on, $H^+ \to tb$ decay is allowed. In the right panel of figure 8.7, the branching ratio of H^+ is shown. In this panel, $Z_7^I = 1$ and $\rho_{tt} = 0.1$ are taken. The decay modes are $H^+ \to W^+Z$ (blue), tb (orange), W^+H_1 (green), W^+H_2 (red), and W^+H_3 (purple). In this parameter set, only $H^+ \to W^+Z$, tb and W^+H_2 can be significant. The black dashed line shows the perturbative unitarity bound, $\xi_{\rm Max} \equiv {\rm Max}\{a_0\} = 0.5$, where $\{a_0\}$ is a set of the eigenvalues of s-wave amplitude matrix for the elastic scatterings among the longitudinal modes of the gauge bosons and the neutral and charged scalar bosons in the high energy limit [167]. The line for $\xi_{\rm Max} = 1$ is out of this figure. In the region $m_{H_2} > m_{H^\pm} - m_W$, the dominant decay modes are $H^+ \to tb$ and $H^+ \to W^+Z$. As the mass difference $m_{H_2} - m_{H^\pm}$ becomes large, the branching ratio ${\rm Br}(H^+ \to W^+Z)$ increases.

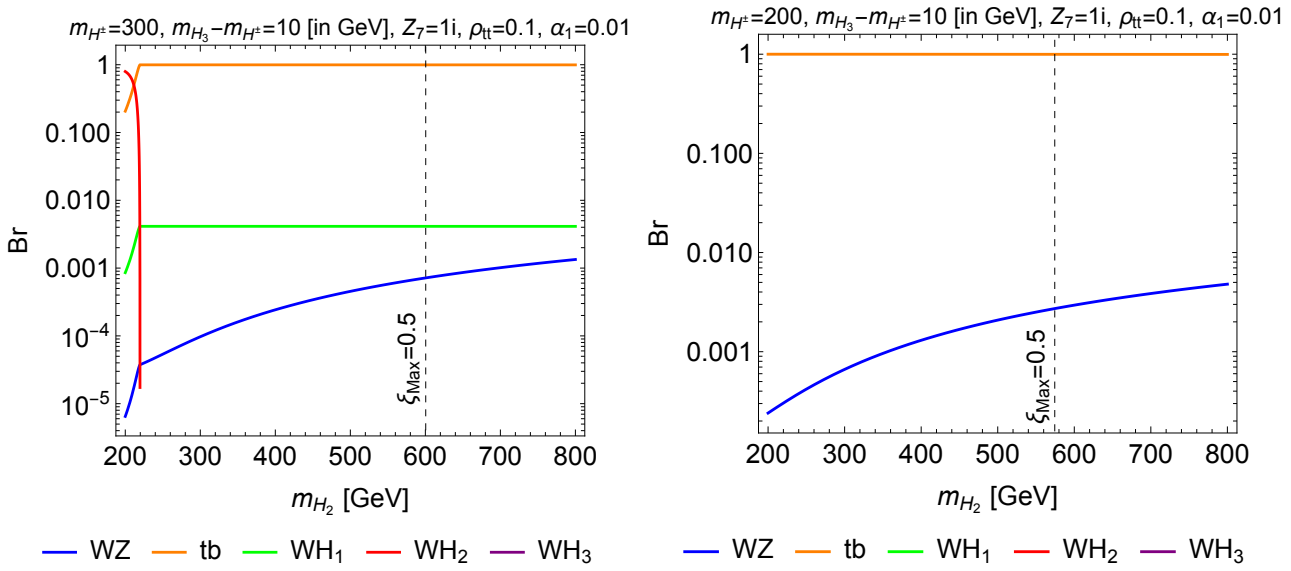

Figure 8.8: m_{H_2} dependence of the branching ratio of H^+ with the non-zero mixing angle α_1 (left: $m_{H^\pm} = 300$ GeV, right: $m_{H^\pm} = 200$ GeV).

In figure 8.8, analyses for the branching ratio with a non-alignment case are shown. In the left (right) panel, $m_{H^\pm} = 300$ GeV ($m_{H^\pm} = 200$ GeV), $m_{H_3} = m_{H^\pm} + 10$ GeV, $Z_7^I = 1$, $\rho_{tt} = 0.1$, $\alpha_1 = 0.01$, and $\alpha_2 = 0$ are taken. As shown in the left panel, when $m_{H^\pm} > m_W + m_{H_1}$, $\mathrm{Br}(H^+ \to W^+Z)$ is suppressed by the $H^+ \to W^+H_1$ decay, which is caused by non-zero $\mathcal{R}_{12}$. On the other hand, when $m_{H^\pm} < m_W + m_{H_1}$, as shown in the right panel, H^+ decays into tb or W^+Z, so that $\mathrm{Br}(H^+ \to W^+Z) \gtrsim O(10^{-3})$ is realized for $\xi_{\mathrm{Max}} \leq 0.5$.

In figure 8.9, the results for ρ_{tt} dependence of the branching ratio are shown. As shown in the left panel, where $m_{H^\pm} = 300$ GeV, the dominant decay mode is $H^+ \to W^+H_1$ in the region of $\rho_{tt} \lesssim 0.006$, and $H^+ \to tb$ becomes dominant as ρ_{tt} increases. In the right panel, where $m_{H^\pm} = 200$ GeV, $H^+ \to W^+H_1$ is kinematically forbidden. As a result, in the region of $\rho_{tt} \lesssim 0.003$, $H^+ \to tb$ is suppressed, and $\mathrm{Br}(H^+ \to W^+Z)$ can be large.

8.4.3 Asymmetry in the decays of $H^+ \to W^+Z$ and $H^- \to W^-Z$

In the previous subsection, the numerical results for H^+ decays are shown. The decay $H^- \to W^-Z$ also behaves in a similar way to the decay $H^+ \to W^+Z$. However, an asymmetry between them is caused by the interference of the scalar and fermion contributions. In this subsection, we give numerical results for the CP asymmetry in these decays.

For the discussions of the CP violation, we define

$$\Delta(H^\pm \to W^\pm Z) \equiv \Gamma(H^+ \to W^+Z) - \Gamma(H^- \to W^-Z), \tag{8.21}$$

and the CP violating quantity [375]

$$\delta_{\mathrm{CP}} \equiv \frac{\Gamma(H^+ \to W^+Z) - \Gamma(H^- \to W^-Z)}{\Gamma(H^+ \to W^+Z) + \Gamma(H^- \to W^-Z)}. \tag{8.22}$$

By definition, the decay rate for H^- is given by

$$\Gamma(H^- \to W^-Z) = \frac{1 - \delta_{\mathrm{CP}}}{1 + \delta_{\mathrm{CP}}} \Gamma(H^+ \to W^+Z). \tag{8.23}$$

The behavior of these quantities are shown in figure 8.10, where $m_{H^\pm} = 200$ GeV, $m_{H_2} = 500$ GeV, $m_{H_3} = m_{H^\pm} + 10$ GeV, $\rho_{tt} = 0.1$, and $\alpha_1 = \alpha_2 = 0$ are taken. In the left and

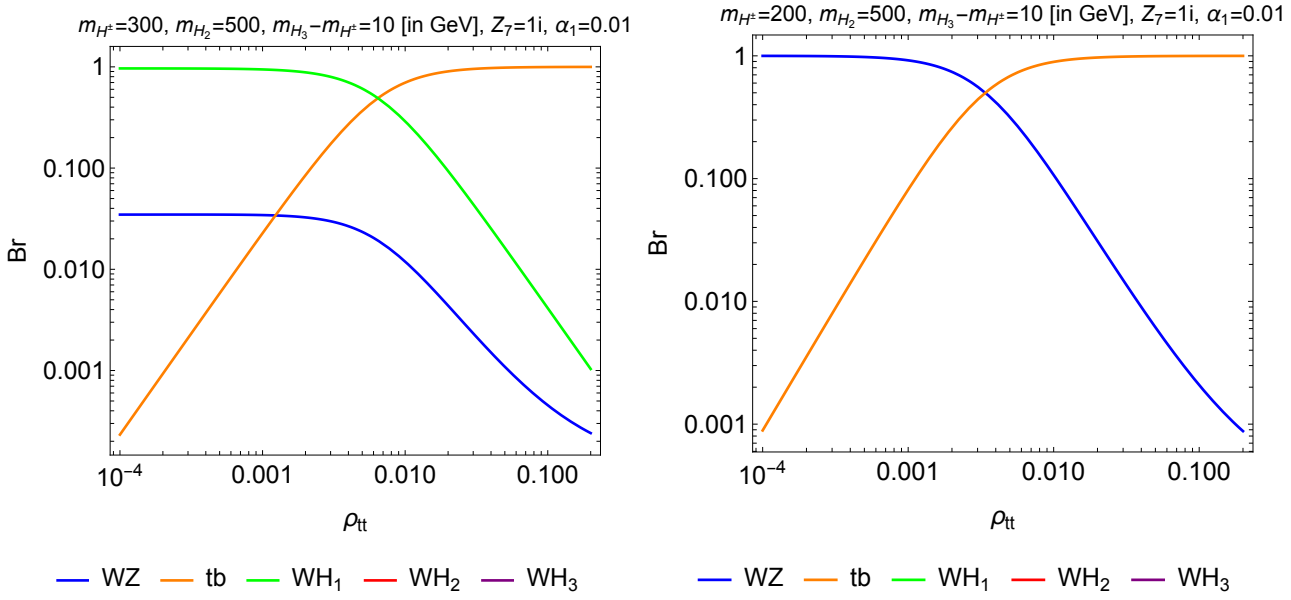

Figure 8.9: ρ_{tt} dependence of the branching ratio of H^+ (left: $m_{H^\pm} = 300$ GeV, right: $m_{H^\pm} = 200$ GeV). In this parameter set, the decay modes $H^+ \to W^+Z$, tb and W^+H_1 are relevant.

right panel, the contour figures of $\Delta(H^\pm \to W^\pm Z) \times 10^5$ and δ_{CP} in the $|Z_7|$-arg$[Z_7]$ plane are shown, respectively. The red shaded regions do not satisfy the BFB conditions. At arg$[Z_7] = \pi/2$, $\Delta(H^\pm \to W^\pm Z)$ and $\delta_{\rm CP}$ take the maximal value, while at arg$[Z_7] = -\pi/2$, they take the minimal value. This feature can be understood as follows: each decay amplitude can be approximately written as

$$\begin{aligned}
\mathcal{M}(H^+ \to W^+Z) &\simeq i\big(\rho^R_{tt} f_1 + Z_7^R(m^2_{H^\pm} - m^2_{H_3}) f_2\big) + \big(\rho^I_{tt} f_1 + Z_7^I(m^2_{H^\pm} - m^2_{H_2}) f_3\big), \\
\mathcal{M}(H^- \to W^-Z) &\simeq -i\big(\rho^R_{tt} f_1 + Z_7^R(m^2_{H^\pm} - m^2_{H_3}) f_2\big) + \big(\rho^I_{tt} f_1 + Z_7^I(m^2_{H^\pm} - m^2_{H_2}) f_3\big),
\end{aligned} \tag{8.24}$$

where $f_{1,2,3}$ are mass dependent functions. When $m_{H^\pm} > m_t + m_b$, the loop functions in f_1 have the imaginary parts, so that $\delta_{\rm CP}$ can be expressed as[2]

$$\begin{aligned}
\delta_{\rm CP} &\propto \Delta(H^\pm \to W^\pm Z) \propto |\mathcal{M}(H^+ \to W^+Z)|^2 - |\mathcal{M}(H^- \to W^-Z)|^2 \\
&\propto \rho^R_{tt} Z_7^I (m^2_{H^\pm} - m^2_{H_2}) f_3 {\rm Im}[f_1^*] + \rho^I_{tt} Z_7^R (m^2_{H^\pm} - m^2_{H_3}) f_2 {\rm Im}[f_1].
\end{aligned} \tag{8.25}$$

As a result, the dependence of $Z_7^I \propto \sin(\arg[Z_7])$ appears in figure 8.10, where non-zero $m_{H^\pm} - m_{H_2}$ and ρ^R_{tt} are taken. Due to the denominator in Eq. (8.22), as $|Z_7|$ increases, $\delta_{\rm CP}$ gets large at first, but it turns to decrease.

In figure 8.11, the ρ_{tt} dependence of $\delta_{\rm CP}$ is shown. We have set the phase of Z_7 as arg$[Z_7] = \pi/2$. The blue, orange, and green lines show the results of $|Z_7| = 0.1$, 0.5 and 1, respectively. The point of ρ_{tt}, where $\delta_{\rm CP}$ takes a maximal value, depends on the size of Z_7. The maximal value of $\delta_{\rm CP}$ in this figure is around 0.7, so that $\Gamma(H^- \to W^-Z)$ is about 17 % of $\Gamma(H^+ \to W^+Z)$.

At the pp collider like LHC, production cross sections of H^+ and H^- via the vector boson fusion mechanism and the associated production mechanism with neutral scalar bosons are in general different [186, 187, 388]. In addition, as we find, the decays of $H^+ \to W^+Z$ and $H^- \to W^-Z$ can be different by the CP violating phase effect.

[2]This kind of CP violation is so-called direct CP violation [402].

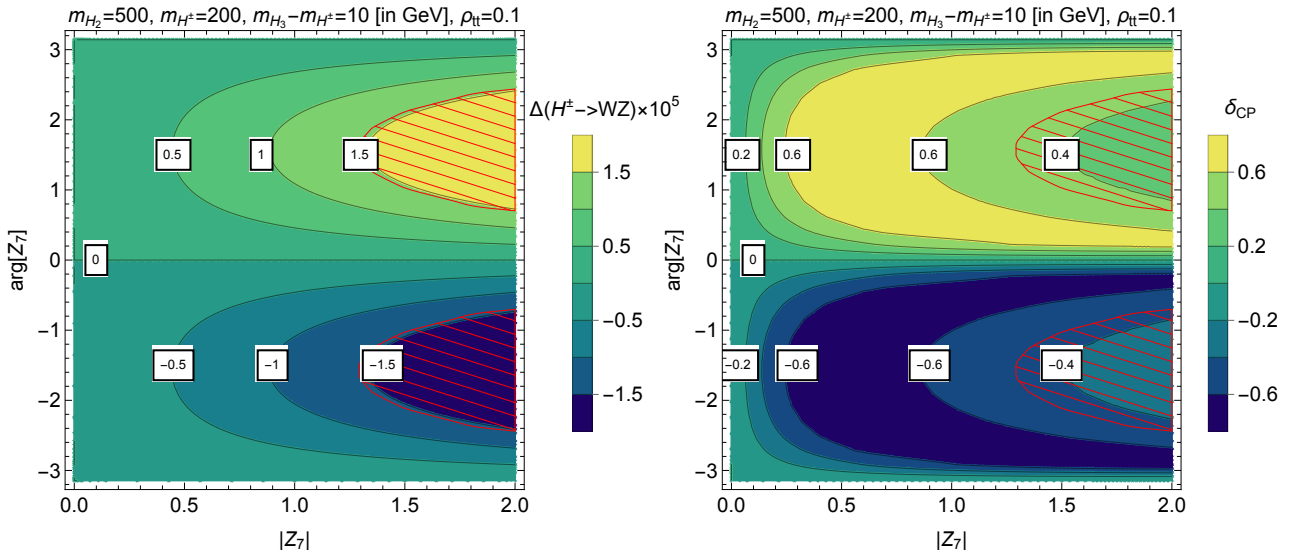

Figure 8.10: The contour plots of $\Delta(H^{\pm} \to W^{\pm}Z) \times 10^5$ (left) and $\delta_{\rm CP}$ (right) in $|Z_7|$-arg$[Z_7]$ plane. The red shaded regions do not satisfy the BFB conditions.

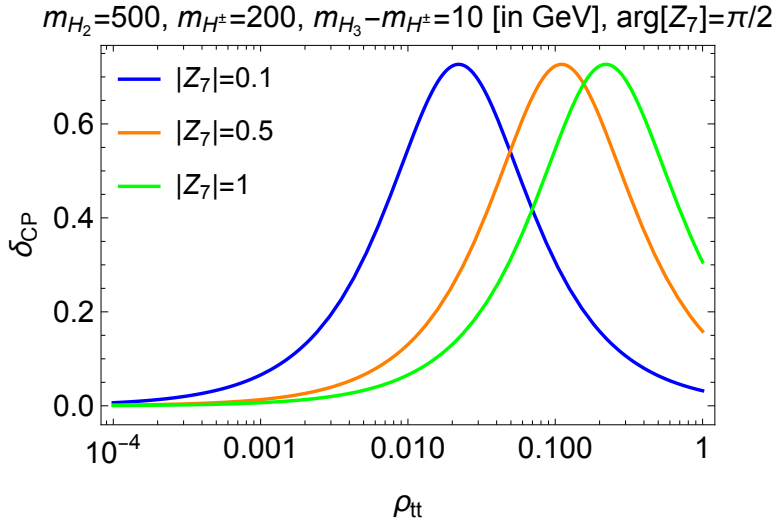

Figure 8.11: The ρ_{tt} dependence of $\delta_{\rm CP}$ with several $|Z_7|$ values. $|Z_7| = 0.1$ (blue), $|Z_7| = 0.5$ (orange), and $|Z_7| = 1$ (green).

8.5 Discussions

First, we discuss the signature for the $H^{\pm}W^{\mp}Z$ vertices at the hadron colliders. Based on the analyses in the former sections, we set two benchmark points which are given in table 8.1. The difference in BP1 and BP2 is the size of ρ_{tt}, and the other parameters are the same. As discussed in section 8.4, for the production of H^+, the WZ fusion process ($pp(W^+Z) \to H^+X$) and the top-associated process ($gb \to H^+t$) are important in the hadron collider. (At a pp collider, the production cross section for $pp(W^-Z) \to H^-X$ is smaller than that for $pp(W^+Z) \to H^+X$ [388].) The former production process is loop-induced, and it has been evaluated in Refs. [372, 388, 389]. From figure 13 in Ref. [372], the WZ fusion cross section can be obtained as $\sigma_{WZ} \simeq 2|F|^2 \times 10^3$ fb for $m_{H^\pm} = 200$ GeV at the LHC with $\sqrt{s} = 13$ TeV. The latter process depends on ρ_{tt}, and its cross section has been evaluated by $\sigma_{gb} \simeq 10^2$ fb for $|\rho_{tt}| \simeq 1/8$ and $m_{H^\pm} = 200$ GeV at the LHC with $\sqrt{s} = 13$ TeV [100]. Therefore, ρ_{tt} dependence of this cross section can be estimated as $\sigma_{gb} \simeq 64|\rho_{tt}|^2 \times 10^2$ fb for $m_{H^\pm} = 200$ GeV. In figure 8.12, ρ_{tt} dependence of $\sigma_{WZ} \times {\rm Br}(H^+ \to W^+Z)$ and $\sigma_{gb} \times {\rm Br}(H^+ \to W^+Z)$ are

(in GeV)	$m_{H^{\pm}}$	m_{H_2}	m_{H_3}	Z_7	ρ_{tt}	$\alpha_1 = -\alpha_2$
BP1	200	500	210	$1.3e^{2.0i}$	0.1	0.01
BP2	200	500	210	$1.3e^{2.0i}$	0.001	0.01

Table 8.1: Benchmark points for the discussions of collider phenomenology. In BP1 and BP2, the same parameters are taken except for ρ_{tt}.

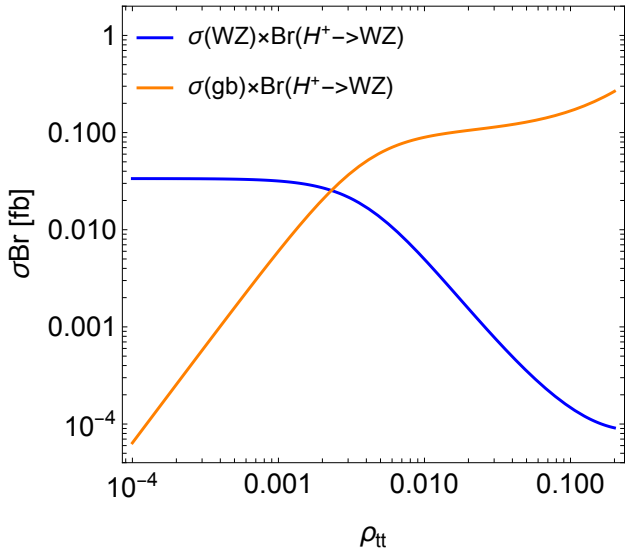

Figure 8.12: ρ_{tt} dependence of the cross section $\sigma(pp \to H^+X \to W^+ZX)$ in fb. The charged scalar boson is produced via the WZ fusion process (blue) or the top-associated process (orange).

shown. The point $\rho_{tt} = 0.1$ (0.001) in figure 8.12 corresponds to BP1 (BP2). The numerical values of $|F|^2$, $\mathrm{Br}(H^+ \to W^+Z)$, and the cross sections at these points are summarized in table 8.2. For relatively large ρ_{tt}, e.g. in BP1, in spite of the suppression of $\mathrm{Br}(H^+ \to W^+Z)$, $\sigma_{gb} \times \mathrm{Br}$ has advantage because the top-associated production process is enhanced by ρ_{tt}. On the other hand, in the case of relatively small ρ_{tt}, e.g. in BP2, the top-associated production process and the $H^+ \to tb$ decay are suppressed. As a result, the WZ fusion production process is important in this case.

From the data collected at the 13 TeV LHC with 139 fb^{-1} [179], an upper bound $\sigma_{WZ} \times \mathrm{Br} \lesssim O(10^2)$ fb for $m_{H^{\pm}} = 200$ GeV has been obtained, which is much larger than the estimated value in BP2. However, at the HL-LHC with 3000 fb^{-1}, we can expect $O(10^2)$ number of this events in BP2. This signal is also important in the high energy upgrade of the LHC [393]. Even in BP1, in which ρ_{tt} is relatively large, the process $\sigma_{gb} \times \mathrm{Br}$ might be important in the future hadron colliders because $\sigma_{gb} \times \mathrm{Br}$ in BP1 is about 5 times larger than $\sigma_{WZ} \times \mathrm{Br}$ in BP2. Consequently, the $H^{\pm}W^{\mp}Z$ vertices in our model are expected to be tested at the HL-LHC.

Second, we give discussions for the testability in the lepton collider. For example, in the high energy e^+e^- collider such as the ILC with $\sqrt{s} = 500$ GeV and 1 TeV [24,25], the pair production process $e^+e^- \to H^+H^-$ is important, and its cross section only depends on $m_{H^{\pm}}$ [403]. In addition, single $H^{\pm}$ production has been discussed in Refs. [384, 390, 404]. When we consider $m_{H^{\pm}} = 200$ GeV, the production cross section of a pair of the charged scalar bosons is given by $\sigma(H^+H^-) \simeq 3.0 \times 10$ fb (2.0×10 fb) at the ILC 500 GeV (1 TeV) [384]. Therefore, in BP1 (BP2), $\sigma(H^+H^-) \times \mathrm{Br}(H^+ \to W^+Z)$ is estimated as $\sigma \times \mathrm{Br} \simeq 7.8 \times 10^{-2}$ fb (2.8×10 fb) at the ILC 500 GeV and $\sigma \times \mathrm{Br} \simeq 5.2 \times 10^{-2}$ fb (1.9×10 fb) at the ILC 1 TeV. This pair production process is independent of ρ_{tt}, so that numerous events can be expected in BP2, in which almost all H^+ decays to the W and Z bosons. More detailed analysis in these hadron and lepton colliders will be given in the following study [405].

	BP1	BP2
$\lvert F\rvert^2$	2.8×10^{-5}	1.7×10^{-5}
$\mathrm{Br}(H^+ \to W^+Z)$	2.6×10^{-3}	9.4×10^{-1}
σ_{WZ} [fb]	5.6×10^{-2}	3.4×10^{-2}
$\sigma_{WZ} \times \mathrm{Br}$ [fb]	1.5×10^{-4}	3.2×10^{-2}
σ_{gb} [fb]	6.4×10	6.4×10^{-3}
$\sigma_{gb} \times \mathrm{Br}$ [fb]	1.7×10^{-1}	6.0×10^{-3}

Table 8.2: Summary of several values for $|F|^2$, $\mathrm{Br}(H^+ \to W^+Z)$ and the cross sections in BP1 and BP2.

Third, our calculation has been done in the Higgs basis, and it can be applied to the softly-broken $\mathbb{Z}_2$ symmetric 2HDM by using the basis rotation from the $\mathbb{Z}_2$ basis to the Higgs basis [137]. As shown in table 4.1, the CP violating phases do not exist in the Yukawa sector in the softly-broken $\mathbb{Z}_2$ symmetric 2HDM, and the ρ^f coupling constants are not independent of the parameters in the potential. On the other hand, in the general 2HDM, ρ^f are the arbitrary complex matrices, and they can have the CP violating phases, some of which are important sources to produce the BAU via the mechanism of the electroweak baryogenesis [37–43, 45, 47–49]. Due to the independence between ρ^f and the coupling constants in the potential, it is possible to consider parameter points, such as BP2, in which $\mathrm{Br}(H^+ \to W^+Z)$ is close to unity.

Finally, in this chapter, we have discussed the relation between the $H^{\pm}W^{\mp}Z$ vertices and the CP violation. As we have mentioned in section 8.3, the decays $H^{\pm} \to W^{\pm}Z$ cannot be the observable for $\mathrm{Im}[Z_5^* Z_7^2]$, which is the CP violating invariant in the potential. However, the difference in the decays $H^+ \to W^+Z$ and $H^- \to W^-Z$ is sensitive to $\mathrm{Im}[Z_7\rho^f]$, as we have discussed in section 8.4. Therefore, as shown in figure 8.10, if we know the phase of ρ^f, the phase of Z_7 can be determined by measuring the difference between $\Gamma(H^+ \to W^+Z)$ and $\Gamma(H^- \to W^-Z)$. For example, in our model, it has been known that the rephasing invariant $Z_5\rho^2_{\tau\tau}$ can be measured by using azimuthal angle dependence of the hadronic decay of the tau leptons, which are decay products of the pair of H_2 and H_3 [83, 358]. More realistic analyses for measuring the CP phase via the $H^{\pm}W^{\mp}Z$ vertices will be discussed somewhere [405].

8.6 Short summary of chapter 8

In this chapter, we have discussed the $H^{\pm}W^{\mp}Z$ vertices in the most general 2HDM with the CP violation. It has been known that the CP violating potential in the 2HDM violates the custodial symmetry. The $H^{\pm}W^{\mp}Z$ vertices are one of the phenomenological consequences of the custodial symmetry violation. We have calculated the $H^{\pm}W^{\mp}Z$ vertices at the one-loop level with the most general setup, and we have found that there are both contributions from the CP conserving and CP violating coupling constants. The scalar loop contributions disappear at the one-loop level when the custodial symmetry is respected in the Higgs potential. We have discussed the decays $H^{\pm} \to W^{\pm}Z$ in several parameter sets. We have found that the decay rates can be significantly enhanced by the loop effects of the additional scalar bosons in the most general 2HDM with the CP violation. We have also found that the asymmetry between the decay rates of $H^+ \to W^+Z$ and $H^- \to W^-Z$ can be an important observable to see the CP violating phases in the model. Finally, we have given discussions for the testability of these vertices at current and future high energy collider experiments.

Chapter 9

Landau pole problem and electroweak baryogenesis

In this chapter, we discuss ultraviolet (UV) behavior of models for EWBG. In the SM, the effective Higgs self coupling constant becomes negative at a scale between 10^9 GeV and the Planck scale [170,172]. It has been found that the electroweak vacuum is metastable [168–172]. On the other hand, new physics models with multi scalar bosons tend to induce the Landau pole, in which coupling constants in the model blow up at a scale [158, 159, 406–414]. If this scale is much smaller than the Planck scale, perturbative calculation in the model is no longer valid around the Landau pole, and we should consider a more fundamental theory beyond the Landau pole.

The reason why the Landau pole easily appears in the multi scalar models is that the beta function for the scalar boson is positive at the leading order. Furthermore, in some classes of models for EWBG, e.g. in the 2HDM, the SFOPT for providing out-of-equilibrium situation around bubble walls is caused by large corrections to the effective potential from relatively large scalar couplings. If these masses of additional scalar bosons are strongly coupled to the SM Higgs boson, the vacuum structure is changed by non-decoupling quantum effects. For these reasons, the typical scale of the Landau pole in the model for EWBG with the non-decoupling effects has been estimated at much lower than the Plank scale, i.e. TeV scale [37, 44, 415, 416]. In the 2HDM, according to Ref. [37], almost all of the successful parameter regions predict the Landau pole below 3 TeV, and it might be a reason to consider other mechanisms to cause SFOPT [75].

The ultraviolet (UV) behavior of those models can be explored based on the analysis using Renormalization Group Equations (RGEs). The energy dependence of effective coupling constants is determined by the beta function. The modified Minimal Subtraction ($\overline{\text{MS}}$) scheme [417] is one of the most famous treatments for renormalization. The beta function obtained by this scheme is a function of only the coupling constants, and masses and the renormalization scale do not explicitly appear in the beta function. This Mass-Independent (MI) beta function has been widely used to study various high energy phenomena.

However, in the analysis with the RGE in the context of EWBG, less care about threshold correction has been taken. As it will be discussed, the coupling constants defined in $\overline{\text{MS}}$ scheme are not physical directly, so that we need to match them to the physical observable with a condition. This condition is so-called matching condition, and some corrections at the threshold enter into the running of the couplings.

In the following sections, we first revisit to consider the matching condition and the threshold correction, and we then introduce momentum subtraction scheme to include finite corrections in counter terms to beta functions. We explain the mass dependence beta function in $\lambda\phi^4$ theory, which is obtained by the application of the momentum subtraction scheme. We apply

this scheme to a pure scalar toy model, in which we can consider the non-decoupling situation, deriving the mass dependent beta function. We also apply to more the realistic extended Higgs model, the Inert doublet model, to estimate the scale of the Landau pole. In the end of this chapter, discussions and a short summary are given.

9.1 Matching condition and threshold correction

The effective coupling constants in the MI scheme are not directly connected to physical observables. In addition, in the method using the MI beta function, there is no mechanism to treat the effect of the appearance of a heavy particle around the scale of that particle's mass. Therefore, to calculate running coupling constants from a low energy effective theory to a theory where heavy particles become active, matching conditions for the coupling constants have to be taken into account. This is so-called Threshold Correction (TC) [418,419], where the effects of heavy particles are switched on through the use of a step function in the beta function.

We briefly explain the TC and the beta function in the $\overline{\rm MS}$ scheme. A bare parameter θ^0 is expressed by scale dependent $\theta(\mu)$ and scale independent $\theta_{\rm OS}$, which are defined in the $\overline{\rm MS}$ scheme and the On-Shell (OS) scheme, respectively. We have a relation

$$\theta^0 = \theta^{\rm OS} - \delta\theta^{\rm OS} = \theta(\mu) - \delta\theta^{\overline{\rm MS}}, \tag{9.1}$$

where the counter term $\delta\theta^{\overline{\rm MS}}$ ($\delta\theta^{\rm OS}$) contains only a divergence (a divergence and finite parts). At a scale $\mu = Q_m$, the $\overline{\rm MS}$ parameter is matched to the observable by using the matching condition

$$\theta(\mu = Q_m) = \theta^{\rm OS} + \delta\theta^{\overline{\rm MS}} - \delta\theta^{\rm OS} \equiv \theta^{\rm OS} + \Delta\theta, \tag{9.2}$$

where $\Delta\theta$ is a finite correction beyond the one-loop level.

We suppose a U(1) gauge theory where a heavy fermion ψ with the mass M couple to the gauge field. We also suppose massless particles also couple to the gauge field. We denote the contribution to the beta function for the gauge coupling g from the light particles as $g^2 b_0$, and from ψ as $g^2 b_1$. The $\overline{\rm MS}$ beta function is given by $\beta_g = dg/d\ln\mu = g^2(b_0 + b_1)$. On the other hand, if we consider the effective field theory [418,419] by integrating out ψ, we get $\beta_g^{\rm IR} = b_0$. By using the matching condition, the gauge coupling is connected to the observable, and we use $g(Q_m \simeq M) = g_{obs}$ as the tree level condition. Based on this boundary condition, we can solve the beta function as

$$\frac{1}{g_{obs}} = \frac{1}{g(Q_0)} - b_0 \log\frac{Q_m}{Q_0}, \tag{9.3}$$

for $Q_0 < \mu < Q_m$, and

$$\frac{1}{g(\Lambda)} = \frac{1}{g_{obs}} - \Big(b_0 + b_1\Big)\log\frac{\Lambda}{Q_m}, \tag{9.4}$$

for $Q_m < \mu < \Lambda$. As a result, we have

$$\frac{1}{g(Q_0)} = \frac{1}{g(\Lambda)} - \Big(b_0 + b_1\Big)\log\frac{Q_m}{\Lambda} - b_0\log\frac{Q_0}{Q_m}. \tag{9.5}$$

This result is same as the one using

$$\beta_g = b_0 + b_1\theta(\mu/M), \tag{9.6}$$

where $\theta(\mu/M)$ is the Heaviside step function. If we use the matching condition at the one-loop level, higher order corrections enter in the discussion.

In discussions of grand unified theories [420–424], it has been shown that the TC of the heavy particles plays an important role. For example, when we discuss the renormalization group analysis at the one-loop level, the tree level TC is often used [418], as we have shown. However, the non-zero probability to find the particle in loop diagrams below that mass scale is not taken into account. If we choose a different matching scale, a logarithmic difference arises [425]. Furthermore, additional errors from higher-order loop corrections $\Delta\theta$ can enter into the matching conditions when the MI coupling constants are expressed in terms of the physical observables, as indicated in Refs. [419] and [170, 425, 426]. Therefore, many efforts have been made to reduce these uncertainties by taking into account the higher order TCs.

On the contrary, in the momentum subtraction (MOM) renormalization scheme, the coupling constants are directly connected to the physical observables, and the threshold effects are included in the counter term in a natural way. As a result, in the method using the Mass-Dependent (MD) beta function, which is obtained by the MOM scheme, the quantum effects of heavy particles are automatically included. Therefore, the MD beta functions do not suffer from the uncertainty of the TC. Actually, an analysis in the MOM scheme is more complicated than one in the MI scheme because finite parts are included in the counter terms. For instance, in the massless QCD theory, the $\overline{\rm MS}$ beta function is available at the five-loop level [427–430], in contrast, the MOM beta function at the four-loop level from the three-loop vertex functions has been calculated [431]. Nevertheless, the MOM scheme is useful in some cases. As we will discuss in this chapter, the MOM scheme is advantageous when new particles with multiple scales appear in a theory, or when coupling constants in the MI scheme may blow up at relatively low energies. This method has been used in early studies [432, 433] to discuss the energy dependence of the effective QCD coupling constant for different numbers of quarks in the theory. In addition, the electroweak running coupling constants [434] and the vacuum stability [426] in the SM, the proton decay [435] and unification of the coupling constants [434, 436–439] in grand unified theories, etc., have also been studied using this method. However, it has not yet been applied to the physics of extended Higgs sectors.

9.2 Mass-dependent beta function

In order to introduce the MD beta function, we first consider the $\lambda\phi^4$ scalar theory with mass m. The Lagrangian is given by

$$\mathcal{L} = \frac{1}{2}\partial_\mu\phi\partial^\mu\phi - \frac{1}{2}m^2\phi^2 - \frac{1}{4!}\lambda\phi^4, \tag{9.7}$$

The renormalization conditions for the n-point vertex function $\Gamma^{(n)}_{\phi\cdots\phi}(k_a, m^2, \lambda)$ are given by

$$\Gamma^{(2)}_{\phi\phi}\Big|_{k^2=m^2} = 0, \quad \frac{\partial}{\partial k^2}\Gamma^{(2)}_{\phi\phi}\Big|_{k^2=-Q^2} = 1, \quad \Gamma^{(4)}_{\phi\phi\phi\phi}\Big|_{k_a\cdot k_b=-Q^2\delta_{ab}+\frac{1}{3}Q^2(1-\delta_{ab})} = -\lambda, \tag{9.8}$$

where k_a $(a = 1, \cdots, n)$ are the external momenta. The equations in the first line are the conditions for the mass parameter m to be the pole mass and for the wave function to be unity at $k^2 = -Q^2$. The equation in the second line is the condition that the four-point function coincides with the tree level value at the symmetric point, where $k_a \cdot k_b = -Q^2\delta_{ab} + \frac{1}{3}Q^2(1-\delta_{ab})$ are satisfied. The UV divergence in the four-point function is renormalized in the MOM scheme. From these renormalization conditions, at the one-loop level, we obtain the MD beta function as

$$\beta\Big(\lambda, \frac{Q}{m}\Big) = \frac{3\lambda^2}{16\pi^2}\Big[-\frac{1}{2}\mathcal{D}_Q B_0\Big(-\frac{4}{3}Q^2, m^2, m^2\Big)\Big], \tag{9.9}$$

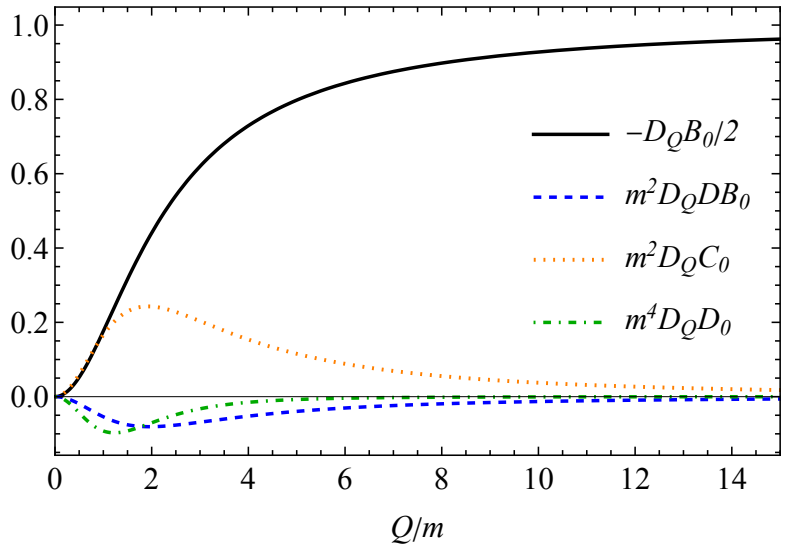

Figure 9.1: Derivatives with $\mathcal{D}_Q \equiv Q(\partial/\partial Q)_0$ of $-B_0/2$ (black solid), $m^2 DB_0 (DB_0 \equiv \partial B_0/\partial k^2)$ (blue dashed), $m^2 C_0$ (orange dotted) and $m^4 D_0$ (green dot-dashed). For $Q/m \to 0$, corresponding to the particle decoupling from diagrams, these functions become 0. For $Q/m \to \infty$, only $-\mathcal{D}_Q B_0/2$ becomes 1 and the other functions become 0.

where B_0 is the Passarino–Veltman two-point scalar function [400, 401], which contains an UV logarithmic divergence. We define $\mathcal{D}_Q \equiv Q(\partial/\partial Q)_0$, where the subscript zero means derivative for the fixed bare parameters. As a function of Q/m, the quantity $-\mathcal{D}_Q B_0/2$ in Eq. (9.9) is shown in figure 9.1 as the black solid line. This quantity takes a value between 0 and 1 for $0 < Q/m < \infty$, and represents how the particle with mass m contributes to the beta function at the scale Q. If we take the limit $Q/m \to \infty$, Eq. (9.9) coincides with the well-known form given in the MI scheme (e.g., the $\overline{\text{MS}}$ scheme). In the $\overline{\text{MS}}$ scheme, only the coefficients of $1/\epsilon = 2/(4-D)$ (D is the space-time dimension), in the vertex functions are relevant to the beta function. In the limit $Q/m \to \infty$, $B_0 = 2(1/\epsilon - \log Q) + c$ is shown with a constant c. Therefore, the quantity $-\mathcal{D}_Q B_0/2$ becomes unity in this limit, and the MD beta function coincides with the $\overline{\text{MS}}$ beta function obtained by the coefficients of $1/\epsilon$. On the other hand, in the $\lambda\phi^4$ theory, the beta function is 0 for $Q/m \to 0$ because the quantum effect of the particle to the beta function decouples. In figure 9.1, we also show the lines corresponding to derivatives with $\mathcal{D}_Q$ of $m^2 DB_0 (DB_0 \equiv \partial B_0/\partial k^2)$ (blue dashed), $m^2 C_0$ (orange dotted) and $m^4 D_0$ (green dot-dashed), where C_0 and D_0 are the Passarino–Veltman three and four point scalar functions, respectively.

In the following, we apply the MD beta function to extended Higgs models. We are interested in the case where additional scalar bosons obtain masses mainly from the electroweak symmetry breaking. Such a case is relevant for the realization of the SFOPT [51–53]. We then show the importance of the method using the MD beta function, in which the decoupling mechanism of heavy particles is naturally equipped.

We here give a comment on the dependence of the renormalization scheme. Although the explicit form of the vertex functions is different among different renormalization schemes, physical observables are scheme-independent. However, due to the truncation at a finite order of perturbative calculation, different results can appear depending on the scheme. For example, it has been known that the scale dependence of the QCD coupling constant is different between the $\overline{\text{MS}}$ scheme and the MOM scheme at the two-loop level [440]. By taking into account higher order corrections from higher loop diagrams, the scheme difference becomes milder [441, 442].

9.3 A toy model: Simplest example of the non-decoupling case

In this section, we discuss a scalar toy model to explain our method, in which only two complex scalar fields, ϕ_1 and ϕ_2, are introduced. We impose two global symmetries, $\mathrm{U}(1)_1$ and $\mathrm{U}(1)_2$, with the transformations $\phi_1 \to \phi_1 e^{i\theta_1}$ and $\phi_2 \to \phi_2 e^{i\theta_2}$ ($\theta_{1,2} \in \mathbb{R}$), respectively. The renormalizable Lagrangian is given by

$$\begin{aligned}\mathcal{L} = &\partial_\mu \phi_{1,b}^\dagger \partial^\mu \phi_{1,b} + \partial_\mu \phi_{2,b}^\dagger \partial^\mu \phi_{2,b} - \mu_{1,b}^2 \phi_{1,b}^\dagger \phi_{1,b} - \mu_{2,b}^2 \phi_{2,b}^\dagger \phi_{2,b} \\ &- \frac{1}{2}\lambda_{1,b}|\phi_{1,b}|^4 - \frac{1}{2}\lambda_{2,b}|\phi_{2,b}|^4 - \lambda_{3,b}|\phi_{1,b}|^2|\phi_{2,b}|^2,\end{aligned} \tag{9.10}$$

where μ_i^2 ($i = 1, 2$) and λ_j ($j = 1, 2, 3$) are real parameters, and the subscript b represents the bare parameter. We assume that $\mathrm{U}(1)_1$ is spontaneously broken while $\mathrm{U}(1)_2$ is not: i.e., $\mu_1^2 < 0$ and $\mu_2^2 > 0$.

At the tree level, the subscript b can be dropped. We parametrize the field ϕ_1 as

$$\phi_1 = \frac{1}{\sqrt{2}}(v + \rho + i\eta), \tag{9.11}$$

where v is the Vacuum Expectation Value (VEV). The stationary condition gives a relation among the parameters:

$$\left.\frac{\partial V}{\partial \rho}\right|_{\{\rho,\eta,\phi_2\}=\mathbf{0}} = 0 \;\Leftrightarrow\; v^2 = \frac{-2\mu_1^2}{\lambda_1}. \tag{9.12}$$

By using this tree-level relation, we can change the set of free parameters from $(\mu_1, \mu_2, \lambda_1, \lambda_2, \lambda_3)$ to $(v, \mu_2, \lambda_1, \lambda_2, \lambda_3)$. Masses of the physical states ρ, η and ϕ_2 are given by

$$\begin{aligned}&m_\rho^2 = \lambda_1 v^2, \quad m_\eta^2 = 0, \\ &m_{\phi_2}^2 = \mu_2^2 + \frac{1}{2}\lambda_3 v^2.\end{aligned} \tag{9.13}$$

The field η is the NG boson related to the spontaneous breaking of $\mathrm{U}(1)_1$.

In the case of $\mu_2^2 \gg \lambda_3 v^2 \simeq \lambda_1 v^2$, we have $m_{\phi_2}^2 \simeq \mu_2^2$ ($\gg m_\rho^2$). The coupling constants λ_j are independent of $|\mu_2| \simeq m_{\phi_2}$, and in the low energy region $Q \ll m_{\phi_2} \simeq |\mu_2|$, the effect of m_{ϕ_2} only appears in the internal propagators of the vertex functions for ρ and η [443]. The finite correction from ϕ_2 takes a form of some powers of $1/\mu_2^2$ because the internal propagator is given by $1/(m_{\phi_2}^2 - k^2) \simeq 1/m_{\phi_2}^2$, where k is the relevant momentum. As a result, the effective theory is described by the renormalized Lagrangian in which ρ and η fields participate while ϕ_2 does not.

On the contrary, if $m_{\phi_2}^2$ is mainly given by $\lambda_3 v^2 (\gtrsim \mu_2^2)$, quantum corrections to the low energy observables do not decouple in the large mass limit. This is what we call the non-decoupling effect. Non-decoupling quantum effects of ϕ_2 can appear as powerlike or logarithmic mass contributions [221]. In such a case, λ_3 is relatively large at low energy scales, so that it can quickly blow up at high energies. In other words, if we impose the requirement that the coupling constants do not exceed a critical value (such as 4π) below a cutoff scale Λ, the coupling constants are constrained from above as a function of Λ. Such a theoretical bound is called the triviality bound [444].

9.3.1 Renormalization conditions

In the following, we perform a renormalization group analysis with the MD beta function and give a constraint from the triviality bound at the one-loop level. We define seven renormalization constants as

$$\begin{aligned}
&\phi_1 = Z_{\phi_1}^{-\frac{1}{2}}\phi_{1,b}, \quad \phi_2 = Z_{\phi_2}^{-\frac{1}{2}}\phi_{2,b}, \\
&\mu_1^2 = Z_{\mu_1}^{-1}Z_{\phi_1}\mu_{1,b}^2, \quad \mu_2^2 = Z_{\mu_2}^{-1}Z_{\phi_2}\mu_{2,b}^2, \\
&\lambda_1 = Z_{\lambda_1}^{-1}Z_{\phi_1}^2\lambda_{1,b}, \quad \lambda_2 = Z_{\lambda_2}^{-1}Z_{\phi_2}^2\lambda_{2,b}, \quad \lambda_3 = Z_{\lambda_3}^{-1}Z_{\phi_1}Z_{\phi_2}\lambda_{3,b}.
\end{aligned} \tag{9.14}$$

They are determined by seven renormalization conditions.

First, the renormalized VEV is defined as the right-hand side of Eq. (9.12) with the renormalized coupling constants, and we define the renormalized shifted fields as $\phi_1 = (v+\rho+i\eta)/\sqrt{2}$. The tadpole term for the field ρ, which is proportional to $Z_{\mu_1} - Z_{\lambda_1}$, appears in the Lagrangian. We impose a renormalization condition that the left-hand side of Eq. (9.12) is satisfied at the one-loop level. The tadpole term is eliminated by this condition, and then m_η is kept to be zero at the one-loop level.

Second, we set the renormalization conditions as

$$\begin{aligned}
&\Gamma^{(2)}_{\rho\rho}\Big|_{k^2=m_\rho^2} = \Gamma^{(2)}_{\phi_2\phi_2^\dagger}\Big|_{k^2=m_{\phi_2}^2} = 0, \\
&\frac{\partial}{\partial k^2}\Gamma^{(2)}_{\rho\rho}\Big|_{k^2=-Q^2} = \frac{\partial}{\partial k^2}\Gamma^{(2)}_{\phi_2\phi_2^\dagger}\Big|_{k^2=-Q^2} = 1,
\end{aligned} \tag{9.15}$$

where the first and second lines are the pole mass conditions and the wave function renormalization conditions, respectively. From the pole mass conditions, we obtain $\mathcal{D}_Q m_\rho^2 = \mathcal{D}_Q m_{\phi_2}^2 = 0$.

Finally, we impose two conditions for Z_{λ_3} and Z_{λ_2} as

$$\Gamma^{(4)}_{\rho\rho\phi_2\phi_2^\dagger}\Big|_{k=\text{sym.}} = -\lambda_3, \quad \Gamma^{(4)}_{\phi_2\phi_2^\dagger\phi_2\phi_2^\dagger}\Big|_{k=\text{sym.}} = -2\lambda_2, \tag{9.16}$$

where the renormalization point is the symmetric point. At this point, the four-point functions coincide with the tree-level values. In appendix F, explicit formulae for these vertex functions are shown at the one-loop level.

9.3.2 Renormalization group equation analysis

With the renormalization conditions imposed above, we derive the RGE for the renormalized effective action Γ. The relation between the renormalized action depending Q and the bare action regularized by dimensional regularization scheme is

$$\Gamma\big(\phi_1, \phi_2; \mu_1^2, \mu_2^2, \lambda_1, \lambda_2, \lambda_3; Q\big) = \Gamma_0\big(\phi_{1,b}, \phi_{2,b}; \mu_{1,b}^2, \mu_{2,b}^2, \lambda_{1,b}, \lambda_{2,b}, \lambda_{3,b}; \epsilon\big), \tag{9.17}$$

By acting $\mathcal{D}_Q$ on this equation, we have

$$\begin{aligned}
&D_Q\Gamma = 0 \\
&\Leftrightarrow \left(\frac{\partial}{\partial Q} - \sum_{i=1,2}\gamma_{\phi_i}\phi_i\frac{\delta}{\delta\phi_i} - \gamma_{m_\rho}m_\rho^2\frac{\partial}{\partial m_\rho^2} - \gamma_{m_{\phi_2}}m_{\phi_2}^2\frac{\partial}{\partial m_{\phi_2}^2} + \sum_{j=1,2,3}\beta_j\frac{\partial}{\partial\lambda_j}\right)\Gamma = 0,
\end{aligned} \tag{9.18}$$

where

$$\gamma_{\phi_i} = -\mathcal{D}_Q\ln\phi_i, \quad \gamma_{m_\rho} = -\mathcal{D}_Q\ln m_\rho^2, \quad \gamma_{m_{\phi_2}} = -\mathcal{D}_Q\ln m_{\phi_2}^2, \quad \beta_{\lambda_j} = \mathcal{D}_Q\lambda_j. \tag{9.19}$$

Here we have changed independent parameters from (μ_1^2, μ_2^2) to $(m_\rho^2, m_{\phi_2}^2)$. We can show $\gamma_{m_\rho} = \gamma_{m_{\phi_2}} = 0$ by using the renormalization conditions for the tadpole and the mass term. Therefore, we obtain

$$\left(Q\frac{\partial}{\partial Q} - \sum_{i=1,2}\gamma_{\phi_i}\phi_i\frac{\delta}{\delta\phi_i} + \sum_{j=1,2,3}\beta_{\lambda_j}\frac{\partial}{\partial\lambda_j}\right)\Gamma = 0. \tag{9.20}$$

At the one-loop level, β_{λ_j} $(j = 1, 2, 3)$ are given by

$$\begin{aligned}
\beta_{\lambda_1} &= \frac{1}{16\pi^2}\mathcal{D}_Q(DB_0, C_0, D_0 \text{ terms}),\\
\beta_{\lambda_2} &= \frac{1}{16\pi^2}\left\{\lambda_3^2 + \lambda_3^2 f^Q_{m_\rho,m_\rho} + 10\lambda_2^2 f^Q_{m_{\phi_2},m_{\phi_2}} + \mathcal{D}_Q(DB_0, C_0, D_0 \text{ terms})\right\},\\
\beta_{\lambda_3} &= \frac{1}{16\pi^2}\left\{\lambda_1\lambda_3 + 3\lambda_1\lambda_3 f^Q_{m_\rho,m_\rho} + 4\lambda_3^2 f^Q_{m_{\phi_2},m_\rho} + 4\lambda_2\lambda_3 f^Q_{m_{\phi_2},m_{\phi_2}} + \mathcal{D}_Q(DB_0, C_0, D_0 \text{ terms})\right\}.
\end{aligned} \tag{9.21}$$

We have defined mass dependent functions

$$f^Q_{m,m} \equiv -\frac{1}{2}\mathcal{D}_Q B_0\Big(-\frac{4}{3}Q^2, m^2, m^2\Big). \tag{9.22}$$

Each $\mathcal{D}_Q DB_0$, $\mathcal{D}_Q C_0$, $\mathcal{D}_Q D_0$ terms in each β_{λ_j} is different, and the full expressions can be obtained by using the formulae shown in appendix F. As shown in figure 9.1, only the derivative of B_0, namely $f^Q_{m,m}$, is relevant to the beta functions in the limit $Q/m \to \infty$, while the other functions $\mathcal{D}_Q DB_0, \mathcal{D}_Q C_0$ and $\mathcal{D}_Q D_0$ are not. This is because, in this limit, DB_0, C_0 and D_0 are constants. Although the beta functions β_{λ_2} and β_{λ_3} depend on Q/m, they coincide with the MI beta functions in the high energy limit because $f^Q_{m,m} \to 1$ as $Q/m \to \infty$. In the limit $Q/m \to 0$, the effect from the massive particles decouples, and only the UV divergent diagrams, in which the NG bosons are involved, contribute to β_{λ_2} and β_{λ_3}. In the numerical analysis below, we include the contributions from $\mathcal{D}_Q(DB_0, C_0, D_0 \text{ terms})$ in the MD beta functions.

Since we have imposed the tadpole condition in Eq. (9.12) and the on-shell condition for m_ρ in Eq. (9.15), β_{λ_1} is asymptotically zero for $Q/m \to \infty$ in this model. On the other hand, $\Gamma^{(4)}_{\rho\rho\rho\rho}$ depends on the external momenta, and corrections of $O(\frac{\lambda}{16\pi^2}\log s/m_\rho^2)$ arise at the one-loop level, where $\sqrt{s}$ is the center-of-mass energy of the scattering $\rho\rho \to \rho\rho$. In the following, we do not consider this four point vertex function, and only focus on the energy dependence of $\lambda_j (j = 1, 2, 3)$.

In order to obtain analytic formulae for the vertex functions, we use `FeynCalc` [445–447], `FeynArts` [448, 449] and `FeynRules` [450, 451]. For the numerical value of the Passarino–Veltmann functions, we use the `LoopTools` [452] and `FeynHelpers` packages [453].

In figure 9.2, the scale dependence of λ_3 and λ_2 with the MD beta functions are shown as the blue and orange solid lines, respectively. We take the input parameters as $(v, m_\rho, m_{\phi_2}) = (246, 125, 400)$ GeV. We consider the non-decoupling case with large λ_3, and we set $\lambda_3(Q_0) = 5.3$ and $\lambda_2(Q_0) = 0.01$ as input values at $Q = Q_0 \equiv 90$ GeV. The dashed lines are the solutions of the MI beta functions obtained by the $\overline{\text{MS}}$ scheme.

We define the scale $\Lambda_{4\pi}$ at which the largest coupling constant in the model becomes 4π. As we can see from figure 9.2, the MI beta functions imply that $\Lambda_{4\pi}$ is around 3 TeV. With the MD beta functions, however, we obtain $\Lambda_{4\pi} \simeq 60$ TeV. This is because the MD beta functions include the reduction factor $f^Q_{m,m}$ for the heavy particles. Consequently, the running of the coupling constants is delayed. Even if λ_2 is taken to be large at $Q = Q_0$, this behavior of the delayed running is unchanged. As we see in the next section, the scheme difference of the running coupling constants is prominent for the non-decoupling case.

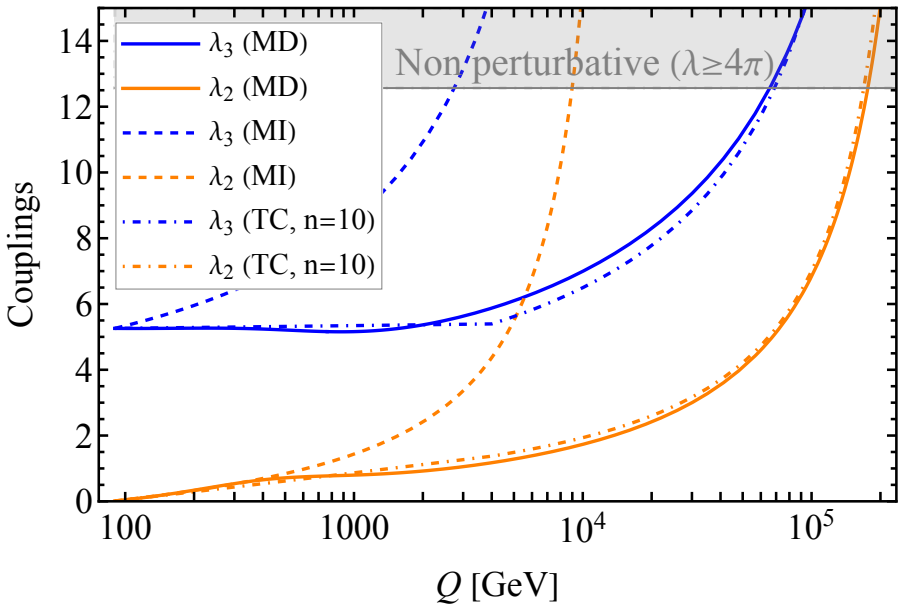

Figure 9.2: Energy dependence of λ_3 (blue) and λ_2 (orange) with the MD (solid), MI (dashed) and TC (dot-dashed) beta functions in the $\mathrm{U}(1)_1 \times \mathrm{U}(1)_2$ model. With the MD beta functions, which include a decoupling mechanism of the heavy particles by the factor $f^Q_{m,m}$, the scale $\Lambda_{4\pi}$ shifts to the high energy region, as compared to that found with the MI beta functions.

In figure 9.2, we also show the case with the improved MI beta functions, in which the TC is added by hand, as dot-dashed lines. As the tree-level TC, the Heaviside step function $\theta(Q/m)$ is often used in the beta function to include a contribution from particles with the mass m [454]. Generalizing this, we define the function $\theta^n(Q/m_{\phi_2})$ which takes 1 (0) for $Q \geq nm_{\phi_2}$ ($Q < nm_{\phi_2}$). The improved MI beta functions of λ_j are given by

$$\begin{aligned}
\beta^{\mathrm{TC}}_{\lambda_1} &= \frac{1}{16\pi^2}\left(10\lambda_1^2 + 2\lambda_3^2\theta^n\right), \\
\beta^{\mathrm{TC}}_{\lambda_2} &= \frac{1}{16\pi^2}\left(10\lambda_2^2\theta^n + 2\lambda_3^2\right), \\
\beta^{\mathrm{TC}}_{\lambda_3} &= \frac{1}{16\pi^2}\left(4\lambda_1\lambda_3 + 4(\lambda_2\lambda_3 + \lambda_3^2)\theta^n\right).
\end{aligned} \tag{9.23}$$

In figure 9.2, the solutions of the MI beta functions with the TC are shown for $n = 10$ as the dot-dashed lines. The value of $\Lambda_{4\pi}$ obtained by the TC beta function with $n = 10$ is the closest to the value found from the MD beta function among $n \in \mathbb{Z}$. From figure 9.2, it can be seen that the delay of the running couplings in $Q \lesssim m$ is realized by using this step function approximation.

We note that the treatment of the TC with one matching scale contains uncertainty where we insert the threshold step function [425]. The delayed running in the scheme with the MD beta function is a model independent result. On the contrary, in the analysis with the TC beta functions, the optimized value of n chosen to provide same $\Lambda_{4\pi}$ as in the MD beta function depends on the input parameters or the models. Therefore, for more realistic models in which multiple heavy particles with different masses are introduced, using the TC beta function becomes rather complicated. On the other hand, by using our scheme with the MD beta function, the treatment for such a case becomes much simpler.

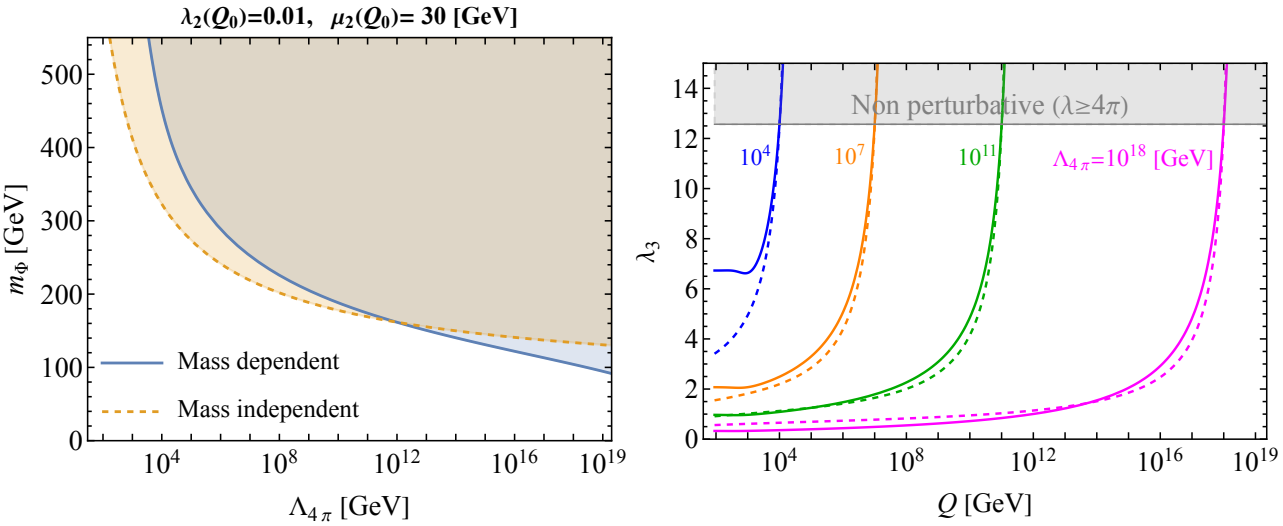

Figure 9.3: Left: Triviality bound for the degenerated masses of the additional scalar bosons m_Φ in the IDM as a function of $\Lambda_{4\pi}$. The blue solid and orange dashed lines show the results with the MD beta function and the MI beta function without the TC, respectively. Right: The energy dependence of λ_3 for each fixed value of $\Lambda_{4\pi}$, i.e., 10^4 (blue), 10^7 (orange), 10^{11} (green) and 10^{18} GeV (magenta). The solid and dashed lines are obtained by using the MD beta function and the MI beta function without the TC, respectively. Due to the delayed running with the reduction factor $f^Q_{m,m}$ in the MD beta function, the scheme difference stands out for the small cutoff scale, namely, $\Lambda_{4\pi} = 10^4$ GeV.

9.4 Application to extended Higgs models

In this section, we apply our method to the extended Higgs model. We consider the IDM [150], in which an additional $\mathrm{SU}(2)_L$ scalar doublet η is added to the SM, which is odd under the unbroken Z_2 symmetry. The potential is given by

$$\begin{aligned} V &= \mu_1^2|\Phi|^2 + \mu_2^2|\eta|^2 + \frac{1}{2}\lambda_1|\Phi|^4 + \frac{1}{2}\lambda_2|\eta|^4 \\ &+ \lambda_3|\Phi|^2|\eta|^2 + \lambda_4|\Phi^\dagger\eta|^2 + \frac{\lambda_5}{2}\left((\Phi^\dagger\eta)^2 + \text{h.c.}\right), \end{aligned} \tag{9.24}$$

where Φ corresponds to the SM Higgs doublet. The coupling constants $\lambda_{1,2,3,4,5}$ are real. Taking $\mu_1^2 < 0$ and $\mu_2^2 > 0$, the electroweak symmetry is spontaneously broken.

We parametrize the fields as

$$\Phi = \begin{pmatrix} G^+ \\ \frac{1}{\sqrt{2}}(v + h + iG^0) \end{pmatrix}, \quad \eta = \begin{pmatrix} H^+ \\ \frac{1}{\sqrt{2}}(H + iA) \end{pmatrix}, \tag{9.25}$$

where v $(= \sqrt{-2\mu_1^2/\lambda_1})$ is the VEV, h is the SM Higgs boson, H and A are Z_2-odd neutral scalar bosons, and $H^\pm$ are the Z_2-odd charged scalar bosons. $G^\pm$ and G^0 are the NG bosons absorbed as the longitudinal modes of the weak gauge bosons. Squared masses are given by $m_h^2 = \lambda_1 v^2$, $m_{H^\pm}^2 = \mu_2^2 + \frac{1}{2}\lambda_3 v^2$ and $m_{H,A}^2 = m_{H^\pm}^2 + \frac{1}{2}(\lambda_4 \pm \lambda_5)v^2$ with the sign $+(-)$ for $H(A)$.

The discussion for the MD beta function is the same as the case of the toy model except for the following points: (i) λ_4 and λ_5 cause a mass difference among the additional neutral scalar bosons. By performing the renormalization of m_H and m_A as the pole masses, $\mathcal{D}_Q(\lambda_4 v^2) = \mathcal{D}_Q(\lambda_5 v^2) = 0$ are shown. As a result, $\beta_{\lambda_4}/\lambda_4$ and $\beta_{\lambda_5}/\lambda_5$ are equal to $\beta_{\lambda_1}/\lambda_1$. (ii) Masses of the W and Z bosons and the top quark t are renormalized on mass-shell, so that the beta functions of the gauge coupling constants (g_1 and g_2) and the top-Yukawa coupling constant

(y_t) are related to that of λ_1; i.e., $2\beta_{g_1}/g_1 = 2\beta_{g_2}/g_2 = 2\beta_{y_t}/y_t = \beta_{\lambda_1}/\lambda_1$. (iii) The Slavnov–Taylor identity [455, 456] among the renormalization constants does not hold in the MOM scheme. This difficulty can be avoided [457] by using the background field method [458–461]. We here choose the Feynman gauge for the internal propagators in the vertex functions. We construct the model files for `FeynRules` for the IDM with the background field method based on Ref. [462].

In the IDM, one-loop effects of additional scalar bosons give positive contributions to the beta functions of the scalar coupling constants. If they are relatively large at the electroweak scale, the Landau pole can appear below the Planck scale. Then, m_H, m_A and $m_{H^\pm}$ are constrained by the triviality bound [158, 159, 406–414].

In the left panel of figure 9.3, the triviality bound is shown as a function of $\Lambda_{4\pi}$ for the degenerated masses ($m_\Phi \equiv m_H = m_A = m_{H^\pm}$). The solid and dashed lines are obtained by the MD beta function and the MI beta function without the TC, respectively. We take $\lambda_2(Q_0) = 0.01$ and $\mu_2(Q_0) = 30$ GeV as the input, so that the non-decoupling situation is realized by a large m_Φ. As shown in figure 9.3, for both the MI and MD beta functions, a larger m_Φ predicts a lower $\Lambda_{4\pi}$. Remarkably, the scheme difference of the upper bound for fixed $\Lambda_{4\pi}$ is significant, especially in such a non-decoupling case.

In the right panel of figure 9.3, the energy dependence of λ_3 is shown for each fixed cutoff scale $\Lambda_{4\pi} = 10^4$ (blue), 10^7 (orange), 10^{11} (green) and 10^{18} GeV (magenta). As we can see from the blue lines in this figure, when $\lambda_3(Q_0)$ is large with the fixed relatively small value of $\mu_2(Q_0)$ (= 30 GeV), the scalar coupling constants quickly blow up for the MI beta function without the TC. However, because the MD beta functions are relatively small in low energy regions due to the reduction factor $f^Q_{m,m}$, a weaker triviality bound is predicted for lower $\Lambda_{4\pi}$. As a result, we can see the conspicuous difference in the lower $\Lambda_{4\pi}$ region.

We note that in the IDM a similar non-decoupling effect can also be realized when a large mass difference appears among the additional scalar bosons. Such a large mass difference affects β_{λ_3} and β_{λ_2}, causing these coupling constants to rapidly blow up. Even in this case, $\Lambda_{4\pi}$ calculated by the MD beta functions is higher than that calculated by the MI beta functions. If a mass difference among the additional scalar bosons is large enough that λ_4 or λ_5 is nearly 4π at the renormalized point Q_0, quantum corrections to the related vertex functions become large. Consequently, perturbative calculation breaks down as external momenta grow.

9.5 Discussions and conclusions

We here give comments on the results.

First, as shown in figs. 9.2 and 9.3, the difference in the triviality bounds found from the MI and MD beta functions becomes large in the non-decoupling case. This is because the threshold effects are automatically included in the MD beta function. The importance of the delayed running of the coupling constants can be understood as follows. The MI beta function of the scalar field with the coupling λ can be written as $\beta_\lambda \simeq c\lambda^2$ with a positive constant c. On the other hand, for the analysis using the MD beta function with the automatically included delayed running, the initial value of the MD coupling that results in the same $\Lambda_{4\pi}$ as the MI scheme satisfies the relation,

$$\lambda(Q_0)^{\rm MD} - \lambda(Q_0) = \frac{c\lambda(Q_0)^2 \log\frac{Q_1}{Q_0}}{1 - c\lambda(Q_0)\log\frac{Q_1}{Q_0}}, \tag{9.26}$$

where Q_0 is the renormalization scale, and $Q_1 (> Q_0)$ is the scale where the running begins in the analysis based on the MD beta function. The left-hand side describes the difference in the triviality bound between the renormalization schemes. The right-hand side is the monotonic

increasing function for the initial value $\lambda(Q_0)$ within the perturbative region. Therefore, for the case of the non-decoupling situation where $\lambda(Q_0)$ is relatively large, the difference in the triviality bound becomes large due to the delayed running in the MD scheme. In this scheme, such delayed running is automatically included, because the threshold effect appears in the counter term. We emphasize that both methods are, in principle, equivalent in the end. However, in the case with multiple new particles, an analysis using the MD beta functions is useful because complicated treatment of the TCs can be avoided.

In this section, the MD beta functions are evaluated at the one-loop level, but our method can also be applied to higher loop corrections. From an analysis using the MI beta functions at the two-loop level, it has been known that $\Lambda_{4\pi}$ can be higher than that of the one-loop level in the two Higgs doublet model [411]. Traditionally, for the two-loop MI beta function, the one-loop level TC is used [419]. Recently, however, it has been indicated by J. Braathen et al. [425] that in the non-decoupling case, an n-loop level TC should be used for an n-loop level beta function. It is known that $\Lambda_{4\pi}$ is larger when taking into account a higher order TC, because a higher order TC tends to make the MI parameters corresponding to physics quantities smaller. Therefore, it is expected that predictions from the one-loop MI scheme (using one-loop beta functions with one-loop TCs) will approach the results found from the one-loop MD scheme. We also expect that these scheme differences can be reduced by taking into account higher order corrections, as in the case of the QCD coupling constant [441, 442].

For the phenomenological aim of evaluating the energy upper bound in models for non-decoupling physics, e.g., that for EWBG, our one-loop analysis gives a very important insight. In this chapter, the difference between the MOM scheme and the MI scheme without the TC is shown to be large at the one-loop level. As a result, the previous argument based on the MI beta function at the one-loop level [37, 44], as we have mentioned before, would be modified. This modification is the result of our physical MD beta function, in which the threshold effects are naturally included.

9.6 Short summary of chapter 9

In this chapter, the UV behavior of the effective coupling constants in the extended Higgs models has been discussed by using RGEs with the MD beta functions. We first have demonstrated how to evaluate the effective coupling constants in the $U(1)_1 \times U(1)_2$ model, in which non-decoupling situation can be considered. We then have applied our method to the IDM. We have found that $\Lambda_{4\pi}$ evaluated with the MD beta functions is higher than that obtained with the MI beta functions without the TC, in cases where the non-decoupling effect is important.

Chapter 10

Grand summary

In this chapter, we summarize this Ph.D thesis.

In chapter 2, we have reviewed the Glashow–Weinberg–Salam theory and the quantum-chromo-dynamics, which describe the theory of the electroweak and strong interactions. We also have reviewed experimental results for the Higgs boson, and currently those results are consistent with the SM. In chapter 3, we have introduced the problems beyond the SM, the origin of tiny neutrino mass, the relic abundance of the DM, and the baryon asymmetry of the Universe. These problems cannot be solved in the SM, so that we need new physics beyond the SM. Once the Higgs sector is extended, those problems can be solved.

In chapter 4, we have defined the extended Higgs models including the 2HDM, which are motivated to solve those problems. We have started the discussions from the most general 2HDM. We then have explained the softly broken $\mathbb{Z}_2$ symmetric 2HDM and the Inert doublet model. We also have discussed the $\mathrm{U}(1)_{B-L}$ gauge extended Inert doublet model with the right-handed neutrinos.

In chapter 5, we have shown the problems of the neutrino mass and the DM can be solved in the extended Higgs model with the $\mathrm{U}(1)_{B-L}$ gauge symmetry. We have not discussed baryogenesis in this model, however, as a first step, we have found the available benchmark points for the neutrino and the DM problems under the current experiments are shown.

In chapter 6, the mechanism of EWBG has been explained and the method to calculate the BAU have been given. The necessary CP violation for EWBG can be tested by the EDM experiments, and some EWBG models are constrained by the current EDM bounds. In chapter 7, EWBG in the 2HDM has been discussed. In our model, the severe constraints from the EDM can be avoided by using destructive interference between the independent CP phases. There are two scenarios for what particles have the important role of the CP violation around the bubble wall. We have focused on the top-transport and the top-charm transport scenario in the 2HDM, and the viable scenarios have been shown. We also have discussed other phenomenology for future collider and flavor experiments and future space-based gravitational waves observables.

In chapter 8, the $H^{\pm}W^{\mp}Z$ vertices as a probe of the CP violation in the general 2HDM have been introduced. We have given the complete formulae of these vertices in the general 2HDM at the one-loop level, and have found that the asymmetry in the decays $H^+ \to W^+Z$ and $H^- \to W^-Z$ is sensitive to the CP phases in the model. This observable would be important to test the scenario of EWBG in the 2HDM in future collider experiments.

In chapter 9, we have discussed the theoretical problem of EWBG, the Landau pole problem. We have proposed the appropriate treatment of the renormalization to include the threshold corrections for analyzing the renormalization group running in the non-decoupling situation. By taking into account these threshold effects, we have found that these problems can be weaker than what was considered.

At the end of this Ph.D thesis, we clarify where each chapter stands in the research. In this

Ph.D thesis, EWBG in the extended Higgs models has mainly been discussed. EWBG is the testable scenario, so that from now on, it will be more important to study what models are viable, which parameter space of the model is survived, and how to test such regions. As we have demonstrated in chapter 7, in spite of the strong constraints from the current experiments, we still have the possibility to realize EWBG in the extended Higgs models. The EDM observables, the K and B meson physics, the GW signals, and several collider signatures, such as the triple Higgs coupling can be a key for testing EWBG. In addition, as one of the nice probes for the CP violation, we have proposed the $H^{\pm}W^{\mp}Z$ vertices in chapter 8. We expect that this observable reveal the symmetry structure of the Higgs sector in future collider experiments. We also note that the Landau pole discussed in chapter 9 can be the probe of the SFOPT needed by EWBG, as well as the triple Higgs coupling, the Higgs di-photon decay, and the GW signals. The existence of the Landau pole implying a more fundamental theory would also be tested by the future high energy experiments. In chapter 5, by the extension of the gauge group, we have shown the DM and neutrino mass problems can be solved at the TeV scale physics, which can be reached in the future collider experiments. This implies that the extended Higgs models have the possibility to solve the problems beyond the SM simultaneously. The extended Higgs models solving those problems can be a strong candidate for new physics, and such models can be settled in the future.

Appendix A

Effective potential in the two Higgs doublet model

The renormalization conditions for the effective potential are given by

$$\begin{aligned}
&\delta Z_1 v^2 = \frac{1}{v}V_{1,\varphi_1} - V_{1,\varphi_1\varphi_1}, && \delta Y_1^2 = \frac{1}{2}\left(\frac{3}{v}V_{1,\varphi_1} - V_{1,\varphi_1\varphi_1}\right),\\
&\delta Z_{6R} v^2 = \frac{1}{v}V_{1,\varphi_2} - V_{1,\varphi_1\varphi_2}, && \delta Y_{3R}^2 = \frac{1}{2}\left(\frac{3}{v}V_{1,\varphi_2} - V_{1,\varphi_1\varphi_2}\right),\\
&\delta Z_{6I} v^2 = -\frac{1}{v}V_{1,\varphi_3} + V_{1,\varphi_1\varphi_3}, && \delta Y_{3I}^2 = \frac{1}{2}\left(-\frac{3}{v}V_{1,\varphi_3} + V_{1,\varphi_1\varphi_3}\right),\\
&\delta Z_3 v^2 = -\left(V_{1,\varphi_2\varphi_2} + V_{1,\varphi_3\varphi_3}\right), && \delta Z_{5R} v^2 = -(V_{1,\varphi_2\varphi_2} - V_{1,\varphi_3\varphi_3}),\\
&\delta Z_{5I} v^2 = 2V_{1,\varphi_2\varphi_3}, &&
\end{aligned} \tag{A.1}$$

where we have denoted the derivative with respect to the VEVs as $\partial V_1/\partial\varphi = V_{1,\varphi}$.

The field dependent mass for the top quark is given by

$$\tilde{m}_t^2 = \frac{1}{2}\left\{\left(y_t\varphi_1 + |\rho_{tt}|(\cos\theta_{tt}\varphi_2 + \sin\theta_{tt}\varphi_3)\right)^2 + |\rho_{tt}|^2(\sin\theta_{tt}\varphi_2 + \cos\theta_{tt}\varphi_3)^2\right\}. \tag{A.2}$$

For the gauge bosons (W_μ^a, B_μ), the field dependent mass and the thermal corrections are

$$\tilde{m}_{\text{gauge}} = \begin{pmatrix} \frac{1}{4}g^2\phi^2 & 0 & 0 & 0\\ 0 & \frac{1}{4}g^2\phi^2 & 0 & 0\\ 0 & 0 & \frac{1}{4}g^2\phi^2 & -\frac{1}{4}gg'\phi^2\\ 0 & 0 & -\frac{1}{4}gg'\phi^2 & \frac{1}{4}g'^2\phi^2 \end{pmatrix} + \begin{pmatrix} 2g^2T^2 & 0 & 0 & 0\\ 0 & 2g^2T^2 & 0 & 0\\ 0 & 0 & 2g^2T^2 & 0\\ 0 & 0 & 0 & 2g'^2T^2 \end{pmatrix}\delta_{\mu||}, \tag{A.3}$$

where $\phi^2 \equiv \varphi_1^2 + \varphi_2^2 + \varphi_3^2$ and $||$ means the longitudinal mode. For the charged and the neutral scalar bosons, we have

$$\begin{aligned}
\tilde{m}_{G^+G^-} &= -Y_1^2 + \frac{1}{2}Z_1\varphi_1^2 + \frac{1}{2}Z_3(\varphi_2^2 + \varphi_3^2) + (Z_{6R}\varphi_2 - Z_{6I}\varphi_3)\varphi_1\\
&\quad + \frac{T^2}{24}\left(3Z_1 + 4Z_3 + 2Z_4 + 6y_t^2 + \frac{9}{2}g^2 + \frac{3}{2}g'^2\right),\\
\tilde{m}_{G^+H^-} &= -(Y_3^2)^* + \frac{1}{2}Z_4\varphi_1(\varphi_2 + i\varphi_3) + \frac{1}{2}Z_5^*\varphi_1(\varphi_2 - i\varphi_3) + \frac{1}{2}Z_6^*\varphi_1^2 + \frac{1}{2}Z_7^*(\varphi_2^2 + \varphi_3^2)\\
&\quad + \frac{T^2}{24}(6Z_6^* + 6Z_7^* + 6y_t\rho_{tt}),\\
\tilde{m}_{H^+G^-} &= (\tilde{m}_{G^+H^-})^*,
\end{aligned}$$

$$\begin{aligned}
\tilde{m}_{H^+H^-} &= -Y_2^2 + \frac{1}{2}Z_2(\varphi_2^2+\varphi_3^2) + \frac{1}{2}Z_3\varphi_1^2 + (Z_{7R}\varphi_2 - Z_{7I}\varphi_3)\varphi_1 \\
&\quad + \frac{T^2}{24}\left(6Z_2 + 4Z_3 + 2Z_4 + 6|\rho_{tt}|^2 + \frac{9}{2}g^2 + \frac{3}{2}g'^2\right), \qquad \text{(A.4)}
\end{aligned}$$

$$\begin{aligned}
\tilde{m}_{h_1h_1} &= -Y_1^2 + \frac{3}{2}Z_1\varphi_1^2 + \frac{1}{2}(Z_3+Z_4)(\varphi_2^2+\varphi_3^2) + \frac{1}{2}\left(Z_{5R}(\varphi_2^2-\varphi_3^2) - 2Z_{5I}\varphi_2\varphi_3\right) \\
&\quad + 3(Z_{6R}\varphi_2 - Z_{6I}\varphi_3)\varphi_1 + \frac{T^2}{24}\left(6Z_1 + 4Z_3 + 2Z_4 + 6y_t^2 + \frac{9}{2}g^2 + \frac{3}{2}g'^2\right), \\
\tilde{m}_{G^0G^0} &= -Y_1^2 + \frac{1}{2}Z_1\varphi_1^2 + \frac{1}{2}(Z_3+Z_4)(\varphi_2^2+\varphi_3^2) - \frac{1}{2}\left(Z_{5R}(\varphi_2^2-\varphi_3^2) - 2Z_{5I}\varphi_2\varphi_3\right) \\
&\quad + (Z_{6R}\varphi_2 - Z_{6I}\varphi_3)\varphi_1 + \frac{T^2}{24}\left(6Z_1 + 4Z_3 + 2Z_4 + 6y_t^2 + \frac{9}{2}g^2 + \frac{3}{2}g'^2\right), \\
\tilde{m}_{h_2h_2} &= -Y_2^2 + \frac{1}{2}Z_2(3\varphi_2^2+\varphi_3^2) + \frac{1}{2}(Z_3+Z_4)\varphi_1^2 + \frac{1}{2}Z_{5R}\varphi_1^2 + (3Z_{7R}\varphi_2 - Z_{7I}\varphi_3)\varphi_1 \\
&\quad + \frac{T^2}{24}\left(6Z_2 + 4Z_3 + 2Z_4 + 6|\rho_{tt}|^2 + \frac{9}{2}g^2 + \frac{3}{2}g'^2\right), \\
\tilde{m}_{h_3h_3} &= -Y_2^2 + \frac{1}{2}Z_2(\varphi_2^2+3\varphi_3^2) + \frac{1}{2}(Z_3+Z_4)\varphi_1^2 - \frac{1}{2}Z_{5R}\varphi_1^2 + (Z_{7R}\varphi_2 - 3Z_{7I}\varphi_3)\varphi_1 \\
&\quad + \frac{T^2}{24}\left(6Z_2 + 4Z_3 + 2Z_4 + 6|\rho_{tt}|^2 + \frac{9}{2}g^2 + \frac{3}{2}g'^2\right), \\
\tilde{m}_{h_1G^0} &= \frac{1}{2}\left(2Z_{5R}\varphi_2\varphi_3 + Z_{5I}(\varphi_2^2-\varphi_3^2)\right) + (Z_{6I}\varphi_2 + Z_{6R}\varphi_3)\varphi_1 \\
\tilde{m}_{h_1h_2} &= -Y_{3R}^2 + (Z_3+Z_4)\varphi_1\varphi_2 + (Z_{5R}\varphi_2 - Z_{5I}\varphi_3)\varphi_1 + \frac{3}{2}Z_{6R}\varphi_1^2 \\
&\quad + \frac{1}{2}(3Z_{7R}\varphi_2^2 + Z_{7R}\varphi_3^2 - 2Z_{7I}\varphi_2\varphi_3) + \frac{T^2}{24}(6Z_{6R} + 6Z_{7R} + 6y_t|\rho_{tt}|\cos\theta_{tt}), \\
\tilde{m}_{h_1h_3} &= Y_{3I}^2 + (Z_3+Z_4)\varphi_1\varphi_3 - (Z_{5I}\varphi_2 + Z_{5R}\varphi_3)\varphi_1 - \frac{3}{2}Z_{6I}\varphi_1^2 \\
&\quad - \frac{1}{2}(Z_{7I}\varphi_2^2 + 3Z_{7I}\varphi_3^2 - 2Z_{7R}\varphi_2\varphi_3) + \frac{T^2}{24}(-6Z_{6I} - 6Z_{7I} + 6y_t|\rho_{tt}|\sin\theta_{tt}), \\
\tilde{m}_{G^0h_2} &= -Y_{3I}^2 + (Z_{5I}\varphi_2 + Z_{5R}\varphi_3)\varphi_1 + \frac{1}{2}Z_{6I}\varphi_1^2 + \frac{1}{2}(3Z_{7I}\varphi_2^2 + Z_{7I}\varphi_3^2 + 2Z_{7R}\varphi_2\varphi_3) \\
&\quad + \frac{T^2}{24}(6Z_{6I} + 6Z_{7I} - 6y_t|\rho_{tt}|\sin\theta_{tt}), \\
\tilde{m}_{G^0h_3} &= -Y_{3R}^2 + (Z_{5R}\varphi_2 - Z_{5I}\varphi_3)\varphi_1 + \frac{1}{2}Z_{6R}\varphi_1^2 + \frac{1}{2}(Z_{7R}\varphi_2^2 + 3Z_{7R}\varphi_3^2 + 2Z_{7I}\varphi_2\varphi_3) \\
&\quad + \frac{T^2}{24}(6Z_{6R} + 6Z_{7R} + 6y_t|\rho_{tt}|\cos\theta_{tt}), \\
\tilde{m}_{h_2h_3} &= Z_2\varphi_2\varphi_3 - \frac{1}{2}Z_{5I}\varphi_1^2 + (Z_{7R}\varphi_3 - Z_{7I}\varphi_2)\varphi_1. \qquad \text{(A.5)}
\end{aligned}$$

Appendix B

Thermal integral of the transport equations

The coefficients in the transport equations are given by

$$
\begin{aligned}
D_l &\equiv \left\langle \left(\frac{p_z}{E}\right)^l f'_{0w} \right\rangle, & Q_l &\equiv \left\langle \left(\frac{p_z^{l-1}}{2E^l}\right) f''_{0w} \right\rangle, \\
Q_l^8 &\equiv \left\langle \frac{\mathrm{sign}(p_z) p_z^{l-1}}{2E^l E_z} f'_{0w} \right\rangle, & Q_l^9 &\equiv \left\langle \frac{\mathrm{sign}(p_z) p_z^{l-1}}{4E^{l+1} E_z} \left(\frac{1}{E} f'_{0w} - \gamma f''_{0w}\right) \right\rangle, \\
Q_l^e &\equiv \left\langle \frac{p_z^{l-1}}{2E^l} f'_{0w}, \right\rangle,
\end{aligned}
\tag{B.1}
$$

where

$$
\langle X \rangle = \frac{1}{N_1} \int d^3p \; X. \tag{B.2}
$$

From the factorization assumption, we have

$$
\left\langle \frac{1}{2E^2} \delta f_e \right\rangle = \left[\frac{1}{2p_z E}\right] u_1 \equiv \overline{R} u_1. \tag{B.3}
$$

The explicit formulae of the coefficients for each particle are

- Normalization

$$
\begin{aligned}
N_1 &= -\gamma \frac{2\pi^3}{3} T^2, \\
N_{0t} &= 4\pi\gamma T^3 \int_0^\infty dp \; \frac{p^2}{e^{\sqrt{p^2+x^2}} + 1}, \qquad N_{0b} = 6\pi\gamma T^3 \zeta(3), \quad N_{0h} = 8\pi\gamma T^3 \zeta(3), \\
K_{0i} &= -\frac{N_{0i}}{N_1 T}.
\end{aligned}
\tag{B.4}
$$

- Top

$$
\begin{aligned}
\overline{R}_t &= \frac{\pi T}{\gamma N_{0t}} \int_x^\infty dE \; \ln \frac{|\sqrt{E^2 - x^2} - v_w E|}{|\sqrt{E^2 - x^2} + v_w E|} \times \frac{1}{e^E + 1}, \\
D_{1t} &= v_w \frac{4\pi\gamma T^2}{N_1} \int_0^\infty dp \; p^2 \frac{e^{\sqrt{p^2+x^2}}}{(e^{\sqrt{p^2+x^2}} + 1)^2} = -v_w D_{0t},
\end{aligned}
$$

$$
\begin{aligned}
D_{2t} &= \frac{3}{\pi^2\gamma}\int_x^\infty dw\ \int_{-1}^1 dy\ \frac{\tilde{p}_w\tilde{p}_z^2}{\tilde{E}}\frac{e^w}{(e^w+1)^2},\\
Q_{1t} &= \frac{2\pi}{N_1}\int_0^\infty dp\ \frac{p^2}{\sqrt{p^2+x^2}}\frac{e^{\sqrt{p^2+x^2}}(e^{\sqrt{p^2+x^2}}-1)}{(e^{\sqrt{p^2+x^2}}+1)^3},\\
Q_{2t} &= -\frac{3}{2\pi^2\gamma T^2}\int_x^\infty dw\ \int_{-1}^1 dy\ \frac{\tilde{p}_w\tilde{p}_z}{\tilde{E}}\frac{e^w(e^w-1)}{(e^w+1)^3},\\
Q_{1t}^8 &= \frac{3}{2\pi^2\gamma T^2}\int_x^\infty dw\ \int_{-1}^1 dy\ \frac{\tilde{p}_w\mathrm{sign}(\tilde{p}_z)}{\sqrt{\tilde{p}_z^2+x^2}}\frac{e^w}{(e^w+1)^2},\\
Q_{1t}^9 &= \frac{3}{4\pi^2\gamma T^4}\int_x^\infty dw\ \int_{-1}^1 dy\ \frac{\tilde{p}_w\mathrm{sign}(\tilde{p}_z)}{\tilde{E}\sqrt{\tilde{p}_z^2+x^2}}\frac{e^w}{(e^w+1)^2}\left\{\frac{1}{\tilde{E}}+\gamma\frac{e^w-1}{e^w+1}\right\},\\
Q_{2t}^8 &= \frac{3}{2\pi^2\gamma T^2}\int_x^\infty dw\ \int_{-1}^1 dy\ \frac{\tilde{p}_w|\tilde{p}_z|}{\tilde{E}\sqrt{\tilde{p}_z^2+x^2}}\frac{e^w}{(e^w+1)^2},\\
Q_{2t}^9 &= \frac{3}{4\pi^2\gamma T^4}\int_x^\infty dw\ \int_{-1}^1 dy\ \frac{\tilde{p}_w|\tilde{p}_z|}{\tilde{E}^2\sqrt{\tilde{p}_z^2+x^2}}\frac{e^w}{(e^w+1)^2}\left\{\frac{1}{\tilde{E}}+\gamma\frac{e^w-1}{e^w+1}\right\}.
\end{aligned}
\tag{B.5}
$$

- Bottom and Higgs

$$
\begin{aligned}
D_{1b} &= -v_w,\\
D_{2b} &= \frac{3}{\pi^2\gamma}\int_0^\infty dw\ \int_{-1}^1 dy\ \frac{\tilde{p}_w\tilde{p}_z^2}{\tilde{E}}\frac{e^w}{(e^w+1)^2}\\
&= \frac{1}{v_w^3}\left(-v_w+2v_w^3+(v_w^2-1)^2\tanh^{-1}(v_w)\right),\\
D_{1h} &= -2v_w,\\
D_{2h} &= \frac{3}{\pi^2\gamma}\int_0^\infty dw\ \int_{-1}^1 dy\ \frac{\tilde{p}_w\tilde{p}_z^2}{\tilde{E}}\frac{e^w}{(e^w-1)^2}\\
&= 2D_{2b},\\
K_{4b} &= \frac{1}{3},\qquad K_{4h} = \frac{2}{3}.
\end{aligned}
\tag{B.6}
$$

Appendix C

Basis independency of source terms

In order to reinforce the discussion in section 7.3, we here show the basis independency of the source terms in the Boltzmann equation.

First, we show that the VIA source term is same in the weak and mass basis. The kinetic equation of fermion ψ is given by [337]

$$\partial_\mu^X j_\psi^\mu = -\int d^3\boldsymbol{w}\int_{-\infty}^{T} dw^0\ \mathrm{Tr}\Big[\Sigma_\psi^>(X,w)G_\psi^<(w,X) - \Sigma_\psi^<(X,w)G_\psi^>(w,X) - G_\psi^>(X,w)\Sigma_\psi^<(w,X) + G_\psi^<(X,w)\Sigma_\psi^>(w,X)\Big], \tag{C.1}$$

where $G_\psi^{<,>}$ and $\Sigma_\psi^{<,>}$ are Wightman functions and self energies, respectively, following notations in Ref. [463]. The trace is taken in the spinor space. By definition, the sum of the divergence of currents of left-handed top and charm quarks is basis independent as

$$\partial_\mu j_{t'_L}^\mu + \partial_\mu j_{c'_L}^\mu = \partial_\mu j_{t_L}^\mu + \partial_\mu j_{c_L}^\mu. \tag{C.2}$$

As shown in the following, the right hand side of Eq. (C.1) is also basis independent at the leading order in VIA.

The relevant lagrangian of the top and charm quarks is given by

$$\mathcal{L}_y = -\overline{u'_{i,L}}\big(Y^u_{1,ij}\phi_1^{0*} + Y^u_{2,ij}\phi_2^{0*}\big)u'_{j,R} + \text{h.c.}. \tag{C.3}$$

The relations between Yukawa matrices in the weak basis Y_1^u, Y_2^u and the mass basis Y_d^u, ρ^u are given by Eq. (2.12). Here we define matrices as

$$\begin{aligned} A(u) &\equiv Y_1^u v_1^*(u) + Y_2^u v_2^*(u) \\ &= V_L^{u\dagger}\big(Y_\mathrm{d}^u v_1^*(u) + \rho^u v_2^*(u)\big)V_R^u \\ &\equiv V_L^{u\dagger}B(u)V_R^u, \end{aligned} \tag{C.4}$$

where the space-time dependent VEVs $v_k(u) = \sqrt{2}\langle\phi_k^0\rangle$ $(k = 1, 2)$ are defined in the Higgs basis.

We calculate the first term in right hand side of Eq. (C.1). At the 2nd order in VIA as shown in the left panel of figure C.1, the self energy of the left-handed top quarks in the weak basis is written by

$$\begin{aligned} \Sigma^>_{t'_L}(u,v) &= -\frac{1}{2}\Big(A_{tt}(u)G^>_{t'_Rt'_R}(u,v)A^*_{tt}(v) + A_{tc}(u)G^>_{c'_Rc'_R}(u,v)A^*_{tc}(v)\Big) \\ &= -\frac{1}{2}\sum_{q=c,t}\Big(A_{tq}(u)G^>_{q'_Rq'_R}(u,v)A^*_{tq}(v)\Big). \end{aligned} \tag{C.5}$$

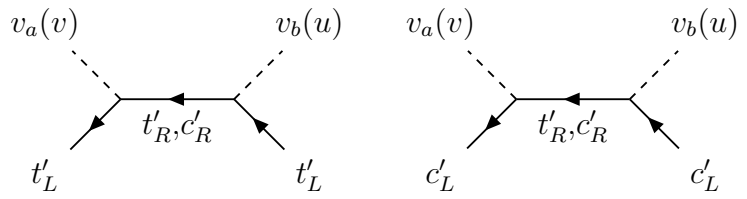

Figure C.1: Self energy of left-handed top and charm quarks in the weak basis ($a, b = 1, 2$).

We define a 2×2 matrix which has flavor indices as

$$G^{>}_{R}(u,v) = G^{>}_{q_{iR}q_{jR}}(u,v) = -i\langle q_{iR}(u)\overline{q_{jR}}(v)\rangle, \tag{C.6}$$

and the basis transformation is given by

$$G^{>}_{R'}(u,v) = G^{>}_{q'_{iR}q'_{jR}}(u,v) = V^{*}_{R,ik}G^{>}_{q_{kR}q_{mR}}(u,v)V_{R,mj} = V^{\dagger}_{R}G^{>}_{R}(u,v)V_{R}. \tag{C.7}$$

Here we have omitted the up-type subscript in the rotation matrix V_R. By using Eqs. (C.4) and (C.7), the self energy can be written by

$$\Sigma^{>}_{t'_L}(u,v) = -\sum_{p,q=c,t}\frac{1}{2}\Big(A_{tp}(u)G^{>}_{p'_Rq'_R}(u,v)A^{*}_{tq}(v)\Big) = -\frac{1}{2}\big(V^{\dagger}_{L}B(u)G^{>}_{R}(u,v)B^{\dagger}(v)V_L\big)_{tt}, \tag{C.8}$$

at the level at which we are considering in VIA. We have used the fact that $G^{>}_{q_{iR}q_{jR}}$ $(i \neq j)$ first appear at 2nd order in VIA. Therefore, we find that

$$\begin{aligned}
\Sigma^{>}_{t'_L}(X,w)G^{<}_{t'_Lt'_L}(w,X) &= -\frac{1}{2}\big(V^{\dagger}_{L}B(X)G^{>}_{R}(X,w)B^{\dagger}(w)V_L\big)_{tt}G^{<}_{t'_Lt'_L}(w,X) \\
&= -\frac{1}{2}\big(V^{\dagger}_{L}B(X)G^{>}_{R}(X,w)B^{\dagger}(w)V_LG^{<}_{L'}(w,X)\big)_{tt} \\
&= -\frac{1}{2}\big(V^{\dagger}_{L}B(X)G^{>}_{R}(X,w)B^{\dagger}(w)G^{<}_{L}(w,X)V_L\big)_{tt},
\end{aligned} \tag{C.9}$$

where we have also defined the matrix $G^{<}_{L}$ for the left-handed fields, and we have used the transformation low $G^{<}_{L'}(u,v) = V^{\dagger}_{L}G^{<}_{L}(u,v)V_L$.

In the same way, we obtain the contribution from the self energy of the left-handed charm quarks in the weak basis shown in the right panel of figure C.1 as

$$\Sigma^{>}_{c'_L}(X,w)G^{<}_{c'_Lc'_L}(w,X) = -\frac{1}{2}\big(V^{\dagger}_{L}B(X)G^{>}_{R}(X,w)B^{\dagger}(w)G^{<}_{L}(w,X)V_L\big)_{cc}, \tag{C.10}$$

so that the sum of the contributions of the top and charm quarks is given by

$$\begin{aligned}
\Sigma^{>}_{t'_L}G^{<}_{t'_Lt'_L} + \Sigma^{>}_{c'_L}G^{<}_{c'_Lc'_L} &= -\frac{1}{2}\mathrm{Tr}\Big[V^{\dagger}_{L}BG^{>}_{R}B^{\dagger}G^{<}_{L}V_L\Big] \\
&= -\frac{1}{2}\mathrm{Tr}\Big[BG^{>}_{R}B^{\dagger}G^{<}_{L}\Big].
\end{aligned} \tag{C.11}$$

The trace is taken in the flavor space. Similarly, we can show that V_L and V_R dependencies in the other terms in Eq. (C.1) disappear. As a result, the right hand side of Eq. (C.1) calculated in the weak basis coincides with the one in the mass basis. This result is a consequence of summing up the contribution of the charm quark defined in the weak basis.

When we consider CP conserving Higgs potential and $v_1, v_2 \in \mathbb{R}$, the source term relevant to ρ_{tc} is given by

$$S^{\mathrm{VIA}}_{t_L} \supset \frac{1}{2}|\rho_{tc}|^2v_2^2(X)\int d^3\boldsymbol{w}\int_{-\infty}^{T}dw^0\mathrm{Re}\Big[\mathrm{Tr}\big[G^{>}_{c_R}G^{<}_{t_R} - G^{<}_{c_R}G^{>}_{t_R}\big]\Big], \tag{C.12}$$

so that CP violating source term does not appear at the leading order in VIA,[1] and only CP conserving source term arises from the kinetic equation. This source just generates scattering terms for a process $t_L \leftrightarrow c_R$ induced by the collision with the bubble wall. However, these effects are much smaller than the other chirality flip processes due to the smallness of $v_2 (\ll v_1)$. If we assume CP violating VEV $v_2 \in \mathbb{C}$, $\arg(v_2)$ causes CP violating source terms, which are proportional to the absolute value of ρ_{tc}.

Second, we show the basis independency of the source term derived by the semi-classical force mechanism in the WKB approximation. We denote mass matrices which can be obtained in the weak and mass basis as M' and M, respectively. From Eq. (2.12), the relation of these matrices can be written by

$$V_L M' V_R^\dagger = M. \tag{C.13}$$

Dirac equations of these bases are given by

$$\begin{aligned} &(i\not{\partial} - M'^\dagger P_L - M' P_R)\psi' = 0, && \text{(weak basis)} \\ &(i\not{\partial} - M^\dagger P_L - M P_R)\psi = 0, && \text{(mass basis)} \end{aligned} \tag{C.14}$$

where

$$\begin{aligned} \psi'_i &= (u'_{iL}, u'_{iR})^T = \left((V_L^\dagger u_L)_i, (V_R^\dagger u_R)_i\right)^T, \\ \psi_i &= (u_{iL}, u_{iR})^T. \end{aligned} \tag{C.15}$$

With the same discussion in Ref. [308], we obtain the equation in the weak basis as

$$\left\{\omega^2 + \partial_z^2 - M' M'^\dagger + is(M' \partial_z M'^{-1})(\omega - is\partial_z)\right\} L'_s = 0, \tag{C.16}$$

where $L'_s = (c'_L, t'_L)$. The only difference between the two bases is primed or not, so that the equation in the mass basis can be obtained by omitting the primes. From the weak and mass basis to the locally diagonalized basis by a unitary matrix U, the respective equations are

$$\begin{aligned} &\left\{\omega^2 + \partial_z^2 - m'^2_D + 2U'_1 \partial_z + U_2 + isA'_1(\omega - is\partial_z) + A'_2\right\} L_s^{D\prime} = 0, && \text{(weak basis)} \\ &\left\{\omega^2 + \partial_z^2 - m_D^2 + 2U_1 \partial_z + U_2 + isA_1(\omega - is\partial_z) + A_2\right\} L_s^{D} = 0, && \text{(mass basis)} \end{aligned} \tag{C.17}$$

where

$$\begin{aligned} U_1^{(\prime)} &\equiv U^{(\prime)} \partial_z U^{(\prime)\dagger}, & A_1^{(\prime)} &\equiv U^{(\prime)} (M^{(\prime)} \partial_z M^{(\prime)-1}) U^{(\prime)\dagger}, \\ U_2^{(\prime)} &\equiv U^{(\prime)} \partial_z^2 U^{(\prime)\dagger}, & A_2^{(\prime)} &\equiv A_1^{(\prime)} U_1^{(\prime)}, \\ L_s^{(\prime)D} &\equiv U^{(\prime)} L_s^{(\prime)}, & m_D^{(\prime)2} &\equiv U^{(\prime)} M^{(\prime)} M^{(\prime)\dagger} U^{(\prime)\dagger} = \mathrm{diag}(m_+^{(\prime)2}, m_-^{(\prime)2}). \end{aligned} \tag{C.18}$$

The diagonalized mass matrix from the weak basis is written by

$$m'^2_D = U' M' M'^\dagger U'^\dagger = U' V_L^\dagger M M^\dagger V_L U'^\dagger, \tag{C.19}$$

so that $m'^2_D = m_D^2$ is concluded by uniqueness of eigenvalue, but $U' V_L^\dagger = U$ is not. The relation between L_s^D and $L_s^{D\prime}$ is given by

$$L_s^D = U L_s = U V_L L'_s = U V_L U'^\dagger L_s^{D\prime} \equiv Q L_s^{D\prime}. \tag{C.20}$$

[1] If we consider 4th order in VIA, the phases of the off-diagonal couplings may appear in the self energy. However, such contributions are suppressed about $O(\delta^2)$.

By using $L_s^{D\prime}$, the equation of the mass basis in Eq. (C.17) can be written by

$$Q\Big\{\omega^2+\partial_z^2-m_D^2+Q^\dagger\partial_z^2Q+2Q^\dagger(\partial_zQ)\partial_z+2Q^\dagger U_1Q\partial_z+2Q^\dagger U_1(\partial_zQ) \\ +Q^\dagger U_2Q+isQ^\dagger A_1Q(\omega-is\partial_z)+sQ^\dagger A_1(\partial_zQ)+Q^\dagger A_2Q\Big\}L_s^{D\prime}=0. \tag{C.21}$$

At the leading order in derivative expansion, CP violating source terms arise from the second term in the second line, so that from Eqs. (C.13), (C.18) and (C.20), we obtain

$$Q^\dagger A_1Q=A_1'. \tag{C.22}$$

Appendix D

Definition of the loop functions

We here show the definitions of the Passarino–Veltmann loop functions.

$$
\begin{aligned}
&\frac{1}{16\pi^2}A_0[m^2] = \mu^{2\epsilon}\int\frac{d^Dl}{i(2\pi)^D}\frac{1}{l^2-m^2+i\varepsilon},\\
&\frac{1}{16\pi^2}B_{\{0,\mu,\mu\nu\}}[k;m_a^2,m_b^2] = \mu^{2\epsilon}\int\frac{d^Dl}{i(2\pi)^D}\frac{\{1,l_\mu,l_\mu l_\nu\}}{l^2-m_a^2+i\varepsilon}\frac{1}{(l+k)^2-m_b^2+i\varepsilon},\\
&\frac{1}{16\pi^2}C_{\{0,\mu,\mu\nu\}}[k_1,k_2;m_a^2,m_b^2,m_c^2] =\\
&\qquad\mu^{2\epsilon}\int\frac{d^Dl}{i(2\pi)^D}\frac{\{1,l_\mu,l_\mu l_\nu\}}{l^2-m_a^2+i\varepsilon}\frac{1}{(l+k_1)^2-m_b^2+i\varepsilon}\frac{1}{(l+k_1+k_2)^2-m_c^2+i\varepsilon},
\end{aligned}
\tag{D.1}
$$

where $D = 4-2\epsilon$. The tensor decompositions are performed as

$$
\begin{aligned}
&B_\mu[k;m_a^2,m_b^2] = B_1k_\mu,\\
&B_{\mu\nu}[k;m_a^2,m_b^2] = B_{21}k_\mu k_\nu + B_{22}g_{\mu\nu},\\
&C_\mu[k_1,k_2;m_a^2,m_b^2,m_c^2] = C_{11}k_{1\mu} + C_{12}k_{2\mu},\\
&C_{\mu\nu}[k_1,k_2;m_a^2,m_b^2,m_c^2] = C_{21}k_{1\mu}k_{1\nu} + C_{22}k_{2\mu}k_{2\nu} + C_{23}(k_{1\mu}k_{2\nu}+k_{2\mu}k_{1\nu}) + C_{24}g_{\mu\nu}.
\end{aligned}
\tag{D.2}
$$

We sometimes use momentum squared notation,

$$
\begin{aligned}
&B[k;m_a^2,m_b^2] = B[k^2;m_a^2,m_b^2]\\
&C[k_1,k_2;m_a^2,m_b^2,m_c^2] = C[k_1^2,k_2^2,(k_1+k_2)^2;m_a^2,m_b^2,m_c^2].
\end{aligned}
\tag{D.3}
$$

Appendix E

Analytic formulae for the $H^{\pm}W^{\mp}Z$ vertices in the general two Higgs doublet model

In this appendix, we give analytic formulae for the diagrams which are shown in figures 8.2-8.5.

First, the C type contributions are given by

$$F_+^{(C1)} = \frac{-2i}{16\pi^2 c_W}(\mathcal{R}_{i2} - i\mathcal{R}_{i3})(\mathcal{R}_{i3}\mathcal{R}_{j2} - \mathcal{R}_{i2}\mathcal{R}_{j3})(Z_3\mathcal{R}_{j1} + Z_7^R\mathcal{R}_{j2} - Z_7^I\mathcal{R}_{j3})C_{24}[m^2_{H^\pm}, m^2_{H_i}, m^2_{H_j}],$$

$$G_+^{(C1)} = \frac{-2im_W^2}{16\pi^2 c_W}(\mathcal{R}_{i2} - i\mathcal{R}_{i3})(\mathcal{R}_{i3}\mathcal{R}_{j2} - \mathcal{R}_{i2}\mathcal{R}_{j3})(Z_3\mathcal{R}_{j1} + Z_7^R\mathcal{R}_{j2} - Z_7^I\mathcal{R}_{j3}) \times (C_{23} + C_{12})[m^2_{H^\pm}, m^2_{H_i}, m^2_{H_j}],$$

$$F_+^{(C2)} = \frac{2c_{2W}}{16\pi^2 c_W}(\mathcal{R}_{i2} - i\mathcal{R}_{i3})(Z_3\mathcal{R}_{i1} + Z_7^R\mathcal{R}_{i2} - Z_7^I\mathcal{R}_{i3})C_{24}[m^2_{H_i}, m^2_{H^\pm}, m^2_{H^\pm}],$$

$$G_+^{(C2)} = \frac{2m_W^2 c_{2W}}{16\pi^2 c_W}(\mathcal{R}_{i2} - i\mathcal{R}_{i3})(Z_3\mathcal{R}_{i1} + Z_7^R\mathcal{R}_{i2} - Z_7^I\mathcal{R}_{i3})(C_{23} + C_{12})[m^2_{H_i}, m^2_{H^\pm}, m^2_{H^\pm}],$$

$$F_+^{(C3)} = \frac{-2i}{16\pi^2 c_W}\mathcal{R}_{i1}(\mathcal{R}_{i3}\mathcal{R}_{j2} - \mathcal{R}_{i2}\mathcal{R}_{j3})\Big(\frac{1}{2}(Z_4 + Z_5)\mathcal{R}_{j2} - \frac{i}{2}(Z_4 - Z_5)\mathcal{R}_{j3} + Z_6\mathcal{R}_{j1}\Big) \times C_{24}[m^2_{G^\pm}, m^2_{H_i}, m^2_{H_j}],$$

$$G_+^{(C3)} = \frac{-2im_W^2}{16\pi^2 c_W}\mathcal{R}_{i1}(\mathcal{R}_{i3}\mathcal{R}_{j2} - \mathcal{R}_{i2}\mathcal{R}_{j3}) \times \Big(\frac{1}{2}(Z_4 + Z_5)\mathcal{R}_{j2} - \frac{i}{2}(Z_4 - Z_5)\mathcal{R}_{j3} + Z_6\mathcal{R}_{j1}\Big)(C_{23} + C_{12})[m^2_{G^\pm}, m^2_{H_i}, m^2_{H_j}],$$

$$F_+^{(C4)} = \frac{-2}{16\pi^2 c_W}\mathcal{R}_{i1}\Big(\frac{1}{2}(Z_4 + Z_5)\mathcal{R}_{i2} - \frac{i}{2}(Z_4 - Z_5)\mathcal{R}_{i3} + Z_6\mathcal{R}_{i1}\Big)C_{24}[m^2_{G^\pm}, m^2_{G^0}, m^2_{H_i}],$$

$$G_+^{(C4)} = \frac{-2m_W^2}{16\pi^2 c_W}\mathcal{R}_{i1}\Big(\frac{1}{2}(Z_4 + Z_5)\mathcal{R}_{i2} - \frac{i}{2}(Z_4 - Z_5)\mathcal{R}_{i3} + Z_6\mathcal{R}_{i1}\Big)(C_{23} + C_{12})[m^2_{G^\pm}, m^2_{G^0}, m^2_{H_i}],$$

$$F_+^{(C5)} = \frac{2c_{2W}}{16\pi^2 c_W}\mathcal{R}_{i1}\Big(\frac{1}{2}(Z_4 + Z_5)\mathcal{R}_{i2} - \frac{i}{2}(Z_4 - Z_5)\mathcal{R}_{i3} + Z_6\mathcal{R}_{i1}\Big)C_{24}[m^2_{H_i}, m^2_{G^\pm}, m^2_{G^\pm}],$$

$$G_+^{(C5)} = \frac{2m_W^2 c_{2W}}{16\pi^2 c_W}\mathcal{R}_{i1}\Big(\frac{1}{2}(Z_4 + Z_5)\mathcal{R}_{i2} - \frac{i}{2}(Z_4 - Z_5)\mathcal{R}_{i3} + Z_6\mathcal{R}_{i1}\Big)(C_{23} + C_{12})[m^2_{H_i}, m^2_{G^\pm}, m^2_{G^\pm}],$$

$$F_+^{(C6)} = \frac{2i}{16\pi^2 c_W}\frac{m_W^2}{v^2}\mathcal{R}_{i1}(\mathcal{R}_{i3}\mathcal{R}_{j2} - \mathcal{R}_{i2}\mathcal{R}_{j3})(\mathcal{R}_{j2} - i\mathcal{R}_{j3})C_{24}[m^2_W, m^2_{H_i}, m^2_{H_j}],$$

$$G_+^{(C6)} = \frac{2im_W^2}{16\pi^2 c_W}\frac{m_W^2}{v^2}\mathcal{R}_{i1}(\mathcal{R}_{i3}\mathcal{R}_{j2} - \mathcal{R}_{i2}\mathcal{R}_{j3})(\mathcal{R}_{j2} - i\mathcal{R}_{j3})(C_{23} + C_{12} + 2C_{11} + 2C_0)[m^2_W, m^2_{H_i}, m^2_{H_j}],$$

$$
\begin{aligned}
F_+^{(C7)} &= \frac{2c_{2W}}{16\pi^2 c_W}\frac{m_Z^2}{v^2}\mathcal{R}_{i1}(\mathcal{R}_{i2}-i\mathcal{R}_{i3})C_{24}[m_{H^\pm}^2, m_{H_i}^2, m_Z^2],\\
G_+^{(C7)} &= \frac{2m_W^2 c_{2W}}{16\pi^2 c_W}\frac{m_Z^2}{v^2}\mathcal{R}_{i1}(\mathcal{R}_{i2}-i\mathcal{R}_{i3})(C_{23}-C_{12})[m_{H^\pm}^2, m_{H_i}^2, m_Z^2],\\
F_+^{(C8)} &= \frac{2s_W^2 m_Z^2}{16\pi^2 c_W}\mathcal{R}_{i1}\Big(\frac{1}{2}(Z_4+Z_5)\mathcal{R}_{i2}-\frac{i}{2}(Z_4-Z_5)\mathcal{R}_{i3}+Z_6\mathcal{R}_{i1}\Big)C_0[m_{G^\pm}^2, m_Z^2, m_{H_i}^2],\\
G_+^{(C8)} &= 0,\\
F_+^{(C9)} &= \frac{2s_W^2 m_W^2}{16\pi^2 c_W}\mathcal{R}_{i1}\Big(\frac{1}{2}(Z_4+Z_5)\mathcal{R}_{i2}-\frac{i}{2}(Z_4-Z_5)\mathcal{R}_{i3}+Z_6\mathcal{R}_{i1}\Big)C_0[m_{H_i}^2, m_W^2, m_{G^\pm}^2],\\
G_+^{(C9)} &= 0,\\
F_+^{(C10)} &= \frac{2}{16\pi^2 c_W}\frac{s_W^2 m_W^2}{v^2}\mathcal{R}_{i1}(\mathcal{R}_{i2}-i\mathcal{R}_{i3})C_{24}[m_{H_i}^2, m_{G^\pm}^2, m_W^2],\\
G_+^{(C10)} &= \frac{2m_W^2}{16\pi^2 c_W}\frac{s_W^2 m_W^2}{v^2}\mathcal{R}_{i1}(\mathcal{R}_{i2}-i\mathcal{R}_{i3})(C_{23}-C_{12})[m_{H_i}^2, m_{G^\pm}^2, m_W^2],\\
F_+^{(C11)} &= \frac{2}{16\pi^2 c_W}\frac{c_W^2 m_W^2}{v^2}\mathcal{R}_{i1}(\mathcal{R}_{i2}-i\mathcal{R}_{i3})\Big((D-1)C_{24}+(m_Z^2-m_W^2)C_0\\
&\quad -2k_3\cdot(k_2C_{11}+k_3C_{12})+m_W^2C_{21}+m_Z^2C_{22}+2k_2\cdot k_3C_{23}\Big)[m_{H_i}^2, m_W^2, m_W^2],\\
G_+^{(C11)} &= \frac{2m_W^2}{16\pi^2 c_W}\frac{c_W^2 m_W^2}{v^2}\mathcal{R}_{i1}(\mathcal{R}_{i2}-i\mathcal{R}_{i3})(4C_{11}-3C_{12}-C_{23})[m_{H_i}^2, m_W^2, m_W^2],\\
F_+^{(C12)} &= \frac{-2}{16\pi^2 c_W}\frac{m_W^2}{v^2}\mathcal{R}_{i1}(\mathcal{R}_{i2}-i\mathcal{R}_{i3})\Big((D-1)C_{24}+4(k_2+k_3)\cdot k_2C_0\\
&\quad +2(2k_2+k_3)\cdot(k_2C_{11}+k_3C_{12})+m_W^2C_{21}+m_Z^2C_{22}+2k_2\cdot k_3C_{23}\Big)[m_W^2, m_Z^2, m_{H_i}^2],\\
G_+^{(C12)} &= \frac{-2m_W^2}{16\pi^2 c_W}\frac{m_W^2}{v^2}\mathcal{R}_{i1}(\mathcal{R}_{i2}-i\mathcal{R}_{i3})\Big(-2C_0+2C_{11}-5C_{12}-C_{23}\Big)[m_W^2, m_Z^2, m_{H_i}^2],\\
H_+^{(C\text{ type})} &= 0.
\end{aligned}
\tag{E.1}
$$

where $c_W \equiv \cos\theta_W$, $s_W \equiv \sin\theta_W$, $c_{2W} \equiv \cos 2\theta_W$ and D is the space-time dimension. In these formulae, we have omitted the summation of the indices for the neutral scalar bosons, and we have used a shorthand notation for the C_{ij} functions as

$$
C_{ij}[m_a^2, m_b^2, m_c^2] \equiv C_{ij}[-k_2, -k_3; m_a^2, m_b^2, m_c^2]. \tag{E.2}
$$

The divergent parts of the C type contributions are

$$
\begin{aligned}
F_+^{(C1+C2)}|_{\rm div} &= -\frac{s_W^2}{2}Z_7\Delta,\\
F_+^{(C4+C5)}|_{\rm div} &= -\frac{s_W^2}{2}Z_6\Delta,\\
F_+^{(\text{others } C\text{s})}|_{\rm div} &= 0,
\end{aligned}
\tag{E.3}
$$

where we define the divergent quantity Δ as

$$
\Delta \equiv \frac{2}{16\pi^2 c_W}B_0|_{\rm div}. \tag{E.4}
$$

Second, the B type contributions are

$$
F_+^{(B1)} = \frac{2}{16\pi^2 c_W}\frac{s_W^2}{2}(\mathcal{R}_{i2}-i\mathcal{R}_{i3})(Z_3\mathcal{R}_{i1}+Z_7^R\mathcal{R}_{i2}-Z_7^I\mathcal{R}_{i3})B_0[-k_1; m_{H^\pm}^2, m_{H_i}^2],
$$

$$
\begin{aligned}
F_+^{(B2)} &= \frac{2}{16\pi^2 c_W}\frac{s_W^2}{2}\mathcal{R}_{i1}\Big(\frac{1}{2}(Z_4+Z_5)\mathcal{R}_{i2} - \frac{i}{2}(Z_4-Z_5)\mathcal{R}_{i3} + Z_6\mathcal{R}_{i1}\Big)B_0[-k_1; m_{G^\pm}^2, m_{H_i}^2],\\
F_+^{(B3)} &= \frac{2}{16\pi^2 c_W}\frac{s_W^2 m_W^2}{v^2}\mathcal{R}_{i1}(\mathcal{R}_{i2} - i\mathcal{R}_{i3})B_0[-k_2; m_W^2, m_{H_i}^2],\\
F_+^{(B4)} &= \frac{2}{16\pi^2 c_W}\frac{s_W^2 m_Z^2}{v^2}\mathcal{R}_{i1}(\mathcal{R}_{i2} - i\mathcal{R}_{i3})B_0[-k_3; m_Z^2, m_{H_i}^2],\\
F_+^{(B5)} &= \frac{2}{16\pi^2 c_W}\frac{m_W^4 s_W^2}{v^2}\frac{1}{m_{H^\pm}^2 - m_W^2}\mathcal{R}_{i1}(\mathcal{R}_{i2} - i\mathcal{R}_{i3})(B_0 - B_1)[-k_1; m_{H^\pm}^2, m_W^2],\\
F_+^{(B6)} &= \frac{2}{16\pi^2 c_W}\frac{m_W^2 s_W^2}{2}\frac{1}{m_{H^\pm}^2 - m_W^2}(\mathcal{R}_{i2} - i\mathcal{R}_{i3})(Z_3\mathcal{R}_{i1} + Z_7^R\mathcal{R}_{i2} - Z_7^I\mathcal{R}_{i3})\\
&\quad\times(B_0 + 2B_1)[-k_1; m_{H_i}^2, m_{H^\pm}^2],\\
F_+^{(B7)} &= \frac{2}{16\pi^2 c_W}\frac{m_W^2 s_W^2}{2}\frac{1}{m_{H^\pm}^2 - m_W^2}\mathcal{R}_{i1}\\
&\quad\times\Big(\frac{1}{2}(Z_4+Z_5)\mathcal{R}_{i2} - \frac{i}{2}(Z_4-Z_5)\mathcal{R}_{i3} + Z_6\mathcal{R}_{i1}\Big)(B_0 + 2B_1)[-k_1; m_{H_i}^2, m_{G^\pm}^2],\\
F_+^{(B8)} &= \frac{2}{16\pi^2 c_W}\frac{m_W^2}{v^2}\frac{s_W^2}{2}\frac{-1}{m_{H^\pm}^2 - m_{G^\pm}^2}\mathcal{R}_{i1}(\mathcal{R}_{i2} - i\mathcal{R}_{i3})\big(m_{H^\pm}^2(B_0 - 2B_1) + \tilde{B}_0\big)[-k_1; m_{H_i}^2, m_W^2],\\
F_+^{(B9)} &= \frac{2}{16\pi^2 c_W}\frac{s_W^2}{2}\frac{1}{m_{H^\pm}^2 - m_{G^\pm}^2}\Big(\frac{1}{2}(Z_4+Z_5)\mathcal{R}_{i2} - \frac{i}{2}(Z_4-Z_5)\mathcal{R}_{i3} + Z_6\mathcal{R}_{i1}\Big)\\
&\quad\times(Z_3\mathcal{R}_{i1} + Z_7^R\mathcal{R}_{i2} - Z_7^I\mathcal{R}_{i3})v^2 B_0[-k_1; m_{H_i}^2, m_{H^\pm}^2],\\
F_+^{(B10)} &= \frac{2}{16\pi^2 c_W}\frac{s_W^2}{2}\frac{1}{m_{H^\pm}^2 - m_{G^\pm}^2}\Big(\frac{1}{2}(Z_4+Z_5)\mathcal{R}_{i2} - \frac{i}{2}(Z_4-Z_5)\mathcal{R}_{i3} + Z_6\mathcal{R}_{i1}\Big)\\
&\quad\times(Z_1\mathcal{R}_{i1} + Z_6^R\mathcal{R}_{i2} - Z_6^I\mathcal{R}_{i3})v^2 B_0[-k_1; m_{H_i}^2, m_{G^\pm}^2],\\
G_+^{(B\text{ type})} &= H_+^{(B\text{ type})} = 0,
\end{aligned}
\tag{E.5}
$$

where $\tilde{B}_0$ is defined by [372]

$$
\tilde{B}_0[k; m_a^2, m_b^2] \equiv (k^2 B_{21} + D B_{22})[k; m_a^2, m_b^2] = A_0[m_b^2] + m_a^2 B_0[k; m_a^2, m_b^2]. \tag{E.6}
$$

The divergent parts of the B type contributions are given by

$$
\begin{aligned}
F_+^{(B1)}|_{\rm div} &= \frac{s_W^2}{2}Z_7\Delta,\\
F_+^{(B2)}|_{\rm div} &= \frac{s_W^2}{2}Z_6\Delta,\\
F_+^{(B8)}|_{\rm div} &= \frac{s_W^2}{2}\frac{m_W^2}{v^2}\frac{-1}{m_{H^\pm}^2 - m_{G^\pm}^2}\mathcal{R}_{i1}(\mathcal{R}_{i2} - i\mathcal{R}_{i3})m_{H_i}^2\Delta,\\
F_+^{(B9)}|_{\rm div} &= \frac{s_W^2}{2}\frac{1}{m_{H^\pm}^2 - m_{G^\pm}^2}\Big(\frac{1}{2}(Z_4+Z_5)Z_7^R + \frac{i}{2}(Z_4-Z_5)Z_7^I + Z_3 Z_6\Big)v^2\Delta,\\
F_+^{(B10)}|_{\rm div} &= \frac{s_W^2}{2}\frac{1}{m_{H^\pm}^2 - m_{G^\pm}^2}\Big(\frac{1}{2}(Z_4+Z_5)Z_6^R + \frac{i}{2}(Z_4-Z_5)Z_6^I + Z_1 Z_6\Big)v^2\Delta,\\
F_+^{(\text{other } Bs)}|_{\rm div} &= 0.
\end{aligned}
\tag{E.7}
$$

Third, the fermion contributions are given by

$$
F_+^{(F1)} = \frac{2\sqrt{2}N_c}{16\pi^2 c_W v}(V_{\rm CKM}^\dagger)_{lm}\Bigg[\Gamma_{ml}^u m_{u_m}\Big\{m_{d_l}^2(g_V^d - g_A^d)C_0 - (g_V^d + g_A^d)\big(g_{\alpha\beta}C^{\alpha\beta} - 2C_{24} + (2k_2 + k_3)\cdot
$$

$$(k_2C_{11}+k_3C_{12})+k_2\cdot(k_2+k_3)C_0\Big)\Big\}+\Gamma^d_{ml}m_{d_l}\Big\{-(g^d_V+g^d_A)\big(g_{\alpha\beta}C^{\alpha\beta}-2C_{24}+k_2\cdot$$
$$(k_2C_{11}+k_3C_{12})\big)+(g^d_V-g^d_A)\big(g_{\alpha\beta}C^{\alpha\beta}+(k_2+k_3)\cdot(k_2C_{11}+k_3C_{12})\big)\Big\}\Big][m^2_{u_m},m^2_{d_l},m^2_{d_l}],$$
$$+\frac{2\sqrt{2}}{16\pi^2c_Wv}\Gamma^e_{ll}m_{e_l}\Big\{-(g^e_V+g^e_A)\big(g_{\alpha\beta}C^{\alpha\beta}-2C_{24}+k_2\cdot(k_2C_{11}+k_3C_{12})\big)$$
$$+(g^e_V-g^e_A)\big(g_{\alpha\beta}C^{\alpha\beta}+(k_2+k_3)\cdot(k_2C_{11}+k_3C_{12})\big)\Big\}[0,m^2_{e_l},m^2_{e_l}],$$
$$G^{(F1)}_+=\frac{2\sqrt{2}m^2_WN_c}{16\pi^2c_Wv}(V^\dagger_{\rm CKM})_{lm}\Big[\Gamma^u_{ml}m_{u_m}(g^d_V+g^d_A)(2C_{12}+2C_{23}+C_{11}+C_0)$$
$$+\Gamma^d_{ml}m_{d_l}\Big\{(g^d_V+g^d_A)(C_{12}+2C_{23})+(g^d_V-g^d_A)(C_{12}-C_{11})\Big\}\Big][m^2_{u_m},m^2_{d_l},m^2_{d_l}]$$
$$+\frac{2\sqrt{2}m^2_W}{16\pi^2c_Wv}\Gamma^e_{ll}m_{e_l}\Big\{(g^e_V+g^e_A)(C_{12}+2C_{23})+(g^e_V-g^e_A)(C_{12}-C_{11})\Big\}[0,m^2_{e_l},m^2_{e_l}],$$
$$H^{(F1)}_+=i\frac{2\sqrt{2}m^2_WN_c}{16\pi^2c_Wv}(V^\dagger_{\rm CKM})_{lm}\Big[\Gamma^u_{ml}m_{u_m}(g^d_V+g^d_A)(C_{11}+C_0)$$
$$+\Gamma^d_{ml}m_{d_l}\Big\{(g^d_V+g^d_A)C_{12}-(g^d_V-g^d_A)(C_{12}-C_{11})\Big\}\Big][m^2_{u_m},m^2_{d_l},m^2_{d_l}]$$
$$+i\frac{2\sqrt{2}m^2_W}{16\pi^2c_Wv}\Gamma^e_{ll}m_{e_l}\Big\{(g^e_V+g^e_A)C_{12}-(g^e_V-g^e_A)(C_{12}-C_{11})\Big\}[0,m^2_{e_l},m^2_{e_l}],$$
$$F^{(F2)}_+=\frac{2\sqrt{2}N_c}{16\pi^2c_Wv}(V^\dagger_{\rm CKM})_{lm}\Big[\Gamma^d_{ml}m_{d_l}\Big\{m^2_{u_m}(g^u_V-g^u_A)C_0-(g^u_V+g^u_A)\big(g_{\alpha\beta}C^{\alpha\beta}-2C_{24}+(2k_2+k_3)\cdot$$
$$(k_2C_{11}+k_3C_{12})+k_2\cdot(k_2+k_3)C_0\Big)\Big\}+\Gamma^u_{ml}m_{u_m}\Big\{-(g^u_V+g^u_A)\big(g_{\alpha\beta}C^{\alpha\beta}-2C_{24}+k_2\cdot$$
$$(k_2C_{11}+k_3C_{12})\big)+(g^u_V-g^u_A)\big(g_{\alpha\beta}C^{\alpha\beta}+(k_2+k_3)\cdot(k_2C_{11}+k_3C_{12})\big)\Big\}\Big][m^2_{d_l},m^2_{u_m},m^2_{u_m}]$$
$$+\frac{2\sqrt{2}}{16\pi^2c_Wv}\Gamma^e_{ll}m_{e_l}\Big\{-(g^\nu_V+g^\nu_A)\big(g_{\alpha\beta}C^{\alpha\beta}-2C_{24}+(2k_2+k_3)\cdot(k_2C_{11}+k_3C_{12})$$
$$+k_2\cdot(k_2+k_3)C_0\big)\Big\}[m^2_{e_l},0,0],$$
$$G^{(F2)}_+=\frac{2\sqrt{2}m^2_WN_c}{16\pi^2c_Wv}(V^\dagger_{\rm CKM})_{lm}\Big[\Gamma^d_{ml}m_{d_l}(g^u_V+g^u_A)(2C_{12}+2C_{23}+C_{11}+C_0)$$
$$+\Gamma^u_{ml}m_{u_m}\Big\{(g^u_V+g^u_A)(C_{12}+2C_{23})+(g^u_V-g^u_A)(C_{12}-C_{11})\Big\}\Big][m^2_{d_l},m^2_{u_m},m^2_{u_m}],$$
$$+\frac{2\sqrt{2}m^2_W}{16\pi^2c_Wv}\Gamma^e_{ll}m_{e_l}(g^\nu_V+g^\nu_A)(2C_{12}+2C_{23}+C_{11}+C_0)[m^2_{e_l},0,0],$$
$$H^{(F2)}_+=i\frac{2\sqrt{2}m^2_WN_c}{16\pi^2c_Wv}(V^\dagger_{\rm CKM})_{lm}\Big[-\Gamma^d_{ml}m_{d_l}(g^u_V+g^u_A)(C_{11}+C_0)$$
$$-\Gamma^u_{ml}m_{u_m}\Big\{(g^u_V+g^u_A)C_{12}-(g^u_V-g^u_A)(C_{12}-C_{11})\Big\}\Big][m^2_{d_l},m^2_{u_m},m^2_{u_m}]$$
$$-i\frac{2\sqrt{2}m^2_W}{16\pi^2c_Wv}\Gamma^e_{ll}m_{e_l}(g^\nu_V+g^\nu_A)(C_{11}+C_0)[m^2_{e_l},0,0],$$

$$
\begin{aligned}
F_+^{(F3)} &= \frac{2\sqrt{2}c_W N_c}{16\pi^2 v}\frac{m_W^2-m_Z^2}{m_W^2-m_{H^\pm}^2}(V_{\rm CKM}^\dagger)_{lm}\Big(\Gamma^u_{ml}m_{u_m}B_1+\Gamma^d_{ml}m_{d_l}(B_0+B_1)\Big)[-k_1;m_{d_l}^2,m_{u_m}^2]\\
&\quad+\frac{2\sqrt{2}c_W}{16\pi^2 v}\frac{m_W^2-m_Z^2}{m_W^2-m_{H^\pm}^2}\Gamma^e_{ll}m_{e_l}(B_0+B_1)[-k_1;m_{e_l}^2,0],\\
F_+^{(F4)} &= \frac{2\sqrt{2}s_W^2 N_c}{16\pi^2 c_W v}\frac{1}{m_W^2-m_{H^\pm}^2}(V_{\rm CKM}^\dagger)_{lm}\Big\{(-\Gamma^u_{ml}m_{u_m}m_{d_l}^2+\Gamma^d_{ml}m_{u_m}^2m_{d_l})B_0\\
&\quad+(-\Gamma^d_{ml}m_{d_l}+\Gamma^u_{ml}m_{u_m})(\tilde{B}_0+k_1^2B_1)\Big\}[-k_1;m_{d_l}^2,m_{u_m}^2]\\
&\quad-\frac{2\sqrt{2}s_W^2}{16\pi^2 c_W v}\frac{1}{m_W^2-m_{H^\pm}^2}\Gamma^e_{ll}m_{e_l}(\tilde{B}_0+k_1^2B_1)[-k_1;m_{e_l}^2,0],\\
G_+^{(F3,F4)} &= H_+^{(F3,F4)}=0,
\end{aligned}
\tag{E.8}
$$

where the summation for the flavor indices l,m is implicit, and $C^{\alpha\beta}$ is the C type tensor function which satisfies the relation [464]

$$
\begin{aligned}
&g_{\alpha\beta}C^{\alpha\beta}[k_1,k_2;m_a^2,m_b^2,m_c^2]=k_1^2C_{21}+k_2^2C_{22}+2k_1\cdot k_2C_{23}+DC_{24}\\
&=B_0[k_2;m_b^2,m_c^2]+m_a^2C_0[k_1,k_2;m_a^2,m_b^2,m_c^2].
\end{aligned}
\tag{E.9}
$$

The definition of the coupling constants are given by

$$
\begin{aligned}
&\Gamma^u_{lm}=(\rho^{u\dagger}V_{\rm CKM})_{lm},\quad \Gamma^d_{lm}=-(V_{\rm CKM}\rho^d)_{lm},\quad \Gamma^e_{lm}=-(\rho^e)_{lm}\\
&g_V^f=\frac{1}{2}T_3^f-Q_fs_W^2,\quad g_A^f=\frac{1}{2}T_3^f,
\end{aligned}
\tag{E.10}
$$

where $f=u,d,e,\nu$, and T_3^f and Q_f are the $\mathrm{SU}(2)_L$ isospin and the electromagnetic charge for f, respectively. The divergent parts of the fermion contributions are given by

$$
\begin{aligned}
F_+^{(F\ \text{type})}|_{\rm div} &= \frac{\sqrt{2}s_W^2N_c}{v}\frac{1}{m_W^2-m_{H^\pm}^2}\Big((\rho^{u\dagger})_{ll}m_{u_l}^3+(\rho^d)_{ll}m_{d_l}^3\Big)\Delta\\
&\quad+\frac{\sqrt{2}s_W^2}{v}\frac{1}{m_W^2-m_{H^\pm}^2}(\rho^e)_{ll}m_{e_l}^3\Delta,
\end{aligned}
\tag{E.11}
$$

Finally, the A type contributions are given by

$$
\begin{aligned}
F_+^{(A1)} &= \frac{2}{c_W}\frac{s_W^2}{2}(\mathcal{R}_{i2}-i\mathcal{R}_{i3})\frac{-1}{m_{H_i}^2}\frac{T_i}{v},\\
F_+^{(A2)} &= \frac{2}{c_W}m_W^2s_W^2\frac{1}{2}(\mathcal{R}_{i2}-i\mathcal{R}_{i3})\frac{1}{m_{H^\pm}^2-m_W^2}\frac{-1}{m_{H_i}^2}\frac{T_i}{v},\\
F_+^{(A3)} &= \frac{2}{c_W}\frac{s_W^2}{2}\Big(\frac{1}{2}(Z_4+Z_5)\mathcal{R}_{i2}-\frac{i}{2}(Z_4-Z_5)\mathcal{R}_{i3}+Z_6\mathcal{R}_{i1}\Big)v^2\frac{1}{m_{H^\pm}^2-m_{G^\pm}^2}\frac{-1}{m_{H_i}^2}\frac{T_i}{v},\\
F_+^{(A4)} &= \frac{2}{c_W}\frac{s_W^2}{2}\frac{1}{m_{H^\pm}^2-m_{G^\pm}^2}\Pi_{H^+G^-},\\
G_+^{(A\ \text{type})} &= H_+^{(A\ \text{type})}=0,
\end{aligned}
\tag{E.12}
$$

where we denote the tadpole and the self energy of H^+G^- as

$T_i \equiv$  , $\Pi_{H^+G^-} \equiv$ 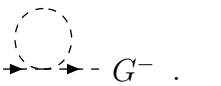

By using the relation between $\mathcal{R}$ and $\mathcal{M}^2$ in Eq. (4.8), the A type contributions can be simplified as

$$F_+^{(A\text{ type})} = \frac{2}{c_W}\frac{s_W^2}{2}\frac{1}{m_{H^\pm}^2 - m_W^2}\Big(- (\mathcal{R}_{i2} - i\mathcal{R}_{i3})\frac{T_i}{v} + \Pi_{H^+G^-}\Big). \tag{E.13}$$

When we write the tadpole of H_i as $T_i^{(p)}$, where a particle p runs inside the loop, they are given by

$$\begin{aligned}
T_i^{(G^\pm)} &= \frac{1}{16\pi^2 v}(Z_1\mathcal{R}_{i1} + Z_6^R\mathcal{R}_{i2} - Z_6^I\mathcal{R}_{i3})v^2 A_0[m_{G^\pm}^2],\\
T_i^{(G^0)} &= \frac{1}{16\pi^2 v}\frac{1}{2}(Z_1\mathcal{R}_{i1} + Z_6^R\mathcal{R}_{i2} - Z_6^I\mathcal{R}_{i3})v^2 A_0[m_{G^0}^2],\\
T_i^{(H^\pm)} &= \frac{1}{16\pi^2 v}(Z_3\mathcal{R}_{i1} + Z_7^R\mathcal{R}_{i2} - Z_7^I\mathcal{R}_{i3})v^2 A_0[m_{H^\pm}^2],\\
T_i^{(H_j)} &= \frac{1}{16\pi^2 v}(\lambda_{ijj}^H + \lambda_{jij}^H + \lambda_{jji}^H)v^2 A_0[m_{H_j}^2],\\
T_i^{(u_l)} &= -\frac{\sqrt{2}N_c}{16\pi^2}\Big(\mathcal{R}_{i2}(\rho_u + \rho_u^\dagger)_{ll} - i\mathcal{R}_{i3}(\rho_u - \rho_u^\dagger)_{ll}\Big)m_{u_l}A_0[m_{u_l}^2],\\
T_i^{(d_l)} &= -\frac{\sqrt{2}N_c}{16\pi^2}\Big(\mathcal{R}_{i2}(\rho_d + \rho_d^\dagger)_{ll} + i\mathcal{R}_{i3}(\rho_d - \rho_d^\dagger)_{ll}\Big)m_{d_l}A_0[m_{d_l}^2],\\
T_i^{(e_l)} &= -\frac{\sqrt{2}}{16\pi^2}\Big(\mathcal{R}_{i2}(\rho_e + \rho_e^\dagger)_{ll} + i\mathcal{R}_{i3}(\rho_e - \rho_e^\dagger)_{ll}\Big)m_{e_l}A_0[m_{e_l}^2].
\end{aligned} \tag{E.14}$$

We here have defined λ_{ijk}^H as

$$\begin{aligned}
\lambda_{ijk}^H \equiv{}& \frac{1}{2}\mathcal{R}_{i1}\mathcal{R}_{j1}\big(Z_1\mathcal{R}_{k1} + 3Z_6^R\mathcal{R}_{k2} - 3Z_6^I\mathcal{R}_{k3}\big)\\
&+ \frac{1}{2}\mathcal{R}_{j2}\mathcal{R}_{k2}\big((Z_3 + Z_4 + Z_5)\mathcal{R}_{i1} + Z_7^R\mathcal{R}_{i2} - Z_7^I\mathcal{R}_{i3}\big)\\
&+ \frac{1}{2}\mathcal{R}_{j3}\mathcal{R}_{k3}\big((Z_3 + Z_4 - Z_5)\mathcal{R}_{i1} + Z_7^R\mathcal{R}_{i2} - Z_7^I\mathcal{R}_{i3}\big).
\end{aligned} \tag{E.15}$$

We note that the gauge and ghost fields cause the tadpole diagram for H_i, however, they do not give the A type contributions. This is because the scalar-gauge-gauge and the scalar-ghost-ghost interactions are proportional to $\mathcal{R}_{i1}$, and the A type contributions from these tadpole are proportional to $\sum_i \mathcal{R}_{i1}(\mathcal{R}_{i2} - i\mathcal{R}_{i3}) = 0$. The self energies $\Pi_{H^+G^-}^{(p)}$, where a scalar particle p runs inside the loop, are given by

$$\begin{aligned}
\Pi_{H^+G^-}^{(G^\pm)} &= \frac{1}{16\pi^2 v^2}2Z_6 v^2 A_0[m_{G^\pm}^2],\\
\Pi_{H^+G^-}^{(G^0)} &= \frac{1}{16\pi^2 v^2}\frac{1}{2}Z_6 v^2 A_0[m_{G^0}^2],\\
\Pi_{H^+G^-}^{(H^\pm)} &= \frac{1}{16\pi^2 v^2}2Z_7 v^2 A_0[m_{H^\pm}^2],\\
\Pi_{H^+G^-}^{(H_i)} &= \frac{1}{16\pi^2 v^2}\frac{1}{2}\Big((Z_4 + Z_5)\mathcal{R}_{i1}\mathcal{R}_{i2} - i(Z_4 - Z_5)\mathcal{R}_{i1}\mathcal{R}_{i3}\\
&\qquad + Z_6\mathcal{R}_{i1}\mathcal{R}_{i1} + Z_7(\mathcal{R}_{i2}\mathcal{R}_{i2} + \mathcal{R}_{i3}\mathcal{R}_{i3})\Big)v^2 A_0[m_{H_i}^2].
\end{aligned} \tag{E.16}$$

The divergent parts of the A type contributions are given by

$$F_+^{(A\text{ type})}|_{\text{div}} = \frac{s_W^2}{2}\frac{1}{m_{H^\pm}^2 - m_W^2}(Z_6 m_W^2 + Z_7 m_{H^\pm}^2)\Delta$$

$$+\frac{s_W^2}{2}\frac{1}{m_{H^\pm}^2-m_W^2}\frac{v^2}{2}\Big(-2Z_7\frac{m_{H^\pm}^2}{v^2}-2Z_1Z_6-2Z_3Z_6-Z_4Z_6-Z_4Z_7-Z_5Z_6^*-Z_5Z_7^*\Big)\Delta$$
$$-\frac{\sqrt{2}s_W^2}{v}\frac{1}{m_W^2-m_{H^\pm}^2}\Big(N_c(\rho_u^\dagger)_{ll}m_{u_l}^3+N_c(\rho_d)_{ll}m_{d_l}^3+(\rho_e)_{ll}m_{e_l}^3\Big)\Delta. \tag{E.17}$$

From Eqs. (E.3), (E.7), (E.11) and (E.17), all of the divergences are cancel out.

By using the above results, we can derive the coefficients of the tensor decomposition for the decay $H^- \to W^- Z$. The coefficients F_-, G_- and H_- from the A, B and C type contributions can be obtained by just taking complex conjugate of the coupling constants in front of the loop functions in the above results. The fermion contributions of F_-, G_- and H_- can be obtained by replacing as

$$\Gamma^f_{ml} \to \left(\Gamma^{f\dagger}\right)_{lm} \quad (f=u,d,e), \qquad (V_{\rm CKM}^\dagger)_{lm} \to (V_{\rm CKM})_{ml}, \tag{E.18}$$

and $i \to -i$ in $F_+^{(F\ \text{type})}$, $G_+^{(F\ \text{type})}$ and $H_+^{(F\ \text{type})}$.

Appendix F

Formulae of the vertex functions for the mass-dependent beta function in the toy model

In this appendix, analytic formulae for the vertex functions in the toy model are given at the one-loop level.

The one-point vertex function of ρ is given by

$$\Gamma^{(1)}_{\rho}(0) = \frac{1}{16\pi^2}\left(\frac{3}{2}\lambda_1 v A_0[m^2_\rho] + \lambda_3 v A_0[m^2_{\phi_2}]\right) + \frac{1}{2}v m^2_\rho\big(Z_{\mu_1} - Z_{\lambda_1}\big), \tag{F.1}$$

where A_0 does not have any momentum dependence.

The self energies for ρ and ϕ_2 fields are given by

$$\begin{aligned}\Pi_{\rho\rho}(k^2) = \frac{1}{16\pi^2}\Bigg(&\frac{3}{2}\lambda_1 A_0[m^2_\rho] + \lambda_3 A_0[m^2_{\phi_2}] + \frac{9}{2}\lambda_1 m^2_\rho B_0[k^2; m^2_\rho, m^2_\rho] + \frac{1}{2}\lambda_1 m^2_\rho B_0[k^2; 0, 0] \\ &+ \lambda^2_3 v^2 B_0[k^2; m^2_{\phi_2}, m^2_{\phi_2}]\Bigg) + (Z_{\phi_1} - 1)k^2 - \frac{1}{2}\Big(3(Z_{\lambda_1} - 1) - (Z_{\mu_1} - 1)\Big)m^2_\rho,\end{aligned} \tag{F.2}$$

and

$$\begin{aligned}\Pi_{\phi_2\phi_2^\dagger}(k^2) = \frac{1}{16\pi^2}&\left(2\lambda_2 A_0[m^2_{\phi_2}] + \frac{1}{2}\lambda_3 A_0[m^2_\rho] + \lambda^2_3 v^2 B_0[k^2; m^2_\rho, m^2_{\phi_2}]\right) + (Z_{\phi_2} - 1)k^2 \\ &- \Big((Z_{\mu_2} - 1)\mu^2_2 + \frac{1}{2}(Z_{\lambda_3} - 1)\lambda_3 v^2\Big).\end{aligned} \tag{F.3}$$

The corresponding two-point vertex function is obtained by

$$\Gamma^{(2)}(k^2) = k^2 - m^2 + \Pi(k^2). \tag{F.4}$$

The four-point vertex functions at the symmetric point are given by

$$\begin{aligned}16\pi^2\Gamma^{(4)}_{\rho\rho\phi_2\phi_2^\dagger}\Big|_{k=\text{sym.}} &= -16\pi^2 Z_{\lambda_3}\lambda_3 + \frac{3}{2}\lambda_1\lambda_3 B_0[m^2_\rho, m^2_\rho] + \frac{1}{2}\lambda_1\lambda_3 B_0[0,0] + 2\lambda_2\lambda_3 B_0[m^2_{\phi_2}, m^2_{\phi_2}] \\ &+ 2\lambda^2_3 B_0[m^2_{\phi_2}, m^2_\rho] + 9\lambda_1\lambda_3 m^2_\rho C_0[m^2_\rho, m^2_\rho, m^2_\rho] + \lambda_1\lambda_3 m^2_\rho C_0[0,0,0] + 12\lambda^2_3 m^2_\rho C_0[m^2_{\phi_2}, m^2_\rho, m^2_\rho] \\ &+ 3\lambda^2_3 m^2_\rho C_0[m^2_\rho, m^2_\rho, m^2_{\phi_2}] + 4\lambda_2\lambda^2_3 v^2 C_0[m^2_{\phi_2}, m^2_{\phi_2}, m^2_{\phi_2}] + \lambda^3_3 v^2 C_0[m^2_{\phi_2}, m^2_{\phi_2}, m^2_\rho] \\ &+ 4\lambda^3_3 v^2 C_0[m^2_{\phi_2}, m^2_\rho, m^2_{\phi_2}] + 18\lambda^2_3 m^4_\rho D_0[m^2_{\phi_2}, m^2_\rho, m^2_\rho, m^2_\rho] + 6\lambda^3_3 m^2_\rho v^2 D_0[m^2_{\phi_2}, m^2_\rho, m^2_{\phi_2}, m^2_\rho] \\ &+ 2\lambda^4_3 v^4 D_0[m^2_{\phi_2}, m^2_{\phi_2}, m^2_{\phi_2}, m^2_\rho],\end{aligned} \tag{F.5}$$

and

$$16\pi^2\Gamma^{(4)}_{\phi_2\phi_2^\dagger\phi_2\phi_2^\dagger}\Big|_{k=\text{sym.}} = -32\pi^2 Z_{\lambda_2}\lambda_2 + 10\lambda_2^2 B_0[m_{\phi_2}^2, m_{\phi_2}^2] + \lambda_3^2 B_0[m_\rho^2, m_\rho^2] + \lambda_3^2 B_0[0,0]$$
$$+ 12\lambda_2\lambda_3^2 v^2 C_0[m_{\phi_2}^2, m_{\phi_2}^2, m_\rho^2] + 4\lambda_3^3 v^2 C_0[m_\rho^2, m_\rho^2, m_{\phi_2}^2] + 4\lambda_3^4 v^4 D_0[m_{\phi_2}^2, m_{\phi_2}^2, m_\rho^2, m_\rho^2]. \quad \text{(F.6)}$$

Here we have defined shorthand notations as

$$\begin{aligned}
&B_0[a,b] \equiv B_0\Big[-\frac{4}{3}Q^2; a, b\Big],\\
&C_0[a,b,c] \equiv C_0\Big[-\frac{4}{3}Q^2, -Q^2, -Q^2; a, b, c\Big],\\
&D_0[a,b,c,d] \equiv\\
&D_0\Big[-\frac{4}{3}Q^2, -Q^2, -\frac{4}{3}Q^2, -Q^2, -Q^2, -Q^2; a, b, c, d\Big].
\end{aligned} \quad \text{(F.7)}$$

After imposing the seven renormalization conditions given in Eqs. (9.12), (9.15) and (9.16), the MD beta functions are obtained as

$$\begin{aligned}
\beta_{\lambda_1} &= \mathcal{D}_Q\lambda_1 = \lambda_1\mathcal{D}_Q \log\big(Z_{\lambda_1}^{-1} Z_{\phi_1}^2\big),\\
\beta_{\lambda_2} &= \mathcal{D}_Q\lambda_2 = \lambda_2\mathcal{D}_Q \log\big(Z_{\lambda_2}^{-1} Z_{\phi_2}^2\big),\\
\beta_{\lambda_3} &= \mathcal{D}_Q\lambda_3 = \lambda_3\mathcal{D}_Q \log\big(Z_{\lambda_3}^{-1} Z_{\phi_1} Z_{\phi_2}\big).
\end{aligned} \quad \text{(F.8)}$$

Bibliography

[1] S. L. Glashow. Partial Symmetries of Weak Interactions. *Nucl. Phys.*, 22:579–588, 1961.

[2] Steven Weinberg. A Model of Leptons. *Phys. Rev. Lett.*, 19:1264–1266, 1967.

[3] Abdus Salam. Weak and Electromagnetic Interactions. *Conf. Proc. C*, 680519:367–377, 1968.

[4] Harald Fritzsch and Murray Gell-Mann. Current algebra: Quarks and what else? *eConf*, C720906V2:135–165, 1972.

[5] H. Fritzsch, Murray Gell-Mann, and H. Leutwyler. Advantages of the Color Octet Gluon Picture. *Phys. Lett. B*, 47:365–368, 1973.

[6] Steven Weinberg. Nonabelian Gauge Theories of the Strong Interactions. *Phys. Rev. Lett.*, 31:494–497, 1973.

[7] Steven Weinberg. Current algebra and gauge theories. 2. NonAbelian gluons. *Phys. Rev. D*, 8:4482–4498, 1973.

[8] D. J. Gross and Frank Wilczek. Asymptotically Free Gauge Theories - I. *Phys. Rev. D*, 8:3633–3652, 1973.

[9] Peter W. Higgs. Broken Symmetries and the Masses of Gauge Bosons. *Phys. Rev. Lett.*, 13:508–509, 1964.

[10] Georges Aad et al. Observation of a new particle in the search for the Standard Model Higgs boson with the ATLAS detector at the LHC. *Phys. Lett. B*, 716:1–29, 2012.

[11] Serguei Chatrchyan et al. Observation of a New Boson at a Mass of 125 GeV with the CMS Experiment at the LHC. *Phys. Lett. B*, 716:30–61, 2012.

[12] Pierre Fayet. Supergauge Invariant Extension of the Higgs Mechanism and a Model for the electron and Its Neutrino. *Nucl. Phys. B*, 90:104–124, 1975.

[13] Steven Weinberg. Implications of Dynamical Symmetry Breaking. *Phys. Rev. D*, 13:974–996, 1976. [Addendum: Phys.Rev.D 19, 1277–1280 (1979)].

[14] Leonard Susskind. Dynamics of Spontaneous Symmetry Breaking in the Weinberg-Salam Theory. *Phys. Rev. D*, 20:2619–2625, 1979.

[15] Lisa Randall and Raman Sundrum. A Large mass hierarchy from a small extra dimension. *Phys. Rev. Lett.*, 83:3370–3373, 1999.

[16] H. Georgi and S. L. Glashow. Unity of All Elementary Particle Forces. *Phys. Rev. Lett.*, 32:438–441, 1974.

[17] Y. Fukuda et al. Evidence for oscillation of atmospheric neutrinos. *Phys. Rev. Lett.*, 81:1562–1567, 1998.

[18] N. Aghanim et al. Planck 2018 results. VI. Cosmological parameters. *Astron. Astrophys.*, 641:A6, 2020. [Erratum: Astron.Astrophys. 652, C4 (2021)].

[19] Georges Aad et al. A detailed map of Higgs boson interactions by the ATLAS experiment ten years after the discovery. *Nature*, 607(7917):52–59, 2022. [Erratum: Nature 612, E24 (2022)].

[20] Armen Tumasyan et al. A portrait of the Higgs boson by the CMS experiment ten years after the discovery. *Nature*, 607(7917):60–68, 2022. [Erratum: Nature 623, (2023)].

[21] M. Cepeda et al. Report from Working Group 2: Higgs Physics at the HL-LHC and HE-LHC. *CERN Yellow Rep. Monogr.*, 7:221–584, 2019.

[22] Hiroaki Aihara et al. The International Linear Collider. A Global Project. 1 2019.

[23] Shinya Kanemura, Yasuhiro Okada, and Eibun Senaha. Electroweak baryogenesis and quantum corrections to the triple Higgs boson coupling. *Phys. Lett. B*, 606:361–366, 2005.

[24] Keisuke Fujii et al. Physics Case for the International Linear Collider. 6 2015.

[25] Philip Bambade et al. The International Linear Collider: A Global Project. 3 2019.

[26] A. D. Sakharov. Violation of CP Invariance, C asymmetry, and baryon asymmetry of the universe. *Pisma Zh. Eksp. Teor. Fiz.*, 5:32–35, 1967.

[27] V. A. Kuzmin, V. A. Rubakov, and M. E. Shaposhnikov. On the Anomalous Electroweak Baryon Number Nonconservation in the Early Universe. *Phys. Lett. B*, 155:36, 1985.

[28] N. S. Manton. Topology in the Weinberg-Salam Theory. *Phys. Rev. D*, 28:2019, 1983.

[29] Nicola Cabibbo. Unitary Symmetry and Leptonic Decays. *Phys. Rev. Lett.*, 10:531–533, 1963.

[30] Makoto Kobayashi and Toshihide Maskawa. CP Violation in the Renormalizable Theory of Weak Interaction. *Prog. Theor. Phys.*, 49:652–657, 1973.

[31] Patrick Huet and Eric Sather. Electroweak baryogenesis and standard model CP violation. *Phys. Rev. D*, 51:379–394, 1995.

[32] K. Kajantie, M. Laine, K. Rummukainen, and Mikhail E. Shaposhnikov. Is there a hot electroweak phase transition at $m_H \gtrsim m_W$? *Phys. Rev. Lett.*, 77:2887–2890, 1996.

[33] Michela D'Onofrio and Kari Rummukainen. Standard model cross-over on the lattice. *Phys. Rev. D*, 93(2):025003, 2016.

[34] Neil Turok and John Zadrozny. Electroweak baryogenesis in the two doublet model. *Nucl. Phys. B*, 358:471–493, 1991.

[35] James M. Cline, Kimmo Kainulainen, and Axel P. Vischer. Dynamics of two Higgs doublet CP violation and baryogenesis at the electroweak phase transition. *Phys. Rev. D*, 54:2451–2472, 1996.

[36] Lars Fromme, Stephan J. Huber, and Michael Seniuch. Baryogenesis in the two-Higgs doublet model. *JHEP*, 11:038, 2006.

[37] James M. Cline, Kimmo Kainulainen, and Michael Trott. Electroweak Baryogenesis in Two Higgs Doublet Models and B meson anomalies. *JHEP*, 11:089, 2011.

[38] Sean Tulin and Peter Winslow. Anomalous B meson mixing and baryogenesis. *Phys. Rev. D*, 84:034013, 2011.

[39] Tao Liu, Michael J. Ramsey-Musolf, and Jing Shu. Electroweak Beautygenesis: From b \to s CP-violation to the Cosmic Baryon Asymmetry. *Phys. Rev. Lett.*, 108:221301, 2012.

[40] M. Ahmadvand. Baryogenesis within the two-Higgs-doublet model in the Electroweak scale. *Int. J. Mod. Phys. A*, 29(20):1450090, 2014.

[41] Cheng-Wei Chiang, Kaori Fuyuto, and Eibun Senaha. Electroweak Baryogenesis with Lepton Flavor Violation. *Phys. Lett. B*, 762:315–320, 2016.

[42] Huai-Ke Guo, Ying-Ying Li, Tao Liu, Michael Ramsey-Musolf, and Jing Shu. Lepton-Flavored Electroweak Baryogenesis. *Phys. Rev. D*, 96(11):115034, 2017.

[43] Kaori Fuyuto, Wei-Shu Hou, and Eibun Senaha. Electroweak baryogenesis driven by extra top Yukawa couplings. *Phys. Lett. B*, 776:402–406, 2018.

[44] G. C. Dorsch, S. J. Huber, T. Konstandin, and J. M. No. A Second Higgs Doublet in the Early Universe: Baryogenesis and Gravitational Waves. *JCAP*, 05:052, 2017.

[45] Tanmoy Modak and Eibun Senaha. Electroweak baryogenesis via bottom transport. *Phys. Rev. D*, 99(11):115022, 2019.

[46] Philipp Basler, Lisa Biermann, Margarete Mühlleitner, and Jonas Müller. Electroweak baryogenesis in the CP-violating two-Higgs doublet model. *Eur. Phys. J. C*, 83(1):57, 2023.

[47] Kazuki Enomoto, Shinya Kanemura, and Yushi Mura. Electroweak baryogenesis in aligned two Higgs doublet models. *JHEP*, 01:104, 2022.

[48] Kazuki Enomoto, Shinya Kanemura, and Yushi Mura. New benchmark scenarios of electroweak baryogenesis in aligned two Higgs double models. *JHEP*, 09:121, 2022.

[49] Shinya Kanemura and Yushi Mura. Electroweak baryogenesis via top-charm mixing. *JHEP*, 09:153, 2023.

[50] Mayumi Aoki and Hiroto Shibuya. Electroweak baryogenesis between broken phases in multi-step phase transition. *Phys. Lett. B*, 843:138041, 2023.

[51] Koichi Funakubo, Akira Kakuto, and Kazunori Takenaga. The Effective potential of electroweak theory with two massless Higgs doublets at finite temperature. *Prog. Theor. Phys.*, 91:341–352, 1994.

[52] A. T. Davies, C. D. froggatt, G. Jenkins, and R. G. Moorhouse. Baryogenesis constraints on two Higgs doublet models. *Phys. Lett. B*, 336:464–470, 1994.

[53] James M. Cline and Pierre-Anthony Lemieux. Electroweak phase transition in two Higgs doublet models. *Phys. Rev. D*, 55:3873–3881, 1997.

[54] Jose R. Espinosa, Ben Gripaios, Thomas Konstandin, and Francesco Riva. Electroweak Baryogenesis in Non-minimal Composite Higgs Models. *JCAP*, 01:012, 2012.

[55] James M. Cline and Kimmo Kainulainen. Electroweak baryogenesis and dark matter from a singlet Higgs. *JCAP*, 01:012, 2013.

[56] James M. Cline, Avi Friedlander, Dong-Ming He, Kimmo Kainulainen, Benoit Laurent, and David Tucker-Smith. Baryogenesis and gravity waves from a UV-completed electroweak phase transition. *Phys. Rev. D*, 103(12):123529, 2021.

[57] Chikako Idegawa and Eibun Senaha. Electron electric dipole moment and electroweak baryogenesis in a complex singlet extension of the Standard Model with degenerate scalars. *Phys. Lett. B*, 848:138332, 2024.

[58] Christophe Grojean and Geraldine Servant. Gravitational Waves from Phase Transitions at the Electroweak Scale and Beyond. *Phys. Rev. D*, 75:043507, 2007.

[59] Chiara Caprini et al. Science with the space-based interferometer eLISA. II: Gravitational waves from cosmological phase transitions. *JCAP*, 04:001, 2016.

[60] Mitsuru Kakizaki, Shinya Kanemura, and Toshinori Matsui. Gravitational waves as a probe of extended scalar sectors with the first order electroweak phase transition. *Phys. Rev. D*, 92(11):115007, 2015.

[61] Katsuya Hashino, Mitsuru Kakizaki, Shinya Kanemura, and Toshinori Matsui. Synergy between measurements of gravitational waves and the triple-Higgs coupling in probing the first-order electroweak phase transition. *Phys. Rev. D*, 94(1):015005, 2016.

[62] Jose R. Espinosa, Thomas Konstandin, Jose M. No, and Geraldine Servant. Energy Budget of Cosmological First-order Phase Transitions. *JCAP*, 06:028, 2010.

[63] Pau Amaro-Seoane et al. Laser Interferometer Space Antenna. 2 2017.

[64] Naoki Seto, Seiji Kawamura, and Takashi Nakamura. Possibility of direct measurement of the acceleration of the universe using 0.1-Hz band laser interferometer gravitational wave antenna in space. *Phys. Rev. Lett.*, 87:221103, 2001.

[65] Vincent Corbin and Neil J. Cornish. Detecting the cosmic gravitational wave background with the big bang observer. *Class. Quant. Grav.*, 23:2435–2446, 2006.

[66] M. J. G. Veltman. Limit on Mass Differences in the Weinberg Model. *Nucl. Phys. B*, 123:89–99, 1977.

[67] D. Toussaint. Renormalization Effects From Superheavy Higgs Particles. *Phys. Rev. D*, 18:1626, 1978.

[68] Michael S. Chanowitz, M. A. Furman, and I. Hinchliffe. Weak Interactions of Ultraheavy Fermions. *Phys. Lett. B*, 78:285, 1978.

[69] Rick Lytel. Weak Isospin Breaking and Higher Order Corrections. *Phys. Rev. D*, 22:505, 1980.

[70] M. B. Einhorn, D. R. T. Jones, and M. J. G. Veltman. Heavy Particles and the rho Parameter in the Standard Model. *Nucl. Phys. B*, 191:146–172, 1981.

[71] M. Baak, M. Goebel, J. Haller, A. Hoecker, D. Kennedy, R. Kogler, K. Moenig, M. Schott, and J. Stelzer. The Electroweak Fit of the Standard Model after the Discovery of a New Boson at the LHC. *Eur. Phys. J. C*, 72:2205, 2012.

[72] M. Baak, J. Cúth, J. Haller, A. Hoecker, R. Kogler, K. Mönig, M. Schott, and J. Stelzer. The global electroweak fit at NNLO and prospects for the LHC and ILC. *Eur. Phys. J. C*, 74:3046, 2014.

[73] R. L. Workman et al. Review of Particle Physics. *PTEP*, 2022:083C01, 2022.

[74] P. Sikivie, Leonard Susskind, Mikhail B. Voloshin, and Valentin I. Zakharov. Isospin Breaking in Technicolor Models. *Nucl. Phys. B*, 173:189–207, 1980.

[75] J. Cline. LHC Signals of Electroweak Baryogenesis. `https://indico.cern.ch/event/1102363/contributions/4820799/attachments/2439752/4184584/LHC2.pdf`.

[76] Shinya Kanemura, Osamu Seto, and Takashi Shimomura. Masses of dark matter and neutrino from TeV scale spontaneous $U(1)_{B-L}$ breaking. *Phys. Rev. D*, 84:016004, 2011.

[77] Debasish Borah, Dibyendu Nanda, Nimmala Narendra, and Narendra Sahu. Right-handed neutrino dark matter with radiative neutrino mass in gauged $B-L$ model. *Nucl. Phys. B*, 950:114841, 2020.

[78] Osamu Seto and Takashi Shimomura. Atomki anomaly and dark matter in a radiative seesaw model with gauged $B-L$ symmetry. *Phys. Rev. D*, 95(9):095032, 2017.

[79] Lars Fromme and Stephan J. Huber. Top transport in electroweak baryogenesis. *JHEP*, 03:049, 2007.

[80] Ligong Bian, Tao Liu, and Jing Shu. Cancellations Between Two-Loop Contributions to the Electron Electric Dipole Moment with a CP-Violating Higgs Sector. *Phys. Rev. Lett.*, 115:021801, 2015.

[81] Kaori Fuyuto, Wei-Shu Hou, and Eibun Senaha. Cancellation mechanism for the electron electric dipole moment connected with the baryon asymmetry of the Universe. *Phys. Rev. D*, 101(1):011901, 2020.

[82] Kingman Cheung, Adil Jueid, Ying-Nan Mao, and Stefano Moretti. Two-Higgs-doublet model with soft CP violation confronting electric dipole moments and colliders. *Phys. Rev. D*, 102(7):075029, 2020.

[83] Shinya Kanemura, Mitsunori Kubota, and Kei Yagyu. Aligned CP-violating Higgs sector canceling the electric dipole moment. *JHEP*, 08:026, 2020.

[84] J. A. Grifols and A. Mendez. The $WZH^{\pm}$ Coupling in $SU(2) \times U(1)$ Gauge Models. *Phys. Rev. D*, 22:1725, 1980.

[85] Thomas G. Rizzo. One Loop Induced WZH Coupling in the Two Higgs Doublet Model. *Mod. Phys. Lett. A*, 4:2757, 1989.

[86] Shinya Kanemura, Yushi Mura, and Guohao Ying. Revisiting the model for radiative neutrino masses with dark matter in the $\mathrm{U}(1)_{B-L}$ gauge theory. 10 2024.

[87] Shinya Kanemura and Yushi Mura. Loop induced $H^{\pm}W^{\pm}Z$ vertices in the general two Higgs doublet model with CP violation. *JHEP*, 10:041, 2024.

[88] Shinya Kanemura and Yushi Mura. Criterion of perturbativity with the mass-dependent beta function in extended Higgs models. *Phys. Rev. D*, 110(7):075016, 2024.

[89] S. L. Glashow, J. Iliopoulos, and L. Maiani. Weak Interactions with Lepton-Hadron Symmetry. *Phys. Rev. D*, 2:1285–1292, 1970.

[90] Ling-Lie Chau and Wai-Yee Keung. Comments on the Parametrization of the Kobayashi-Maskawa Matrix. *Phys. Rev. Lett.*, 53:1802, 1984.

[91] C. Jarlskog. A Basis Independent Formulation of the Connection Between Quark Mass Matrices, CP Violation and Experiment. *Z. Phys. C*, 29:491–497, 1985.

[92] C. Jarlskog. Commutator of the Quark Mass Matrices in the Standard Electroweak Model and a Measure of Maximal CP Nonconservation. *Phys. Rev. Lett.*, 55:1039, 1985.

[93] S. Navas et al. Review of particle physics. *Phys. Rev. D*, 110(3):030001, 2024.

[94] Kazuo Fujikawa. Path Integral Measure for Gauge Invariant Fermion Theories. *Phys. Rev. Lett.*, 42:1195–1198, 1979.

[95] Kazuo Fujikawa. Path Integral for Gauge Theories with Fermions. *Phys. Rev. D*, 21:2848, 1980. [Erratum: Phys.Rev.D 22, 1499 (1980)].

[96] Frans R. Klinkhamer and N. S. Manton. A Saddle Point Solution in the Weinberg-Salam Theory. *Phys. Rev. D*, 30:2212, 1984.

[97] Michael E. Peskin and Tatsu Takeuchi. A New constraint on a strongly interacting Higgs sector. *Phys. Rev. Lett.*, 65:964–967, 1990.

[98] Michael E. Peskin and Tatsu Takeuchi. Estimation of oblique electroweak corrections. *Phys. Rev. D*, 46:381–409, 1992.

[99] J R Andersen et al. Handbook of LHC Higgs Cross Sections: 3. Higgs Properties. 7 2013.

[100] D. de Florian et al. Handbook of LHC Higgs Cross Sections: 4. Deciphering the Nature of the Higgs Sector. 2/2017, 10 2016.

[101] Georges Aad et al. Combined Measurement of the Higgs Boson Mass from the H$\to\gamma\gamma$ and H$\to$ZZ$^*\to 4\ell$ Decay Channels with the ATLAS Detector Using s=7, 8, and 13 TeV pp Collision Data. *Phys. Rev. Lett.*, 131(25):251802, 2023.

[102] Aram Hayrapetyan et al. Measurement of the Higgs boson mass and width using the four-lepton final state in proton-proton collisions at $\sqrt{s} = 13$ TeV. 9 2024.

[103] ATLAS. A detailed map of Higgs boson interactions by the ATLAS experiment ten years after the discovery. `https://atlas.web.cern.ch/Atlas/GROUPS/PHYSICS/PAPERS/HIGG-2021-23/`.

[104] CMS. A portrait of the Higgs boson by the CMS experiment ten years after the discovery. `https://cms-results.web.cern.ch/cms-results/public-results/publications/HIG-22-001/index.html`.

[105] Georges Aad et al. Constraints on the Higgs boson self-coupling from single- and double-Higgs production with the ATLAS detector using pp collisions at s=13 TeV. *Phys. Lett. B*, 843:137745, 2023.

[106] B. Pontecorvo. Inverse beta processes and nonconservation of lepton charge. *Zh. Eksp. Teor. Fiz.*, 34:247, 1957.

[107] Ziro Maki, Masami Nakagawa, and Shoichi Sakata. Remarks on the unified model of elementary particles. *Prog. Theor. Phys.*, 28:870–880, 1962.

[108] Peter Minkowski. $\mu \to e\gamma$ at a Rate of One Out of 10^9 Muon Decays? *Phys. Lett. B*, 67:421–428, 1977.

[109] Tsutomu Yanagida. Horizontal gauge symmetry and masses of neutrinos. *Conf. Proc. C*, 7902131:95–99, 1979.

[110] Murray Gell-Mann, Pierre Ramond, and Richard Slansky. Complex Spinors and Unified Theories. *Conf. Proc. C*, 790927:315–321, 1979.

[111] Pierre Ramond. The Family Group in Grand Unified Theories. In *International Symposium on Fundamentals of Quantum Theory and Quantum Field Theory*, 2 1979.

[112] T. P. Cheng and Ling-Fong Li. Neutrino Masses, Mixings and Oscillations in SU(2) $\times$ U(1) Models of Electroweak Interactions. *Phys. Rev. D*, 22:2860, 1980.

[113] J. Schechter and J. W. F. Valle. Neutrino Masses in SU(2) $\times$ U(1) Theories. *Phys. Rev. D*, 22:2227, 1980.

[114] George Lazarides, Q. Shafi, and C. Wetterich. Proton Lifetime and Fermion Masses in an SO(10) Model. *Nucl. Phys. B*, 181:287–300, 1981.

[115] Rabindra N. Mohapatra and Goran Senjanovic. Neutrino Mass and Spontaneous Parity Nonconservation. *Phys. Rev. Lett.*, 44:912, 1980.

[116] Rabindra N. Mohapatra and Goran Senjanovic. Neutrino Masses and Mixings in Gauge Models with Spontaneous Parity Violation. *Phys. Rev. D*, 23:165, 1981.

[117] M. Magg and C. Wetterich. Neutrino Mass Problem and Gauge Hierarchy. *Phys. Lett. B*, 94:61–64, 1980.

[118] Robert Foot, H. Lew, X. G. He, and Girish C. Joshi. Seesaw Neutrino Masses Induced by a Triplet of Leptons. *Z. Phys. C*, 44:441, 1989.

[119] A. Zee. A Theory of Lepton Number Violation, Neutrino Majorana Mass, and Oscillation. *Phys. Lett. B*, 93:389, 1980. [Erratum: Phys.Lett.B 95, 461 (1980)].

[120] A. Zee. Quantum Numbers of Majorana Neutrino Masses. *Nucl. Phys. B*, 264:99–110, 1986.

[121] K. S. Babu. Model of 'Calculable' Majorana Neutrino Masses. *Phys. Lett. B*, 203:132–136, 1988.

[122] Lawrence M. Krauss, Salah Nasri, and Mark Trodden. A Model for neutrino masses and dark matter. *Phys. Rev. D*, 67:085002, 2003.

[123] Zhi-jian Tao. Radiative seesaw mechanism at weak scale. *Phys. Rev. D*, 54:5693–5697, 1996.

[124] Ernest Ma. Verifiable radiative seesaw mechanism of neutrino mass and dark matter. *Phys. Rev. D*, 73:077301, 2006.

[125] Mayumi Aoki, Shinya Kanemura, and Osamu Seto. Neutrino mass, Dark Matter and Baryon Asymmetry via TeV-Scale Physics without Fine-Tuning. *Phys. Rev. Lett.*, 102:051805, 2009.

[126] Benjamin W. Lee and Steven Weinberg. Cosmological Lower Bound on Heavy Neutrino Masses. *Phys. Rev. Lett.*, 39:165–168, 1977.

[127] Gerard Jungman, Marc Kamionkowski, and Kim Griest. Supersymmetric dark matter. *Phys. Rept.*, 267:195–373, 1996.

[128] Edward W. Kolb. *The Early Universe*, volume 69. Taylor and Francis, 5 2019.

[129] E. Aprile et al. First Dark Matter Search with Nuclear Recoils from the XENONnT Experiment. *Phys. Rev. Lett.*, 131(4):041003, 2023.

[130] Yue Meng et al. Dark Matter Search Results from the PandaX-4T Commissioning Run. *Phys. Rev. Lett.*, 127(26):261802, 2021.

[131] J. Aalbers et al. First Dark Matter Search Results from the LUX-ZEPLIN (LZ) Experiment. *Phys. Rev. Lett.*, 131(4):041002, 2023.

[132] J. Aalbers et al. Dark Matter Search Results from 4.2 Tonne-Years of Exposure of the LUX-ZEPLIN (LZ) Experiment. 10 2024.

[133] Motohiko Yoshimura. Unified Gauge Theories and the Baryon Number of the Universe. *Phys. Rev. Lett.*, 41:281–284, 1978. [Erratum: Phys.Rev.Lett. 42, 746 (1979)].

[134] Steven Weinberg. Cosmological Production of Baryons. *Phys. Rev. Lett.*, 42:850–853, 1979.

[135] Ian Affleck and Michael Dine. A New Mechanism for Baryogenesis. *Nucl. Phys. B*, 249:361–380, 1985.

[136] M. Fukugita and T. Yanagida. Baryogenesis Without Grand Unification. *Phys. Lett. B*, 174:45–47, 1986.

[137] Sacha Davidson and Howard E. Haber. Basis-independent methods for the two-Higgs-doublet model. *Phys. Rev. D*, 72:035004, 2005. [Erratum: Phys.Rev.D 72, 099902 (2005)].

[138] Howard E. Haber and Deva O'Neil. Basis-independent methods for the two-Higgs-doublet model. II. The Significance of $\tan\beta$. *Phys. Rev. D*, 74:015018, 2006. [Erratum: Phys.Rev.D 74, 059905 (2006)].

[139] Andreas Crivellin, Ahmet Kokulu, and Christoph Greub. Flavor-phenomenology of two-Higgs-doublet models with generic Yukawa structure. *Phys. Rev. D*, 87(9):094031, 2013.

[140] T. D. Lee. A Theory of Spontaneous T Violation. *Phys. Rev. D*, 8:1226–1239, 1973.

[141] Sheldon L. Glashow and Steven Weinberg. Natural Conservation Laws for Neutral Currents. *Phys. Rev. D*, 15:1958, 1977.

[142] E. A. Paschos. Diagonal Neutral Currents. *Phys. Rev. D*, 15:1966, 1977.

[143] H. E. Haber, Gordon L. Kane, and T. Sterling. The Fermion Mass Scale and Possible Effects of Higgs Bosons on Experimental Observables. *Nucl. Phys. B*, 161:493–532, 1979.

[144] John F. Donoghue and Ling Fong Li. Properties of Charged Higgs Bosons. *Phys. Rev. D*, 19:945, 1979.

[145] Lawrence J. Hall and Mark B. Wise. FLAVOR CHANGING HIGGS - BOSON COUPLINGS. *Nucl. Phys. B*, 187:397–408, 1981.

[146] John F. Gunion, Howard E. Haber, Gordon L. Kane, and Sally Dawson. *The Higgs Hunter's Guide*, volume 80. 2000.

[147] Vernon D. Barger, J. L. Hewett, and R. J. N. Phillips. New Constraints on the Charged Higgs Sector in Two Higgs Doublet Models. *Phys. Rev. D*, 41:3421–3441, 1990.

[148] Mayumi Aoki, Shinya Kanemura, Koji Tsumura, and Kei Yagyu. Models of Yukawa interaction in the two Higgs doublet model, and their collider phenomenology. *Phys. Rev. D*, 80:015017, 2009.

[149] G. C. Branco, P. M. Ferreira, L. Lavoura, M. N. Rebelo, Marc Sher, and Joao P. Silva. Theory and phenomenology of two-Higgs-doublet models. *Phys. Rept.*, 516:1–102, 2012.

[150] Nilendra G. Deshpande and Ernest Ma. Pattern of Symmetry Breaking with Two Higgs Doublets. *Phys. Rev. D*, 18:2574, 1978.

[151] Howard E. Haber and Deva O'Neil. Basis-independent methods for the two-Higgs-doublet model III: The CP-conserving limit, custodial symmetry, and the oblique parameters S, T, U. *Phys. Rev. D*, 83:055017, 2011.

[152] Alex Pomarol and Roberto Vega. Constraints on CP violation in the Higgs sector from the rho parameter. *Nucl. Phys. B*, 413:3–15, 1994.

[153] J. M. Gerard and M. Herquet. A Twisted custodial symmetry in the two-Higgs-doublet model. *Phys. Rev. Lett.*, 98:251802, 2007.

[154] John F. Gunion and Howard E. Haber. Conditions for CP-violation in the general two-Higgs-doublet model. *Phys. Rev. D*, 72:095002, 2005.

[155] F. J. Botella and Joao P. Silva. Jarlskog - like invariants for theories with scalars and fermions. *Phys. Rev. D*, 51:3870–3875, 1995.

[156] K. G. Klimenko. On Necessary and Sufficient Conditions for Some Higgs Potentials to Be Bounded From Below. *Theor. Math. Phys.*, 62:58–65, 1985.

[157] Marc Sher. Electroweak Higgs Potentials and Vacuum Stability. *Phys. Rept.*, 179:273–418, 1989.

[158] Shuquan Nie and Marc Sher. Vacuum stability bounds in the two Higgs doublet model. *Phys. Lett. B*, 449:89–92, 1999.

[159] Shinya Kanemura, Takashi Kasai, and Yasuhiro Okada. Mass bounds of the lightest CP even Higgs boson in the two Higgs doublet model. *Phys. Lett. B*, 471:182–190, 1999.

[160] Shinya Kanemura, Takashi Kasai, Guey-Lin Lin, Yasuhiro Okada, Jie-Jun Tseng, and C. P. Yuan. Phenomenology of Higgs bosons in the Zee model. *Phys. Rev. D*, 64:053007, 2001.

[161] P. M. Ferreira, R. Santos, and A. Barroso. Stability of the tree-level vacuum in two Higgs doublet models against charge or CP spontaneous violation. *Phys. Lett. B*, 603:219–229, 2004. [Erratum: Phys.Lett.B 629, 114–114 (2005)].

[162] Henning Bahl, Marcela Carena, Nina M. Coyle, Aurora Ireland, and Carlos E. M. Wagner. New tools for dissecting the general 2HDM. *JHEP*, 03:165, 2023.

[163] Benjamin W. Lee, C. Quigg, and H. B. Thacker. Weak Interactions at Very High-Energies: The Role of the Higgs Boson Mass. *Phys. Rev. D*, 16:1519, 1977.

[164] Shinya Kanemura, Takahiro Kubota, and Eiichi Takasugi. Lee-Quigg-Thacker bounds for Higgs boson masses in a two doublet model. *Phys. Lett. B*, 313:155–160, 1993.

[165] Andrew G. Akeroyd, Abdesslam Arhrib, and El-Mokhtar Naimi. Note on tree level unitarity in the general two Higgs doublet model. *Phys. Lett. B*, 490:119–124, 2000.

[166] I. F. Ginzburg and I. P. Ivanov. Tree-level unitarity constraints in the most general 2HDM. *Phys. Rev. D*, 72:115010, 2005.

[167] Shinya Kanemura and Kei Yagyu. Unitarity bound in the most general two Higgs doublet model. *Phys. Lett. B*, 751:289–296, 2015.

[168] Fedor Bezrukov, Mikhail Yu. Kalmykov, Bernd A. Kniehl, and Mikhail Shaposhnikov. Higgs Boson Mass and New Physics. *JHEP*, 10:140, 2012.

[169] Giuseppe Degrassi, Stefano Di Vita, Joan Elias-Miro, Jose R. Espinosa, Gian F. Giudice, Gino Isidori, and Alessandro Strumia. Higgs mass and vacuum stability in the Standard Model at NNLO. *JHEP*, 08:098, 2012.

[170] Dario Buttazzo, Giuseppe Degrassi, Pier Paolo Giardino, Gian F. Giudice, Filippo Sala, Alberto Salvio, and Alessandro Strumia. Investigating the near-criticality of the Higgs boson. *JHEP*, 12:089, 2013.

[171] A. V. Bednyakov, B. A. Kniehl, A. F. Pikelner, and O. L. Veretin. Stability of the Electroweak Vacuum: Gauge Independence and Advanced Precision. *Phys. Rev. Lett.*, 115(20):201802, 2015.

[172] Stephen P. Martin and David G. Robertson. Standard model parameters in the tadpole-free pure $\overline{\text{MS}}$ scheme. *Phys. Rev. D*, 100(7):073004, 2019.

[173] Anirban Karan, Víctor Miralles, and Antonio Pich. Updated global fit of the aligned two-Higgs-doublet model with heavy scalars. *Phys. Rev. D*, 109(3):035012, 2024.

[174] G. Abbiendi et al. Search for Charged Higgs bosons: Combined Results Using LEP Data. *Eur. Phys. J. C*, 73:2463, 2013.

[175] Morad Aaboud et al. Search for charged Higgs bosons decaying via $H^{\pm} \to \tau^{\pm}\nu_{\tau}$ in the τ+jets and τ+lepton final states with 36 fb^{-1} of pp collision data recorded at $\sqrt{s} = 13$ TeV with the ATLAS experiment. *JHEP*, 09:139, 2018.

[176] Albert M Sirunyan et al. Search for charged Higgs bosons in the $\mathrm{H}^{\pm} \to \tau^{\pm}\nu_{\tau}$ decay channel in proton-proton collisions at $\sqrt{s} = 13$ TeV. *JHEP*, 07:142, 2019.

[177] Georges Aad et al. Search for charged Higgs bosons decaying into a top quark and a bottom quark at $\sqrt{\mathrm{s}} = 13$ TeV with the ATLAS detector. *JHEP*, 06:145, 2021.

[178] Shinya Kanemura, Michihisa Takeuchi, and Kei Yagyu. Probing double-aligned two-Higgs-doublet models at the LHC. *Phys. Rev. D*, 105(11):115001, 2022.

[179] Georges Aad et al. Search for resonant WZ production in the fully leptonic final state in proton–proton collisions at $\sqrt{\mathbf{s}} = \mathbf{13}$ TeV with the ATLAS detector. *Eur. Phys. J. C*, 83(7):633, 2023.

[180] Albert M Sirunyan et al. Search for charged Higgs bosons produced in vector boson fusion processes and decaying into vector boson pairs in proton–proton collisions at $\sqrt{s} =$ 13 TeV. *Eur. Phys. J. C*, 81(8):723, 2021.

[181] Georges Aad et al. Search for heavy Higgs bosons decaying into two tau leptons with the ATLAS detector using *pp* collisions at $\sqrt{s} = 13$ TeV. *Phys. Rev. Lett.*, 125(5):051801, 2020.

[182] Morad Aaboud et al. Search for heavy particles decaying into top-quark pairs using lepton-plus-jets events in proton–proton collisions at $\sqrt{s} = 13$ TeV with the ATLAS detector. *Eur. Phys. J. C*, 78(7):565, 2018.

[183] Georges Aad et al. Search for heavy neutral Higgs bosons decaying into a top quark pair in 140 fb^{-1} of proton-proton collision data at $\sqrt{s} = 13$ TeV with the ATLAS detector. 4 2024.

[184] Albert M Sirunyan et al. Search for heavy Higgs bosons decaying to a top quark pair in proton-proton collisions at $\sqrt{s} = 13$ TeV. *JHEP*, 04:171, 2020. [Erratum: JHEP 03, 187 (2022)].

[185] Masashi Aiko, Shinya Kanemura, Mariko Kikuchi, Kentarou Mawatari, Kodai Sakurai, and Kei Yagyu. Probing extended Higgs sectors by the synergy between direct searches at the LHC and precision tests at future lepton colliders. *Nucl. Phys. B*, 966:115375, 2021.

[186] Shinya Kanemura and C. P. Yuan. Testing supersymmetry in the associated production of CP odd and charged Higgs bosons. *Phys. Lett. B*, 530:188–196, 2002.

[187] Qing-Hong Cao, Shinya Kanemura, and C. P. Yuan. Associated production of CP odd and charged Higgs bosons at hadron colliders. *Phys. Rev. D*, 69:075008, 2004.

[188] Alexander Belyaev, Qing-Hong Cao, Daisuke Nomura, Kazuhiro Tobe, and C. P. Yuan. Light MSSM Higgs boson scenario and its test at hadron colliders. *Phys. Rev. Lett.*, 100:061801, 2008.

[189] Georges Aad et al. Search for supersymmetry in events with four or more charged leptons in 139 fb^{-1} of $\sqrt{s} = 13$ TeV pp collisions with the ATLAS detector. *JHEP*, 07:167, 2021.

[190] Martin Jung, Antonio Pich, and Paula Tuzon. The B -> Xs gamma Rate and CP Asymmetry within the Aligned Two-Higgs-Doublet Model. *Phys. Rev. D*, 83:074011, 2011.

[191] Martin Jung, Antonio Pich, and Paula Tuzon. Charged-Higgs phenomenology in the Aligned two-Higgs-doublet model. *JHEP*, 11:003, 2010.

[192] Martin Jung, Xin-Qiang Li, and Antonio Pich. Exclusive radiative B-meson decays within the aligned two-Higgs-doublet model. *JHEP*, 10:063, 2012.

[193] Xin-Qiang Li, Jie Lu, and Antonio Pich. $B^0_{s,d} \to \ell^+\ell^-$ Decays in the Aligned Two-Higgs-Doublet Model. *JHEP*, 06:022, 2014.

[194] Andreas Crivellin, Dario Müller, and Christoph Wiegand. $b \to s\ell^+\ell^-$ transitions in two-Higgs-doublet models. *JHEP*, 06:119, 2019.

[195] Yasmine Sara Amhis et al. Averages of b-hadron, c-hadron, and τ-lepton properties as of 2018. *Eur. Phys. J. C*, 81(3):226, 2021.

[196] Johannes Haller, Andreas Hoecker, Roman Kogler, Klaus Mönig, Thomas Peiffer, and Jörg Stelzer. Update of the global electroweak fit and constraints on two-Higgs-doublet models. *Eur. Phys. J. C*, 78(8):675, 2018.

[197] Morad Aaboud et al. Study of the rare decays of B_s^0 and B^0 mesons into muon pairs using data collected during 2015 and 2016 with the ATLAS detector. *JHEP*, 04:098, 2019.

[198] Albert M Sirunyan et al. Measurement of properties of $\mathrm{B}_\mathrm{s}^0 \to \mu^+\mu^-$ decays and search for $\mathrm{B}^0 \to \mu^+\mu^-$ with the CMS experiment. *JHEP*, 04:188, 2020.

[199] Roel Aaij et al. Measurement of the $B_s^0 \to \mu^+\mu^-$ decay properties and search for the $B^0 \to \mu^+\mu^-$ and $B_s^0 \to \mu^+\mu^-\gamma$ decays. *Phys. Rev. D*, 105(1):012010, 2022.

[200] M. Bona et al. Model-independent constraints on $\Delta F = 2$ operators and the scale of new physics. *JHEP*, 03:049, 2008.

[201] UTfit Collaboration. `http://www.utfit.org/UTfit/ResultsSummer2018NP`.

[202] Chuan-Hung Chen and Takaaki Nomura. $Re(\epsilon'_K/\epsilon_K)$ and $K \to \pi\nu\bar{\nu}$ in a two-Higgs doublet model. *JHEP*, 08:145, 2018.

[203] Antonio Pich and Paula Tuzon. Yukawa Alignment in the Two-Higgs-Doublet Model. *Phys. Rev. D*, 80:091702, 2009.

[204] K. Afanaciev et al. A search for $\mu^+ \to e^+\gamma$ with the first dataset of the MEG II experiment. *Eur. Phys. J. C*, 84(3):216, 2024.

[205] U. Bellgardt et al. Search for the Decay $\mu^+ \to e^+e^+e^-$. *Nucl. Phys. B*, 299:1–6, 1988.

[206] Bernard Aubert et al. Searches for Lepton Flavor Violation in the Decays $\tau^\pm \to e^\pm\gamma$ and $\tau^\pm \to \mu^\pm\gamma$. *Phys. Rev. Lett.*, 104:021802, 2010.

[207] Baris Altunkaynak, Wei-Shu Hou, Chung Kao, Masaya Kohda, and Brent McCoy. Flavor Changing Heavy Higgs Interactions at the LHC. *Phys. Lett. B*, 751:135–142, 2015.

[208] Wei-Shu Hou, Tanmoy Modak, and Tilman Plehn. A final word on FCNC-Baryogenesis from two Higgs doublets. *SciPost Phys.*, 10(6):150, 2021.

[209] Morad Aaboud et al. Search for top-quark decays $t \to Hq$ with 36 fb^{-1} of pp collision data at $\sqrt{s} = 13$ TeV with the ATLAS detector. *JHEP*, 05:123, 2019.

[210] Albert M Sirunyan et al. Search for the flavor-changing neutral current interactions of the top quark and the Higgs boson which decays into a pair of b quarks at $\sqrt{s} = 13$ TeV. *JHEP*, 06:102, 2018.

[211] Masaya Kohda, Tanmoy Modak, and Wei-Shu Hou. Searching for new scalar bosons via triple-top signature in $cg \to tS^0 \to tt\bar{t}$. *Phys. Lett. B*, 776:379–384, 2018.

[212] Syuhei Iguro and Yuji Omura. Status of the semileptonic B decays and muon g-2 in general 2HDMs with right-handed neutrinos. *JHEP*, 05:173, 2018.

[213] Wei-Shu Hou, Masaya Kohda, and Tanmoy Modak. Implications of Four-Top and Top-Pair Studies on Triple-Top Production. *Phys. Lett. B*, 798:134953, 2019.

[214] Wei-Shu Hou, Masaya Kohda, and Tanmoy Modak. Constraining a Lighter Exotic Scalar via Same-sign Top. *Phys. Lett. B*, 786:212–216, 2018.

[215] Search for heavy Higgs bosons from a g2HDM in multilepton plus b-jets final states in pp collisions at 13 TeV with the ATLAS detector. 2022.

[216] Albert M Sirunyan et al. Search for standard model production of four top quarks with same-sign and multilepton final states in proton–proton collisions at $\sqrt{s} = 13\,\text{TeV}$. *Eur. Phys. J. C*, 78(2):140, 2018.

[217] Albert M Sirunyan et al. Search for production of four top quarks in final states with same-sign or multiple leptons in proton-proton collisions at $\sqrt{s} = 13$ TeV. *Eur. Phys. J. C*, 80(2):75, 2020.

[218] Syuhei Iguro. Revival of H- interpretation of RD(*) anomaly and closing low mass window. *Phys. Rev. D*, 105(9):095011, 2022.

[219] A. M. Sirunyan et al. Search for narrow resonances in the b-tagged dijet mass spectrum in proton-proton collisions at $\sqrt{s} = 8$ TeV. *Phys. Rev. Lett.*, 120(20):201801, 2018.

[220] Shinya Kanemura, Shingo Kiyoura, Yasuhiro Okada, Eibun Senaha, and C. P. Yuan. New physics effect on the Higgs selfcoupling. *Phys. Lett. B*, 558:157–164, 2003.

[221] Shinya Kanemura, Yasuhiro Okada, Eibun Senaha, and C. P. Yuan. Higgs coupling constants as a probe of new physics. *Phys. Rev. D*, 70:115002, 2004.

[222] Johannes Braathen and Shinya Kanemura. On two-loop corrections to the Higgs trilinear coupling in models with extended scalar sectors. *Phys. Lett. B*, 796:38–46, 2019.

[223] Johannes Braathen and Shinya Kanemura. Leading two-loop corrections to the Higgs boson self-couplings in models with extended scalar sectors. *Eur. Phys. J. C*, 80(3):227, 2020.

[224] Oscar J. P. Eboli, G. C. Marques, S. F. Novaes, and A. A. Natale. TWIN HIGGS BOSON PRODUCTION. *Phys. Lett. B*, 197:269–272, 1987.

[225] Duane A. Dicus, Chung Kao, and Scott S. D. Willenbrock. Higgs Boson Pair Production From Gluon Fusion. *Phys. Lett. B*, 203:457–461, 1988.

[226] E. W. Nigel Glover and J. J. van der Bij. HIGGS BOSON PAIR PRODUCTION VIA GLUON FUSION. *Nucl. Phys. B*, 309:282–294, 1988.

[227] T. Plehn, M. Spira, and P. M. Zerwas. Pair production of neutral Higgs particles in gluon-gluon collisions. *Nucl. Phys. B*, 479:46–64, 1996. [Erratum: Nucl.Phys.B 531, 655–655 (1998)].

[228] A. Djouadi, W. Kilian, M. Muhlleitner, and P. M. Zerwas. Production of neutral Higgs boson pairs at LHC. *Eur. Phys. J. C*, 10:45–49, 1999.

[229] Xin Li and M. B. Voloshin. Remarks on double Higgs boson production by gluon fusion at threshold. *Phys. Rev. D*, 89(1):013012, 2014.

[230] Dorival Gonçalves, Tao Han, Felix Kling, Tilman Plehn, and Michihisa Takeuchi. Higgs boson pair production at future hadron colliders: From kinematics to dynamics. *Phys. Rev. D*, 97(11):113004, 2018.

[231] Junping Tian. Study of Higgs self-coupling at the ILC based on the full detector simulation at $\sqrt{}$ s = 500 GeV and $\sqrt{}$ s = 1 TeV. In *3rd Linear Collider Forum*, pages 224–247, Hamburg, 2013. DESY.

[232] Eri Asakawa, Daisuke Harada, Shinya Kanemura, Yasuhiro Okada, and Koji Tsumura. Higgs boson pair production in new physics models at hadron, lepton, and photon colliders. *Phys. Rev. D*, 82:115002, 2010.

[233] Masakazu Kurata, Tomohiko Tanabe, Junping Tian, Keisuke Fujii, and Taikan Suehara. The Higgs self coupling analysis using the events containing H $\rightarrow$ WW* decay. `https://flc.desy.de/lcnotes/notes/localfsExplorer_read?currentPath=/afs/desy.de/group/flc/lcnotes/LC-REP-2013-025.pdf`.

[234] J. A. Casas and A. Ibarra. Oscillating neutrinos and $\mu \rightarrow e, \gamma$. *Nucl. Phys. B*, 618:171–204, 2001.

[235] Vernon Barger, Paul Langacker, Mathew McCaskey, Michael Ramsey-Musolf, and Gabe Shaughnessy. Complex Singlet Extension of the Standard Model. *Phys. Rev. D*, 79:015018, 2009.

[236] I. F. Ginzburg, K. A. Kanishev, M. Krawczyk, and D. Sokolowska. Evolution of Universe to the present inert phase. *Phys. Rev. D*, 82:123533, 2010.

[237] Kaori Fuyuto and Eibun Senaha. Improved sphaleron decoupling condition and the Higgs coupling constants in the real singlet-extended standard model. *Phys. Rev. D*, 90(1):015015, 2014.

[238] A. Abdesselam et al. Search for lepton-flavor-violating tau-lepton decays to $\ell\gamma$ at Belle. *JHEP*, 10:19, 2021.

[239] K. Hayasaka et al. Search for Lepton Flavor Violating τ Decays into Three Leptons with 719 Million Produced $\tau^+\tau^-$ Pairs. *Phys. Lett. B*, 687:139–143, 2010.

[240] C. Dohmen et al. Test of lepton flavor conservation in mu —> e conversion on titanium. *Phys. Lett. B*, 317:631–636, 1993.

[241] Wilhelm H. Bertl et al. A Search for muon to electron conversion in muonic gold. *Eur. Phys. J. C*, 47:337–346, 2006.

[242] Erik Lundstrom, Michael Gustafsson, and Joakim Edsjo. The Inert Doublet Model and LEP II Limits. *Phys. Rev. D*, 79:035013, 2009.

[243] the SLD Electroweak. A Combination of preliminary electroweak measurements and constraints on the standard model. 12 2003.

[244] Marcela Carena, Alejandro Daleo, Bogdan A. Dobrescu, and Timothy M. P. Tait. Z' gauge bosons at the Tevatron. *Phys. Rev. D*, 70:093009, 2004.

[245] G. Cacciapaglia, C. Csaki, G. Marandella, and A. Strumia. The Minimal Set of Electroweak Precision Parameters. *Phys. Rev. D*, 74:033011, 2006.

[246] Georges Aad et al. Search for high-mass dilepton resonances using 139 fb^{-1} of pp collision data collected at $\sqrt{s}$ =13 TeV with the ATLAS detector. *Phys. Lett. B*, 796:68–87, 2019.

[247] Georges Aad et al. Search for new resonances in mass distributions of jet pairs using 139 fb^{-1} of pp collisions at $\sqrt{s} = 13$ TeV with the ATLAS detector. *JHEP*, 03:145, 2020.

[248] Albert M Sirunyan et al. Search for resonant and nonresonant new phenomena in high-mass dilepton final states at $\sqrt{s} = 13$ TeV. *JHEP*, 07:208, 2021.

[249] Armen Tumasyan et al. Search for narrow resonances in the b-tagged dijet mass spectrum in proton-proton collisions at $\sqrt{s}$ =13 TeV. *Phys. Rev. D*, 108(1):012009, 2023.

[250] Tania Robens and Tim Stefaniak. Status of the Higgs Singlet Extension of the Standard Model after LHC Run 1. *Eur. Phys. J. C*, 75:104, 2015.

[251] Grace Dupuis. Collider Constraints and Prospects of a Scalar Singlet Extension to Higgs Portal Dark Matter. *JHEP*, 07:008, 2016.

[252] Vernon Barger, Paul Langacker, Mathew McCaskey, Michael J. Ramsey-Musolf, and Gabe Shaughnessy. LHC Phenomenology of an Extended Standard Model with a Real Scalar Singlet. *Phys. Rev. D*, 77:035005, 2008.

[253] Shinya Kanemura, Yasuhiro Okada, Hiroyuki Taniguchi, and Koji Tsumura. Indirect bounds on heavy scalar masses of the two-Higgs-doublet model in light of recent Higgs boson searches. *Phys. Lett. B*, 704:303–307, 2011.

[254] Nobuchika Okada and Osamu Seto. Higgs portal dark matter in the minimal gauged $U(1)_{B-L}$ model. *Phys. Rev. D*, 82:023507, 2010.

[255] Alexander Belyaev, Giacomo Cacciapaglia, Igor P. Ivanov, Felipe Rojas-Abatte, and Marc Thomas. Anatomy of the Inert Two Higgs Doublet Model in the light of the LHC and non-LHC Dark Matter Searches. *Phys. Rev. D*, 97(3):035011, 2018.

[256] Laura Lopez Honorez, Emmanuel Nezri, Josep F. Oliver, and Michel H. G. Tytgat. The Inert Doublet Model: An Archetype for Dark Matter. *JCAP*, 02:028, 2007.

[257] Amit Dutta Banik and Debasish Majumdar. Inert doublet dark matter with an additional scalar singlet and 125 GeV Higgs boson. *Eur. Phys. J. C*, 74(11):3142, 2014.

[258] Mohammed Omer Khojali, Ammar Abdalgabar, Amine Ahriche, and Alan S. Cornell. Dark matter in a singlet-extended inert Higgs-doublet model. *Phys. Rev. D*, 106(9):095039, 2022.

[259] Takashi Toma and Avelino Vicente. Lepton Flavor Violation in the Scotogenic Model. *JHEP*, 01:160, 2014.

[260] Ernesto Arganda and Maria J. Herrero. Testing supersymmetry with lepton flavor violating tau and mu decays. *Phys. Rev. D*, 73:055003, 2006.

[261] Amon Ilakovac, Apostolos Pilaftsis, and Luka Popov. Charged lepton flavor violation in supersymmetric low-scale seesaw models. *Phys. Rev. D*, 87(5):053014, 2013.

[262] Marco Ardu and Gianantonio Pezzullo. Introduction to Charged Lepton Flavor Violation. *Universe*, 8(6):299, 2022.

[263] A. M. Baldini et al. MEG Upgrade Proposal. 1 2013.

[264] A. Blondel et al. Research Proposal for an Experiment to Search for the Decay $\mu \to eee$. 1 2013.

[265] Paolo Gondolo and Graciela Gelmini. Cosmic abundances of stable particles: Improved analysis. *Nucl. Phys. B*, 360:145–179, 1991.

[266] G. Alguero, G. Belanger, F. Boudjema, S. Chakraborti, A. Goudelis, S. Kraml, A. Mjallal, and A. Pukhov. micrOMEGAs 6.0: N-component dark matter. *Comput. Phys. Commun.*, 299:109133, 2024.

[267] Jisuke Kubo, Ernest Ma, and Daijiro Suematsu. Cold Dark Matter, Radiative Neutrino Mass, $\mu \to e\gamma$, and Neutrinoless Double Beta Decay. *Phys. Lett. B*, 642:18–23, 2006.

[268] Eugenio Del Nobile. The Theory of Direct Dark Matter Detection: A Guide to Computations. *Lect.Notes Phys. 996 (2022)*, 4 2021.

[269] Mayumi Aoki, Shinya Kanemura, and Hiroshi Yokoya. Reconstruction of Inert Doublet Scalars at the International Linear Collider. *Phys. Lett. B*, 725:302–309, 2013.

[270] Shinya Kanemura, Mariko Kikuchi, and Kodai Sakurai. Testing the dark matter scenario in the inert doublet model by future precision measurements of the Higgs boson couplings. *Phys. Rev. D*, 94(11):115011, 2016.

[271] Tomohiro Abe and Ryosuke Sato. Quantum corrections to the spin-independent cross section of the inert doublet dark matter. *JHEP*, 03:109, 2015.

[272] S. Moretti. Pair production of charged Higgs scalars from electroweak gauge boson fusion. *J. Phys. G*, 28:2567–2582, 2002.

[273] Alexandre Alves and Tilman Plehn. Charged Higgs boson pairs at the CERN LHC. *Phys. Rev. D*, 71:115014, 2005.

[274] Jan Kalinowski, Wojciech Kotlarski, Tania Robens, Dorota Sokolowska, and Aleksander Filip Zarnecki. Benchmarking the Inert Doublet Model for e^+e^- colliders. *JHEP*, 12:081, 2018.

[275] Lorenzo Basso, Alexander Belyaev, Stefano Moretti, and Giovanni Marco Pruna. Probing the Z-prime sector of the minimal B-L model at future Linear Colliders in the $e^+e^- \to \mu^+\mu^-$ process. *JHEP*, 10:006, 2009.

[276] Y. Mura S. Kanemura and G. Ying. In preparation.

[277] L. Dolan and R. Jackiw. Symmetry Behavior at Finite Temperature. *Phys. Rev. D*, 9:3320–3341, 1974.

[278] Sidney R. Coleman. The Fate of the False Vacuum. 1. Semiclassical Theory. *Phys. Rev. D*, 15:2929–2936, 1977. [Erratum: Phys.Rev.D 16, 1248 (1977)].

[279] Curtis G. Callan, Jr. and Sidney R. Coleman. The Fate of the False Vacuum. 2. First Quantum Corrections. *Phys. Rev. D*, 16:1762–1768, 1977.

[280] Andrei D. Linde. Fate of the False Vacuum at Finite Temperature: Theory and Applications. *Phys. Lett. B*, 100:37–40, 1981.

[281] Guy D. Moore. Measuring the broken phase sphaleron rate nonperturbatively. *Phys. Rev. D*, 59:014503, 1999.

[282] V. Andreev et al. Improved limit on the electric dipole moment of the electron. *Nature*, 562(7727):355–360, 2018.

[283] Tanya S. Roussy et al. A new bound on the electron's electric dipole moment. 12 2022.

[284] C. Abel et al. Measurement of the Permanent Electric Dipole Moment of the Neutron. *Phys. Rev. Lett.*, 124(8):081803, 2020.

[285] B. Graner, Y. Chen, E. G. Lindahl, and B. R. Heckel. Reduced Limit on the Permanent Electric Dipole Moment of Hg199. *Phys. Rev. Lett.*, 116(16):161601, 2016. [Erratum: Phys.Rev.Lett. 119, 119901 (2017)].

[286] B. K. Sahoo. Improved limits on the hadronic and semihadronic CP violating parameters and role of a dark force carrier in the electric dipole moment of ^{199}Hg. *Phys. Rev. D*, 95(1):013002, 2017.

[287] A. Hiramoto et al. SiPM module for the ACME III electron EDM search. *Nucl. Instrum. Meth. A*, 1045:167513, 2023.

[288] A. C. Vutha, M. Horbatsch, and E. A. Hessels. Orientation-dependent hyperfine structure of polar molecules in a rare-gas matrix: A scheme for measuring the electron electric dipole moment. *Phys. Rev. A*, 98(3):032513, 2018.

[289] Marco Ardu, Moinul Hossain Rahat, Nicola Valori, and Oscar Vives. Electric Dipole Moments as indirect probes of dark sectors. *JHEP*, 11:049, 2024.

[290] M. W. Ahmed et al. A New Cryogenic Apparatus to Search for the Neutron Electric Dipole Moment. *JINST*, 14(11):P11017, 2019.

[291] Ricardo Alarcon et al. Electric dipole moments and the search for new physics. In *Snowmass 2021*, 3 2022.

[292] R. D. Peccei and Helen R. Quinn. CP Conservation in the Presence of Instantons. *Phys. Rev. Lett.*, 38:1440–1443, 1977.

[293] R. D. Peccei and Helen R. Quinn. Constraints Imposed by CP Conservation in the Presence of Instantons. *Phys. Rev. D*, 16:1791–1797, 1977.

[294] M. E. Pospelov and I. B. Khriplovich. Electric dipole moment of the W boson and the electron in the Kobayashi-Maskawa model. *Sov. J. Nucl. Phys.*, 53:638–640, 1991.

[295] Stephen M. Barr and A. Zee. Electric Dipole Moment of the Electron and of the Neutron. *Phys. Rev. Lett.*, 65:21–24, 1990. [Erratum: Phys.Rev.Lett. 65, 2920 (1990)].

[296] Maxim Pospelov and Adam Ritz. Neutron EDM from electric and chromoelectric dipole moments of quarks. *Phys. Rev. D*, 63:073015, 2001.

[297] Junji Hisano, Jeong Yong Lee, Natsumi Nagata, and Yasuhiro Shimizu. Reevaluation of Neutron Electric Dipole Moment with QCD Sum Rules. *Phys. Rev. D*, 85:114044, 2012.

[298] Kaori Fuyuto, Junji Hisano, Natsumi Nagata, and Koji Tsumura. QCD Corrections to Quark (Chromo)Electric Dipole Moments in High-scale Supersymmetry. *JHEP*, 12:010, 2013.

[299] Tomohiro Abe, Junji Hisano, Teppei Kitahara, and Kohsaku Tobioka. Gauge invariant Barr-Zee type contributions to fermionic EDMs in the two-Higgs doublet models. *JHEP*, 01:106, 2014. [Erratum: JHEP 04, 161 (2016)].

[300] Kunio Kaneta, Natsumi Nagata, Keith A. Olive, Maxim Pospelov, and Liliana Velasco-Sevilla. Quantifying limits on CP violating phases from EDMs in supersymmetry. *JHEP*, 03:250, 2023.

[301] Steven Weinberg. Larger Higgs Exchange Terms in the Neutron Electric Dipole Moment. *Phys. Rev. Lett.*, 63:2333, 1989.

[302] Duane A. Dicus. Neutron Electric Dipole Moment From Charged Higgs Exchange. *Phys. Rev. D*, 41:999, 1990.

[303] Durmus A. Demir, Maxim Pospelov, and Adam Ritz. Hadronic EDMs, the Weinberg operator, and light gluinos. *Phys. Rev. D*, 67:015007, 2003.

[304] Martin Jung and Antonio Pich. Electric Dipole Moments in Two-Higgs-Doublet Models. *JHEP*, 04:076, 2014.

[305] V. M. Khatsimovsky, I. B. Khriplovich, and A. S. Yelkhovsky. Neutron Electric Dipole Moment, T Odd Nuclear Forces and Nature of CP Violation. *Annals Phys.*, 186:1–14, 1988.

[306] Glenn Boyd, Arun K. Gupta, Sandip P. Trivedi, and Mark B. Wise. Effective Hamiltonian for the Electric Dipole Moment of the Neutron. *Phys. Lett. B*, 241:584–588, 1990.

[307] Ngee-Pong Chang and Da-Xi Li. The Evolution of Weinberg's Gluonic CP Operator and Gauge Dependence. *Phys. Rev. D*, 42:871–873, 1990.

[308] James M. Cline, Michael Joyce, and Kimmo Kainulainen. Supersymmetric electroweak baryogenesis. *JHEP*, 07:018, 2000.

[309] James M. Cline and Kimmo Kainulainen. Electroweak baryogenesis at high bubble wall velocities. *Phys. Rev. D*, 101(6):063525, 2020.

[310] Michael Joyce, Tomislav Prokopec, and Neil Turok. Electroweak baryogenesis from a classical force. *Phys. Rev. Lett.*, 75:1695–1698, 1995. [Erratum: Phys.Rev.Lett. 75, 3375 (1995)].

[311] Michael Joyce, Tomislav Prokopec, and Neil Turok. Nonlocal electroweak baryogenesis. Part 1: Thin wall regime. *Phys. Rev. D*, 53:2930–2957, 1996.

[312] Michael Joyce, Tomislav Prokopec, and Neil Turok. Nonlocal electroweak baryogenesis. Part 2: The Classical regime. *Phys. Rev. D*, 53:2958–2980, 1996.

[313] Guy D. Moore and Tomislav Prokopec. Bubble wall velocity in a first order electroweak phase transition. *Phys. Rev. Lett.*, 75:777–780, 1995.

[314] Guy D. Moore and Tomislav Prokopec. How fast can the wall move? A Study of the electroweak phase transition dynamics. *Phys. Rev. D*, 52:7182–7204, 1995.

[315] P. John and M. G. Schmidt. Do stops slow down electroweak bubble walls? *Nucl. Phys. B*, 598:291–305, 2001. [Erratum: Nucl.Phys.B 648, 449–452 (2003)].

[316] Thomas Konstandin, Germano Nardini, and Ingo Rues. From Boltzmann equations to steady wall velocities. *JCAP*, 09:028, 2014.

[317] Jonathan Kozaczuk. Bubble Expansion and the Viability of Singlet-Driven Electroweak Baryogenesis. *JHEP*, 10:135, 2015.

[318] Guy D. Moore. Sphaleron rate in the symmetric electroweak phase. *Phys. Rev. D*, 62:085011, 2000.

[319] Sidney R. Coleman and Erick J. Weinberg. Radiative Corrections as the Origin of Spontaneous Symmetry Breaking. *Phys. Rev. D*, 7:1888–1910, 1973.

[320] Sebastian Baum, Marcela Carena, Nausheen R. Shah, Carlos E. M. Wagner, and Yikun Wang. Nucleation is more than critical: A case study of the electroweak phase transition in the NMSSM. *JHEP*, 03:055, 2021.

[321] Johannes Braathen and Mark D. Goodsell. Avoiding the Goldstone Boson Catastrophe in general renormalisable field theories at two loops. *JHEP*, 12:056, 2016.

[322] Rajesh R. Parwani. Resummation in a hot scalar field theory. *Phys. Rev. D*, 45:4695, 1992. [Erratum: Phys.Rev.D 48, 5965 (1993)].

[323] Carroll L. Wainwright. CosmoTransitions: Computing Cosmological Phase Transition Temperatures and Bubble Profiles with Multiple Fields. *Comput. Phys. Commun.*, 183:2006–2013, 2012.

[324] John R. Ellis, Mary K. Gaillard, and Dimitri V. Nanopoulos. A Phenomenological Profile of the Higgs Boson. *Nucl. Phys. B*, 106:292, 1976.

[325] Mikhail A. Shifman, A. I. Vainshtein, M. B. Voloshin, and Valentin I. Zakharov. Low-Energy Theorems for Higgs Boson Couplings to Photons. *Sov. J. Nucl. Phys.*, 30:711–716, 1979.

[326] M. B. Gavela, G. Girardi, C. Malleville, and P. Sorba. A Nonlinear R(xi) Gauge Condition for the Electroweak SU(2) X U(1) Model. *Nucl. Phys. B*, 193:257–268, 1981.

[327] A. Barroso, L. Brucher, and R. Santos. Is there a light fermiophobic Higgs? *Phys. Rev. D*, 60:035005, 1999.

[328] A. Arhrib, M. Capdequi Peyranere, W. Hollik, and S. Penaranda. Higgs decays in the two Higgs doublet model: Large quantum effects in the decoupling regime. *Phys. Lett. B*, 579:361–370, 2004.

[329] Abdelhak Djouadi. The Anatomy of electro-weak symmetry breaking. II. The Higgs bosons in the minimal supersymmetric model. *Phys. Rept.*, 459:1–241, 2008.

[330] A. G. Akeroyd, Marco A. Diaz, and Maximiliano A. Rivera. Effect of Charged Scalar Loops on Photonic Decays of a Fermiophobic Higgs. *Phys. Rev. D*, 76:115012, 2007.

[331] Paul Posch. Enhancement of h —> gamma gamma in the Two Higgs Doublet Model Type I. *Phys. Lett. B*, 696:447–453, 2011.

[332] Georges Aad et al. Measurement of the properties of Higgs boson production at $\sqrt{s} = 13$ TeV in the $H \to \gamma\gamma$ channel using 139 fb^{-1} of pp collision data with the ATLAS experiment. *JHEP*, 07:088, 2023.

[333] Michael Benzke, Seung J. Lee, Matthias Neubert, and Gil Paz. Long-Distance Dominance of the CP Asymmetry in $B \to X_{s,d} + \gamma$ Decays. *Phys. Rev. Lett.*, 106:141801, 2011.

[334] S. Watanuki et al. Measurements of isospin asymmetry and difference of direct CP asymmetries in inclusive $B \to X_s\gamma$ decays. *Phys. Rev. D*, 99(3):032012, 2019.

[335] W. Altmannshofer et al. The Belle II Physics Book. *PTEP*, 2019(12):123C01, 2019. [Erratum: PTEP 2020, 029201 (2020)].

[336] J. W. Martin. Current status of neutron electric dipole moment experiments. *J. Phys. Conf. Ser.*, 1643(1):012002, 2020.

[337] A. Riotto. The More relaxed supersymmetric electroweak baryogenesis. *Phys. Rev. D*, 58:095009, 1998.

[338] Kimmo Kainulainen. CP-violating transport theory for electroweak baryogenesis with thermal corrections. *JCAP*, 11(11):042, 2021.

[339] Marieke Postma, Jorinde van de Vis, and Graham White. Resummation and cancellation of the VIA source in electroweak baryogenesis. *JHEP*, 12:121, 2022.

[340] Syuhei Iguro and Yuji Omura. The direct CP violation in a general two Higgs doublet model. *JHEP*, 08:098, 2019.

[341] Wei-Shu Hou and Girish Kumar. Strange processes in general two Higgs doublet model. *JHEP*, 10:129, 2022.

[342] Eduardo Cortina Gil et al. Measurement of the very rare $K^+ \to \pi^+ \nu\bar{\nu}$ decay. *JHEP*, 06:093, 2021.

[343] Michal Zamkovský et al. Measurement of the very rare $K^+ \to \pi^+ \nu\bar{\nu}$ decay. *PoS*, DISCRETE2020-2021:070, 2022.

[344] J. K. Ahn et al. Search for the $K_L \to \pi^0 \nu\bar{\nu}$ and $K_L \to \pi^0 X^0$ decays at the J-PARC KOTO experiment. *Phys. Rev. Lett.*, 122(2):021802, 2019.

[345] Yuval Grossman and Yosef Nir. K(L) —> pi0 neutrino anti-neutrino beyond the standard model. *Phys. Lett. B*, 398:163–168, 1997.

[346] Kazuya Aoki et al. Extension of the J-PARC Hadron Experimental Facility: Third White Paper. 10 2021.

[347] Andrzej J. Buras, Dario Buttazzo, Jennifer Girrbach-Noe, and Robert Knegjens. $K^+ \to \pi^+ \nu\bar{\nu}$ and $K_L \to \pi^0 \nu\bar{\nu}$ in the Standard Model: status and perspectives. *JHEP*, 11:033, 2015.

[348] J. R. Batley et al. A Precision measurement of direct CP violation in the decay of neutral kaons into two pions. *Phys. Lett. B*, 544:97–112, 2002.

[349] A. Alavi-Harati et al. Measurements of direct CP violation, CPT symmetry, and other parameters in the neutral kaon system. *Phys. Rev. D*, 67:012005, 2003. [Erratum: Phys.Rev.D 70, 079904 (2004)].

[350] E. Abouzaid et al. Precise Measurements of Direct CP Violation, CPT Symmetry, and Other Parameters in the Neutral Kaon System. *Phys. Rev. D*, 83:092001, 2011.

[351] T. Blum et al. $K \to \pi\pi$ $\Delta I = 3/2$ decay amplitude in the continuum limit. *Phys. Rev. D*, 91(7):074502, 2015.

[352] R. Abbott et al. Direct CP violation and the $\Delta I = 1/2$ rule in $K \to \pi\pi$ decay from the standard model. *Phys. Rev. D*, 102(5):054509, 2020.

[353] V. Cirigliano, H. Gisbert, A. Pich, and A. Rodríguez-Sánchez. Isospin-violating contributions to ϵ'/ϵ. *JHEP*, 02:032, 2020.

[354] Masashi Aiko, Shinya Kanemura, and Kodai Sakurai. Radiative corrections to decays of charged Higgs bosons in two Higgs doublet models. *Nucl. Phys. B*, 973:115581, 2021.

[355] Shinya Kanemura, Mariko Kikuchi, and Kei Yagyu. Next-to-leading order corrections to decays of the heavier CP-even Higgs boson in the two Higgs doublet model. *Nucl. Phys. B*, 983:115906, 2022.

[356] R. Aaij et al. Implications of LHCb measurements and future prospects. *Eur. Phys. J. C*, 73(4):2373, 2013.

[357] D. Jeans and G. W. Wilson. Measuring the CP state of tau lepton pairs from Higgs decay at the ILC. *Phys. Rev. D*, 98(1):013007, 2018.

[358] Shinya Kanemura, Mitsunori Kubota, and Kei Yagyu. Testing aligned CP-violating Higgs sector at future lepton colliders. *JHEP*, 04:144, 2021.

[359] Katsuya Hashino, Ryusuke Jinno, Mitsuru Kakizaki, Shinya Kanemura, Tomo Takahashi, and Masahiro Takimoto. Selecting models of first-order phase transitions using the synergy between collider and gravitational-wave experiments. *Phys. Rev. D*, 99(7):075011, 2019.

[360] James M. Cline and Benoit Laurent. Electroweak baryogenesis from light fermion sources: A critical study. *Phys. Rev. D*, 104(8):083507, 2021.

[361] A. Cerri et al. Report from Working Group 4: Opportunities in Flavour Physics at the HL-LHC and HE-LHC. *CERN Yellow Rep. Monogr.*, 7:867–1158, 2019.

[362] Wei-Shu Hou, Ting-Hsiang Hsu, and Tanmoy Modak. Constraining the $t \to u$ flavor changing neutral Higgs coupling at the LHC. *Phys. Rev. D*, 102(5):055006, 2020.

[363] Syuhei Iguro and Kazuhiro Tobe. $R(D^{(*)})$ in a general two Higgs doublet model. *Nucl. Phys. B*, 925:560–606, 2017.

[364] Dilip Kumar Ghosh, Wei-Shu Hou, and Tanmoy Modak. Sub-TeV H^+ Boson Production as Probe of Extra Top Yukawa Couplings. *Phys. Rev. Lett.*, 125(22):221801, 2020.

[365] Shinya Kanemura, Ryo Nagai, and Masanori Tanaka. Electroweak phase transition in the nearly aligned Higgs effective field theory. *JHEP*, 06:027, 2022.

[366] Filippo Sala. A bound on the charm chromo-EDM and its implications. *JHEP*, 03:061, 2014.

[367] Ryohei Matsumiya et al. The Precision nEDM Measurement with UltraCold Neutrons at TRIUMF. In *24th International Symposium on Spin Physics*, 7 2022.

[368] Michel Capdequi Peyranere, Howard E. Haber, and Paulo Irulegui. H+- —> W+- gamma and H+- —> W+- Z in two Higgs doublet models. 1. The Large fermion mass limit. *Phys. Rev. D*, 44:191–201, 1991.

[369] Shinya Kanemura. Enhancement of loop induced $H^{\pm}W^{\mp}Z^0$ vertex in two Higgs doublet model. *Phys. Rev. D*, 61:095001, 2000.

[370] J. L. Diaz-Cruz, J. Hernandez-Sanchez, and J. J. Toscano. An Effective Lagrangian description of charged Higgs decays $H^+ \to W^+\gamma$, W^+Z and W^+ h0. *Phys. Lett. B*, 512:339–348, 2001.

[371] Abdesslam Arhrib, Rachid Benbrik, and Mohamed Chabab. Charged Higgs bosons decays $H^{\pm} \to W^{\pm}$ (γ, Z) revisited. *J. Phys. G*, 34:907–928, 2007.

[372] Gauhar Abbas, Diganta Das, and Monalisa Patra. Loop induced $H^{\pm} \to W^{\pm}Z$ decays in the aligned two-Higgs-doublet model. *Phys. Rev. D*, 98(11):115013, 2018.

[373] A. Mendez and A. Pomarol. One loop induced $H^{+}W^{+}Z$ vertex in the minimal supersymmetry model. *Nucl. Phys. B*, 349:369–380, 1991.

[374] Abdesslam Arhrib, Rachid Benbrik, and Mohamed Chabab. Left-right squarks mixings effects in charged Higgs bosons decays $H^{\pm} \to W^{\pm}$ (γ, Z) in the MSSM. *Phys. Lett. B*, 644:248–255, 2007.

[375] Abdesslam Arhrib, Rachid Benbrik, Mohamed Chabab, Wei Ting Chang, and Tzu-Chiang Yuan. CP violation in Charged Higgs Bosons decays $\mathrm{H}^{\pm} \to \mathrm{W}^{\pm}$ (γ, Z) in the Minimal Supersymmetric Standard Model (MSSM). *Int. J. Mod. Phys. A*, 22:6022–6032, 2007.

[376] Howard Georgi and Marie Machacek. DOUBLY CHARGED HIGGS BOSONS. *Nucl. Phys. B*, 262:463–477, 1985.

[377] Michael S. Chanowitz and Mitchell Golden. Higgs Boson Triplets With M (W) = M (Z) $\cos\theta\omega$. *Phys. Lett. B*, 165:105–108, 1985.

[378] Stefano Moretti, Diana Rojas, and Kei Yagyu. Enhancement of the $H^{\pm}W^{\mp}Z$ vertex in the three scalar doublet model. *JHEP*, 08:116, 2015.

[379] Nabarun Chakrabarty, Indrani Chakraborty, and Dilip Kumar Ghosh. Fingerprinting the contribution of colored scalars to the $H^{+}W^{-}Z(\gamma)$ vertex. *Eur. Phys. J. C*, 80(12):1120, 2020.

[380] Rohini Godbole, Biswarup Mukhopadhyaya, and Marek Nowakowski. Triplet Higgs bosons at e+ e- colliders. *Phys. Lett. B*, 352:388–393, 1995.

[381] King-man Cheung, Roger J. N. Phillips, and Apostolos Pilaftsis. Signatures of Higgs triplet representations at TeV e+ e- colliders. *Phys. Rev. D*, 51:4731–4737, 1995.

[382] Dilip Kumar Ghosh, Rohini M. Godbole, and Biswarup Mukhopadhyaya. Unusual charged Higgs signals at LEP-2. *Phys. Rev. D*, 55:3150–3155, 1997.

[383] Shinya Kanemura. Possible enhancement of the e+ e- —> H+- W-+ cross-section in the two Higgs doublet model. *Eur. Phys. J. C*, 17:473–486, 2000.

[384] Shinya Kanemura, Stefano Moretti, and Kosuke Odagiri. Single charged Higgs boson production at next generation linear colliders. *JHEP*, 02:011, 2001.

[385] K. Huitu, J. Laitinen, J. Maalampi, and N. Romanenko. Singly charged Higgses at linear collider. *Nucl. Phys. B*, 598:13–29, 2001.

[386] Kingman Cheung and Dilip Kumar Ghosh. Triplet Higgs boson at hadron colliders. *JHEP*, 11:048, 2002.

[387] Heather E. Logan and Shu-fang Su. Associated Production of $H^{\pm}$ and W^{mp} in High-Energy $e^{+}e^{-}$ Collisions in the Minimal Supersymmetric Standard Model. *Phys. Rev. D*, 66:035001, 2002.

[388] Eri Asakawa and Shinya Kanemura. The H+- W-+ Z0 vertex and single charged Higgs boson production via W Z fusion at the large hadron collider. *Phys. Lett. B*, 626:111–119, 2005.

[389] Eri Asakawa, Shinya Kanemura, and Junichi Kanzaki. Potential for measuring the H+- W-+ Z0 vertex from WZ fusion at the Large Hadron Collider. *Phys. Rev. D*, 75:075022, 2007.

[390] Shinya Kanemura, Kei Yagyu, and Kazuya Yanase. Testing Higgs models via the $H^{\pm}W^{\mp}Z$ vertex by a recoil method at the International Linear Collider. *Phys. Rev. D*, 83:075018, 2011.

[391] Cheng-Wei Chiang, Shinya Kanemura, and Kei Yagyu. Novel constraint on the parameter space of the Georgi-Machacek model with current LHC data. *Phys. Rev. D*, 90(11):115025, 2014.

[392] Cheng-Wei Chiang, Shinya Kanemura, and Kei Yagyu. Phenomenology of the Georgi-Machacek model at future electron-positron colliders. *Phys. Rev. D*, 93(5):055002, 2016.

[393] Amit Adhikary, Nabarun Chakrabarty, Indrani Chakraborty, and Jayita Lahiri. Probing the $H^{\pm}W^{\mp}Z$ interaction at the high energy upgrade of the LHC. *Eur. Phys. J. C*, 81(6):554, 2021.

[394] J. F. Gunion, Gordon L. Kane, and Jose Wudka. Search Techniques for Charged and Neutral Intermediate Mass Higgs Bosons. *Nucl. Phys. B*, 299:231–278, 1988.

[395] Sreerup Raychaudhuri and Amitava Raychaudhuri. Detection of charged Higgs bosons through the rare decay H+ —> W+ gamma. *Phys. Lett. B*, 297:159–165, 1992.

[396] S. Raychaudhuri and A. Raychaudhuri. Rare decay H+ —> W+ gamma in the minimal supersymmetric standard model. *Phys. Rev. D*, 50:412–427, 1994.

[397] J. Hernandez-Sanchez, M. A. Perez, G. Tavares-Velasco, and J. J. Toscano. Decay H+ —> W+ gamma in a nonlinear R(xi)-gauge. *Phys. Rev. D*, 69:095008, 2004.

[398] J. E. Barradas Guevara, F. C. Cazarez Bush, A. Cordero Cid, O. Felix Beltran, J. Hernandez Sanchez, and R. Noriega Papaqui. Implications of Yukawa Textures in the decay $H^+ \to W^+\gamma$ within the 2HDM-III. *J. Phys. G*, 37:115008, 2010.

[399] John M. Cornwall, David N. Levin, and George Tiktopoulos. Derivation of Gauge Invariance from High-Energy Unitarity Bounds on the s Matrix. *Phys. Rev. D*, 10:1145, 1974. [Erratum: Phys.Rev.D 11, 972 (1975)].

[400] Gerard 't Hooft and M. J. G. Veltman. Scalar One Loop Integrals. *Nucl. Phys. B*, 153:365–401, 1979.

[401] G. Passarino and M. J. G. Veltman. One Loop Corrections for e+ e- Annihilation Into mu+ mu- in the Weinberg Model. *Nucl. Phys. B*, 160:151–207, 1979.

[402] Gustavo C. Branco, Luis Lavoura, and Joao P. Silva. *CP Violation*, volume 103. 1999.

[403] Sachio Komamiya. Searching for Charged Higgs Bosons at O (1/2-tev to 1-tev) e^+e^- Colliders. *Phys. Rev. D*, 38:2158, 1988.

[404] J. F. Gunion, L. Roszkowski, A. Turski, H. E. Haber, G. Gamberini, Boris Kayser, S. F. Novaes, Fredrick I. Olness, and J. Wudka. Production Mechanisms for Nonminimal Higgs Bosons at an e^+e^- Collider. *Phys. Rev. D*, 38:3444, 1988.

[405] S. Kanemura L. Humphrey and Y. Mura. In preparation.

[406] Kenzo Inoue, Akira Kakuto, Hiromasa Komatsu, and Seiichiro Takeshita. Low-Energy Parameters and Particle Masses in a Supersymmetric Grand Unified Model. *Prog. Theor. Phys.*, 67:1889, 1982.

[407] Ricardo A. Flores and Marc Sher. Higgs Masses in the Standard, Multi-Higgs and Supersymmetric Models. *Annals Phys.*, 148:95, 1983.

[408] Dimitris Kominis and R. Sekhar Chivukula. Triviality bounds in two doublet models. *Phys. Lett. B*, 304:152–158, 1993.

[409] P. M. Ferreira and D. R. T. Jones. Bounds on scalar masses in two Higgs doublet models. *JHEP*, 08:069, 2009.

[410] A. Goudelis, B. Herrmann, and O. Stål. Dark matter in the Inert Doublet Model after the discovery of a Higgs-like boson at the LHC. *JHEP*, 09:106, 2013.

[411] Debtosh Chowdhury and Otto Eberhardt. Global fits of the two-loop renormalized Two-Higgs-Doublet model with soft Z_2 breaking. *JHEP*, 11:052, 2015.

[412] Shinya Kanemura, Mariko Kikuchi, Kodai Sakurai, and Kei Yagyu. H-COUP: a program for one-loop corrected Higgs boson couplings in non-minimal Higgs sectors. *Comput. Phys. Commun.*, 233:134–144, 2018.

[413] Shinya Kanemura, Mariko Kikuchi, Kentarou Mawatari, Kodai Sakurai, and Kei Yagyu. H-COUP Version 2: a program for one-loop corrected Higgs boson decays in non-minimal Higgs sectors. *Comput. Phys. Commun.*, 257:107512, 2020.

[414] Masashi Aiko, Shinya Kanemura, Mariko Kikuchi, Kodai Sakurai, and Kei Yagyu. H-COUP Version 3: A program for one-loop corrected decays of any Higgs bosons in non-minimal Higgs models. 11 2023.

[415] Shinya Kanemura, Eibun Senaha, Tetsuo Shindou, and Toshifumi Yamada. Electroweak phase transition and Higgs boson couplings in the model based on supersymmetric strong dynamics. *JHEP*, 05:066, 2013.

[416] Shinya Kanemura, Eibun Senaha, and Tetsuo Shindou. First-order electroweak phase transition powered by additional F-term loop effects in an extended supersymmetric Higgs sector. *Phys. Lett. B*, 706:40–45, 2011.

[417] Gerard 't Hooft and M. J. G. Veltman. Regularization and Renormalization of Gauge Fields. *Nucl. Phys. B*, 44:189–213, 1972.

[418] H. Georgi, Helen R. Quinn, and Steven Weinberg. Hierarchy of Interactions in Unified Gauge Theories. *Phys. Rev. Lett.*, 33:451–454, 1974.

[419] Steven Weinberg. Effective Gauge Theories. *Phys. Lett. B*, 91:51–55, 1980.

[420] Lawrence J. Hall. Grand Unification of Effective Gauge Theories. *Nucl. Phys. B*, 178:75–124, 1981.

[421] John R. Ellis, S. Kelley, and Dimitri V. Nanopoulos. A Detailed comparison of LEP data with the predictions of the minimal supersymmetric SU(5) GUT. *Nucl. Phys. B*, 373:55–72, 1992.

[422] John R. Ellis, S. Kelley, and Dimitri V. Nanopoulos. Constraints from gauge coupling unification on the scale of supersymmetry breaking. *Phys. Lett. B*, 287:95–100, 1992.

[423] Youichi Yamada. SUSY and GUT threshold effects in SUSY SU(5) models. *Z. Phys. C*, 60:83–94, 1993.

[424] Kaoru Hagiwara and Y. Yamada. Grand unification threshold effects in supersymmetric SU(5) models. *Phys. Rev. Lett.*, 70:709–712, 1993.

[425] Johannes Braathen, Mark D. Goodsell, Manuel E. Krauss, Toby Opferkuch, and Florian Staub. N-loop running should be combined with N-loop matching. *Phys. Rev. D*, 97(1):015011, 2018.

[426] Alexander Spencer-Smith. Higgs Vacuum Stability in a Mass-Dependent Renormalisation Scheme. 5 2014.

[427] P. A. Baikov, K. G. Chetyrkin, and J. H. Kühn. Five-Loop Running of the QCD coupling constant. *Phys. Rev. Lett.*, 118(8):082002, 2017.

[428] Thomas Luthe, Andreas Maier, Peter Marquard, and York Schroder. The five-loop Beta function for a general gauge group and anomalous dimensions beyond Feynman gauge. *JHEP*, 10:166, 2017.

[429] F. Herzog, B. Ruijl, T. Ueda, J. A. M. Vermaseren, and A. Vogt. The five-loop beta function of Yang-Mills theory with fermions. *JHEP*, 02:090, 2017.

[430] K. G. Chetyrkin, G. Falcioni, F. Herzog, and J. A. M. Vermaseren. Five-loop renormalisation of QCD in covariant gauges. *JHEP*, 10:179, 2017. [Addendum: JHEP 12, 006 (2017)].

[431] Alexander Bednyakov and Andrey Pikelner. Four-loop QCD MOM beta functions from the three-loop vertices at the symmetric point. *Phys. Rev. D*, 101(7):071502, 2020.

[432] A. De Rujula and H. Georgi. Counting Quarks in e+ e- Annihilation. *Phys. Rev. D*, 13:1296–1301, 1976.

[433] Howard Georgi and H. David Politzer. Freedom at Moderate Energies: Masses in Color Dynamics. *Phys. Rev. D*, 14:1829, 1976.

[434] D. A. Ross. Threshold Effects in Gauge Theories. *Nucl. Phys. B*, 140:1–30, 1978.

[435] J. Terrance Goldman and D. A. Ross. How Accurately Can We Estimate the Proton Lifetime in an SU(5) Grand Unified Model? *Nucl. Phys. B*, 171:273–300, 1980.

[436] Alon E. Faraggi and Benjamin Grinstein. Light Threshold Effects in Supersymmetric Grand Unified Theories. *Nucl. Phys. B*, 422:3–36, 1994.

[437] Jonathan Bagger, Konstantin T. Matchev, and Damien Pierce. Precision corrections to supersymmetric unification. *Phys. Lett. B*, 348:443–450, 1995.

[438] M. Bastero-Gil and J. Perez-Mercader. Effective couplings and perturbative unification. *Nucl. Phys. B*, 450:21–59, 1995.

[439] Michael Binger and Stanley J. Brodsky. Physical renormalization schemes and grand unification. *Phys. Rev. D*, 69:095007, 2004.

[440] F. Jegerlehner and O. V. Tarasov. Exact mass dependent two loop anti-alpha(s)(Q**2) in the background MOM renormalization scheme. *Nucl. Phys. B*, 549:481–498, 1999.

[441] Yang Ma and Xing-Gang Wu. Renormalization scheme dependence of high-order perturbative QCD predictions. *Phys. Rev. D*, 97(3):036024, 2018.

[442] R. H. Mason and J. A. Gracey. Kinematic scheme study of the O(a4) Bjorken sum rule and R ratio. *Phys. Rev. D*, 108(11):116018, 2023.

[443] Thomas Appelquist and J. Carazzone. Infrared Singularities and Massive Fields. *Phys. Rev. D*, 11:2856, 1975.

[444] Roger F. Dashen and Herbert Neuberger. How to Get an Upper Bound on the Higgs Mass. *Phys. Rev. Lett.*, 50:1897, 1983.

[445] R. Mertig, M. Bohm, and Ansgar Denner. FEYN CALC: Computer algebraic calculation of Feynman amplitudes. *Comput. Phys. Commun.*, 64:345–359, 1991.

[446] Vladyslav Shtabovenko, Rolf Mertig, and Frederik Orellana. New Developments in FeynCalc 9.0. *Comput. Phys. Commun.*, 207:432–444, 2016.

[447] Vladyslav Shtabovenko, Rolf Mertig, and Frederik Orellana. FeynCalc 9.3: New features and improvements. *Comput. Phys. Commun.*, 256:107478, 2020.

[448] J. Kublbeck, M. Bohm, and Ansgar Denner. Feyn Arts: Computer Algebraic Generation of Feynman Graphs and Amplitudes. *Comput. Phys. Commun.*, 60:165–180, 1990.

[449] Thomas Hahn. Generating Feynman diagrams and amplitudes with FeynArts 3. *Comput. Phys. Commun.*, 140:418–431, 2001.

[450] Neil D. Christensen and Claude Duhr. FeynRules - Feynman rules made easy. *Comput. Phys. Commun.*, 180:1614–1641, 2009.

[451] Adam Alloul, Neil D. Christensen, Céline Degrande, Claude Duhr, and Benjamin Fuks. FeynRules 2.0 - A complete toolbox for tree-level phenomenology. *Comput. Phys. Commun.*, 185:2250–2300, 2014.

[452] Thomas Hahn. Automatic loop calculations with FeynArts, FormCalc, and LoopTools. *Nucl. Phys. B Proc. Suppl.*, 89:231–236, 2000.

[453] Vladyslav Shtabovenko. FeynHelpers: Connecting FeynCalc to FIRE and Package-X. *Comput. Phys. Commun.*, 218:48–65, 2017.

[454] Howard E. Haber and Ralf Hempfling. The Renormalization group improved Higgs sector of the minimal supersymmetric model. *Phys. Rev. D*, 48:4280–4309, 1993.

[455] A. A. Slavnov. Ward Identities in Gauge Theories. *Theor. Math. Phys.*, 10:99–107, 1972.

[456] J. C. Taylor. Ward Identities and Charge Renormalization of the Yang-Mills Field. *Nucl. Phys. B*, 33:436–444, 1971.

[457] Anton Rebhan. Momentum Subtraction Scheme and the Background Field Method in QCD. *Z. Phys. C*, 30:309, 1986.

[458] Bryce S. DeWitt. Quantum Theory of Gravity. 2. The Manifestly Covariant Theory. *Phys. Rev.*, 162:1195–1239, 1967.

[459] Bryce S. DeWitt. Quantum Theory of Gravity. 3. Applications of the Covariant Theory. *Phys. Rev.*, 162:1239–1256, 1967.

[460] L. F. Abbott. The Background Field Method Beyond One Loop. *Nucl. Phys. B*, 185:189–203, 1981.

[461] Ansgar Denner, Georg Weiglein, and Stefan Dittmaier. Application of the background field method to the electroweak standard model. *Nucl. Phys. B*, 440:95–128, 1995.

[462] Celine Degrande. Automatic evaluation of UV and R2 terms for beyond the Standard Model Lagrangians: a proof-of-principle. *Comput. Phys. Commun.*, 197:239–262, 2015.

[463] Tomislav Prokopec, Michael G. Schmidt, and Steffen Weinstock. Transport equations for chiral fermions to order h bar and electroweak baryogenesis. Part 1. *Annals Phys.*, 314:208–265, 2004.

[464] Herbi K. Dreiner, Howard E. Haber, and Stephen P. Martin. *From Spinors to Supersymmetry*. Cambridge University Press, Cambridge, UK, 7 2023.